Plasma Physics Reports, Vol. 28, No. 3, 2002, pp. 171–176. From Fizika Plazmy, Vol. 28, No. 3, 2002, pp. 195–201.
Original English Text Copyright © 2002 by Tsytovich, Morfill.

DUSTY PLASMA

Collective Attraction of Equal-Sign Charged Grains in Plasmas[1]

V. N. Tsytovich* and G. E. Morfill**
**Institute of General Physics, Russian Academy of Sciences, ul. Vavilova 38, Moscow, 119991 Russia*
e-mail: tdytov@td.lpi.ac.ru
***Max-Planck Institut für Extraterrestrische Physik, 85740 Garching, Postfach 1312, Germany*
e-mail: gem@mpe.mpg.de

Received September 25, 2001

Abstract—It is shown that, in the presence of many grains embedded in a plasma, any two grains with the same charge sign can attract each other. The attraction is caused by collective effects. Both the strength of attraction and the distance at which the attraction is located depend on the average dust density. In the limit of strong collective interaction, the potential energy of interaction is found to be equal to the Coulomb interaction with an amplitude periodically changing its sign at a sequence of interdust distances. The condition for collective effects to dominate lead to a threshold condition that is fulfilled in existing experiments. The effect of collective attraction is applied for the physical interpretation of the observed phenomenon of the formation of dust crystals in laboratory experiments. *© 2002 MAIK “Nauka/Interperiodica”.*

1. INTRODUCTION

Experimental discovery of crystal states [1–5] formed by dust grains embedded in plasma leads to a dilemma for distinguishing the physical process responsible for the formation of dust crystals: *Is it related to strong coupling as in usual crystals or is it related to attraction forces between the grains?* The attraction of equal-sign charged particles is a new phenomenon not met in usual particle physics and could be partially related to the finite size of grains and to the possibility of them to absorb the plasma particles. The possibility of attraction between two grains with equal charge sign was considered theoretically in the recent publications [6–8], where it was shown that, to maintain the large charges, the grains should create the flux of plasma particles toward their surface and that the shadow of the plasma flux to one of the interacting grains by another grain creates an attractive bombardment force, which is inversely proportional to the square of interdust distance (as in the case of the Coulomb repulsion forces) and is proportional to the fourth power of dust size a. These attraction forces are relatively weak forces with an amplitude $(\lambda_{Di}/a)^2 \gg 1$ times less than the amplitude of the nonscreened Coulomb potential (a being the grain size and λ_{Di} being the ion Debye screening length). Since these forces are not screened, they can dominate Coulomb repulsion forces at the distances larger than the Debye screening length $\lambda_D \approx \lambda_{Di}$ and, therefore, can contribute to the process of dust crystal formation if the interdust distance is larger than the ion Debye screening length.

In the present paper, we discuss a new type of attraction force of electrostatic nature (not of bombardment nature), which can be substantially stronger than the bombardment shadow attraction forces for the parameters of existing experiments and which can have an amplitude approximately equal to the nonscreened Coulomb potential. The forces considered here are collective; i.e., they operate in the presence of many dust grains and depend on the average dust density. This collective attraction can determine the dust–dust interaction for the parameters of existing experiments. In the presence of effective dust–dust attraction, the dust crystals could be formed by these attraction forces and one can, therefore, assume that, when the collective attraction dominates, the observed dusty crystals will represent quite an unusual state of matter not found or not expected to be found previously in nature.

It is interesting to note that some indirect experimental evidence [9, 10] was found for the presence of attraction forces in the interaction of grains in the presently observed dusty crystals and in dusty plasmas preceding the transformation to the dust crystal state (laser pressure action on some grains in crystals, attraction of the near grains by a grain falling onto the linear dust crystal structure, etc.).

Theoretically, the possibility of dust attraction was first noticed in [11], where it was shown that the total electrostatic energy of two equal-sign charged grains embedded in plasma will decrease with decreasing interdust distance, rather than increase as was thought before. This effect is caused by a decrease in the grain charges and is absent in the case when the charges do not change with the distance. A decrease in the dust

---

[1] This article was submitted by the authors in English.

charges when they approach each other is a simple consequence of the charging process, which keeps the total potential at the grain surface close to the electron temperature T_e (floating potential condition). The law according to which the grain charge decreases was derived in [11] (see also [12]) and was confirmed by numerical simulations [13]. A decrease in the total electrostatic energy at $r \gg a$ follows from a simple algebra [11] showing that the change of the self-energy is opposite in sign and two times larger than the interaction energy, and it looks like the interaction energy changes the sign. Nevertheless, as is well known from [14] (see also argumentation given in [12]), in general, the forces acting on dust grains' cannot be calculated from the change of the total electrostatic energy. One need also to take into account the work produced by external sources that keep the fixed value of the potential at the grains surfaces. In thermal equilibrium, this work compensates for the change in self-energy [14]. The decrease in the total electrostatic energy with decreasing distance can be regarded as a possible reservoir of energy, which can cause attraction in nonequilibrium systems [15]. The electrostatic forces (even in nonequilibrium systems) can be calculated from the interaction energy. Note that the shadow attraction forces are related to the bombardment of the grain surface by the plasma particles and are not of electrostatic nature.

In this paper, we will consider only the electrostatic interaction and will show that the electrostatic interaction energy itself can change the sign when the collective effects are taken into account.

Note that in real plasma experiments [1–5], where the dust crystals are formed, the system cannot be in thermal equilibrium due to the rather fast absorption of plasma particles by grains on time scales several orders of magnitude less than the time of crystal formation. The constant rate of plasma particle absorption is necessary to keep the large grain charges. The plasma density is kept almost constant by the large rate of ionization. In the experiments cited above, the ionization sources are related to an external RF power that provides a homogeneous ionization with a constant rate, thus compensating the absorption of plasma particles on grains and keeping the plasma density constant. Such a system is obviously an open system. The statement we would like to prove is that, under conditions close to those of experiments [1–5], where the ionization source is approximately homogeneous in space, the interdust electrostatic potential energy changes its sign with interdust distance and the forces become attractive within a certain range of distances around r_i, where r_i is a set of certain interdust distances ($i = 1, 2, \ldots$). The attraction potential equals the opposite-sign Coulomb potential close to these distances r_i; i.e., within this range of distances, it is equal to $V_i = -Q^2/r_i$, where Q is the grain charge. The largest potential well is determined by the smallest r_i, whose value depends on the average dust density. This attraction well is large because it does not contain the small parameter a^2/λ_D^2 as for the shadow bombardment forces. The effect of attraction that we will consider is purely collective; i.e., it occurs only in the presence of many grains. It depends strongly on the average grain density, and the two interacting grains are just any two test grains from the "sea" of other grains. The presence of many grains provides a stationary state where the plasma particle absorption on the grains is balanced by the external ionization source. The interaction between two test grains is regarded as a perturbation of this state. For the parameters of existing experiments, where $a^2/\lambda_{Di}^2 \approx 2 \times 10^{-2}$, the collective attraction forces exceed substantially the shadow attraction forces. Estimates show that the dust density in the existing experiments is sufficiently high to provide collective grain attraction. We will give simple criteria to distinguish between the case where the crystals are formed by strong coupling and the case where the crystals are formed by the attraction forces as discussed here. In the existing experiments, these criteria are almost satisfied (the parameter that should be much less than unity is on the order of 1/4–1/2), and it is not difficult to satisfy these criteria with a better accuracy by a rather moderate increase in the grain size. If this will be performed, the observed dust crystals will surely represent a new state of matter formed by attraction forces between charges of equal sign, rather than by strong coupling as in ordinary matter. For the parameters of the present experiments, we found that the attraction forces can play a more important role than was thought before (because collective attraction was previously not taken into account), although strong coupling can also be important.

2. COLLECTIVE GRAIN ATTRACTION

Let us consider a plasma consisting of electrons, singly charged positive ions, and negatively charged dust grains. We introduce the parameter $P \equiv n_d Z_d / n_i$, which is equal to the ratio of the dust charge density to the ion charge density. Here, $Z_d = |Q/e|$ is the grain charge number, n_d is the dust density, and n_i is the ion density. The plasma in the ground state is characterized by the parameter $P_0 = n_d Z_{d,\,0}/n_{i,\,0}$ (index 0 is used to mark the ground state). The parameter P_0 is a natural parameter to characterize the contribution of grains to the ground state, because the grain in the ground state changes mainly the electrostatic charge balance. This parameter will be considered the main parameter characterizing the basic (ground) state. Note that there exist several possibilities to chose other parameters as the main characteristics of the ground state (another parameter that can be chosen is, e.g., the ionization rate); however, all of them are related to each other, leaving only one parameter free. The two test grains will perturb the ground state, which causes their interaction [16]. The parameter P will then differ from P_0.

We will assume that $\tau \equiv T_i/T_e \ll 1$ because, for existing experiments, $\tau \approx (1–2) \times 10^{-2}$. We also assume for simplicity that the charges of two interacting grains are equal to each other.

We can introduce the relative ion density $n = n_i/n_{i,0}$ and the relative electron density $n^e = n_e/n_{i,0}$. The ground state is determined by two conditions—the quasineutrality condition and the condition for the balance between the absorption of plasma by grains and plasma ionization. From the quasineutrality condition, we have

$$n_0^e = 1 - P_0 \tag{1}$$

($n_0 = 1$ by definition), which shows that the ratio between the electron and ion densities in the ground state is determined by the parameter P_0. The grain charge depends only on this ratio (if the ratio between the ion and electron temperatures τ is fixed). If n_0^e is known, the charging equation allows us to find the dimensionless dust charge $z = Z_d e^2/aT_e$. Thus, the grain charge $Z_{d,0}$ in the ground state is determined by the value of P_0; therefore, the ratio between the dust and ion densities is known for a given value of P_0.

In the second equation for the ground state, we use a simplest ionization model, in which the ionization rate dn_i/dt is assumed to be proportional to the electron density: $dn_i/dt = \nu_i n^e$ with ν_i being the ionization coefficient. Then, the ionization rate in the ground state can be expressed through the parameter P_0 and through the ionization coefficient ν_i. Since the rate of plasma absorption on the grains is proportional to nP, this rate in the ground state is also determined only by P_0 (because $n_0 = 1$). Thus, the balance between the absorption and the ionization processes gives the ionization coefficient as a function of P_0:

$$\nu_i(1 - P_0) = -\alpha_{\text{ch}} P_0, \tag{2}$$

where α_{ch} is a constant coefficient of absorption of ions on grains [17]. Thus, all the parameters of the ground state are expressed through P_0.

We will assume that, for the interaction between two test dust grains at large distances (such that the collective effects are important), the linear approximation for the responses can be used to find the electrostatic potential of each grain. This assumption is reasonable because, in experiments, the separation of grains is much larger than their size and usually larger than λ_{Di}. The assumption that the collective effects in the interaction occur at large distances can be checked from the final results, which can give some restrictions on the value of the parameter P_0 (see below). If the potential of one grain at the distance r from the other grain is $\phi(\mathbf{r})$, the potential of interaction of the two grains will be $Q\phi(\mathbf{r})$. Since the potential of the grain can be described in the linear approximation by a static dielectric constant $\epsilon_{\mathbf{k}}$, we have, for the electrostatic energy $V(\mathbf{r})$ of two interacting grains,

$$V(\mathbf{r}) = \frac{Q^2}{2\pi^2}\int \frac{\exp(i\mathbf{k}\cdot\mathbf{r})}{k^2\epsilon_{\mathbf{k}}}. \tag{3}$$

The collective effects do change the usual static dielectric constant. The possibility of attraction appears in the case where the dielectric constant $\epsilon_{\mathbf{k}}$ is negative within a certain range of wavenumbers k, which means the possibility of the change of the sign of V. The two particles can be any two probe particles in the sea of dust particles. In this sense, we will consider the collective effect in dust–dust interaction, depending on the parameter P_0 (the average dust charge density).

In order to describe the perturbations of the ground state and determine the static dielectric constant, we will use the time-independent balance equations. In particular, we will use the time-independent ion continuity equation with the term $(\partial/\partial\mathbf{r})n\mathbf{u}$ on the left-hand side and two terms on the right-hand side: the ionization source n^e/τ_i and the plasma sink $\alpha_{\text{ch}}Pn$, where $\mathbf{u}$ is the ion drift velocity appearing because of the perturbations of the ground state; τ_i is the ionization coefficient, which can be expressed through P_0 by Eq. (2); and α_{ch} is the absorption coefficient, directly related to the dust charging process [17]. If the distance is normalized to the mean free path (see below) and the ion drift velocity is normalized to $\sqrt{2}v_{Ti}$, then the absorption coefficient is equal to $1/2\sqrt{\pi}$. Another two equations for perturbations are the ion and electron force balance equations. The ion force balance equation contains the electric field force $e\mathbf{E}$ due to electric fields appearing in the perturbed state, the ion friction force on dust, and the ion pressure force. The ion friction is determined by the ion–dust collisions [17], whose rate is on the order of $\nu_{\text{ch}}P_0 \approx v_{Ti}P_0 a/\lambda_{Di}^2$ and the characteristic mean free path for ion–dust collisions is on the order of $\lambda_{id} \approx \lambda_{Di}^2/aP_0$, where v_{Ti} is the ion thermal velocity and λ_{Di} is the ion Debye radius. In the ion pressure force, we take into account only the change of the ion density, assuming that the ion temperature does not change (this is reasonable under conditions of experiments, where the ion temperature is determined by ion–neutral collisions and is almost constant). The electron force balance equation contains only the electric field force and the electron pressure force. Then, the linearized system of equations in dimensionless units takes a rather simple form:

$$i\mathbf{k}\cdot\mathbf{u} = \frac{1}{\tau_i}\delta n_e - P_0\alpha_{\text{ch}}\delta n - \frac{P_0}{z_0}\alpha_{\text{ch}}\delta z, \tag{4}$$

$$e\mathbf{E} = -\frac{1}{n_{e0}}i\mathbf{k}\delta n_e, \tag{5}$$

$$e\mathbf{E} = \tau i\mathbf{k}\delta n + \alpha_{\text{dr}}P_0 z_0\mathbf{u}, \tag{6}$$

where the coefficient in the ion friction force α_{dr} for the same normalization is equal to $(2/3\sqrt{\pi})\ln\Lambda$ ($\ln\Lambda$ being the Coulomb logarithm), **E** is in units of $T_e a/e\lambda_{Di}^2$, and **k** is in units of the inverse mean free path for ion–dust collisions. We take into account the change of the dust charge in perturbations $z = Z_d e^2/aT_e = z_0 + \delta z$ (z_0 being the dust charge in the ground state). The dust charge variations δz, which can be expressed through the electron and ion density perturbations by using the charging equation, will then depend on the wavenumber k. Thus, Eq. (4) takes into account the change of dust charges with the interdust distance. The openness of the system due to the charging effect and the ion friction on dust introduces the most important qualitative changes in the static dielectric response, while the change of the dust charge with distance changes the attraction forces quantitatively. The dielectric constant found from Eqs. (5) and (6) (in conventional units) is

$$\epsilon_k = 1 + \frac{\tau}{\lambda_{Di}^2 k^2}\left[1 - P_0 + \frac{\left(1 - \dfrac{P_0^2 a^2 \alpha_{\mathrm{dr}}\alpha_{\mathrm{ch}} z_0^2}{k^2\lambda_{Di}^4(1+z_0)}\right)}{\left(\tau + \dfrac{P_0^2 a^2 \alpha_{\mathrm{dr}}\alpha_{\mathrm{ch}} z_0^2}{k^2\lambda_{Di}^4(1+z_0)}\right)}\right]. \qquad (7)$$

The dielectric constant indeed can be negative for $k \ll aP_0 z_0/\lambda_{Di}^2\sqrt{(1+z_0)}$. In the limit $P_0 \longrightarrow 0$, expression (7) corresponds to the usual sum of the permittivity of free space (unity) and the two terms corresponding to the electron screening contribution (the first term) and the ion screening contribution (the second term). Integration over k in the expression for the interaction energy (3) can easily be performed by the residues of the poles determined by a quadratic equation for k^2. The result contains two terms with the $1/r$ factor in front of them. One of them corresponds to the exponential screening interaction and another corresponds to the interaction with the cosinusoidal variation in the electrostatic energy in space (periodic change of the energy sign with distance); i.e., it contains a series of attraction minimums. The general form of interaction is

$$V = \frac{Z_d^2 e^2}{r}\left[\nu_a \exp\left(-s_a\frac{r}{\lambda_{Di}}\right) + \nu_b\cos\left(s_b\frac{r}{\lambda_{Di}}\right)\right], \qquad (8)$$

with the coefficients ν_a, s_a, ν_b, and s_b depending on τ, P_0, and η_{col}, where

$$\eta_{\mathrm{col}} = \frac{a^2 P_0^2 z_0^2 \alpha_{\mathrm{dr}}\alpha_{\mathrm{ch}}}{(1+z_0)\lambda_{Di}^2}. \qquad (9)$$

We discuss separately all these coefficients. The first term in expression (8) describes the exponentially screened interaction, where

$$s_a^2 = \frac{1}{2\tau}\left[\sqrt{[(\eta_{\mathrm{col}} + \tau + \tau^2(1-P_0)]^2 + 4\eta_{\mathrm{col}}\tau^2 P_0} + \eta_{\mathrm{col}} + \tau + \tau^2(1-P_0))\right] \approx \left(1 + \frac{\eta_{\mathrm{col}}}{\tau}\right). \qquad (10)$$

The last approximate expression is written for $\tau \ll 1$ and $\eta_{\mathrm{col}} \ll 1$. In the limit $\eta_{\mathrm{col}} \ll \tau$, the exact expression (10) gives $s_a^2 = 1 + \tau(1 - P_0)$, which corresponds exactly to the noncollective expression for the sum of the electron and ion Debye screening effects. In the limit $\eta_{\mathrm{col}} \gg \tau$, we have $s_a^2 = \eta_{\mathrm{col}}/\tau \gg 1$; i.e., the collective effects strongly decrease the screening length, so that it becomes much smaller than the ion Debye length by a factor of $\sqrt{\eta_{\mathrm{col}}}/\tau \gg 1$. The coefficient in front of the exponent is

$$\nu_a = \frac{1}{2}\left[1 + \frac{\tau + \tau^2(1-P_0) - \eta_{\mathrm{col}}}{\sqrt{[\eta_{\mathrm{col}} + \tau + \tau^2(1-P_0)]^2 + 4\eta_{\mathrm{col}}\tau^2 P_0}}\right] \approx \frac{\tau}{\eta_{\mathrm{col}} + \tau}. \qquad (11)$$

For $\eta_{\mathrm{col}} \ll \tau$, coefficient (11) equals unity as for the usual Debye screening, while for $\eta_{\mathrm{col}} \gg \tau$, the coefficient ν_a is η_{col}/τ times less than the usual one. This means also a substantial decrease in the Coulomb potential at all distances including that at the grain surface and, therefore, describes the collective lowering of the grain charge.

The period of the cosinusoidal change of the potential is determined by

$$s_b^2 = \frac{1}{2\tau}\left[\sqrt{[(\eta_{\mathrm{col}} + \tau + \tau^2(1-P_0)]^2 + 4\eta_{\mathrm{col}}\tau^2 P_0} - (\eta_{\mathrm{col}} + \tau + \tau^2(1-P_0))\right] \approx \frac{\eta_{\mathrm{col}}\tau P_0}{\eta_{\mathrm{col}} + \tau + \tau^2(1-P_0)}. \qquad (12)$$

For $\eta \ll \tau \ll 1$, we have $s_b^2 \approx \eta_{\mathrm{col}} P_0$; therefore, the cosinusoidal part of the potential creates the first attraction well at the distance $\lambda_{Di}\pi/2\sqrt{\eta_{\mathrm{col}} P_0}$, which is much larger than λ_{Di}. In the opposite limit $\eta_{\mathrm{col}} \gg \tau$, we find $s_b^2 \approx \tau P_0$, which correspond to the distances $1/\sqrt{\tau P_0}$ times larger than λ_{Di}. The coefficient in front of the cosinusoidal part of the potential is

$$\nu_b \approx \frac{\eta_{\mathrm{col}}}{\eta_{\mathrm{col}} + \tau + \tau^2(1-P_0)} \times \left[1 + \frac{\tau^2 P_0}{\eta_{\mathrm{col}} + \tau + \tau^2(1-P_0)}\right]. \qquad (13)$$

For $\eta_{\mathrm{col}} \ll \tau \ll 1$, we find $\nu_b \approx \eta_{\mathrm{col}}/\tau \ll 1$, which means that, in this case, the attraction force can exceed the repulsion force only for the distances where the repulsion is exponentially screened. In the opposite limit, when $\eta_{\mathrm{col}} \gg \tau$, we find that $\nu_b \approx 1$. Since, in this limit, the coefficient by the repulsion force is small ($\nu_a \approx \tau/\eta_{\mathrm{col}} \ll 1$), the cosinusoidal term dominates at all distances: it describes repulsion at small distances, and the location of the first attraction minimum corresponds to $\pi\lambda_{Di}/2\sqrt{\tau P_0}$. For completeness, we write the approximate expression for the total potential energy for $\tau \ll 1$ in the two limits. For $\eta_{\mathrm{col}} \ll \tau$, we have

$$V \approx \frac{Z_d^2 e^2}{r}\left[\exp\left(-\frac{r}{\lambda_{Di}}\right) + \frac{\eta_{\mathrm{col}}}{\tau}\cos\left(\sqrt{\eta_{\mathrm{col}} P_0}\frac{r}{\lambda_{Di}}\right)\right], \quad (14)$$

and, for $\eta_{\mathrm{col}} \gg \tau$, we have

$$V \approx \frac{Z_d^2 e^2}{r}\left[\frac{\tau}{\eta_{\mathrm{col}}}\exp\left(-\sqrt{\frac{\eta_{\mathrm{col}}}{\tau}}\frac{r}{\lambda_{Di}}\right) + \cos\left(\sqrt{\tau P_0}\frac{r}{\lambda_{Di}}\right)\right]. \quad (15)$$

The cosinusoidal-type force was first found in [18] for a plasma source independent of the electron density and without allowance for the ion friction force; therefore, the results of [18] differ from that given here both for the attraction length and for the strength of the attraction force. The strength of the attraction force found in [16] was much smaller than that found here. We used here a model where the ionization source is proportional to the electron density, which is the most reasonable assumption for the RF plasma used in present-day experiments. The collective parameter found here is proportional to the product of α_{dr} and α_{ch}, which shows that the simultaneous presence of both charging and ion friction processes is important.

In calculations presented above, we neglected the ion–neutral collisions; the results are therefore valid for the case where the interdust distance is less than the ion–neutral mean free path λ_{in}. The attraction forces can be obtained in the case where the distance between the two dust grains is larger than the ion–neutral mean free path, when the ion–neutral friction should be substituted for the ion–dust friction and when the effect of ion diffusion in a neutral gas should be taken into account in the continuity equation. It appears that, for $\tau \ll 1$, diffusion can be neglected (finally, in the force balance equation, it contributes τ^{-1} times less than the ion pressure force). The balance between the plasma sink and ionization source is determined by the charging process in the way it was described above. Then, the only change in the results is the value of the collective parameter η_{col}, which now depends on the ion–neutral mean free path λ_{in}. We denote the new collective parameter as $\eta_{\mathrm{col,\,in}}$. Simple calculations yield

$$\eta_{\mathrm{col,\,in}} = \frac{\tau P_0 \alpha_{\mathrm{ch}} z_0}{1 + z_0}\frac{a}{\lambda_{\mathrm{in}}}. \quad (16)$$

Since $a \ll \lambda_{\mathrm{in}}$, the parameter $\eta_{\mathrm{col,\,in}}$ is always less than τ, which means that, in the case where the ion–neutral collisions dominate, the collective effects are described by expression (14) and the attraction occurs at the distances where the Debye screened part of the potential is small. Since the ratio $\eta_{\mathrm{col,\,in}}/\tau$ does not depend on τ, the attraction can dominate for $\exp(-r/\lambda_{Di}) \ll aP_0/\lambda_{\mathrm{in}}$, although the position of the first minimum $\approx \lambda_{Di}\lambda_{\mathrm{in}}/aP_0\tau$ depends strongly on τ.

3. COMPARISON WITH OTHER ATTRACTION FORCES: THRESHOLD CONDITIONS

Another type of attraction between the grains, which is known as shadow forces [6–8], is related to the shadowing of the plasma flux toward one of the interacting dust grains by another grain. The shadow forces are λ_{Di}^2/a^2 times less than the Coulomb forces and, thus, not being screened, can operate only at distances larger than the Debye screening length. The collective forces that we discussed here are also not screened and are proportional to the parameter P_0^2, while the shadow force does not depend on P_0. Thus, the shadow forces can dominate only at a rather small value of the parameter P_0. For present-day experiments, where P_0 is on the order of unity, the collective forces are more important. Indeed, the coefficient in front of them can be on the order of unity if $\eta_{\mathrm{col}} \gg \tau$, while the shadow forces always contain the small parameter $a^2/\lambda_{Di}^2 \ll 1$. Only at $\eta_{\mathrm{col}} \ll \tau$, the collective forces contain the same small parameter a^2/λ_{Di}^2 as the shadow forces do. Then, for $P_0 \approx 1$, the collective attraction forces will be of the same order of magnitude as the shadow forces.

The threshold condition $\eta_{\mathrm{col}} > \tau$ for the collective attraction to dominate can be easily satisfied in present experiments because, in experiments, $\tau \approx 10^{-2}$, while $a/\lambda_{Di} \approx 1/7$–$1/5$ and $a^2/\lambda_{Di}^2 \approx (2–4) \times 10^{-2}$. There will be a larger contribution of collective attraction if the size of the grains will be larger.

The other threshold condition is due to the possible contribution of the ion–neutral collisions. The strong collective attraction is present if the ion–neutral collision mean free path λ_{in} is much larger than the charging length λ_{Di}^2/a. This is satisfied for the typical parameters of present experiments if $a \gg 1$ μm, which is usually the case for most of the present-day dust crystal experiments. However, this condition is not satisfied with a large margin. It depends strongly on the gas pressure and the grain size. It seems to be rather simple, in future experiments, to chose the parameters in such a way that this condition will be satisfied with a large margin.

Note that the new collective attraction creates many attraction minimums with the decreasing value of the potential well with the interdust distances. When we take into account only the first potential well, the form of the total potential is close to the molecular type potential, where the interaction is repulsive at small distances, while at large distances, it is attractive. The spatial dependence of the dust interaction potential, having many potential wells, is similar to that of the effective interaction or correlation functions in crystals and liquids.

It is possible to experimentally distinguish the cases where the crystal is formed by the strong interaction in purely Coulomb systems and the case where the crystal is formed by the collective attraction forces discussed here. The criteria contains the known Γ factor defined by the expression

$$\Gamma = \frac{Q^2 n_d^{1/3}}{T_d}. \quad (17)$$

For Coulomb systems, the transition to the crystal state occurs at $\Gamma \gg 1$ and usually Γ should be on the order of 10^2–10^3 or even higher, while, when the collective attraction operates and the intergrain distance corresponds to the minimum of the first potential well, the necessary condition for a transition to the crystal state is $\Gamma > 1$. This big difference in thresholds can easily be checked experimentally. For this purpose, the experiments with larger size hollow dust grains are preferable.

Note that there exist a simple physical picture of the attraction considered in this paper. For the described attraction, the presence of ionization is rather important and the ionization should create the electron–ion pairs between the two interacting grains. The new created electrons represent a rather mobile component and will be thrown away from the space between the grains (both grains repel them); then, they will adjust rapidly to a Boltzman distribution according to the local potential distribution. The new created ions are attracted by the grains and cannot not leave the interdust region freely due to the presence of the friction force. Therefore, on average, a positive charge density is accumulated between the grains, which causes dust attraction. In terms of interaction caused by wave exchange, this attraction can be regarded as being caused by the exchange of ionization waves, similar to the electron attraction in a superconducting state, which can be regarded as caused by the exchange of phonons.

Note also that, under the conditions considered, the initial state is also unstable against the ionization or structurization instabilities [16]. Investigation of these effects should include the nonlinear treatment of the ionization instability and the treatment of dust–dust interactions with nonlinear responses, which is beyond the scope of the present study. These effects will probably increase the positive charge between the grains and will increase the attraction.

ACKNOWLEDGMENTS

V.N. Tsytovich appreciates the hospitality during his stay in Garching at Max Plank Institute for Extraterrestrial Physics.

REFERENCES

1. H. Thomas, G. Morfill, V. Demmel, *et al.*, Phys. Rev. Lett. **73**, 652 (1994); H. M. Thomas and G. E. Morfill, Nature **379**, 806 (1996).
2. J. H. Chu and I. Lin, Physica **205**, 183 (1994).
3. A. Melzer, T. Trottenberg, and A. Piel, Phys. Lett. A **191**, 301 (1994).
4. W. Steel, D. Law, B. Annaratone, and J. Allen, in *Proceedings of the XXIII International Conference on Phenomena in Ionized Gases, Toulose, 1997,* Vol. 1, p. 194.
5. Y. Hayashi and K. Tachibana, Jpn. J. Appl. Phys. **33**, L804 (1994).
6. V. N. Tsytovich, Y. Khodataev, and R. Bingham, Comm. Plasma Phys. Control. Fusion **17**, 249 (1996).
7. A. M. Ignatov, Kratk. Soobshch. Fiz., Nos. 1–2, 58 (1995).
8. Ya. K. Khodataev, G. Morfill, and V. N. Tsytovich, J. Plasma Phys. (in press).
9. J. E. Allen and B. M. Annoratone, J. Plasma Phys. **7**, 397 (1999).
10. A. P. Nefedov, O. F. Petrov, and V. E. Fortov, Usp. Fiz. Nauk **167**, 1215 (1997) [Phys. Usp. **40**, 1163 (1997)].
11. V. N. Tsytovich, Comm. Plasma Phys. Control. Fusion **15**, 349 (1994).
12. S. Hamaguchi, Comm. Plasma Phys. Control. Fusion **18**, 95 (1997).
13. V. N. Tsytovich, Y. Khodataev, R. Bingham, and V. Tarakanov, in *Advances in Dusty Plasma*, Ed. by P. K. Shukla, D. A. Mendis, and T. Desai (World Scientific, Singapore, 1996), p. 212.
14. L. D. Landau and E. M. Lifshitz, *Electrodynamics of Continuous Media* (Nauka, Moscow, 1970; Pergamon, New York, 1984), Chap. 1.
15. S. V. Vladimirov and V. N. Tsytovich, Comments Mod. Phys. C **2**, C15 (2000).
16. G. Morfill and V. N. Tsytovich, Fiz. Plazmy **26**, 727 (2000) [Plasma Phys. Rep. **26**, 682 (2000)].
17. V. N. Tsytovich, Comments Mod. Phys. C **2**, 41 (1999).
18. V. N. Tsytovich and U. de Angelis, Phys. Plasmas **8**, 1141 (2001).

Plasma Physics Reports, Vol. 28, No. 3, 2002, pp. 177–182. Translated from Fizika Plazmy, Vol. 28, No. 3, 2002, pp. 202–207.
Original Russian Text Copyright © 2002 by Barinov, Budkov, Dolgachev, Maslennikov, Khodeev.

PLASMA DYNAMICS

Raising the Efficiency of a Plasma Opening Switch by Applying an External Magnetic Field

N. U. Barinov†, S. A. Budkov†, G. I. Dolgachev, D. D. Maslennikov, and I. A. Khodeev

Russian Research Centre Kurchatov Institute, pl. Kurchatova 1, Moscow, 123182 Russia

Received September 27, 2001

Abstract—The influence of an external magnetic field on the performance of a high-impedance plasma opening switch is studied experimentally. A 1.5-fold increase in the output voltage of a plasma opening switch operating in the erosion mode is achieved by applying an external magnetic field. The magnetic field strength and the parameters of the plasma opening switch at which the maximum output voltage is attained are determined. It is shown experimentally that the predicted dependence of the maximum output voltage on the Marx generator voltage, U_{POS} [MV] = 3.6 (U_{MG} [MV])$^{4/7}$, is confirmed experimentally. © *2002 MAIK “Nauka/Interperiodica”*.

1. INTRODUCTION

Plasma opening switches (POSs) are widely used in high-power pulsed technology as efficient and relatively inexpensive current sharpers. The possibility of creating super-powerful generators intended for experiments on inertial confinement fusion is currently being considered [1, 2]. Thus, the Baikal program [2, 3] is aimed at gaining a current pulse of 50 MA with a duration of about 150 ns and voltage of up to 10 MV. As an output stage, a POS is proposed. Operation of POS-based facilities in various modes was analyzed in [4] as a function of the plasma density. It was established that, in the MHD mode ($n \sim 10^{16}$–10^{17} cm^{-3}), high-density charges and currents can be passed through a POS and an output voltage of 2 MV can be obtained. In the EMHD mode ($n \sim 10^{14}$–10^{16} cm^{-3}) and in the “erosion” mode ($n \sim 10^{13}$–10^{15} cm^{-3}), the linear density of the charge passed through a POS (and, hence, the POS current) is limited. However, these modes permit one to obtain a higher voltage, which is only limited by the shunting effect of the electron currents. The POS voltage U_{POS} is thereby determined by the specific energy w_{p} spent on plasma erosion, i.e., ion acceleration: $U_{\mathrm{POS}} \sim \beta w_{\mathrm{p}}^{4/7}$. In the majority of devices, the density of the charge q passed through a POS is nearly constant; i.e., $w_{\mathrm{p}} = qU_{\mathrm{MG}}$ and, according to [4], the POS voltage is related to the output voltage of the Marx generator (MG) as

$$U_{\mathrm{POS}}[\mathrm{MV}] = \alpha(U_{\mathrm{MG}}[\mathrm{MV}])^{4/7}. \tag{1}$$

To suppress the electron leakage and increase the POS voltage, it is proposed to apply an external magnetic field. Experiments carried out in the Taina facility [5] showed that $\alpha \simeq 2.5$ MV$^{3/7}$ in a conventional POS and $\alpha \simeq 3.6$ MV$^{3/7}$ in a POS with an external magnetic field. These experiments were performed with the linear (along the circumference of the POS electrode) density of the charge passed through the POS $q_{\mathrm{L}} \le 2.5$–5 mC/cm. In the RS-20 facility [6] under the same conditions, the coefficient α was somewhat lower because of the creepage over the vacuum surface of the insulator.

The aim of this study is to experimentally investigate the influence of the external magnetic field on the performance of the modified RS-20 facility and the value of the charge density passed through a POS, as well as to refine the output voltage scaling.

2. SCHEME AND PARAMETERS OF THE RS-20 FACILITY

The RS-20 facility is an X-ray sterilizer created in 1991 [7] and intended for radiobiological experiments in a repetitive mode (1–2 Hz). Later, the facility (Fig. 1) was modified as follows [8]:

(i) With new capacitors, the energy stored in the MG increased 12.5 times; at the working voltage U_{MG} = 0.85 MV, it attained 180 kJ. As a result, the current rise time and the current amplitude increased to 2 μs and 300 kA, respectively.

(ii) To lower the inductance of the MG–POS circuit, the POS position in the vacuum chamber was changed (Fig. 1).

(iii) The POS circuit (Fig. 2) includes 78 plasma guns, a magnetic field solenoid, and the POS electrodes. The maximum linear (along the circumference of the POS external electrode) charge density q_{L} is ~9 mC/cm, which is nearly twice as high as that in the initial version of the device [5] (2.5–5 mC/cm). The

---

† Deceased.

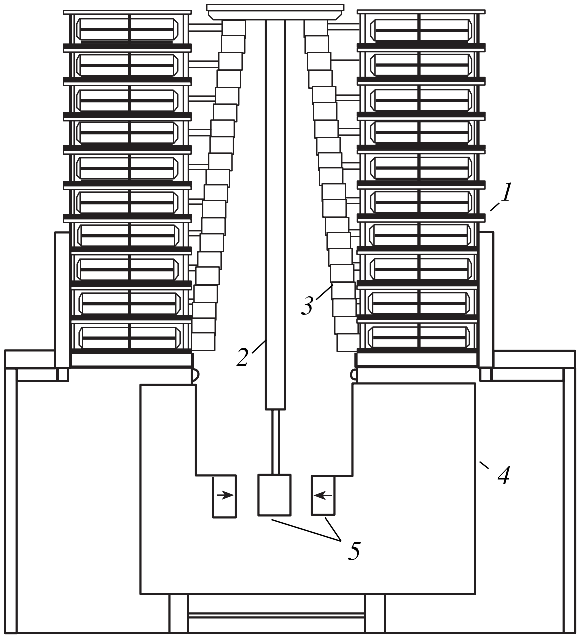

Fig. 1. Schematic of the RS-20 facility: (*1*) MG module, (*2*) high-voltage input, (*3*) insulator, (*4*) vacuum chamber, and (*5*) POS electrodes.

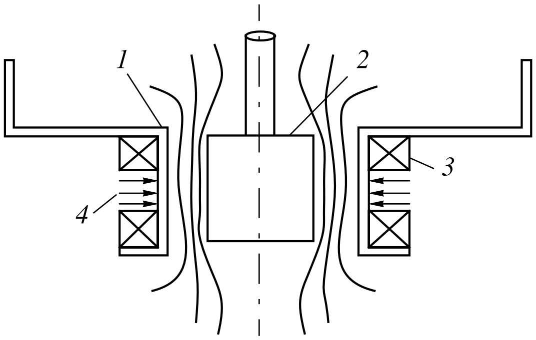

Fig. 2. Schematic of the POS: (*1*) grounded cathode, (*2*) high-voltage anode, (*3*) magnetic field solenoid, and (*4*) plasma guns.

POS electrodes are made from a carbon–carbon material highly resistant to a pulsed action.

(iv) Plasma guns are positioned on the external electrode (the POS cathode) and form three rings spaced 2.5 cm apart. The guns are grouped into six sections, 13 guns in each. Each section is supplied from an individual IK-50-0.4 capacitor. The guns in each section are arranged uniformly along the circumference. A separate operation of different sections is provided.

(v) Due to additional gradient rings, the insulation strength is enhanced to higher than 3.5 MV.

(vi) Provision is made for changing the input POS power at either a constant charge density (by varying the number of the MG stages, i.e., the output MG voltage; in this case, the end MG stage is connected to the high-voltage input of the POS through a gradient ring) or a constant voltage (by varying the number of the MG modules, i.e., the current and, accordingly, the charge density).

(vii) A magnetic coil on the external electrode (the POS cathode) and a copper "pusher" on the internal electrode (the POS anode) allow one to obtain a 16-kG uniform magnetic field in the POS gap. We ruled out the possibility for the magnetic field lines to connect the anode and cathode (more precisely, the areas of the cathode surface where the electric field exceeds the threshold for explosive electron emission). The conventional POS operating mode without an external magnetic field and at the negative polarity of the internal electrode is also possible.

3. MAIN DIAGNOSTICS

Standard electrical diagnostics, such as shunts at the POS input and in the circuit of each MG module, voltage dividers connected to the MG output and the outputs of the first stage of each MG module, and loops arranged near the connection of the MG module with the chamber and near the POS, were employed.

In order to obtain highly reliable values of the POS voltage, which is required for the scaling purposes, we determined the POS voltage independently by measuring the hard edge of the bremsstrahlung γ spectrum of electrons accelerated in the POS (the relevant technique developed by S.A. Dan'ko and Yu.G. Kalinin will be described in detail in a separate paper). The hard edge of the γ spectrum was detected by using the photoneutron activation technique. The two reactions involved were $Be^9(\gamma, n)Be^8$ and $D^2(\gamma, n)p$ with the reaction thresholds $E_{Be} = 1.65$ MeV and $E_D = 2.25$ MeV, respectively. Fast neutrons produced in both reactions were moderated in polyethylene; then, they interacted with indium plates yielding β-active nuclei in the reaction $In^{116}(n, \beta^-)$ Sn^{116}. The emitted β particles were countered on the other side of the indium plates. Avoiding the absolute calibration of the detectors, we used the ratio of indications in two recording channels. The number of counts in each channel was calculated for the peak voltages $U_d \in$ (2–5) MeV. To increase the γ-radiation yield, the anode was covered with a tantalum layer, which, unfortunately, somewhat impaired the POS performance.

4. RESULTS AND DISCUSSION

According to the results of experiments carried out with a four-stage MG operating at an input voltage of 32–48 kV, an output voltage of 128–192 kV, a current of 200–320 kA, and a charge density of 5–9 mC/cm, the

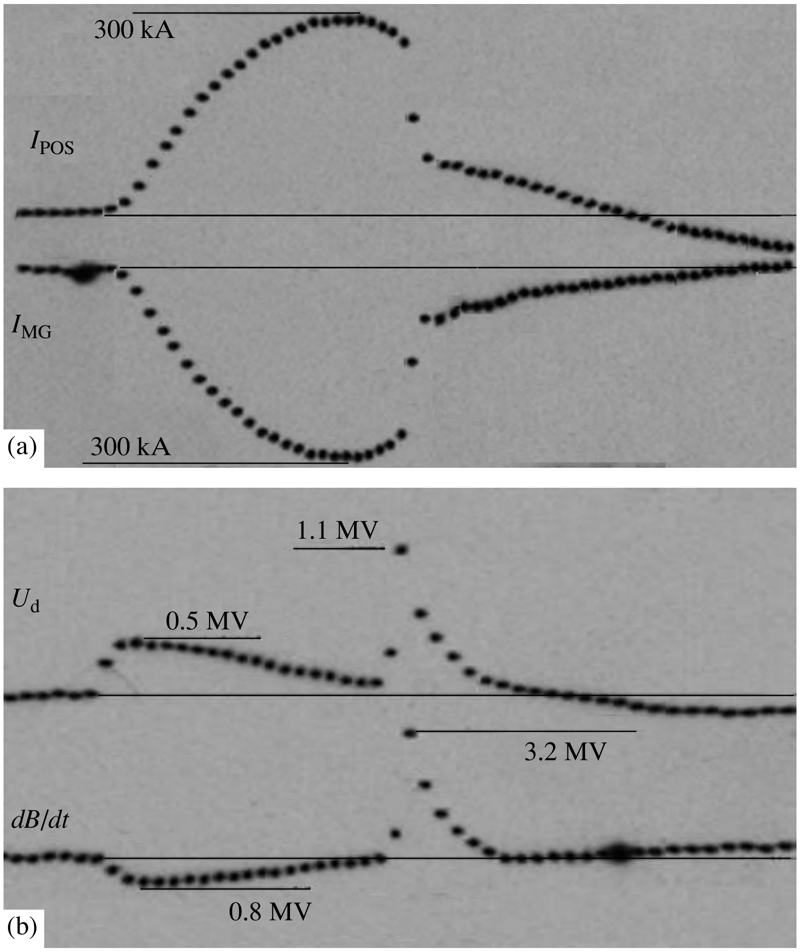

Fig. 3. Waveforms of (a) the POS current I_{POS} and the MG current I_{MG} and (b) the signals from the voltage divider, U_d, and the loop, dB/dt. The points are spaced by 100 ns; four MG modules are involved; the external magnetic field is 16 kG.

coefficient in Eq. (1) is equal to α = 3.2–3.6 MV$^{3/7}$ [8, 9]. Therefore, for a linear charge density higher than 5 mC/cm, the coefficient α and, accordingly, the voltage multiplication factor decrease. With 20 stages and four MG modules (i.e., at q_L = 9 mC/cm), the maximum output voltage is no higher than 3 MV. The reason is that, to increase the density and magnitude of the charge passed through the POS, one has to raise the plasma density and, thus, get out of the erosion mode, which is the most efficient in view of gaining a high voltage. Because of this, we attempted to use a controlled filling of the POS gap with a plasma [10]. In this mode, the plasma is supplied by small portions compensating for the plasma erosion and a great amount of charge can be carried at a limited plasma density. To realize this mode, we first switched on one half of the plasma guns (three sections). Then, the other guns were involved with the interval 6–8 μs and, ~3 μs later, the MG was switched on. In this case, the current is initially carried by the plasma produced by the first group of guns; just by the instant when the current breaking could start, a new plasma portion from the second group of guns arrives. This mode allows a complete transfer of the MG charge and yields a voltage of 3–3.5 MV (Fig. 3). It should be noted that, in the controlled filling mode, it is much more difficult to maintain the initial parameters at a constant level; therefore, the given voltage can be obtained with only a small probability, which was estimated as ~4%.

When using two MG modules, i.e., at q_L = 4.5 mC/cm, the probability of obtaining voltage in the range 3–3.5 MV (Fig. 4) is about 50%. It is this mode in which the activation technique was employed. The measurement accuracy was improved by coating the pyrocarbon anode with a 1-mm-thick tantalum layer. Although, in this case, the POS output voltage was somewhat lower, the X-ray yield and, hence, the accuracy of voltage measurements significantly increased. The measurements showed that the POS output voltage actually exceeded 3 MV. In this case, a close correlation was observed between the data from electrical sensors and those provided by the activation technique. Note

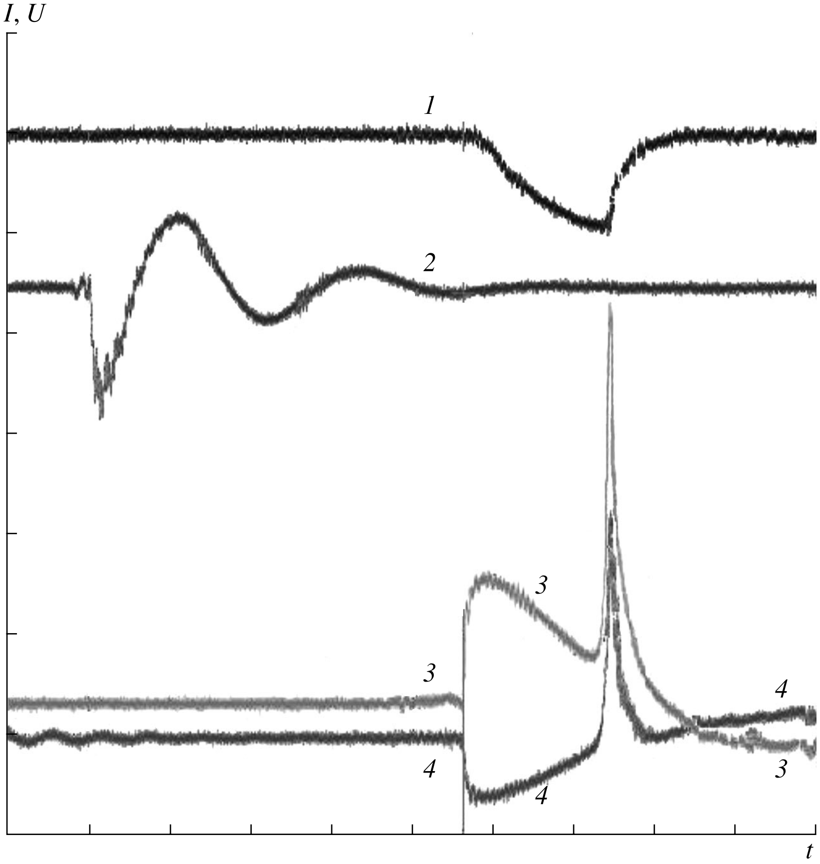

Fig. 4. Waveforms of (*1*) MG current (150 kA/division), (*2*) gun current (arb. units), (*3*) divider voltage (350 kV/division), and (*4*) loop voltage (1.25 MV/division). Time scale is 1 μs/division. Two MG modules are involved; the external magnetic field is 12 kG.

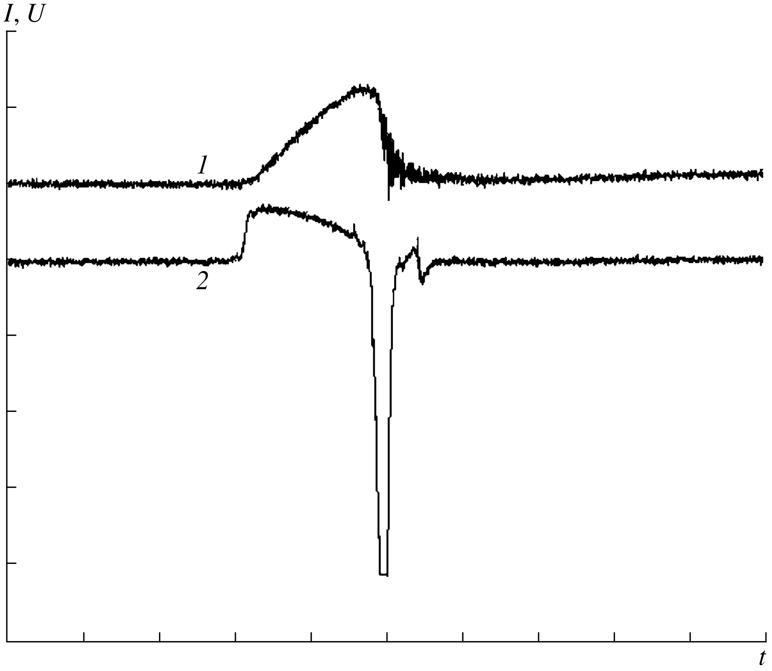

Fig. 5. Waveforms of (*1*) MG current (90 kA/division) and (*2*) loop voltage (220 kV/division) for the facility [4, 12] with an MG voltage of 160 kV, a current of 120 kA, a current rise time of 1 μs, and an external magnetic field of 10 kG. Time scale is 0.5 μs/division.

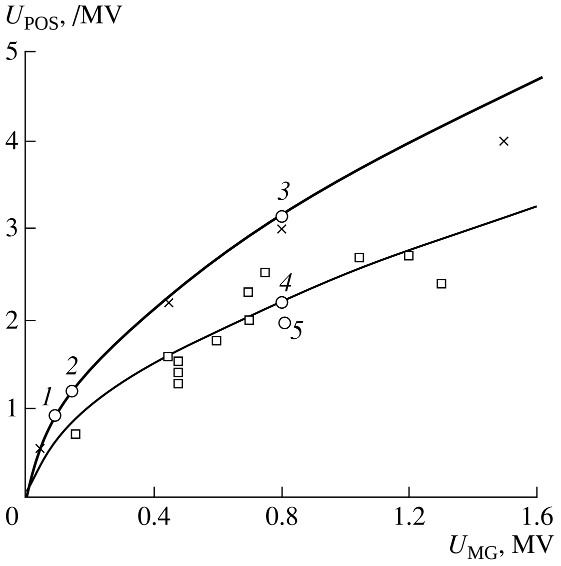

Fig. 6. POS voltage vs. MG voltage. The upper curve U_{POS} [MV] = $3.6(U_{MG}\ [\mathrm{MV}])^{4/7}$ is for facilities with an external magnetic field (data from different facilities are shown by crosses). The lower curve U_{POS} [MV] = $2.5(U_{MG}\ [\mathrm{MV}])^{4/7}$ is for facilities without an external magnetic field (data from different facilities are shown by squares). The facilities are described in [4]. The circles show the values of $U_{POS}(U_{MG})$ obtained in the present study: (*1*) RS-20 with four MG modules with four stages in each ($U_{MG} = 0.128$ MV, $B = 12$ kG), (*2*) the facility [4, 12] with four MG modules with four stages in each ($U_{MG} = 0.16$ MV, $B = 10$ kG), (*3*) RS-20 with two MG modules ($B = 12$ kG) or with four MG modules and the controlled plasma filling of the gap ($B = 16$ kG), (*4*) RS-20 with two MG modules ($B = 0$), and (*5*) RS-20 with four MG modules ($B = 0$).

that the external longitudinal magnetic field not only ensures the magnetic insulation of the POS gap, which occurs when the magnetic field strength exceeds the critical value at which the electrons do not cross the vacuum cathode–anode gap of the POS. For a complete break of current (down to zero), it is necessary that the external magnetic field exceed the magnetic field of the POS current. In this case, the axial component of the electron drift velocity in the crossed E and B fields is less than the azimuthal one, so that the electron drift is almost closed. Otherwise, the axial drift of electrons results in the accumulation of their space charge near the ends of the POS electrodes and, consequently, in the breaking of magnetic insulation. Thus, the experiment [11] demonstrated that applying an additional azimuthal magnetic field produced by an external source causes an increase in the output voltage. However, similar to the case without an additional magnetic field, the current decreases only by one-half after breaking. A complete (down to zero) break of the current can be seen in the waveforms (Fig. 5) obtained in the modified facility [4, 12] with a relatively strong external magnetic field.

The main experimental results are illustrated in Fig. 6, which shows the dependences of U_{POS} on the density of energy deposition (MG voltage) for MG voltages of up to 0.84 MV. New data obtained in this study are well fitted by the curve U_{POS} [MV] = $2.5(U_{MG}\ [\mathrm{MV}])^{4/7}$ in the traditional scheme without an external magnetic field and with the curve U_{POS} [MV] = $3.6(U_{MG}\ [\mathrm{MV}])^{4/7}$ in the scheme with an external magnetic field. The controlled plasma filling of the POS gap allows one, in principle, to increase the linear charge density to 9 mC/cm.

5. CONCLUSION

We have demonstrated that applying an external magnetic field increases the energy expended on plasma erosion; as a result, the POS output voltage increases by a factor of 1.5. The output voltage is described by the dependence U_{POS} [MV] = $3.6(U_{MG}\ [\mathrm{MV}])^{4/7}$. The topology of the external magnetic field was chosen so as to prevent the leakage of electrons from the cathode to the anode along the magnetic field lines. In order for the current to break completely, the external magnetic field should exceed the azimuthal magnetic field of the POS current. The maximum linear charge density at which the POS operates in the erosion mode (the most efficient for attaining the maximum voltage) can be doubled by applying a controlled plasma filling of the POS gap.

ACKNOWLEDGMENTS

This study was supported by INTAS (grant no. 970021), CRDF (grant no. RP1 2113), and the Russian Foundation for Basic Research (project no. 00-15-96599).

REFERENCES

1. K. D. Ware, P. G. Filios, R. L. Gullicks, *et al.*, in *Proceedings of the 11th International Conference on High-Power Particle Beams, Prague, 1996*, Vol. 1, p. 284.
2. V. A. Glukhikh, V. G. Kuchinsky, O. P. Pechersky, *et al.*, in *Proceedings of the 12th International Conference on High-Power Particle Beams, Haifa, Israel, 1998*, Vol. 1, p. 71.
3. V. V. Alexandrov, E. A. Azizov, A. V. Branitsky, *et al.*, in *Abstracts of Papers of the 13th International Conference on High-Power Particle Beams, Nagaoka, Japan, 2000*, p. 214.
4. G. I. Dolgachev and A. G. Ushakov, Fiz. Plazmy **27**, 121 (2001) [Plasma Phys. Rep. **27**, 110 (2001)].
5. G. I. Dolgachev, L. P. Zakatov, and A. G. Ushakov, Fiz. Plazmy **17**, 699 (1991) [Sov. J. Plasma Phys. **17**, 398 (1991)].

6. N. U. Barinov, G. S. Belen'ki, G. I. Dolgachev, *et al.*, in *Proceedings of 11th IEEE Pulsed Power Conference, Baltimore, 1997*, Vol. 2, p. 1222.
7. V. M. Babykin, R. V. Chikin, G. I. Dolgachev, *et al.*, in *Proceedings 9th International Conference on High-Power Particle Beams, Washington, 1992*, Vol. 1, p. 512.
8. N. U. Barinov, G. I. Dolgachev, and D. D. Maslennikov, in *Proceedings of the 1st International Congress on Radiation Physics, High Current Electronics, and Modification of Materials, Tomsk, 2000*, Vol. 1, p. 313.
9. N. U. Barinov, S. A. Dan'ko, S. A. Budkov, *et al.*, Prib. Tekh. Éksp., No. 2 (2002).
10. N. U. Barinov, G. I. Dolgachev, and D. D. Maslennikov, in *Proceedings of the 13th International Conference on High-Power Particle Beams, Nagaoka, Japan, 2000*, p. 100.
11. Yu. P. Golovanov, G. I. Dolgachev, L. P. Zakatov, and A. G. Ushakov, Vopr. At. Nauki Tekh., Ser. Termoyad. Sintez **3**, 28 (1990).
12. G. I. Dolgachev, M. S. Nitishinsky, and A. G. Ushakov, in *Proceedings of the 11th IEEE International Pulsed Power Conference, 1997*, Vol. 1, p. 281.

Translated by A. Sidorova-Biryukova

Plasma Physics Reports, Vol. 28, No. 3, 2002, pp. 183–189. Translated from Fizika Plazmy, Vol. 28, No. 3, 2002, pp. 208–214.
Original Russian Text Copyright © 2002 by Zemskov.

Formation of a Steady-State Shock Front of a Fast Magnetosonic Wave in a Turbulent Plasma

V. R. Zemskov

Received April 9, 2001; in final form, August 9, 2001

Abstract—The question of the existence of a steady-state shock front of a fast magnetosonic wave propagating across the magnetic field against the background of turbulent Alfvén waves is considered. It is shown that the steady-state shock front can form as a result of energy transfer from the turbulent Alfvén wave to the fast magnetosonic wave. *© 2002 MAIK "Nauka/Interperiodica".*

1. INTRODUCTION

As early as 1985, Mikhaĭlovskiĭ and Smolyakov [1] noted that the evolution of a long-wavelength ($kr_{e,\,i} < 1$, where k is the wavenumber and $r_{e,\,i}$ are the electron and ion gyroradii) fast magnetosonic (FMS) wave (see Fig. 1) in a high-temperature plasma with $\beta_e \approx \beta_i \approx 1$ and with low particle densities ($n_e = n_i = 1$–5 cm^{-3}) can be described by the Korteweg–de Vries (KdV) equation. The KdV equation has no steady solutions describing a steady-state shock front [2]. Such a front can form as a result of dissipation associated with collisions between plasma particles, in which case it is necessary to apply the evolutionary Korteweg–de Vries–Burgers (KdVB) equation [3]. In a low-density plasma, in which collisional dissipation is negligible, there may exist turbulence-driven anomalous dissipation. In my earlier paper [4], a study was made of the propagation of a long-wavelength FMS wave against the background of Alfvén waves, which interact with resonant plasma particles and thus are subject to a modulational instability. The geometry of the magnetic and electric fields of the FMS and Alfvén waves, as well as the external magnetic field, are shown in Fig. 1. In [4], the evolutionary equation for an FMS wave was derived for a certain form of the correlation function of the magnetic field of an Alfvén wave and was found to contain dissipative terms. The form of the correlation function of the magnetic field of an unstable Alfvén wave did not allow the dissipative terms responsible for the unsteady character of the shock front of an FMS wave to be eliminated from the evolutionary equation for this wave. The purpose of the present paper is to prove that a certain type of Alfvén turbulence in a plasma may lead to the formation of a steady-state shock front of an FMS wave propagating as shown in Fig. 1.

2. ALFVÉN TURBULENCE

A nonlinear Alfvén wave having the field components $\tilde{b}_x$ and $\tilde{b}_y$ and propagating along the magnetic field $\mathbf{B}_0$ is subject to a modulational instability associated with its nonlinear nature and its interaction with resonant particles. In a plasma with $\beta_e \approx \beta_i \approx 1$ and with a low particle density ($n \sim 1$ cm^{-3}), such a wave is described by the nonlinear Schrödinger equation with the first spatial derivative. The effect of resonant particles is incorporated into the nonlinear integral term [5]. Here, we do not write down this Schrödinger equation and present only the relevant dispersion relation for the linear longitudinal perturbations of a nonlinear Alfvén wave:

$$\nu = \kappa u - i|s|A_0^2\kappa \pm \kappa\sqrt{\kappa^2 - \kappa_0^2 - 2in|s|A_0^2}, \qquad (1)$$

where ν and κ are the frequency and the longitudinal wavenumber of the perturbation, respectively; A_0 is the wave amplitude in dimensionless units; $\kappa_0^2 = A_0^2(A_0^2 - 2u + |s|^2A_0^2)$; and u is the nonlinear shift of the wave phase velocity. The parameter $|s|$ was calculated by

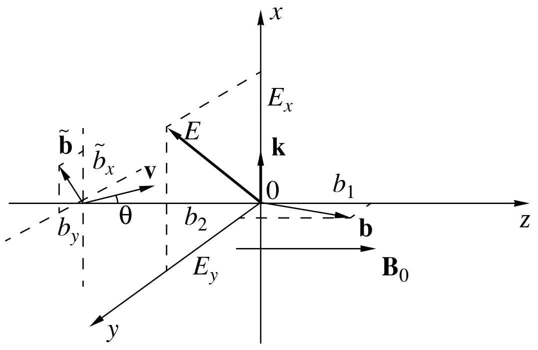

Fig. 1. Geometry of the magnetic and electric fields of an FMS wave propagating across the magnetic field $\mathbf{B}_0 = \mathbf{e}_zB_0$. E is the wave electric field, $\mathbf{b} = \mathbf{e}_zb_1 + \mathbf{e}_yb_2$ is the wave magnetic field (here, $b_2 = b_0$ is assumed to be small), and $\tilde{\mathbf{b}} = \mathbf{e}_x\tilde{b}_x + \mathbf{e}_y\tilde{b}_y$ is the magnetic field of the Alfvén wave.

Mjolhus and Wyller [5] as a function of the plasma parameters. For the plasma under consideration, we have $|s| \approx 1$.

We describe Alfvén-wave turbulence by the following correlation and cross-correlation functions of the magnetic field components $\tilde{b}_x$ and $\tilde{b}_y$ of the Alfvén wave:

$$\langle \tilde{b}_x \tilde{b}'_x \rangle = \langle \tilde{b}_y \tilde{b}'_y \rangle, \langle \tilde{b}_x \tilde{b}'_y \rangle.$$

Here, the angular brackets denote averaging over the ensemble of realizations of the perturbations of the nonlinear Alfvén wave that is used to model plasma turbulence, and the primes indicate time shifts. We describe the nonlinear Alfvén wave under consideration by the following familiar solution to the Schrödinger equation:

$$\tilde{b}_0 = \tilde{b}_x + i\tilde{b}_y = A_0 \cos(k_0\zeta + \alpha) + iA_0 \sin(k_0\zeta + \alpha), \quad (2)$$

where $k_0 = A_0^2 - u$, ζ is the dimensionless coordinate along the z-axis, α is the constant phase, and the quantities A_0 and u are defined in the dispersion relation (1).

The effects of resonant particles and nonlinear processes give rise to longitudinal perturbations of the wave field (2). In the linear approximation, the perturbed wave amplitude can be represented as $A_0 \longrightarrow A_0 + A_{1\kappa}$, where $A_{1\kappa}$ is the Fourier component of the longitudinal perturbation. The correlation functions of the wave perturbations (2) can be obtained by assuming that they have random phases and by representing the wave amplitude as a sum of the unperturbed amplitude and a small correction:

$$\langle \tilde{b}_x \tilde{b}'_x \rangle = \langle \tilde{b}_y \tilde{b}'_y \rangle = \frac{1}{2}\langle b_0^2 \rangle \cos\Omega_0\tau + \sum_\kappa \frac{1}{8}\langle \tilde{b}_1^2 \rangle \exp(-\Gamma\tau)\cos\Omega_1\tau + \sum_\kappa \frac{1}{8}\langle \tilde{b}_1^2 \rangle \exp(-\Gamma\tau)\cos\Omega_2\tau, \quad (3)$$

$$\langle \tilde{b}_y \tilde{b}'_y \rangle = \frac{1}{2}\langle b_0^2 \rangle \sin\Omega_0\tau + \sum_\kappa \frac{1}{8}\langle \tilde{b}_1^2 \rangle \exp(-\Gamma\tau)\sin\Omega_1\tau + \sum_\kappa \frac{1}{8}\langle \tilde{b}_1^2 \rangle \exp(-\Gamma\tau)\sin\Omega_2\tau.$$

Here, the growth rate Γ of perturbations (2) is determined from the dispersion relation (1); the frequencies Ω_0, Ω_1, and Ω_2 are determined from the same relation [see formula (9) below]; τ is the time shift; $\sum_\kappa$ denotes the sum over the Fourier components of the longitudinal perturbation; κ is its wavenumber; and $\langle b_0^2 \rangle$ and $\langle b_1^2 \rangle$ are the correlators of the unperturbed and perturbed wave fields (2), respectively.

We assume that the turbulence modeled by the unstable Alfvén wave under consideration satisfies the conditions

$$\omega_{Be} > \omega_{Bi} > \Gamma > \omega, \quad (4)$$

where ω is the FMS wave frequency, ω_{Be} and ω_{Bi} are the electron and ion gyrofrequencies in the plasma, and Γ is the growth rate of the perturbed Alfvén wave (2).

3. SMALL-SCALE TURBULENCE

Let us consider an Alfvén wave of the form (2) propagating along the magnetic field $\mathbf{B}_0 = \mathbf{e}_z B_0$. The characteristic wavelength of the Alfvén wave is $\tilde{\lambda} = \kappa^{-1}$, where the wavenumber κ is determined from the dispersion relation (1). The turbulent properties of the perturbations of the Alfvén wave are described by the correlation functions (3). To be specific, we assume that

$$\kappa \gg \kappa_0. \quad (5)$$

We call such perturbations short-wavelength perturbations. Passing over to the dimensional variables, we obtain the following estimate for the wavelengths of the perturbations with wavenumbers (5):

$$\tilde{\lambda} = \frac{1}{\kappa} \ll \frac{r_i}{|s|}\left(\frac{B_0}{b}\right)^2, \quad (6)$$

where b is the FMS wave amplitude.

For $b/B_0 = 10^{-2}$, we have $\tilde{\lambda} \ll 10^4 r_i$, and, for $b/B_0 = 10^{-3}$, we have $\tilde{\lambda} \ll 10^6 r_i$ (where r_i is the ion gyroradius).

We use the estimate $\omega = c_\perp k$, where k is the wavenumber of an FMS wave and $c_\perp = c_A(1 + \beta_e + \beta_i)^{1/2}$, and the representation $\Gamma \sim \kappa|s|A_0^2$ and pass over to the dimensional variables. As a result, the dispersion relation (1) and the last of inequalities (4) yield the restriction

$$\tilde{\lambda} < \lambda|s|\left(\frac{b}{B_0}\right)^2, \quad (7)$$

where $\lambda = k^{-1}$ is the wavelength of an FMS wave. From the second of inequalities (4), we obtain

$$\tilde{\lambda} > |s|\left(\frac{b}{B_0}\right)^2 r_i. \quad (8)$$

Inequalities (7) and (8) show that, under conditions (4), there exists an interval of $\tilde{\lambda}$ values in which the perturbations of the Alfvén wave are short-wavelength in the sense of condition (5). From the definition of κ_0, we easily find

$$\kappa_0^2 = k_0^2 - (u^2 - |s|^2 A_0^4),$$

where $u - |s|A_0^2 > 0$. Accordingly, we have $\kappa_0^2 \lesssim k_0^2$, in which case, taking into account condition (5) and using the corresponding formulas from [6], we can write the frequencies Ω_0, Ω_1, and Ω_2 as

$$\begin{aligned} \Omega_0 &= k_0 u = (A_0^2 - u)u, \\ \Omega_1 &= k_0 u - \kappa u - \omega_0 \approx -\kappa u - \omega_0, \\ \Omega_2 &= k_0 u + \kappa u + \omega_0 \approx \kappa u + \omega_0, \end{aligned} \tag{9}$$

where the real part $\omega_0(\kappa)$ of the frequency is determined from the dispersion relation (1). Here, we do not write down the expressions for $\omega_0(\kappa)$ and Γ, which can be obtained from the dispersion relation (1), and present only the relationships

$$\begin{aligned} \omega_0(-\kappa) &= -\omega_0(\kappa), \quad \Omega_1(-\kappa) = -\Omega_1(\kappa), \\ \Gamma(-\kappa) &= -\Gamma(\kappa), \quad \Omega_2(-\kappa) = -\Omega_2(\kappa). \end{aligned} \tag{10}$$

4. DERIVATION OF THE EVOLUTIONARY EQUATION

In modeling plasma turbulence by the unstable Alfvén wave (2) with the correlation functions (3), the evolutionary equation for the FMS wave whose field geometry is shown in Fig. 1 can be derived from Maxwell's equations averaged over an ensemble of the fields $\tilde{b}_1$ [4]:

$$\begin{aligned} \frac{\partial b}{\partial \kappa} &= -\frac{4\pi}{c}\langle j_y + \tilde{j}_y \rangle, \\ \langle j_x + \tilde{j}_x \rangle &= 0, \quad \frac{\partial b}{\partial t} = -c\frac{\partial E_y}{\partial \kappa}, \end{aligned} \tag{11}$$

where E_y is the component of the electric field of an FMS wave and the transverse currents $\tilde{j}_x$ and $\tilde{j}_y$ are induced by the perturbations of the field $\tilde{b}$ of the Alfvén wave. In order to derive the evolutionary equation for the magnetic field of an FMS wave from the first of equations (11), we use the third of these equations to express E_y in terms of b and then use the second equation to express E_x in terms of E_y. Calculating the transverse currents j_x, j_y, $\tilde{j}_x$, and $\tilde{j}_y$ and using the expressions presented in the Appendix, we arrive at the desired evolutionary equation

$$\begin{aligned} \frac{\partial h}{\partial T} + im\frac{\partial h}{\partial \Sigma} + in\frac{\partial^2 h}{\partial \Sigma^2} - ip\frac{\partial^3 h}{\partial \Sigma^3} + \frac{\partial^3 h}{\partial \Sigma^3} + h\frac{\partial h}{\partial \Sigma} \\ = k_2\frac{\partial^2 h}{\partial \Sigma^2} - k_3 h, \end{aligned} \tag{12}$$

where

$$T = \frac{c_\perp t}{a_*}, \quad h = \frac{b}{B_0}\frac{3 + \beta - 3\beta_i}{1 + \beta}, \quad \Sigma = \frac{\kappa - c_\perp^* t}{a_*},$$

$$c_\perp^* = c_\perp\left[1 + \omega_{Be}\left(1 - \frac{3v_{Ti}^2}{c_\perp^2}\right)(6A + B) + \frac{2m_i}{m_e}\omega_{Bi}^2 C\right],$$

$$a_*^2 = a_D^2 + \tilde{a}^2, \quad a_D^2 = \frac{r_i^2(2 + 2\beta + 3\beta_i)}{16(1 + \beta)},$$

$$\beta = \beta_i + \beta_e, \quad c_\perp = c_A(1 + \beta)^{1/2},$$

$$\tilde{a}^2 = \frac{3v_{Ti}^2 - 2c_\perp^2}{12\omega_{Bi}}\left(B - \frac{6\varepsilon}{\omega_{Bi}}\right) - c_\perp^2 C.$$

In Eq. (12), all of the coefficients and normalizing constants for the time, coordinate, and FMS wave field amplitude are expressed in terms of the quantities A, B, C, and ε. In turn, these quantities are represented as integrals over κ and are used in place of the sums in the correlation functions (3):

$$\begin{aligned} A &= \int_{-\infty}^{+\infty} A_{1\kappa}^2 \Gamma(\kappa)\left(\frac{1}{\Gamma^2 + \Omega_1^2} + \frac{1}{\Gamma^2 + \Omega_2^2}\right)d\kappa, \\ B &= \int_{-\infty}^{+\infty} A_{1\kappa}^2 \left(\frac{\Omega_1}{\Gamma^2 + \Omega_1^2} + \frac{\Omega_2}{\Gamma^2 + \Omega_2^2}\right)d\kappa, \\ C &= \int_{-\infty}^{+\infty} A_{1\kappa}^2 \left(\frac{1}{\Gamma^2 + \Omega_1^2} + \frac{1}{\Gamma^2 + \Omega_2^2}\right)d\kappa, \\ \varepsilon &= \int_{-\infty}^{+\infty} A_{1\kappa}^2 d\kappa. \end{aligned} \tag{13}$$

The expression for a_D^2 in Eq. (12) was obtained in [7]. The nonlinear term in Eq. (12) is introduced in the same way as was done in [7]. We assume that this term is independent of the field $\tilde{b}_1$. In terms of integrals (13), the coefficients in Eq. (12) have the form

$$\begin{aligned} m &= 4\varepsilon, \quad n = \frac{4\varepsilon(3v_{Ti}^2 - 2c_\perp^2)}{a_*\omega_{Bi}c_\perp}, \\ p &= \frac{8c_\perp^2 A}{\omega_{Bi}a_*^2}, \quad k_3 = \frac{2m_i\omega_{Bi}a_*}{m_e c_\perp}(B - A), \\ k_2 &= \frac{c_\perp}{a_*}\left(6\omega_{Be}C - 2B - A - \frac{4\varepsilon}{\omega_{Bi}}\right). \end{aligned} \tag{14}$$

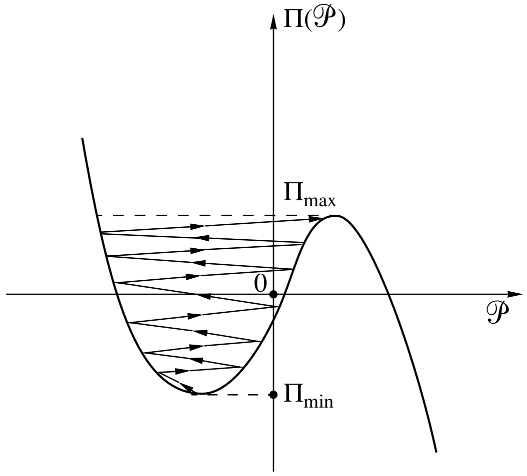

Fig. 2. Plot of the function $\Pi(\mathcal{P})$. The formation of the shock front is analogous to the oscillations of a particle in a potential well that starts from the level $\Pi_{\min}$ and bounces increasingly higher until it reaches the level $\Pi_{\max}$.

An important feature of Eq. (12) is that its coefficients are imaginary; in other words, the FMS wave is polarized and the vector $\tilde{b}$ rotates in the (y, z) plane. In what follows, we assume that the FMS wave is polarized in such a way that the field component b_y is constant. This assumption is indeed consistent with Eqs. (11).

5. FORMATION OF A STEADY-STATE SHOCK FRONT

When the perturbations of the Alfvén wave (2) are short-wavelength and satisfy conditions (7) and (8) [in which case equalities (10) hold], expressions (13) and (14) give

$$A = 0, \quad B = 0, \quad k_3 = 0, \quad p = 0,$$

and Eq. (12) becomes

$$\frac{\partial h}{\partial T} + im\frac{\partial h}{\partial \Sigma} + in\frac{\partial^2 h}{\partial \Sigma^2} + \frac{\partial^3 h}{\partial \Sigma^3} + h\frac{\partial h}{\partial \Sigma} = k_2\frac{\partial^2 h}{\partial \Sigma^2}. \qquad (15)$$

Under the condition

$$\omega_{Bi} \gg \Gamma,$$

it is incorrect to retain the terms with imaginary coefficients in Eq. (15). In fact, the first term in Eq. (15) is larger than the absolute value of the second term and the absolute value of the third term is much smaller than the dissipative term with k_2. Without the second and third terms, Eq. (15) becomes the KdVB equation:

$$\frac{\partial h}{\partial T} + \frac{\partial^3 h}{\partial \Sigma^3} + h\frac{\partial h}{\partial \Sigma} = k_2\frac{\partial^2 h}{\partial \Sigma^2}, \qquad (16)$$

where the dissipative term is determined by the turbulent properties of the plasma. Under the applicability conditions of Eq. (16), this term has the form

$$k_2 = \frac{6c_\perp\omega_{Be}C}{a_*} = \frac{6c_\perp\omega_{Be}}{a_*}\left(\int_{-\infty}^{+\infty}\frac{A_{1\kappa}^2 d\kappa}{\Gamma^2 + \Omega_1^2} + \int_{-\infty}^{+\infty}\frac{A_{1\kappa}^2 d\kappa}{\Gamma^2 + \Omega_2^2}\right). \qquad (17)$$

If $\omega_{Bi} \gtrsim \Gamma$, then, instead of inequality (8), we obtain the following estimate for the perturbation wavelength:

$$\tilde{\lambda} \sim |s|\left(\frac{b}{B_0}\right)r_i,$$

which indicates that the imaginary terms in Eq. (15) cannot be neglected. Let us, however, show that, without these terms, Eq. (15) also has steady solutions describing a steady-state shock front whose shape was determined in [3] from Eq. (16).

We represent the sought-for solution to Eq. (15) as $h = h_1 + ih_2$. Passing over to the variable $\varepsilon = \Sigma - UT$ (where U is the phase velocity of the steady-state shock front), we obtain

$$\begin{aligned} h_1'' - nh_2' - k_2h_1' + \frac{\partial}{\partial h_1}\Pi(h_1, h_2) &= 0, \\ h_2'' + nh_1' - k_2h_2' - \frac{\partial}{\partial h_2}\Pi(h_1, h_2) &= 0, \end{aligned} \qquad (18)$$

where $\Pi(h_1, h_2) = \frac{h_1^3}{6} - \frac{h_1h_2^2}{2} + \frac{Uh_2^2}{2} - \frac{Uh_1^2}{2} - mh_1h_2$.

We assume that the FMS wave described by Eqs. (18) is polarized in such a way that $h_2 = h_0$, where h_0 is a constant. Under this assumption, Eqs. (18) become

$$\begin{aligned} h_1'' - k_2h_1' + \frac{h_1^2}{2} - \frac{h_0^2}{2} - Uh_1 - mh_0 &= 0, \\ nh_1' + h_1h_0 + mh_1 - Uh_0 &= 0. \end{aligned} \qquad (19)$$

According to expression (17), we have $k_2 > 0$. If we discard the term with k_2, then we find that the first of equations (19) has the periodic solution

$$h_1 = U - \mathcal{P}\left(\frac{\varepsilon}{2\sqrt{3}}\right),$$

where $\mathcal{P}$ is the Weierstrass elliptic function. As a result, this first equation can be transformed to

$$\frac{1}{2}\mathcal{P}'^2 + \Pi(\mathcal{P}) = 6E, \qquad (20)$$

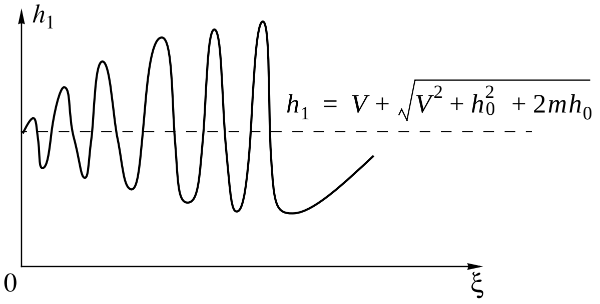

Fig. 3. Schematic representation of the structure of the magnetic field of an FMS wave for the case of increasingly higher particle bounces in a potential well.

where E is an integration constant and the function $\Pi(\mathcal{P})$ has the form

$$\Pi(\mathcal{P}) = (6U^2 + 12h_0^2 + 12mh_0)\mathcal{P}$$
$$-2\mathcal{P}^3 - 4U^3 - 12mh_0U.$$

Equation (20) can be regarded as an equation for the total energy of an oscillator that performs harmonic oscillations in a potential well (Fig. 2). The second of equations (19) has an aperiodic solution, which is steady but does not satisfy the boundary conditions for the complete formation of the steady-state shock front of an FMS wave. The dissipative term with k_2 in the first of equations (19) describes the growth of the magnetic field oscillations in a steady-state shock front. The reason for this is related to the energy transfer from the turbulent Alfvén wave to the FMS wave. In this case, the magnetic field amplitude oscillates around the value

$$h_1 = U + \sqrt{U^2 + h_0^2 + 2mh_0}.$$

The minimum field amplitude at the oscillator energy

$$6E_{\min} = \Pi_{\min}$$
$$= -4(U^2 + h_0^2 + 2mh_0)^{3/2} - 4U(U^2 + 3mh_0)$$

is very small, and the maximum amplitude at the oscillator energy

$$6E_{\max} = \Pi_{\max}$$
$$= 4(U^2 + h_0^2 + 2mh_0)^{3/2} - 4U(U^2 + 3mh_0)$$

corresponds to a soliton at the shock front.

The magnetic field oscillations in a steady-state shock front are schematically illustrated in Fig. 3, and a schematic representation of the development of oscillations in a potential well is shown in Fig. 2.

6. CONCLUSION

If the wavelength of the characteristic perturbations of the nonlinear Alfvén wave (2), which is subject to a modulational instability associated with its interaction with resonant particles in a plasma with $\beta_e \approx \beta_i \approx 1$ and $n \sim 1$ cm^{-3}, satisfies the conditions

$$|s|\left(\frac{b}{B_0}\right)^2 r_i < \tilde{\lambda} < \lambda|s|\left(\frac{b}{B_0}\right)^2 r_i, \quad \lambda \gg r_i, r_e,$$

and if the perturbations are short-wavelength in the sense of condition (6), then the problem of the propagation of an FMS wave against the background of this Alfvén wave (the geometry of the wave fields is shown in Fig. 1) has a solution describing the formation of a steady-state dissipative shock front. When the scale of plasma turbulence is sufficiently short,

$$\tilde{\lambda} \sim |s|\left(\frac{b}{B_0}\right)^2 r_i,$$

the evolutionary equation for the FMS wave has two solutions describing dissipative shock fronts. A particular case of one of these fronts is illustrated in Fig. 3. The derivation of more general solutions to Eqs. (18) requires additional investigations.

The theory developed in this paper may be useful for analyzing the propagation of FMS waves in the solar wind plasma, as well as in interplanetary space and intergalactic space.

APPENDIX

The evolutionary equation (12) can be derived using the kinetic method [4, 7]. We start with the Boltzmann equation

$$\frac{\partial f}{\partial t} + (\mathbf{v}\cdot\boldsymbol{\nabla})f$$
$$+\left(e\mathbf{E} + \frac{e}{c}\mathbf{v}\times\mathbf{B}_0 + \frac{e}{c}\mathbf{v}\times\mathbf{b} + \frac{e}{c}\mathbf{v}\times\tilde{\mathbf{b}}\right)\frac{\partial f}{\partial \mathbf{p}} = 0, \tag{21}$$

where f is the distribution function of the plasma particles, **v** and **p** are their velocity and momentum, **E** and **b** are the electric and magnetic fields of an FMS wave, and $\tilde{b}$ is the magnetic field of the Alfvén wave (2). In Eq. (21), the collision integral is neglected. We represent the solution to Eq. (21) in the form

$$f = f_0 + f_1, \tag{22}$$

where the functions f_0 and f_1 depend on the components of the field $\tilde{b}$. Averaging over an ensemble of the fields $\tilde{b}$ gives

$$\langle f_0\rangle = f_0, \quad \langle f_1\rangle = 0, \quad \langle\tilde{b}\rangle = 0.$$

We substitute representation (22) into Eq. (21) and average the resulting equation over an ensemble of the fields $\tilde{b}$ to obtain

$$\begin{aligned}&\frac{\partial f_0}{\partial t} + (\mathbf{v}\cdot\nabla) f_0 + \frac{e}{c}(\mathbf{v}\times\mathbf{B}_0)\frac{\partial f_0}{\partial \mathbf{p}} \\ &= -e\mathbf{E}\frac{\partial f_0}{\partial \mathbf{p}} - \frac{e}{c}(\mathbf{v}\times\mathbf{b})\frac{\partial f_0}{\partial \mathbf{p}} - \left\langle \frac{e}{c}(\mathbf{v}\times\tilde{\mathbf{b}})\frac{\partial f_1}{\partial \mathbf{p}}\right\rangle.\end{aligned} \tag{23}$$

Subtracting Eq. (23) from Eq. (21) and taking into account representation (22), we have

$$\begin{aligned}&\frac{\partial f_1}{\partial t} + (\mathbf{v}\cdot\nabla) f_1 + \frac{e}{c}(\mathbf{v}\times\mathbf{B}_0)\frac{\partial f_1}{\partial \mathbf{p}} \\ &= -e\mathbf{E}\frac{\partial f_1}{\partial \mathbf{p}} - \frac{e}{c}(\mathbf{v}\times\tilde{\mathbf{b}})\frac{\partial f_0}{\partial \mathbf{p}} - \frac{e}{c}(\mathbf{v}\times\mathbf{b})\frac{\partial f_1}{\partial \mathbf{p}}.\end{aligned} \tag{24}$$

The solution to Eq. (23) with zero on the right-hand side is the Maxwellian distribution function $f_0^{(0)}$. Retaining the term with E on the right-hand side yields the solution

$$f_0^{(1)} = -e\int_0^{+\infty}\left(\mathbf{E}\frac{\partial f_0^{(0)}}{\partial \mathbf{p}}\right)' d\tau. \tag{25}$$

Here, the prime denotes the transformation of the coordinates and time:

$$\begin{aligned}&\kappa \longrightarrow \kappa + \frac{v_\perp}{\omega_{Bi}}\sin\varphi - \frac{v_\perp}{\omega_{Bi}}\sin(\varphi + \omega_{Bi}\tau), \\ &\varphi \longrightarrow \varphi + \omega_{Bi}\tau, \quad t \longrightarrow t - \tau,\end{aligned} \tag{26}$$

where $v_\perp = v\sin\theta$, θ is the angle between the velocity vector and the magnetic field $\mathbf{B}_0$, and φ is the angle of gyration of a particle around the direction of the magnetic field B_0. Now, we take the right-hand side of Eq. (24) with $f_0 = f_0^{(0)} + f_0^{(1)}$ and represent f_1 on the left-hand side as the sum $f_1^l + f_1^n$, where f_1^l and f_1^n are, respectively, linear and nonlinear functions of the fields E and b. In the linear approximation, we omit the nonlinear terms to obtain the following solution to Eq. (24):

$$f_1^l = \frac{e^2}{c}\int_0^{+\infty}\left[(\mathbf{v}\times\tilde{\mathbf{b}})'\frac{\partial}{\partial \mathbf{p}}\int_0^{+\infty}\left(\mathbf{E}\frac{\partial f_0^{(0)}}{\partial \mathbf{p}}\right)'' d\tau\right] d\xi. \tag{27}$$

Then, on the right-hand side of Eq. (23), we replace f_1 by solution (27) and f_0 by solution $f_0^{(1)}$ from (25) to arrive at Eq. (23). Summing all of these solutions gives

$$\begin{aligned}f_0 = &-e\int_0^{+\infty}\left(\mathbf{E}\frac{\partial f_0^{(1)}}{\partial \mathbf{p}}\right)' d\gamma - \frac{e}{c}\int_0^{+\infty}\left[(\mathbf{v}\times\mathbf{b})\frac{\partial f_0^{(1)}}{\partial \mathbf{p}}\right]' d\gamma \\ &- \frac{e^3}{c^2}\int_0^{+\infty}\left\langle(\mathbf{v}\times\tilde{\mathbf{b}})'\frac{\partial}{\partial \mathbf{p}}\int_0^{+\infty}\left[(\mathbf{v}\times\tilde{\mathbf{b}})''\frac{\partial}{\partial \mathbf{p}}\int_0^{+\infty}\left(\mathbf{E}\frac{\partial f_0^{(0)}}{\partial \mathbf{p}}\right)''' d\tau\right] d\xi\right\rangle d\gamma.\end{aligned} \tag{28}$$

The last term in solution (28) is the sought-for correction to the distribution function. The first two terms were used in [7] in order to determine the transverse currents j_x and j_y. These currents are described by the formulas

$$\begin{aligned}\langle j_x\rangle &= e\int v_x\langle f^{(i)} - f^{(e)}\rangle d^3p, \\ \langle j_y\rangle &= e\int v_y\langle f^{(i)} - f^{(e)}\rangle d^3p.\end{aligned} \tag{29}$$

To find the averages $\langle j_x\rangle$ and $\langle j_y\rangle$, we simplify solution (28) by taking into account the long-wavelength character of the fields **b** and **E** and by using the correlation functions (3), transformations (26), and inequalities (4). At each step of the calculation of the integrals in solution (28), we neglect the terms whose order is higher than the required (first) order. As a result, the expressions for $\langle \tilde{j}_x\rangle$ and $\langle \tilde{j}_y\rangle$ have the form

$$\begin{aligned}\langle \tilde{j}_x\rangle = &-\frac{ne^2}{m_i}\Bigg\{A\left(-\frac{\omega^2E_x}{4\omega_{Bi}^2} - \frac{\omega^2E_y}{\omega_{Bi}^2}\right) \\ &+ B\left(-\frac{\omega^2E_x}{9\omega_{Bi}^2} - \frac{5\omega^2E_y}{18\omega_{Bi}^2}\right) + C\left(\frac{i\omega^3E_x}{4\omega_{Bi}^2} + \frac{i\omega^3E_y}{\omega_{Bi}^2}\right) \\ &+ \varepsilon\left(-\frac{\omega^2E_y}{2\omega_{Bi}^3} - \frac{\omega E_x}{\omega_{Bi}^2} + \frac{\omega^2E_x}{\omega_{Bi}^3} - \frac{2\omega E_y}{\omega_{Bi}^2}\right)\Bigg\} \\ &+ \frac{4e^2}{m_e}\Bigg\{A\left(\frac{E_x}{2} + E_y\right) + B\left(-\frac{E_y}{2} - E_x\right) \\ &+ C\left(-\frac{i\omega E_x}{2} - i\omega E_y\right)\Bigg\},\end{aligned} \tag{30}$$

$$\begin{aligned}\langle \tilde{j}_y\rangle = &-\frac{4e^2}{m_i}\Bigg\{A\left(-\frac{\omega^2E_x}{\omega_{Bi}^2} - \frac{\omega^2E_y}{2\omega_{Bi}^2}\right) \\ &+ B\left(-\frac{E_x\omega^2}{4\omega_{Bi}^2} - \frac{\omega^2E_y}{\omega_{Bi}^2}\right) + C\left(\frac{i\omega^3E_x}{\omega_{Bi}^3} + \frac{i\omega^3E_y}{2\omega_{Bi}^2}\right)\end{aligned}$$

$$+\varepsilon\left(-\frac{\omega^2 E_y}{\omega_{Bi}^3}-\frac{2\omega E_x}{\omega_{Bi}^2}+\frac{\omega^2 E_x}{2\omega_{Bi}^3}-\frac{\omega E_y}{\omega_{Bi}^2}\right)\Bigg\}$$

$$+\frac{4e^2}{m_e}\left\{A\left(E_x+\frac{E_y}{2}\right)-BE_y+C\left(-i\omega E_x-\frac{i\omega E_y}{2}\right)\right\},$$

where the quantities A, B, C, and ε are given by formulas (13). When deriving expressions (30), we discarded the terms that are as small as m_e/m_i in comparison with the leading-order terms. The expression for E_x can be found by substituting the expressions for j_x and j_y that follow from the first two terms in solution (28) into the third of equations (11):

$$E_x \approx -\frac{i\omega E_y}{\omega_{Bi}}+i\frac{3k^2 v_{Ti}^2}{2\omega_{Bi}\omega}E_y$$
$$-iE_y\left(\frac{4Am_i\omega_{Bi}^2}{m_e\omega}+\frac{B\omega}{9}-\frac{Bm_i\omega_{Bi}^2}{m_e\omega}\right). \quad (31)$$

Then, we determine the relationship between the field components b and E_y from the third of equations (11):

$$E_y = \frac{\omega}{ck}b.$$

Finally, we substitute this relationship and expression (31) into the first of equations (11) and switch to the dimensionless variables introduced in the body of the paper. As a result, we arrive at the evolutionary equation (12) for the magnetic field of an FMS wave.

Recall that the term with k_3 in Eq. (12) accounts for plasma turbulence. It is because of this term that Eq. (12) has no stable solutions. If the scale of plasma turbulence is small enough to satisfy condition (5), the first two of integrals (13), namely, A and B, vanish identically, thereby ensuring the existence of solutions describing steady-state shock fronts.

REFERENCES

1. A. B. Mikhaĭlovskiĭ and A. I. Smolyakov, Zh. Éksp. Teor. Fiz. **88**, 189 (1985) [Sov. Phys. JETP **61**, 109 (1985)].
2. A. V. Gurevich and L. P. Pitaevskiĭ, Zh. Éksp. Teor. Fiz. **65**, 593 (1973) [Sov. Phys. JETP **38**, 291 (1973)].
3. A. V. Gurevich and L. P. Pitaevskiĭ, Zh. Éksp. Teor. Fiz. **92**, 168 (1987) [Sov. Phys. JETP **66**, 490 (1987)].
4. V. R. Zemskov, Geomagn. Aéronom. **32**, 34 (1992).
5. E. Mjolhus and J. Wyller, J. Plasma Phys. **40**, 299 (1988).
6. V. R. Zemskov, Izv. Vyssh. Uchebn. Zaved., Radiofiz. **35** (8), 63 (1992).
7. S. I. Vainshteĭn, I. N. Toptygin, and A. M. Bykov, *Turbulence, Current Sheets and Shock Waves in Cosmic Plasma* (Nauka, Moscow, 1989).

Translated by O. Khadin

Plasma Physics Reports, Vol. 28, No. 3, 2002, pp. 190–195. Translated from Fizika Plazmy, Vol. 28, No. 3, 2002, pp. 215–220.
Original Russian Text Copyright © 2002 by V. Girka, I. Girka.

PLASMA OSCILLATIONS AND WAVES

Effect of Toroidal Magnetic Field Variations on the Spectra of Azimuthal Surface Waves in Metal Waveguides Entirely Filled with Plasma

V. O. Girka and I. O. Girka
Karazin National University, pl. Svobody 4, Kharkiv, 61077 Ukraine

Received May 11, 2001

Abstract—The propagation of surface waves transverse to the circular axis of a toroidal magnetized metal waveguide entirely filled with a plasma is studied using perturbation theory. The distribution of the fields of these waves in such a waveguide structure is investigated. It is shown that the toroidicity introduces a second-order correction to the eigenfrequency of the surface waves. *© 2002 MAIK “Nauka/Interperiodica”.*

1. INTRODUCTION

Interest in studying the properties of surface waves (SWs) propagating in a hybrid slow-wave structure stems from the promising outlook for their use in microwave electronics [1–6]. The problem of the SW spectra in a toroidal magnetized metal waveguide is important for practical applications concerning not only the development of devices for plasma electronics but also the interpretation of some experimental results in controlled nuclear fusion research, specifically, laboratory data on phenomena in wall plasmas [7, 8].

In a toroidal gaseous plasma [8, 9], the toroidicity manifests itself in the following factors: first, spatial variations of a constant external toroidal magnetic field; second, the radial displacement of magnetic surfaces [10]; and third, the deviation of the shape of the poloidal cross sections of magnetic surfaces from being circular. The influence of the second and third factors on the dispersion properties of azimuthal SWs (ASWs) propagating across a uniform axial magnetic field (and, accordingly, along the minor azimuthal angle) was thoroughly investigated in [6]. The present paper is aimed at studying the influence of the first factor, which is the only important factor for a solid-state plasma.

Our paper is organized as follows. In Section 2, we construct the model and write out the basic equations. In Section 3, we outline the dispersion properties of ASWs in order to provide a starting point for our analysis. In Section 4, Maxwell's equations are solved to first order in the small toroidicity parameter. In Section 5, we solve Maxwell's equation and derive the dispersion relation to second order in this parameter. In the Conclusion, we summarize the main results of our study.

2. FORMULATION OF THE PROBLEM

When there is no dielectric layer between the plasma and the vacuum chamber wall, the magnitude of the external uniform magnetic field has the strongest impact on the dispersion properties of ASWs [11]. Because of this, we consider a toroidal metal waveguide with a circular cross section of radius a, which is assumed to be filled entirely with a plasma and to be homogeneous along the toroidal angle ($\partial/\partial\zeta = 0$). In a right-handed quasitoroidal coordinate system, in which we are working here, the poloidal angle is measured from the direction toward the center of symmetry of the torus. Since the effect of the radial variations of the plasma density on the dispersion properties of ASWs was thoroughly investigated in [12], we assume that the waveguide is filled with a homogeneous plasma. This assumption corresponds, in particular, to an n-semiconductor plasma. The constant external toroidal magnetic field has the form

$$B_{0\xi} = B_0/[1-(r/R)\cos\vartheta], \tag{1}$$

where R is the major radius of the torus. We are investigating the propagation of an E-wave, i.e., a wave with the components E_r, E_ϑ, and B_ξ (recall that a surface H-wave, having the components E_ξ, B_r, and B_ϑ, cannot be excited in waveguides with the above geometry [12]). In semiconductor physics, the SWs under consideration are called magnetoplasma polaritons and the above orientation of the external magnetic field with respect to the plasma–metal boundary corresponds to the Voight geometry.

The vectors of the electric induction and electric field strength are assumed to be related by the dielectric tensor of a cold, weakly collisional, magnetized plasma. In what follows, we will use the following two elements of the dielectric tensor:

$$\varepsilon_{11} = \varepsilon_0 - \sum_\alpha \frac{\omega_{p\alpha}^2}{\omega^2 - \omega_{c\alpha}^2} \equiv \varepsilon_1, \tag{2}$$

$$\varepsilon_{12} = i\sum_{\alpha}\frac{\omega_{c\alpha}\omega_{p\alpha}^{2}}{\omega(\omega^{2}-\omega_{c\alpha}^{2})} \equiv i\varepsilon_{2}, \quad (3)$$

where $\omega_{p\alpha}$ and $\omega_{c\alpha}$ are, respectively, the Langmuir and cyclotron frequencies of particles of species α. The plasma that fills the waveguide is assumed to be dense enough to satisfy the inequality $\omega_{pe}^{2} > \varepsilon_{0}\omega_{ce}^{2}$ [13]. For a gaseous plasma, we have $\varepsilon_0 = 1$. For an *n*-semiconductor plasma, the dielectric constant of the lattice is $\varepsilon_0 > 1$, so that the only nonzero terms in the sums in definitions (2) and (3) are those describing the conduction electrons. Assuming that the toroidicity is small, $\varepsilon_t = a/R \ll 1$, we expand each of the dielectric tensor elements ε_{ij} in a series in the toroidicity parameter:

$$\varepsilon_{1,2} = \varepsilon_{1,2}^{(0)} + \varepsilon_{1,2}^{(1)}\cos\vartheta + \varepsilon_{1,2}^{(2)}. \quad (4)$$

The main terms in expansions (4),

$$\varepsilon_{1}^{(0)} = \varepsilon_{0} - \sum_{\alpha}\frac{\omega_{p\alpha}^{2}}{\omega^{2}-\omega_{c\alpha}^{(0)2}}, \quad \varepsilon_{2}^{(0)} = \sum_{\alpha}\frac{\omega_{c\alpha}^{(0)}\omega_{p\alpha}^{2}}{\omega(\omega^{2}-\omega_{c\alpha}^{(0)2})} \quad (5)$$

are coordinate-independent, $\varepsilon_{1,2}^{(0)} = \varepsilon_{1,2}\big|_{B_{0\zeta} = B_0}$.

The first-order corrections are linear in the minor radius:

$$\begin{aligned}\varepsilon_{1}^{(1)} &= -2\frac{r}{R}\sum_{\alpha}\frac{\omega_{p\alpha}^{2}\omega_{c\alpha}^{(0)2}}{(\omega^{2}-\omega_{c\alpha}^{(0)2})^{2}},\\ \varepsilon_{2}^{(1)} &= -\frac{r}{R}\sum_{\alpha}\frac{\omega_{c\alpha}^{(0)}\omega_{p\alpha}^{2}(\omega^{2}+\omega_{c\alpha}^{(0)2})}{\omega(\omega^{2}-\omega_{c\alpha}^{(0)2})^{2}},\end{aligned} \quad (6)$$

whereas the second-order corrections are quadratic in the minor radius:

$$\begin{aligned}\varepsilon_{1}^{(2)} &= \frac{r^{2}}{2R^{2}}\sum_{\alpha}\frac{\omega_{p\alpha}^{2}\omega_{c\alpha}^{(0)2}(\omega_{c\alpha}^{(0)2}+3\omega^{2})}{(\omega_{c\alpha}^{(0)2}-\omega^{2})^{3}},\\ \varepsilon_{2}^{(2)} &= \frac{r^{2}}{2R^{2}}\sum_{\alpha}\frac{\omega_{c\alpha}^{(0)}\omega_{p\alpha}^{2}\omega(\omega^{2}+3\omega_{c\alpha}^{(0)2})}{(\omega_{c\alpha}^{(0)2}-\omega^{2})^{3}}.\end{aligned} \quad (7)$$

In expansions (4), we can neglect the second-order terms that are proportional to $\exp(2i\vartheta)$, because they make third-order (and higher order) contributions to the eigenfrequency of the ASWs. In expressions (5)–(7), the cyclotron frequency is defined in terms of the uniform toroidal magnetic field B_0 (in the zeroth order approximation).

The toroidal component of the RF magnetic field is determined from the equation

$$\begin{aligned}&\frac{1}{r}\frac{\partial}{\partial r}\left(\frac{r\varepsilon_{1}}{\varepsilon_{\perp}}\frac{\partial B_{\xi}}{\partial r}\right) + \frac{i}{r}\frac{\partial}{\partial\vartheta}\left(\frac{\varepsilon_{2}}{\varepsilon_{\perp}}\right)\frac{\partial B_{\xi}}{\partial r} + \frac{\omega^{2}}{c^{2}}B_{\xi}\\ &+ \frac{1}{r^{2}}\frac{\partial}{\partial\vartheta}\left(\frac{\varepsilon_{1}}{\varepsilon_{2}}\frac{\partial B_{\xi}}{\partial\vartheta}\right) - \frac{i}{r}\frac{\partial}{\partial r}\left(\frac{\varepsilon_{2}}{\varepsilon_{\perp}}\right)\frac{\partial B_{\xi}}{\partial\vartheta} = 0,\end{aligned} \quad (8)$$

where $\varepsilon_{\perp} = \varepsilon_{1}^{2} - \varepsilon_{2}^{2}$. In the zeroth approximation, Eq. (8) describes the independent propagation of ASWs with different azimuthal mode numbers. This circumstance and the symmetry of the problem [see expansions (4)] allow us to represent the sought-for solution to Eq. (8) in the form

$$\begin{aligned}B_{\xi} = [&B_{\xi}^{(0)}(r) + B_{\xi}^{(2)}(r) + B_{\xi}^{(+1)}(r)e^{i\vartheta} + B_{\xi}^{(-1)}(r)e^{-i\vartheta}]\\ &\times\exp(im\vartheta - i\omega t).\end{aligned} \quad (9)$$

The electric field components of the ASWs are described by expressions analogous to formula (9). In addition to the fundamental mode (represented by the term $\propto\exp im\vartheta$), this formula describes the two nearest satellite modes (represented by the terms $\infty\exp i(m \pm 1)\vartheta$). As will be shown below, the toroidal geometry of the waveguide gives rise to only a second-order correction $B_{\xi}^{(2)}$ to the amplitude of the fundamental mode of the ASWs.

For further analysis, we need the relationship of the poloidal component of the wave electric field E_{ϑ} to B_{ξ}:

$$E_{\vartheta}^{(0)}(r) = \frac{c}{i\omega\varepsilon_{\perp}^{(0)}}\left[\varepsilon_{1}^{(0)}\frac{dB_{\xi}^{(0)}}{dr} + \frac{m\varepsilon_{2}^{(0)}}{r}B_{\xi}^{(0)}\right], \quad (10)$$

$$\begin{aligned}E_{\vartheta}^{(\pm1)}(r) = \frac{c}{i\omega\varepsilon_{\perp}^{(0)}}\Bigg[&\varepsilon_{1}^{(0)}\frac{\partial B_{\xi}^{(\pm1)}}{\partial r} + \frac{m\pm1}{r}\varepsilon_{2}^{(0)}B_{\xi}^{(\pm1)}\\ &+ \frac{\varepsilon_{\perp}^{(0)}\varepsilon_{1}^{(1)} - \varepsilon_{\perp}^{(1)}\varepsilon_{1}^{(0)}}{2\varepsilon_{\perp}^{(0)}}\frac{\partial B_{\xi}^{(0)}}{\partial r} + \frac{m(\varepsilon_{\perp}^{(0)}\varepsilon_{2}^{(1)} - \varepsilon_{\perp}^{(1)}\varepsilon_{2}^{(0)})}{2r\varepsilon_{\perp}^{(0)}}B_{\xi}^{(0)}\Bigg],\end{aligned} \quad (11)$$

$$\begin{aligned}E_{\vartheta}^{(2)}(r) = \frac{1}{\varepsilon_{\perp}^{(0)}}\Bigg\{&-\frac{\varepsilon_{\perp}^{(2)}}{2}E_{\vartheta}^{(0)} - \frac{\varepsilon_{\perp}^{(1)}}{2}(E_{\vartheta}^{(+1)} + E_{\vartheta}^{(-1)})\\ &+ \frac{c\varepsilon_{1}^{(1)}}{2i\omega}\frac{\partial}{\partial r}(B_{\xi}^{(+1)} + B_{\xi}^{(-1)}) + \frac{c\varepsilon_{1}^{(0)}}{i\omega}\frac{\partial B_{\xi}^{(2)}}{\partial r} + \frac{c\varepsilon_{1}^{(2)}}{2i\omega}\frac{\partial B_{\xi}^{(0)}}{\partial r}\\ &+ \frac{cm\varepsilon_{2}^{(0)}}{i\omega r}B_{\xi}^{(2)} + \frac{cm\varepsilon_{2}^{(2)}}{2i\omega r}B_{\xi}^{(0)}\\ &+ \frac{cm\varepsilon_{2}^{(1)}}{2i\omega r}[(m+1)B_{\xi}^{(+1)} + (m-1)B_{\xi}^{(-1)}]\Bigg\},\end{aligned} \quad (12)$$

where

$$\varepsilon_\perp^{(0)} = \varepsilon_1^{(0)2} - \varepsilon_2^{(0)2}, \quad \varepsilon_\perp^{(1)} = 2\varepsilon_1^{(0)}\varepsilon_1^{(1)} - 2\varepsilon_2^{(0)}\varepsilon_2^{(1)},$$
$$\varepsilon_\perp^{(2)} = \varepsilon_1^{(1)2} + 2\varepsilon_1^{(0)}\varepsilon_1^{(2)} - \varepsilon_2^{(1)2} - 2\varepsilon_2^{(0)}\varepsilon_2^{(2)}. \tag{13}$$

The solution to Eq. (8) should satisfy the following boundary conditions: the wave field is finite inside the waveguide and the tangential (in the case at hand, poloidal) component of the electric field vanishes at the inner surface of the metal chamber ($E_\vartheta|_{r=a} = 0$).

3. ASW IN A CIRCULAR CYLINDRICAL WAVEGUIDE (THE ZEROTH APPROXIMATION)

In the zeroth approximation, we consider ASWs propagating in the azimuthal direction in a cylindrical metal waveguide with a circular cross section of radius a [13], which is filled entirely with a homogeneous plasma. The constant external magnetic field B_0 is assumed to be parallel to the waveguide axis. Let us briefly outline the main properties of the ASWs.

In the zeroth approximation, the amplitude $B_\xi^{(0)}(r)$ of the fundamental mode is expressed through the modified Bessel function $I_m(\xi)$:

$$B_\xi^{(0)}(r) = I_m(k_\perp r). \tag{14}$$

The penetration depth $k_\perp^{-1}$ of the wave field into the plasma is defined by

$$k_\perp^2 = -(\omega/c)^2\varepsilon_\perp^{(0)}/\varepsilon_1^{(0)} > 0. \tag{15}$$

The solution $\omega_m^{(0)}$ to the zero-order dispersion relation

$$D^{(0)}(\omega_m^{(0)}) = 0 \tag{16}$$

is assumed to be known. The dispersion relation (16) follows from the condition that the amplitude $E_\vartheta^{(0)}(r)$ of the fundamental harmonic of the poloidal electric field of an ASW vanishes at the plasma–metal boundary, $D^{(0)} \equiv E_\vartheta^{(0)}(a)$. The dependence of the ASW eigenfrequency $\omega_m^{(0)}$ on the parameters of the plasma waveguide in the zeroth approximation was thoroughly investigated in [13].

The frequencies of ASWs with positive azimuthal mode numbers are low,

$$\sqrt{\omega_{pi}^2/\varepsilon_0 + \omega_{ci}^2} < \omega_m^{(0)} < |\omega_{ce}|, \tag{17}$$

while the frequencies of ASWs with negative mode numbers m are high,

$$\omega_U < \omega_m^{(0)} < \omega_{11} = \frac{1}{2}|\omega_{ce}| + \sqrt{\frac{1}{4}\omega_{ce}^2 + \frac{\omega_{pe}^2}{\varepsilon_0}}, \tag{18}$$

where $\omega_U = \sqrt{\omega_{ce}^2 + \omega_{pe}^2/\varepsilon_0}$ is the upper hybrid frequency.

4. AMPLITUDES OF THE SATELLITE MODES (THE FIRST APPROXIMATION)

In our analysis, we assume that the amplitudes $B_\xi^{(\pm 1)}$ of the satellite modes are first-order quantities. We substitute expression (9) for the field amplitude B_ξ and expansions (4) for the dielectric tensor elements ε_{ij} into Eq. (8); then, in the resulting equation, we single out first-order terms, which turn out to be proportional either to $\exp[i(m+1)\theta]$ or to $\exp[i(m-1)\theta]$. In other words, taking into account first-order terms does not change the fundamental mode amplitude. Consequently, in the first approximation, there are no toroidicity-induced corrections to the eigenfrequency of the ASW. These first-order terms enter the inhomogeneous Bessel equations for $B^{(\pm 1)}(r)$ with the known right-hand side. These equations have the following solutions, which satisfy the condition for the wave fields to be finite at the waveguide axis:

$$B_\xi^{(\pm 1)}(r) = -I_{m\pm 1}(k_\perp r)\int_a^r K_{m\pm 1}(k_\perp r)\hat{L}_\mp^{(1)} I_m(k_\perp r) r\,dr$$
$$+ C_\pm I_{m\pm 1}(k_\perp r) + K_{m\pm 1}(k_\perp r)\int_0^r I_{m\pm 1}(k_\perp r)\hat{L}_\mp^{(1)} I_m(k_\perp r) r\,dr, \tag{19}$$

where the operator $\hat{L}_\pm^{(1)}$ has the form

$$\hat{L}_\pm^{(1)} = (2\varepsilon_1^{(0)}\varepsilon_\perp^{(0)})^{-1}\left\{\frac{\varepsilon_\perp^{(1)}}{r}\frac{\partial}{\partial r}\left(r\varepsilon_1^{(0)}\frac{\partial}{\partial r}\right)\right.$$
$$+ \frac{\varepsilon_\perp^{(0)}}{r}\frac{\partial}{\partial r}\left(r\varepsilon_1^{(1)}\frac{\partial}{\partial r}\right) - \varepsilon_1^{(0)}\frac{\partial \varepsilon_\perp^{(1)}}{\partial r}\frac{\partial}{\partial r} - \frac{\varepsilon_\perp^{(0)}}{r}\frac{\partial \varepsilon_2^{(1)}}{\partial r}\hat{\Theta}$$
$$+ \frac{\varepsilon_2^{(0)}}{r}\frac{\partial \varepsilon_\perp^{(1)}}{\partial r}\hat{\Theta} - \frac{\varepsilon_\perp^{(1)}}{r^2}\varepsilon_1^{(0)}\hat{\Theta}^2 - \frac{\varepsilon_\perp^{(0)}\varepsilon_1^{(1)}}{r^2}\hat{\Theta}^2 + 2\frac{\omega^2}{c^2}\varepsilon_\perp^{(0)}\varepsilon_\perp^{(1)} \tag{20}$$
$$\left.\mp \frac{\varepsilon_\perp^{(0)}\varepsilon_\perp^{(1)}}{r^2}\hat{\Theta} \pm \frac{\varepsilon_1^{(0)}\varepsilon_\perp^{(1)}}{r^2}\hat{\Theta} \pm \frac{\varepsilon_2^{(1)}\varepsilon_\perp^{(0)}}{r}\frac{\partial}{\partial r} \mp \frac{\varepsilon_2^{(0)}\varepsilon_\perp^{(1)}}{r}\frac{\partial}{\partial r}\right\},$$
$$\hat{\Theta} I_m = -m I_m.$$

The integration constants $C_\pm$ can be found from the condition that the amplitudes of the first satellite harmonics of the poloidal electric field vanish at the metal surface of the waveguide, $E_\vartheta^{(\pm 1)}(a) = 0$:

$$C_\pm = -\left[\varepsilon_1^{(0)} k_\perp K'_{m\pm 1}\int_0^a I_{m\pm 1}\hat{L}_\mp^{(1)} I_m r\,dr\right.$$

$$+\frac{m\pm1}{a}\varepsilon_2^{(0)}K_{m\pm1}\int_0^a I_{m\pm1}\hat{L}_{\mp}^{(1)}I_m r dr$$
$$+\frac{\varepsilon_\perp^{(0)}\varepsilon_1^{(1)}-\varepsilon_\perp^{(1)}\varepsilon_1^{(0)}}{2\varepsilon_\perp^{(0)}}k_\perp I'_m+\frac{m(\varepsilon_\perp^{(0)}\varepsilon_2^{(1)}-\varepsilon_\perp^{(1)}\varepsilon_2^{(0)})}{2a\varepsilon_\perp^{(0)}}I_m\Bigg] \tag{21}$$
$$\times\left[\varepsilon_1^{(0)}k_\perp I'_{m\pm1}+\frac{m\pm1}{a}\varepsilon_2^{(0)}I_{m\pm1}\right]^{-1}\Bigg|_{\substack{r=a\\ \omega=\omega_m^{(0)}}}.$$

5. EIGENFREQUENCY OF THE ASW CORRECTED FOR THE TOROIDAL GEOMETRY OF THE WAVEGUIDE (THE SECOND APPROXIMATION)

The second-order terms in Eq. (8) are proportional to one of the three phase factors: $\exp im\vartheta$ or $\exp i(m\pm2)\vartheta$. Retaining only the terms proportional to $\exp i(m\pm2)\vartheta$ yields equations for the amplitudes of the second satellite modes. In expansion (9), these modes are neglected because they make third-order (and higher order) contributions to the eigenfrequency of the ASW. Keeping the second-order terms that are proportional to $\exp im\vartheta$ gives an inhomogeneous differential Bessel equation for the correction $B_\xi^{(2)}(r)$ to the amplitude of the fundamental mode of the ASW. The solution to this equation that satisfies the condition for the wave fields to be finite at the circular axis of the torus can be found by the method of variation of constants:

$$B_\xi^{(2)}=K_m(k_\perp r)\int_0^r I_m(\hat{L}_-^{(1)}B_\xi^{(-1)}+\hat{L}_+^{(1)}B_\xi^{(+1)}+\hat{L}^{(2)}B_\xi^{(0)})rdr$$
$$-I_m(k_\perp r)\int_0^r K_m(\hat{L}_-^{(1)}B_\xi^{(-1)}+\hat{L}_+^{(1)}B_\xi^{(+1)}+\hat{L}^{(2)}B_\xi^{(0)})rdr \tag{22}$$
$$+C_2I_m(k_\perp r).$$

Solution (22) is the sum of the particular solution to the inhomogeneous differential equation (the first two integral terms) and the general solution to the corresponding differential equation (the third term $C_2I_m(k_\perp r)$). In the general expression (9) for the axial component of the wave magnetic field, the term $C_2I_m(k_\perp r)$ and the amplitude $B_\xi^{(0)}(r)$ are like terms. In other words, the integration constant C_2 is a correction to the normalizing factor, which is set equal to unity in the zeroth approximation. That is why the constant C_2 is found not from the boundary conditions but rather from the following condition, which is analogous to the normalization condition for the wave function in quantum mechanics [14]:

$$\int_0^a[2B_\xi^{(2)}I_m(k_\perp r)+(B_\xi^{(+1)})^2+(B_\xi^{(-1)})^2]rdr=0. \tag{23}$$

This condition implies that the energy of the wave magnetic field calculated in the second approximation should coincide with the energy calculated in the zeroth approximation. At the same time, the form of the second-order dispersion relation, which will be derived below, is independent of the value of the constant C_2.

The method that is used here to solve the problem of eigenwaves in periodically inhomogeneous plasma waveguides has already been applied in the literature. Thus, the splitting of the spectra of MHD plasma oscillations in a rippled magnetic field in the case of degenerate eigenvalues was described in [15] using perturbation theory. In [16], the effect of the helical inhomogeneity of a confining magnetic field on the natural MHD oscillations in a straight stellarator was investigated perturbatively accurate to the second-order terms.

The operator $\hat{L}^{(2)}$ in solution (22) is defined as

$$\hat{L}^{(2)}=[2\varepsilon_1^{(0)}\varepsilon_\perp^{(0)}]^{-1}\Bigg\{\frac{\varepsilon_\perp^{(2)}}{r}\frac{\partial}{\partial r}\left[r\varepsilon_1^{(0)}\frac{\partial}{\partial r}\right]$$
$$+\frac{\varepsilon_\perp^{(1)}}{r}\frac{\partial}{\partial r}\left[r\varepsilon_1^{(0)}\frac{\partial}{\partial r}\right]+\frac{\varepsilon_\perp^{(0)}}{r}\frac{\partial}{\partial r}\left[r\varepsilon_1^{(2)}\frac{\partial}{\partial r}\right]-\frac{\varepsilon_1^{(1)}\varepsilon_\perp^{(1)}}{r}\frac{\partial}{\partial r}$$
$$-\frac{2\varepsilon_1^{(0)}\varepsilon_\perp^{(2)}}{r}\frac{\partial}{\partial r}-\frac{\varepsilon_\perp^{(1)}\varepsilon_2^{(1)}}{r^2}\hat{\Theta}-\frac{2\varepsilon_\perp^{(0)}\varepsilon_2^{(2)}}{r^2}\hat{\Theta}+\frac{\varepsilon_2^{(1)}\varepsilon_\perp^{(1)}}{r^2}\hat{\Theta} \tag{24}$$
$$+\frac{2\varepsilon_2^{(0)}\varepsilon_\perp^{(2)}}{r^2}\hat{\Theta}-\frac{\varepsilon_\perp^{(2)}\varepsilon_1^{(0)}}{r^2}\hat{\Theta}^2-\frac{\varepsilon_\perp^{(1)}\varepsilon_1^{(1)}}{r^2}\hat{\Theta}^2-\frac{\varepsilon_\perp^{(0)}\varepsilon_1^{(2)}}{r^2}\hat{\Theta}^2$$
$$+2\frac{\omega^2}{c^2}\varepsilon_\perp^{(2)}\varepsilon_\perp^{(0)}+\frac{\omega^2}{c^2}\varepsilon_\perp^{(1)}\varepsilon_\perp^{(1)}\Bigg\}.$$

In the second approximation, the boundary condition for the fundamental harmonic of the poloidal component of the wave electric field at a metal surface of the waveguide can be represented in the form

$$D^{(0)}+D^{(2)}=0, \tag{25}$$

where $D^{(2)}=E_\vartheta^{(2)}(a)$.

The toroidal geometry of the waveguide gives rise to only a second-order correction $\omega_m^{(2)}$ to the eigenfrequency of the ASW:

$$\omega_m^{(2)}=-D^{(2)}\left(\frac{\partial D^{(0)}}{\partial\omega}\right)^{-1}\Bigg|_{\omega=\omega_m^{(0)}}. \tag{26}$$

The applicability condition for the approach developed here to determine the dispersion properties of ASWs in toroidal waveguides implies the smallness of the second-order correction with respect to the zero-order eigenfrequency: $\left|\omega_m^{(2)}\right| \ll \omega_m^{(0)}$.

The main advantage of the resulting formula (26) is that it reduces the problem with two-dimensional variations of the toroidal magnetic field (in the poloidal cross section of the waveguide) to the problem with one-dimensional variations (in the radial direction). The main drawback of formula (26) is its complexity. In the limiting case of wide waveguides ($R \gg a \gg |m|/k_\perp$), the eigenfrequency of the ASW can be calculated in the low-frequency (LF) range (17) using the asymptotic expressions

$$\omega_m^{(0)} = \frac{m\delta}{a}|\omega_{ce}|, \tag{27}$$

$$\omega_m^{(2)} = -\frac{1}{4}\varepsilon_t^2\omega_m^{(0)}, \tag{28}$$

whereas, in the high-frequency (HF) range (18), it can be calculated using the asymptotic expressions

$$\omega_m^{(0)} = \sqrt{\omega_n^2 + \frac{m^2c^2}{a^2}}, \tag{29}$$

$$\omega_m^{(2)} = \frac{\varepsilon_t^2}{4}\frac{c^2m^2}{\omega^2a^2}\left(1 + \frac{3|\omega_{ce}|k_\perp a}{\omega|m|}\right)\omega_m^{(0)}, \tag{30}$$

where $\delta = c/\omega_{pe}$.

For the eigenfrequencies of LF ASWs propagating in narrow ($k_\perp a \ll |m|$) toroidal waveguides, formula (26) yields the following asymptotic expressions:

$$\omega_m^{(0)} = |\omega_{ce}|\left[1 - \frac{1}{2}\left(\frac{a}{m\delta}\right)^2\right], \tag{31}$$

$$\omega^{(2)} = \frac{2m^2 - m + 1}{4m^2(m+1)}\varepsilon_t^2\omega_m^{(0)}. \tag{32}$$

In the zeroth approximation, the eigenfrequency $\omega_m^{(0)}$ of HF ASWs is described by expression (29) and the corresponding second-order correction is approximately equal to

$$\omega^{(2)} = \frac{2m^2 + m + 1}{2m^2}\varepsilon_t^2\left(\frac{m\delta}{a}\right)^4\frac{\omega_{pe}}{|\omega_{ce}|}\omega_m^{(0)}. \tag{33}$$

Note that, in narrow waveguides, the radial dependences of the amplitudes of satellite modes are essentially different, $B_\xi^{(\pm 1)}(r) \propto r^{m \pm 1}$; however, at the metal waveguide surface, these amplitudes are of the same order of magnitude because of the difference in the numerical factors $C_\pm$.

In order to analyze the results obtained, we present the asymptotic expressions [17] for the correction $\omega_{\mathrm{el}}^{(2)}$ to the eigenfrequency of the ASW that comes from the ellipticity of the cross section of a metal waveguide entirely filled with plasma. For LF ASWs propagating in wide waveguides, the correction $\omega_{\mathrm{el}}^{(2)}$ has the form

$$\omega_{\mathrm{el}}^{(2)} = -\frac{1}{4}\varepsilon_{\mathrm{el}}^2\left(4 - m^2 + \frac{2a}{\delta}\right)\omega_m^{(0)}. \tag{34}$$

In terms of the ellipticity parameter, the shape of the cross section of the metal chamber is described by the expression $r(\vartheta) = a(1 + \varepsilon_{\mathrm{el}}\cos 2(\vartheta - \pi/2))$. In the case of narrow waveguides, we have

$$\omega_{\mathrm{el}}^{(2)} = -\frac{\varepsilon_{\mathrm{el}}^2}{2m}\frac{2 - 4m^2 - 4m^2}{2 - 4m^2}\frac{a^2}{\delta^2}\omega_m^{(0)}. \tag{35}$$

Consequently, for a narrow waveguide with a fixed shape of the cross section of the chamber filled with a low-density plasma such that $\omega_{pe}^2 \ll \varepsilon_t^2c^2/(\varepsilon_{\mathrm{el}}^2a^2)$, the effect of toroidal variations of the external magnetic field on the ASW spectra is stronger than that of the elliptical shape of the waveguide cross section. Here, we do not compare the effect of the toroidal magnetic field variations with that of the radial displacement of the magnetic surfaces, because this displacement is definitely small near the inner surface of the metal chamber, i.e., in the region where the waves under analysis are localized.

6. CONCLUSION

We have established that ASWs can exist in toroidal metal waveguides and have derived the spatial distributions (10)–(12), (19), and (22) of the wave fields. It is shown that toroidal variations of the external magnetic field in toroidal waveguides cause ASWs to propagate as wave packets. In such a packet, the amplitudes A_{m+N} of the satellite modes are proportional to $\propto \exp[i(m + N)\vartheta]$, so that they are small, $A_{m+N} \sim \varepsilon_t^N A_m$, in comparison with the fundamental mode amplitude, which is proportional to $\propto \exp[im\vartheta]$. The corrections to the fundamental mode amplitude that come from toroidal variations of the external magnetic field are second-order in the small toroidicity parameter ε_t.

We have determined correction (26) to the eigenfrequency of ASWs. This correction, which is introduced by toroidal variations of the external magnetic field, is a second-order quantity. For wide and narrow waveguides, we have obtained simple analytic expressions (27)–(33) for the eigenfrequencies of ASWs in the two frequency ranges in which the waves can exist.

ACKNOWLEDGMENTS

This work was supported in part by the Science and Technology Center of Ukraine, project no. 1112.

REFERENCES

1. E. P. Kurushin and E. I. Nefedov, *Electrodynamics of Anisotropic Wave Guiding Structures* (Nauka, Moscow, 1983).
2. N. N. Beletsky, A. A. Bulgakov, S. I. Khankina, and V. M. Yakovenko, *Plasma Instabilities and Nonlinear Phenomena in Semiconductors* (Naukova Dumka, Kiev, 1984).
3. N. A. Azarenkov, A. N. Kondratenko, and K. N. Ostrikov, Izv. Vyssh. Uchebn. Zaved., Radiofiz. **63**, 335 (1993).
4. I. A. Girka, Fiz. Plazmy **23**, 246 (1997) [Plasma Phys. Rep. **23**, 225 (1997)].
5. V. A. Girka and I. A. Girka, Zh. Tekh. Fiz. **67** (7), 92 (1997) [Tech. Phys. **42**, 803 (1997)].
6. V. A. Girka, I. A. Girka, and I. V. Pavlenko, Fiz. Plazmy **23**, 1037 (1997) [Plasma Phys. Rep. **23**, 959 (1997)].
7. A. V. Nedospasov and M. Z. Tokar’, in *Reviews of Plasma Physics*, Ed. by B. B. Kadomtsev (Énergoatomizdat, Moscow, 1990; Consultants Bureau, New York, 1992), Vol. 18.
8. I. A. Girka and V. A. Girka, in *Proceedings of International Conference on Plasma Physics Combined with 6th Latin American Workshop on Plasma Physics, Foz do Iguacu, Brazil, 1994*, Vol. 1, p. 21.
9. I. A. Girka and K. N. Stepanov, Ukr. Fiz. Zh. **36**, 1051 (1991).
10. B. B. Kadomtsev and O. P. Pogutse, in *Reviews of Plasma Physics*, Ed. by M. A. Leontovich (Atomizdat, Moscow, 1967; Consultants Bureau, New York, 1970), Vol. 5.
11. V. A. Girka, I. A. Girka, A. N. Kondratenko, and V. I. Tkachenko, Radiotekh. Élektron. (Moscow) **33**, 1031 (1988) [Sov. J. Commun. Techn. **33** (8), 37 (1988)].
12. V. A. Girka and I. A. Girka, Izv. Vyssh. Uchebn. Zaved., Radiofiz. **34**, 386 (1991) [Radiophys. Quant. Electron. **34**, 324 (1991)].
13. V. A. Girka, I. A. Girka, A. N. Kondratenko, and V. I. Tkachenko, Radiotekh. Élektron. (Moscow) **34**, 296 (1989) [Sov. J. Commun. Techn. **34** (4), 96 (1989)].
14. L. D. Landau and E. M. Lifshitz, *Quantum Mechanics: Non-Relativistic Theory* (Nauka, Moscow, 1989; Pergamon, New York, 1977).
15. I. A. Girka, V. I. Lapshin, and K. N. Stepanov, Fiz. Plazmy **24**, 1015 (1998) [Plasma Phys. Rep. **24**, 948 (1998)].
16. I. A. Girka and P. K. Kovtun, Fiz. Plazmy **26**, 36 (2000) [Plasma Phys. Rep. **26**, 33 (2000)].
17. I. O. Girka and O. V. Zolotukhin, Ukr. Fiz. Zh. **39**, 682 (1994).

Translated by I. Kalabalyk

Plasma Physics Reports, Vol. 28, No. 3, 2002, pp. 196–203. Translated from Fizika Plazmy, Vol. 28, No. 3, 2002, pp. 221–228.

ION AND PLASMA SOURCES

RF Discharge-Based Plasma Emitter

A. A. Ivanov, I. V. Shikhovtsev, A. A. Podyminogin, I. I. Averboukh, T. D. Akhmetov, V. I. Davydenko, and P. P. Deĭchuli

Budker Institute of Nuclear Physics, Siberian Division, Russian Academy of Sciences,
pr. Akademika Lavrent'eva 11, Novosibirsk, 630090 Russia

Received August 31, 2001

Abstract—An injector of hydrogen atoms for plasma diagnostics in modern tokamaks has been developed at the Budker Institute of Nuclear Physics (Novosibirsk). The ion source of the injector produces a proton (helium ion) beam with a current of up to 2 A (1 A), an ion energy of up to 55 keV, a beam divergence of ~0.6°, and a pulse duration of up to 10 s. An RF discharge-based plasma emitter, which is one of the main parts of the ion source, is described. The emitter diameter is 72 mm, the ion current density is 120 mA/cm^2, and the inhomogeneity of the current density is ±6%. The beam is formed by a four-electrode ion-optical system with 163 round apertures. At a current of 2 A, the ion beam consists of 67% protons, 18% H_2^+ ions, and 15% H_3^+ ions, the total content of heavier ions in the beam being no higher than 2–3%. *© 2002 MAIK "Nauka/Interperiodica".*

1. INTRODUCTION

The injection of hydrogen (deuterium) ion beams is widely applied to active particle diagnostics in large fusion devices. The required beam current density depends on both the diagnostic method used and the plasma parameters. In most cases, a current of several amperes with a particle energy of ~50 keV is sufficient [1–3]. To obtain ion beams with a current of up to 2.5 A and duration of up to 10 s, we developed a plasma emitter based on an RF discharge.

A design of the emitter is described in Section 2. The ion source is described in detail in [4–7]. Section 3 presents the results of studying plasma generation in the RF emitter and optimizing the emitter parameters to precisely form an ion beam, as well as the results of probe measurements of the plasma temperature and density. In Section 4, the data on the species composition of the ion beam extracted from the emitter are presented. Section 5 is devoted to a comparative analysis of the results obtained and the predictions of the numerical model of a plasma emitter.

2. RF PLASMA EMITTER

Figure 1 presents the design of the gas-discharge chamber in which the plasma emitter runs. A 4-mm-thick cylindrical chamber wall *1* is made of Al_2O_3 ceramics. The working gas (hydrogen or helium) is supplied through the hole in the water-cooled copper end flange via a flexible dielectric capillary with an inner diameter of 0.6–0.8 mm. This enables us to insulate the gas-puffing pulsed valve from the chamber, which is at a high (up to 55 kV) potential. A diaphragm with an opening 0.05 mm in diameter is set at the capillary end in order to maintain a sufficiently high pressure in the capillary during the discharge and, thus, to prevent the high-voltage breakdown, which occurs when the pressure is ≤0.5 atm. An MKS (Japan) controller is used as a pulsed valve, which allows us to maintain the gas flow rate at a level of up to 2.5 l torr/s with an accuracy of 0.5%. The measured gas flow setting time (with allowance for the delay related to the flowing through the capillary) is ~0.5–1 s.

The discharge is excited by an RF field at a frequency of 4.65 MHz using an external antenna *3*. The antenna is a PEV-1 wire coil wound by five wires in parallel on a Teflon frame. RF power is supplied to the antenna via an oil-immersed isolating transformer.

The discharge was ignited by applying an RF voltage to the antenna and a pulsed voltage to a trigger device. The trigger device was placed at the rear flange and consisted of two coaxial cylinders separated by a ceramic insulator. To ensure stable ignition of the RF discharge in a wide range of pressures and antenna voltages, a voltage of ~6 kV was applied to the cylinders, which resulted in a breakdown over the insulator surface.

At the rear flange of the gas-discharge chamber, a set of permanent magnets *4* was placed. The magnets scattered the return electrons arriving from the ion-optical system (IOS) thus reducing the thermal load on the rear flange. They also reduced the plasma flow toward the flange thus increasing the discharge energy efficiency. It was found that the magnets caused an asymmetry of the plasma flow profile in the plasma grid plane. Different magnet configurations were used to minimize this asymmetry. The results of these studies are discussed in Section 3.

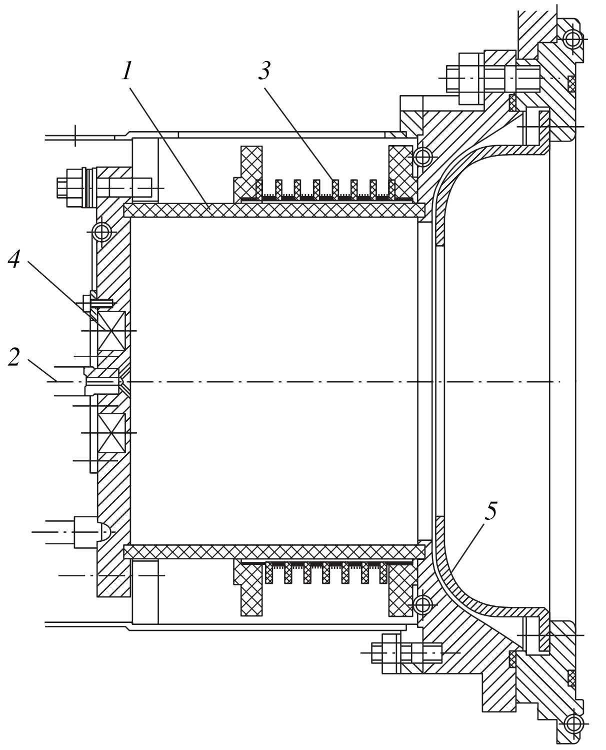

Fig. 1. Design of the plasma emitter: (*1*) ceramic discharge chamber, (*2*) gas supply, (*3*) antenna, (*4*) permanent magnets, and (*5*) plasma grid.

Figure 2 schematically illustrates how the RF power is fed to the antenna, whose inductance is $L_a = 4.8$ μH. A plasma load of the RF generator can be emulated by an R_p active resistance and L_p inductance recalculated for the antenna input. The measurements showed that the load was mainly resistive because, with an RF discharge, the resonance frequency of the anode circuit changed only slightly (by 0.1–0.2 MHz) as compared to the idle mode. Generally, $R_p \sim 900\ \Omega$. When operating with a nominal current density of 120 mA/cm^2, the RF voltage amplitude at the antenna was 2.4 kV and the power dissipated in the discharge was ~3 kW. The reactive current in the antenna was ~20 A.

RF power absorbed in the discharge was determined from the antenna voltage and plasma equivalent resistance by the expression $P = U^2/2R_P$, where U is the antenna voltage amplitude and R_P is the plasma equivalent resistance, which was determined in two steps when running the RF generator in the external excitation mode. The antenna circuit was tuned so that it was in resonance with the driving frequency and the emitter current was maximum. First, the RF voltage at the antenna with a plasma load and the RF voltage amplitude at the input of the final stage, which was tuned in resonance with the generator frequency, were measured. Then, without a plasma, an active resistance was connected in parallel to the antenna; the value of the resistance was chosen such that the antenna voltage was equal to that in the presence of a plasma. During these measurements, the RF voltage amplitude at the input of the final stage was maintained unchanged and the generator excitation frequency was set equal to the resonance frequency of the antenna circuit. The maximum RF voltage at the antenna indicated the tuning to the resonance. The resistance determined in this way was equal to the plasma equivalent resistance.

The RF generator feeding the antenna is a multistage resonance amplifier with an output power of up to 10 kW. Its design allows operation in both the external excitation and self-excitation modes. The latter mode proved to be more preferable because, when operating with a plasma, the tuning of the generator to the resonance occurred automatically and the antenna feed power was maximum.

The generator can also operate with a modulated RF output voltage. This is necessary for both the beam modulation and increasing or decreasing the emitter plasma density during the current pulse in order to recover the source operation after probable electric breakdown in the IOS. To eliminate a breakdown in the IOS during the growth of the high voltage, the emitter current density was set at a minimum level required for sustaining the RF discharge. After reaching the neces-

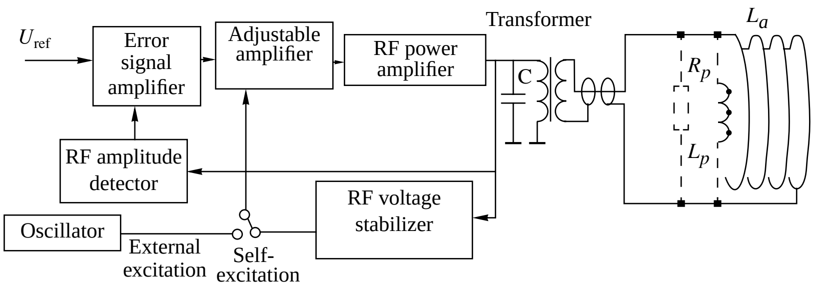

Fig. 2. Schematic of the RF generator.

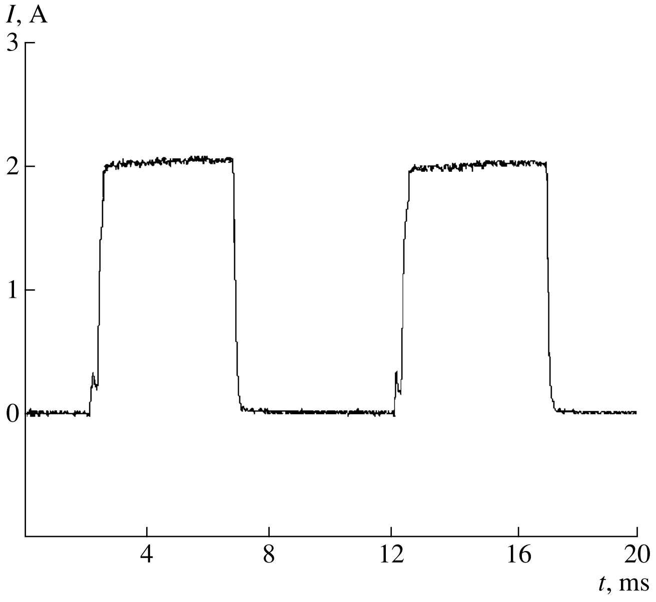

Fig. 3. Waveform of the ion current in the modulation regime.

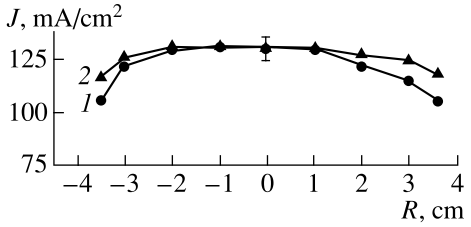

Fig. 4. Profiles of the emitter ion current density: (*1*) without and (*2*) with a magnetic wall composed of four magnets.

sary voltages at the IOS electrodes, the ion current density increased to the nominal value. The rise time of the RF antenna voltage was less than 100 μs, which ensured that the rise time of the beam generated by the plasma emitter was less than 200 μs. A characteristic waveform of the beam current is shown in Fig. 3. A step at the pulse leading edge corresponds to operating at the minimum power of the RF generator.

3. PLASMA EMITTER CHARACTERISTICS

The plasma emitter characteristics were optimized without generating a high-energy ion beam. To simulate gas conditions corresponding to those in the emitter of the acting ion source, a disc with openings for inserting probes was placed at the source end instead of the plasma grid. The total area of these openings was close to the area of the IOS plasma grid openings intended for the beam extraction.

The profile of the ion current density was measured by a multigrid probe moving in the plasma grid plane. The current density profile and the discharge efficiency substantially depend on the number, shape, and mutual orientation of the magnets placed at the gas-discharge chamber end, as well as on the distance between them. Several configurations were investigated: a ring magnet with a yoke of different shape and multipole configurations composed of separate rectangular parallelepiped magnets. The measured profiles were compared with the reference ones measured when the emitter operated without magnets at the rear wall.

A current density profile in the absence of magnets is shown in Fig. 4 (curve *1*); the power deposited in the discharge is 6.2 kW. It is seen that the averaged (over the emitter surface) current density is 120 mA/cm^2 (the total current is 4.8 A) and the nonuniformity of the current density within a circle 72 mm in diameter is ±10%. This nonuniformity decreases when a ring magnet with an iron cover plate (Fig. 5a) is placed at the rear flange of the gas-discharge chamber. In this case, the magnetic field at the magnet surface is 850 G and decreases to ~20 G at the plasma grid. The nonuniformity of the current density is about ±4% and, at the same total emitter current, the power deposited in the discharge is significantly lower (4.8 kW) than in the previous case.

A further increase in the discharge efficiency (by a factor of 1.5–2 as compared to the case without a magnetic field) was attained with multipole magnet configurations. Configurations with two $12 \times 9 \times 40$-mm magnets and four $12 \times 9 \times 20$-mm magnets are shown in Figs. 5b and 5c, respectively; in both cases, the magnets were made of $SmCo_5$ and the magnetic field at the magnet surface was ~3 kG.

The configuration with two magnets turned out to be more efficient (at a constant antenna voltage, the total emitter current was higher by ~10%). Correspondingly, at an antenna voltage of 2.4 kV, the ion beam current increased from 1.8 A (with four magnets) to 2 A (with two magnets).

Although the discharge efficiency with two magnets is somewhat higher than with four magnets, in the former case, there is an azimuthal asymmetry in the current density profile, namely, the profiles along the two mutually perpendicular directions, along and across the magnets (*x*-axis and *y*-axis in Fig. 5), are different. The profile along the *y*-axis corresponds to the plasma shift as a whole, which results in a substantially nonuniform distribution of the current density over the emitter surface (Fig. 6). Nevertheless, irrespective of this nonuniformity, the ion source stably operates at an ion current of 2 A (an ion energy of 50 keV). With four magnets, the nonuniformity in the emitter current density is significantly lower, about ±6% (Fig. 4, curve *2*).

Calculations of the permanent magnetic field show that, with four magnets, the profile of the magnetic field in the plasma grid plane is azimuthally symmetric; it has a dip at the center and increases toward the periphery of the plasma chamber, where the electrons are trapped. In this case, the drop in the ion current density between the center and the periphery is lower than in the absence of the magnetic field.

At an emitter current density of 100–120 mA/cm^2, the increase in the gas flow rate through the discharge chamber from 0.5 to 2.5 l torr/s only slightly affects the profile nonuniformity, which holds at a level of about ±6%. At a constant gas flow rate of 2 l torr/s, the change in the power in a rather wide range (from 1.5 to 10 kW) also slightly affects the profile nonuniformity.

The measured dependence of the total emitter current on the power deposited in the discharge is almost linear up to 10 kW (Fig. 7). The change in the deposited power from 1.5 to 10 kW slightly affects the plasma active equivalent resistance, which changes from 850 to 950 Ω.

According to these measurements, in the regime with an equivalent current of hydrogen atoms of 1 A (an ion current of ~2 A), the power deposited in the discharge is ~3 kW and the emitter efficiency, defined as the ratio of the total ion current to the deposited power, is ~0.7 A/kW. The gas efficiency (the ratio of the ion beam current to the molecule flux of a gas supplied to the discharge chamber) is ~9%.

The plasma density and the electron temperature in the gas-discharge chamber were measured simultaneously using a triple probe [8]. The probe had three similar 2-mm-high and 1-mm-wide loop electrodes made of a tungsten wire 0.1 mm in diameter and placed close to each other. Before every measurement, the probe working surface was cleaned up by heating the probe loops up to a temperature of ~1000°C for one minute with a current of 330 mA.

At the nominal parameters of the RF discharge corresponding to an emitter current density of 120 mA/cm^2, the electron temperature at the axis near the plasma grid was 5 eV. In the central part of the chamber, under the antenna (23 mm away from the plasma grid), the electron temperature was 6 eV, the ion saturation current was 300 mA/cm^2, and the plasma density was 1.3×10^{12} cm^{-3}.

Note that the central electron temperature measured under the same conditions from the current–voltage characteristic of a double probe is somewhat higher (~8 eV). This discrepancy seems to be related to the deviation of the electron energy distribution function from Maxwellian one. The probe measurements show a slight decrease (~1 eV) in the electron temperature near the plasma grid when moving along the radius from the center toward the edge; in contrast, under the antenna, the electron temperature slightly increases (by ~1 eV).

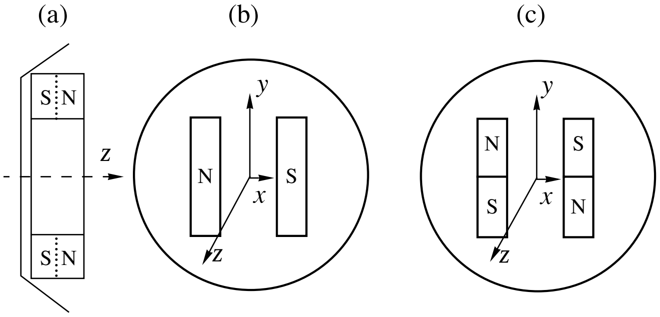

Fig. 5. Magnet configurations at the end wall of the plasma emitter: (a) ring magnet and multipole configurations composed of (b) two and (c) four magnets.

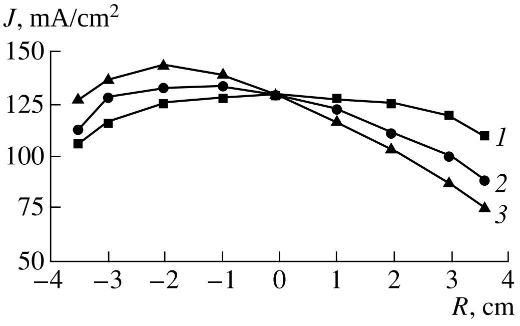

Fig. 6. Profiles of the emitter ion current density with two magnets at the end wall: (*1*) $J(x)$, (*2*) $J((x + y)/\sqrt{2})$, and (*3*) $J(y)$.

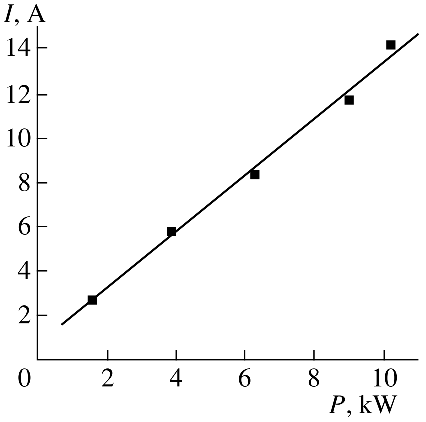

Fig. 7. Total emitter current vs. power deposited in the discharge.

The gas pressure in the discharge was measured using a baratron placed at the rear wall of the discharge chamber. At a hydrogen flow rate of 2 l torr/s, the gas pressure was 0.6 mtorr. These measurements allowed us to roughly estimate the degree of ionization, assuming that the gas and plasma temperatures are the same and uniform throughout the entire discharge. Assuming the temperature to be ~6 eV, we obtain that the neutral particle density is ~7×10^{13} cm^{-3}. Then, assuming that

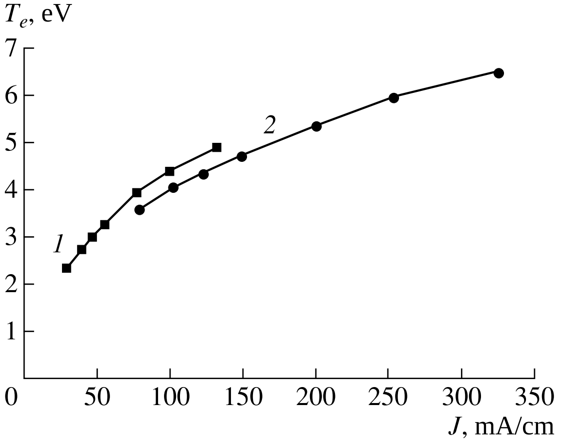

Fig. 8. Plasma electron temperature vs. ion current density at the chamber axis: (*1*) near the plasma grid and (*2*) 23 mm away from the plasma grid.

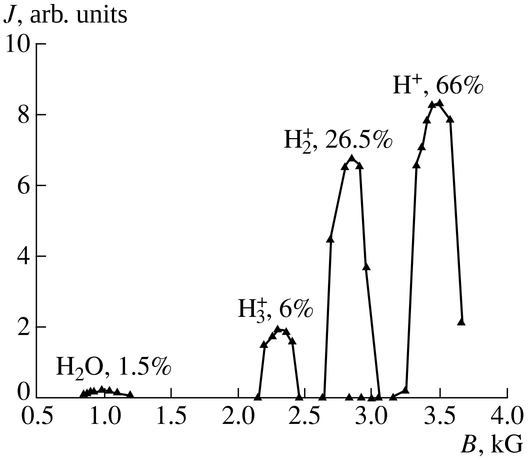

Fig. 9. Mass-analyzer collector current vs. magnetic field.

the ion density is $n_i \sim 10^{12}$ cm^{-3}, the degree of ionization in the discharge can be estimated as ~1.5%.

It was found that the plasma electron temperature increases with the RF power deposited in the discharge. As an illustration, Fig. 8 presents the dependences of the plasma temperature on the ion saturation current density at the chamber axis near and at a distance of 23 mm from the plasma grid (curves *1* and *2*, respectively). The measurements were carried out using the triple probe. As the ion current density changes from 40 to 120 mA/cm^2, the electron temperature in the plasma grid plane increases from 2.5 to 4.5 eV. Under these conditions, the increase in the gas flow rate through the discharge chamber from 0.5 to 2.5 l torr/s only slightly affects the electron temperature.

4. ION BEAM COMPOSITION

A magnetic mass-analyzer was used to measure the species composition of the ion beam extracted from the plasma emitter. The mass-analyzer was placed at the axis 5 m away from the ion source. A small part of the beam was cut out with a diaphragm installed at the entrance to the analyzer and then passed through an equilibrium helium target. In the gas target, H_2^+ and H_3^+ molecular ions dissociate into protons and hydrogen atoms with energies of 1/2 and 1/3 of the total beam particle energy E_b, respectively. After the gas target, the beam composed of protons and hydrogen atoms passed through the magnetic field of the mass-analyzer, in which the beam proton fraction was split into three main components with the energies E_b, $E_b/2$, and $E_b/3$. There is also a peak corresponding to an energy of ~$(1/18)E_b$, which is related to the slow hydrogen ions generated in the dissociation of hydrogen-containing impurity ions (OH^+, H_2O^+, and H_3O^+).

Figure 9 presents a characteristic dependence of the collector current on the mass-analyzer magnetic field. The dependence was measured in a series of discharges in which the magnetic field was changed from shot to shot. In these measurements, the beam particle energy was 50 keV, the beam current was 1.7 A, and the hydrogen flow rate through the source was 1 l torr/s. The percentage of the ion beam species was determined taking into account the number of particles in the molecule and the equilibrium yields of the particles for each energy value (for energies of 50, 25, and 16.7 keV, the proton yield was 50, 39, and 43%, respectively). Figure 9 corresponds to the following beam composition: 66% protons, 26.5% H_2^+ ions, 6% H_3^+ ions, and 1.5% water molecules.

The measurements show that the content of heavy impurities (the proton peak at an energy of ~$(1/18)E_b$) substantially depends on the plasma emitter operation mode. Thus, the running of the plasma emitter for a certain time until the beam is formed (the so-called “preplasma” mode) substantially reduces the percentage of oxygen-containing impurities. In particular, the water content decreases from ~3 to ~1.5% after preliminary conditioning the gas-discharge chamber wall in the discharge for 200 ms. The further increase in the conditioning time does not result in a noticeable lowering of the water content in the beam. Seemingly, in this case, the chemical sputtering of the ceramic wall [9], which leads to the generation of water molecules at the wall surface, comes into play.

It is interesting to note that the surface condition and the water concentration also affect the number of molecular hydrogen ions in the discharge. Thus, in the preplasma mode, the fraction of the proton component in the total energy decreases from 71 to 67% at a beam current of 2 A and gas flow rate of 2 l torr/s. Seemingly,

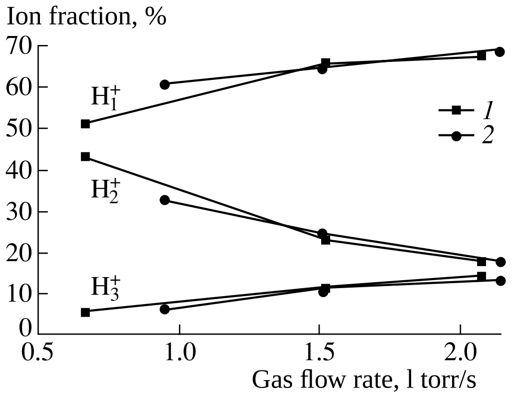

Fig. 10. Ion species composition vs. gas flow rate for an ion beam current of (*1*) 2 A and (*2*) 1.7 A.

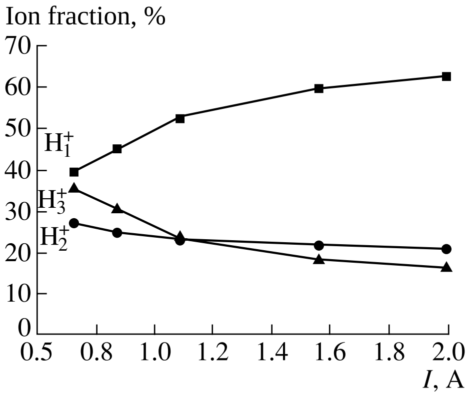

Fig. 11. Ion species composition of a hydrogen beam vs. beam current for a gas flow rate of 2 l torr/s.

this indicates an increase in the recombination rate at the wall with decreasing surface water content [10].

The experimental results on the beam composition presented below were obtained with a preliminary discharge with a duration of 200 ms. The beam composition was measured 10 ms after the beginning of the beam formation. Usually, the beam duration was 20 ms. An experiment with a series of longer pulses (200 ms) carried out to prove the results showed the same beam composition.

At ion beam currents of 1.7 and 2 A and a particle energy of 50 keV, the beam composition was measured as a function of the gas flow rate through the gas-discharge chamber (Fig. 10). The increase in the gas flow rate from 1 to 2 l torr/s increases the H^+ content from 50 to 67%. Simultaneously, the percentage of H_3^+ ions increases at the cost of a decrease in the H_2^+ content. This is related to the increase in the probability of the reaction $H_2^+ + H_2 \longrightarrow H_3^+ + H$, resulting in the loss of H_2^+ ions and the production of H_3^+ ions. Moreover, the increase in the gas pressure in the plasma chamber decreases the temperature in the discharge; as a result, the rate of this reaction significantly increases [11].

Figure 11 shows a typical dependence of the H^+ content on the beam current. It is seen that the proton percentage increases and the H_3^+ percentage significantly decreases with increasing current.

In experiments with the use of an Al_2O_3 ceramic chamber, the maximum proton content was ~71%. RF plasma sources with a quartz chamber are capable of producing beams with an H^+ ion content of 85–90% [12]. It is not quite clear why in the plasma emitter under study, at nearly the same ion current densities, the proton content is lower. Since the coefficient of surface recombination on Al_2O_3 ceramics is fairly low [13], recombination on the surfaces of the metal grids and the copper end flange seems to play an important role at the given geometry of the gas-discharge chamber.

5. MODELING OF AN RF PLASMA EMITTER

The following model of a plasma emitter was used to analyze the experimental data. When calculating the density $n_i(r, z)$ and ion flux $q_{iz}(r, z)$, we assume that the ions generated throughout the entire plasma volume in the RF source have the same velocity and fly away isotropically from the point of origin. We also assume that the ion mean free path is much longer than the chamber size and that the ions are completely absorbed by the wall. The generation of ions is described by the function $P(r, z)$, which specifies the number of ions arising in unit volume per unit time at the point (r, z) due to the electron-impact ionization of hydrogen.

In the straight-trajectory approach, the ion density $n_i(r, z)$ and ion flux $q_{iz}(r, z)$ are determined by integrating $P(r, z)$ over the entire chamber volume. To compare

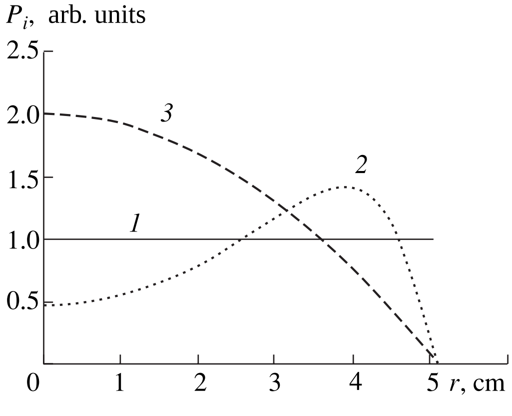

Fig. 12. Model ion source profiles (the wall is at $r = 5.1$ cm).

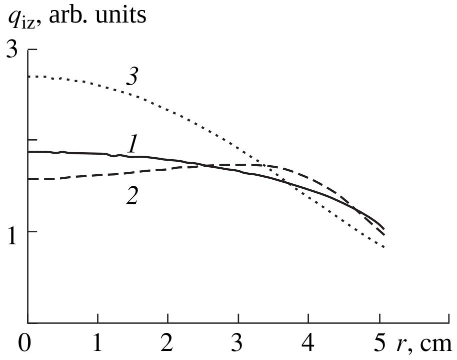

Fig. 13. Profiles of the ion current densities at the emitter. Numerals by the curves correspond to those in Fig. 12.

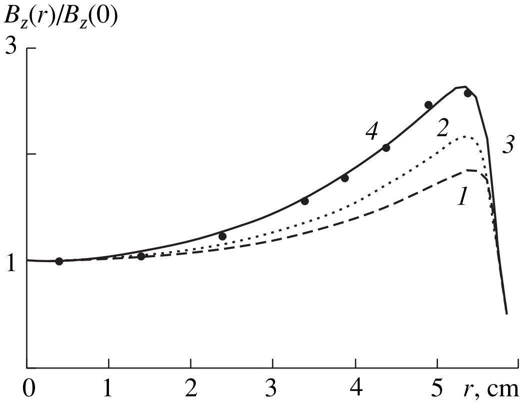

Fig. 14. Normalized magnetic field profiles $B_z(r)/B_z(0)$: (*1*) the antenna is in vacuum, (*2*) the antenna is in an infinitely long conducting tube, (*3*) the antenna in a tube with ends, and (*4*) the measured profile.

the numerical simulation results with the experimental profiles, we considered three model source distributions (see Fig. 12): (*1*) a radially uniform source, (*2*) a source with a maximum at the periphery, and (*3*) a source with a maximum at the axis. To make the comparison more convenient, the source distributions were normalized so that the total number of the generated ions was the same in all of the three versions.

The profiles of the ion current density at the chamber end, where the plasma emitter forms, are shown in Fig. 13. The numerals by the curves correspond to the ion source distributions shown in Fig. 12. Comparing the computed current density profiles with the measured ones, we can conclude that the ion source distribution is, most likely, radially uniform.

An approach similar to that described in [14] was used to calculate the RF field in the plasma volume. We used a model of an axisymmetric plasma placed in a dielectric chamber surrounded by a multiturn helical antenna. The discharge chamber and antenna were enclosed by a cylindrical metal case with several holes and slits. RF current and charge oscillations in the antenna generate alternating magnetic and electric fields in the source volume. This electric field accelerates the electrons, which ionize hydrogen in the chamber, thus sustaining a steady-state RF discharge. The excitation of the fields by the antenna is described by Maxwell's equations with a given external current and the corresponding boundary conditions for the field components at the conducting side wall and the ends of the metal case. The plasma conductivity was described by the permittivity tensor for a cold plasma with allowance for collisions between the electrons and neutrals. Calculations were performed for a real configuration taking into account the outer conducting metal case. According to calculations, the presence of a continuous conducting case with a radius of 8 cm around the antenna with a radius of 5.8 cm reduces the alternating magnetic field at the axis by a factor of ~2; hence, taking into account this reduction is of importance.

Figure 14 compares the normalized measured and calculated $B_z(r)$ profiles. It is seen that the experimental data are in good agreement with computed results for an antenna enclosed by a continuous metal case with ends.

6. CONCLUSION

We have developed and investigated a plasma emitter based on an RF discharge. The emitter enables the formation of a plasma surface with an ion current density of up to 350 mA/cm^2 and inhomogeneity no higher than ±6% within a circle 72 mm in diameter. The ion current density is determined as a function of the discharge parameters, namely, the RF power, the gas flow rate, and the magnitude and configuration of the magnetic field at the end wall. For a beam current of 2 A, the measured proton content in a hydrogen ion beam extracted from the emitter is ~70%.

The emitter design is rather simple and highly reliable. One of the emitter models has worked for two years in the regime with an extracted beam current of 1.8 A and pulse duration of 2 s. Altogether, about 20000 pulses were produced without a substantial degradation of the emitter characteristics. In the future, based on the above scheme, we plan to develop a series of emitters with various diameters.

REFERENCES

1. L. I. Krupnik and V. I. Tereshin, Fiz. Plazmy **20**, 157 (1994) [Plasma Phys. Rep. **20**, 146 (1994)].
2. E. Hintz and B. Schweer, Plasma Phys. Controlled Fusion **37**, A87 (1995).
3. G. V. Roslyakov, in *Proceedings of the International School of Plasma Physics, Varenna, 1982*, p. 311.

4. I. V. Shikhovtsev, G. F. Abdrashitov, V. S. Belkin, *et al.*, in *Proceedings of the XX Symposium on Fusion Technology, Marseilles, 1998*, Vol. 1, p. 605.
5. I. V. Shikhovtsev, G. F. Abdrashitov, V. I. Davydenko, *et al.*, in *Proceedings of the XXIV International Conference on Phenomena in Ionized Gases, Warsaw, 1999*, Vol. III, p. 99.
6. A. A. Ivanov, V. I. Davydenko, P. P. Deichuli, *et al.*, Rev. Sci. Instrum. **71**, 3728 (2000).
7. I. V. Shikhovtsev, I. I. Averbukh, V. I. Davydenko, *et al.*, in *Proceedings of the XXV International Conference on Phenomena in Ionized Gases, Nagoya, 2001*, Vol. I, p. 329.
8. I. M. Zalkind, O. S. Pavlichenko, and V. P. Tarasenko, Vopr. At. Nauki Tekh., Ser. Fiz. Plazmy, Probl. Upravl. Termoyad. Sinteza, No. 2, 69 (1975).
9. D. M. Gruen, B. Siskind, and R. B. Wright, J. Chem. Phys. **65**, 363 (1976).
10. D. Spence, F. McMichael, K. R. Lykke, *et al.*, Rev. Sci. Instrum. **67**, 1642 (1996).
11. C. F. Giese and W. B. Maier, J. Chem. Phys. **39**, 739 (1963).
12. R. Keller, P. Spaudtke, and F. Nouhmayer, in *Proceedings of the International Ion Engineering Congress, Kyoto, 1983* (Inst. of Electrical Engineers of Japan, Tokyo, 1983), p. 39.
13. M. D. Gabovich, *Physics and Technology of Plasma Ion Sources* (Atomizdat, Moscow, 1972), p. 30.
14. I. V. Kamenski and G. G. Borg, Comput. Phys. Commun. **113**, 1 (1998).

Translated by N. Ustinovskiĭ

Plasma Physics Reports, Vol. 28, No. 3, 2002, pp. 204–228. Translated from Fizika Plazmy, Vol. 28, No. 3, 2002, pp. 229–256.
Original Russian Text Copyright © 2002 by Batanov, Kossyi, Silakov.

LOW-TEMPERATURE PLASMA

Gas-Discharge Method for Improving the Environmental Characteristics of the Atmosphere (In memory of G.A. Askar'yan)

G. M. Batanov, I. A. Kossyi, and V. P. Silakov

Institute of General Physics, Russian Academy of Sciences, ul. Vavilova 38, Moscow, 119991 Russia

Received October 8, 2001

Abstract—The possibility of improving the environmental characteristics of the atmosphere with the help of freely localized microwave discharges is analyzed. Theoretical and experimental studies devoted to cleaning the troposphere of ozone-destroying pollutants and creating an artificial ozone layer in the stratosphere are reviewed. Results from the studies of the possibility of the plasmochemical utilization of the accumulated chlorofluorocarbons, capable of depleting the ozone layer, are presented. The results of theoretical and experimental modeling are used to predict the plasmochemical consequences of creating artificial ionized regions in the atmosphere for the purpose of long-range radio and TV communication. *© 2002 MAIK "Nauka/Interperiodica".*

1. INTRODUCTION

In recent years, considerable attention has been given to the problem of the excitation of gas discharges in the atmosphere at different altitudes. These studies are motivated, first of all, by a search for the ways of improving the environmental situation. On the other hand, interest in the excitation of atmospheric gas discharges stems from the fact that the fast-developing modern technology, capable, in principle, of solving the problem of arranging artificial gas-discharge objects in the atmosphere, has initiated a number of studies related to applications that are far from the ecological ones.

The ecological direction of research is aimed at restoration (or protection) of the Earth's ozone layer.

The technological direction is largely related to the problem of creating radio-reflecting plasma mirrors for the purpose of long-range radio and TV communication. To this direction, we can also ascribe the long-range powering of space vehicles, the transmission of information to space vehicles entering the atmosphere, the initial acceleration of rockets without using propellents, etc.

The specific features of microwave power engineering, namely, the capability of wireless power transfer over long distances within the Earth's atmosphere without appreciable absorption on the propagation path, explain the fact that most gas-discharge applications in airspace are related just to microwave discharges.

This review presents an analysis of recent investigations carried out in Russia and devoted to the problem of microwave gas discharges in the atmosphere. Most attention is concentrated on the environmental safety and advisability of various applications, as well as on the possibility of using microwave discharges to improve ecological characteristics of the atmosphere.

First, we consider the studies of the possibility of applying gas discharges for solving the problems of restoration and protection of the Earth's ozone layer.

2. GAS DISCHARGE AS A METHOD FOR RESTORATION (PROTECTION) OF THE EARTH'S OZONE LAYER

2.1. Introduction to the Problem

The depletion of the ozone layer, protecting all living things on Earth from biologically active UV radiation, is one of the most serious environmental problems of concern to mankind. The fact that the O_3 content in the stratosphere is being reduced progressively is beyond question and is confirmed by many measurements (see, e.g., [1]). However, the discussion concerning the main mechanisms and reasons for ozone depletion (see [2–4]) still continues. The situation is such that, until very recent times, there was no commonly accepted view about the reasons for the ozone "trend." However, we can distinguish the most popular hypothesis that chlorofluorocarbons (CFCs) produced industrially and released into the atmosphere in great amounts play a decisive role in ozone destruction.

CFCs (CF_2Cl_2, $CFCl_3$, and others), which are very inert chemically, pass almost freely through the troposphere and reach stratospheric altitudes ($H > 15$–20 km), corresponding to the location of the ozone layer. At these altitudes, CFC molecules are decomposed under the action of solar UV radiation, liberating atomic chlorine and chlorine-containing radicals, destroying the ozone in catalytic reactions of the following type [5]:

$$Cl + O_3 \longrightarrow ClO + O_2, \quad ClO + O \longrightarrow Cl + O_2. \quad (1)$$

CFCs can also substantially affect the Earth's heat balance by enhancing the greenhouse effect. The action of one CF_2Cl_2 or $CFCl_3$ molecule is identical to the action of 10^4 CO_2 molecules, so that, in the immediate future, the role of CFCs in the progressing greenhouse effect can become comparable to the role of carbon dioxide.

When discussing the ways of overcoming the ozone crisis, it is usually proposed to stop the production and application of CFCs throughout the world. However, even in this very problematic case, the amount of CFCs that have already been exhausted into the atmosphere is sufficiently large for "poisoning" the stratosphere during subsequent decades (according to published data, the total CFC content in the atmosphere is currently about 1 megaton).

Therefore, proposals of actively influencing the state of the atmosphere and improving its environmental quality have acquired great importance. All the proposals can be divided into two categories:

(i) the creation of an artificial ozone source in the stratosphere in order to compensate the ozone loss and

(ii) the search for ways of cleaning the troposphere of ozone-destroying pollutants.

Among the variety of projects, we mention the proposal by Stix [6], based on the successive selective resonant excitation of CFC molecules in the Earth's atmosphere with the help of a tunable CO_2 laser. Such action should ultimately result in the excitation of upper vibrational molecular states followed by their decomposition.

Undoubtedly, the idea proposed by Wong *et al.* [7–9] is also of interest. They proposed to use microwaves to efficiently transform the stratospheric atomic chlorine into a negative Cl^- ion, which does not participate in the catalytic decomposition of the ozone by reactions analogous to reaction (1).

In recent years, a number of proposals of using gas discharges to solve the problem of the cleaning and recovery of the stratospheric ozone layer have been put forward. These proposals, made by Russian physicists, have stimulated a series of experimental and theoretical studies that are reviewed in this paper.

2.2. Gas-Discharge Source of Stratospheric Ozone

The creation of an artificial source compensating the loss of O_3 molecules in the stratosphere is one of the most popular proposals aimed to solve the problem of recovering the stratospheric ozone "shield." At different times, for this purpose, it was proposed to install ozonizers on board airplanes, to mount a mirror system on satellites, to use lasers to increase the efficiency of a photochemical ozone source, to send up containers with oxygen, etc. [10].

The gas-discharge method of ozone generation proposed and discussed in a number of papers (see [11, 12]) occupies a particular place among these proposals. A detailed review dedicated to this problem was recently published in [13]. The method for creating a stratospheric O_3 source is shown schematically in Fig. 1b. Ground antennas (*1*) form high-power convergent microwave beams (*2*) intersecting at stratospheric altitudes and exciting a microwave discharge (*3*) where the beams meet. Plasmochemical processes in a gas discharge are accompanied by the dissociation of oxygen molecules to form ozone molecules compensating for the extra loss of O_3 resulting from human activity.

The design presented in Fig. 1b is not original: this is an attempt to solve a new (environmental) problem by applying the method for creating artificial plasma objects that serve as RF-reflecting mirrors for the purpose of long-range radio and TV communication (see [14] for details). An analysis performed in a monograph by Borisov *et al.* [14] unambiguously points to the feasibility of the project at the current level of microwave engineering. Moreover, the papers devoted to the generation of freely suspended plasma RF-reflecting mirrors in the atmosphere are well grounded theoretically. The concept of creating an artificial ionized region in the atmosphere is also supported by a number of laboratory experiments modeling real atmospheric conditions [15].

The problems of high-frequency discharge in air, such as gas breakdown, the maintenance of ionization, the structure of an ionized layer in crossed microwave beams, the reflection of radio waves from an artificially ionized region, and the distortion of a reflected signal, have been studied in sufficient detail both theoretically and experimentally [14–17]. However, little attention has been given to the plasmochemical aspects of the problem, namely, the chemical kinetics during the discharge and in the decaying plasma and the composition of air affected by a gas discharge. These issues are brought to the forefront in discussions on the possibility of using microwave discharges in the stratosphere as an ozone source. A series of experimental and theoretical studies of the plasmochemical consequences of microwave discharges in air will be discussed in the next section.

Here, we only note that some experts in the field of physics of the atmosphere cast doubt on the advisability of overcoming the ozone crisis by introducing an artificial ozone source in the stratosphere to compensate for the ozone loss.

Thus, e.g., Karol' *et al.* [18] used a radiative–photochemical model to estimate the intensity and the optimal altitude of an ozone source for a given increase in the total ozone content under conditions of the arctic and antarctic ozone "holes." The authors have arrived at

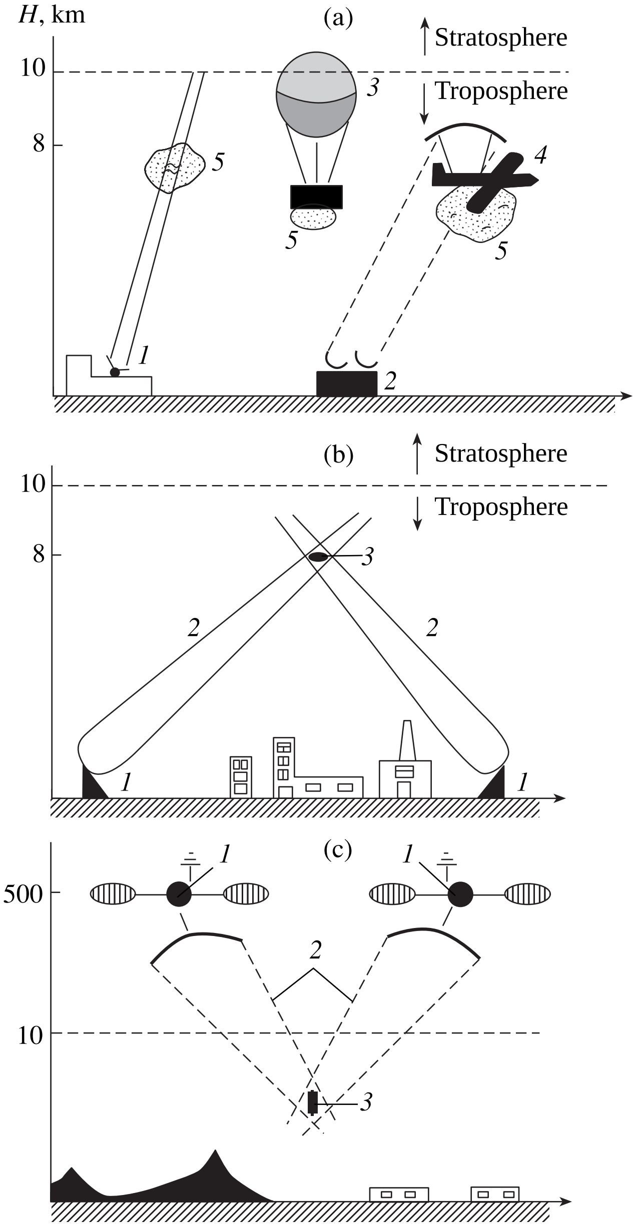

Fig. 1. Sketches of various schemes of the cleaning and restoration of the Earth's ozone layer by means of a gas discharge. (a) Various methods for the excitation of a gas discharge in the troposphere: (*1*) high-power laser, (*2*) microwave antennas, (*3*) balloon, (*4*) airplane with a receiving microwave antenna, and (*5*) gas discharge; (b) the excitation of a gas discharge in crossed microwave beams generated by ground-based sources: (*1*) ground-based microwave antennas, (*2*) microwave beams, and (*3*) microwave discharge; and (c) the excitation of a gas discharge in crossed microwave beams generated by space-based sources: (*1*) satellites with microwave oscillators and antennas, (*2*) microwave beams, and (*3*) microwave discharge.

the conclusion that, to restore the arctic ozonosphere, it is necessary to eject (or produce) 400 t of ozone per hour at altitudes of about 18 km. To solve the same problem for the antarctic hole, it is necessary to eject about 4000 t of ozone per hour at nearly the same altitudes. The continuous production of such a great amount of ozone seems to the authors of [18] unachievable for the current level of technology.

Aleksandrov and Upenek [19] also arrived at the conclusion of the inefficiency of the generation method. As an example, they considered a method proposed by Starik *et al.* [10, 20], who suggested that the missing ozone be produced as follows. Fifty heavy satellites are placed in orbit, each carrying 20 lasers operating at a wavelength of 1.27 or 0.762 μm and power of 1 MW.

In irradiated air, oxygen molecules pass from the ground state to the $^1\Delta_g$ metastable (singlet) state at λ = 1.27 μm or the $^1\Sigma_g^+$ state at λ = 0.762 μm. Oxygen molecules in the ground state can be dissociated under the action of solar radiation at wavelengths equal to or shorter than 242.5 nm. Oxygen molecules in the singlet state can be dissociated under the action of solar radiation at wavelengths shorter than 300 nm. This means that the relatively low laser energy spent on the excitation of molecular oxygen results, at first glance, in a more efficient use of solar energy for ozone production.

From an analysis of the kinetics of the processes in the stratosphere, the authors of [19] draw an unfavorable conclusion that the energy gain in the method based on the laser excitation of oxygen molecules is illusory. In fact, interaction with molecular oxygen and the ozone (not considered by Starik *et al.* [10]) results in a very short lifetime of singlet oxygen and, consequently, a negligibly small (according to calculations of [18]) efficiency of the method proposed.

Finally, we should mention the papers by Batanov *et al.* [21, 22], who, in a way somewhat different from [18, 19], came to the conclusion that there is little hope to solve the ozone problem by generating stratospheric O_3. Both the microwave gas-discharge and optical (laser) methods for generating large-scale artificial ozone layers in the stratosphere were analyzed. A kinetic model elaborated in [23] and incorporating photochemical reactions was used to calculate the plasmochemical consequences of discharges excited in the stratosphere. The results of numerical computation and simple estimates led to the conclusion that the implementation of the optical and gas-discharge methods require that the constant power consumption of ozone sources should be as high as the total power generated throughout the world, or even exceeding this level. Thus, e.g., to eliminate the antarctic ozone hole, a power of ~10^4 GW is required in the gas-discharge method for ozone generation and $P \sim 10^8$ GW in the case of the optical production of O_3.

For this reason, the possibility of using the gas-discharge and optical methods for ozone generation to overcome the ozone crisis seem problematic from both technological and economic standpoints.

Although, in [18, 19, 21, 22], the advisability of creating an artificial ozone layer is assessed to be low, the activity aimed at the experimental and theoretical modeling of the gas-discharge production of ozone in air is, in our opinion, of particular interest for the plasma chemistry of microwave discharges in the Earth's atmosphere. The results of the modeling will be discussed in Section 3.2 of this paper. A proposal by Gurevich *et al.* [13] of using gas discharges in the stratosphere for the active probing of the ozone layer (with the purpose of studying its state and the photochemical processes occurring in it) by introducing a controllable substantial ozone admixture and for creating a local artificial ozone layer undoubtedly deserves attention.

2.3. Microwave Discharge as a Means of Cleaning the Troposphere of Ozone-Destroying Pollutants

The method of atmosphere cleaning proposed and analyzed by Askar'yan *et al.* [24–29] is based on the gas-discharge destruction of ozone-destroying CFCs at relatively low altitudes ($H < 10$–15 km) corresponding to the Earth's troposphere (i.e., CFCs are destroyed before they reach the ozone layer). A gas discharge excited in one way or another in a chosen spatial region of the troposphere efficiently decomposes CFCs, and the produced radicals and stable chemical products are washed away by raindrops and fall onto the ground. Displacing the discharge region, it is possible to treat large volumes of the atmosphere and, thus, provide its global cleaning.

This method differs from the method proposed by Wong *et al.* [7–9] in that the discharge should be excited in the troposphere, rather than the stratosphere. The difference from the laser (alternative to discharge) method proposed by Stix [6] lies, particularly, in that the gas discharge can be excited throughout the entire troposphere, rather than in canyons lying between mountains or at relatively low altitudes.

Let us consider in more detail the physical and plasmochemical mechanisms underlying the gas-discharge method.

Chemically stable CFC molecules in a gas-discharge plasma can be destroyed by electrons whose energy exceeds the bond energy of the atoms in the molecule (i.e., is higher than 3 eV). Electron-impact dissociation proceeds by the scheme

$$CF_2Cl_2 + e \longrightarrow CF_2Cl + Cl + e, \qquad (2)$$

$$CFCl_3 + e \longrightarrow CFCl_2 + Cl + e, \qquad (3)$$

and so on. Since literature data on the rate constants k_d for processes (2) and (3) are lacking, we can only estimate their value from above. For this purpose, we can use the data in [29] on the electron-impact dissociation cross sections for fluorocarbons C_2F_6, CF_4, C_3F_8, etc. Estimates show that, for $\xi \equiv E_{\mathrm{eff}}/n_m \simeq 10^{-15}$ V cm^2, the values of k_{d2} and k_{d3} should not exceed 5×10^{-9} cm^3 s^{-1} (here, E_{eff} is the effective electric field; n_m is the neutral density in air; and k_{d2} and k_{d3} are the constants for processes (2) and (3), respectively).

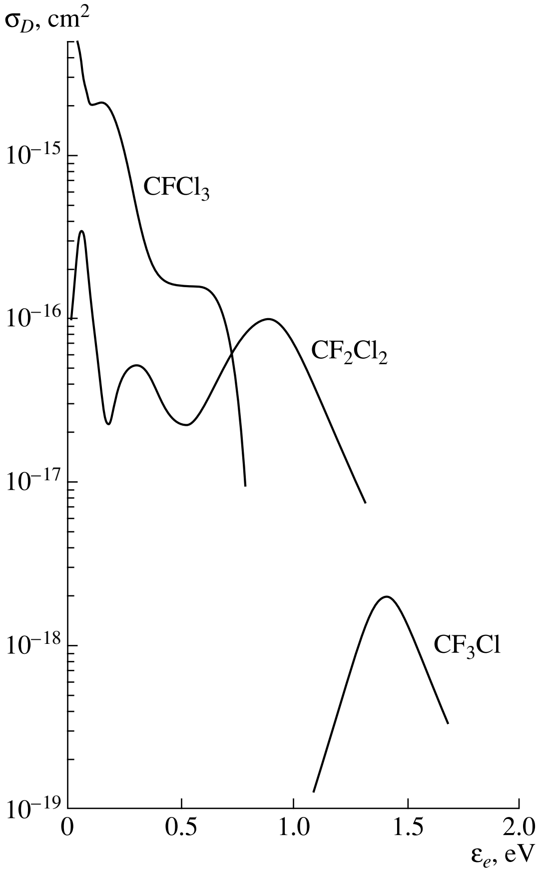

Fig. 2. Cross section of electron attachment to CFCs vs. electron energy.

Dissociation due to the bombardment by fast electrons is the most obvious (but not the most efficient) process of CFC destruction. An analysis performed in [25–29] showed that dissociation attachment can become the dominant process of the gas-discharge decomposition of CFCs, which proceeds by the following scheme:

$$CF_2Cl_2 + e \longrightarrow CF_2Cl + Cl^-, \qquad (4)$$

$$CFCl_3 + e \longrightarrow CFCl_2 + Cl^-, \qquad (5)$$

and so on.

Note that the behavior of CFCs in reactions (4) and (5) is nontrivial. According to [30–32], CFC-11 ($CFCl_3$) and CFC-12 (CF_2Cl_2), which are the most stable against chemical reactions, turn out to be the most "fragile" with respect to the interaction with slow electrons. Figure 2 taken from [31] demonstrates how the total cross section $\sigma_D(\varepsilon_e)$ of electron attachment to CFCs depends on the electron energy. Taking into account that electron attachment is dominantly dissociative in character and assuming the electron energy distribution to be Maxwellian, we obtain

$$\text{(i) } k_4 \equiv k_D^{(\text{CFC-12})} = \langle \sigma_D^{(\text{CFC-12})} v_e \rangle \simeq 2.05 \times 10^{-9}\ \text{cm}^3\ \text{s}^{-1},$$

$$k_5 \equiv k_D^{(\text{CFC-11})} = \langle \sigma_D^{(\text{CFC-11})} v_e \rangle \simeq 8.86 \times 10^{-8}\ \text{cm}^3\ \text{s}^{-1}$$

for $T_e \simeq 0.02707$ eV (240 K) and

$$\text{(ii) } k_4 \equiv k_D^{(\text{CFC-12})} \simeq 1.85 \times 10^{-9}\ \text{cm}^3\ \text{s}^{-1},$$

$$k_5 \equiv k_D^{(\text{CFC-11})} \simeq 2.87 \times 10^{-8}\ \text{cm}^3\ \text{s}^{-1}$$

for $T_e = 0.25$ eV.

Such high values of the reaction constants at a very low electron energy are explained by the fact that the electron affinity of a chlorine atom exceeds the dissociation energy of CFC molecules. For all other molecules constituting atmospheric air, an opposite inequality takes place, which leads to the existence of a threshold energy for the dissociative-attachment cross section [33]. This fact ensures the selective character of CFC dissociation in a cold decaying gas-discharge plasma.

Along with the above-mentioned direct CFC decomposition by plasma electrons, indirect processes can also play a significant role (see [28]). For example, CFCs can be destroyed in collisions with nitrogen and oxygen electronically-excited metastable atoms and molecules.

These decomposition processes can be very efficient. For example, the probability for CFC-11 and CFC-12 to be destroyed in collisions with metastable oxygen atoms in the $O(^1D)$ state is fairly high. The rate constant for this process is close to the gas-kinetic value, $(1\text{–}2) \times 10^{-10}$ cm^3 s^{-1}. However, the high rates of quenching the excited O* atoms in collisions with nitrogen and oxygen molecules makes them noncompetitive against cold plasma electrons (estimates show that this is valid even for the most stable $O(^1S)$ atomic state). In view of the aforesaid, it is also of interest to analyze the role of the electronically excited oxygen molecules $O_2(a^1\Delta_g, v \geq 1)$ and $O_2(b^1\Sigma_g^+)$. The energy balance shows that CFCs can be destroyed in reactions similar to

$$CF_2Cl_2 + O_2(a^1\Delta_g, v \geq 1) \longrightarrow CF_2Cl + ClO_2. \quad (6)$$

Unfortunately, the construction of a developed kinetic model describing the conversion of CFCs in a gas discharge is impeded by the lack of literature data on the elementary processes contributing to CFC decomposition.

The charge exchange processes between negative O_2^- ions and CFC molecules, e.g.,

$$\begin{aligned} CFCl_3 + O_2^- &\longrightarrow Cl^- + CFCl_2 + O_2 \\ &\longrightarrow CFCl_3^- + O_2 \\ &\longrightarrow Cl^- + CFClO + ClO \end{aligned} \quad (7)$$

with the constant $k_7 \simeq 7.6 \times 10^{-10}$ cm^3 s^{-1}, can also be ascribed to CFC destruction channels [34].

Finally, UV radiation efficiently generated by microwave discharges or laser sparks can contribute significantly to CFC destruction. The CFC content in the air surrounding the discharge can decrease due to direct photodissociation,

$$\begin{aligned} CF_2Cl_2 + h\nu &\longrightarrow CF_2Cl + Cl \\ &\longrightarrow CF_2 + 2Cl, \end{aligned} \quad (8)$$

or, indirectly, through the photoionization of the air components with the subsequent dissociative attachment of electrons to CFC molecules:

$$\begin{aligned} O_2 + h\nu &\longrightarrow O_2^+ + e, \\ CF_2Cl_2 + e &\longrightarrow CF_2Cl + Cl^-. \end{aligned} \quad (9)$$

The other possible processes are the photoionization of CFC molecules accompanied by the dissociative attachment of electrons to neutral molecules or the dissociative recombination of CFC ions,

$$CF_2Cl_2 + h\nu \longrightarrow CF_2Cl_2^+ + e, \quad (10)$$

and, then,

$$CF_2Cl_2 + e \longrightarrow CF_2Cl + Cl^-$$

or

$$\begin{aligned} &CF_2Cl_2^+ + Cl^- + M \\ &\longrightarrow \text{dissociative-recombination products.} \end{aligned} \quad (11)$$

It should be noted that even a few of the listed channels can be sufficient to ensure the efficient (with a low energy expenditure) air cleaning by a gas discharge. As was mentioned above, in this case, the dissociative attachment of electrons to CFC molecules is of primary importance. Taking into account the high probability of the destruction of CFC molecules in the dissociative attachment reactions (4) and (5) with the participation of cold electrons, the role of the electric field exciting a discharge reduces merely to the production of an air plasma with a sufficiently high electron density. Most of the CFC molecules are destroyed in the plasma-decay phase between the discharge pulses. It is evident that the longer the medium is in the ionized state after the driving electric field is switched off, the higher the efficiency of air cleaning.

One of the basic requirements is that the electron density in the ionizing pulse should reach the value n_{em} satisfying the inequality

$$n_{em} \gg n_{\text{CFC0}}, \quad (12)$$

where n_{CFC0} is the initial density of CFC molecules. In addition, we assume that the plasma decays via recombination.

With these assumptions, it is easy to estimate the relative number of CFC molecules dissociating via electron attachment over the time t after switching off the driving field,

$$\eta_{\rm CFC} \simeq 1 - (1 + \alpha_r n_{em} t)^{-\gamma}, \qquad (13)$$

where $\eta_{\rm CFC} \equiv \Delta n_{\rm CFC}/n_{\rm CFC0}$; $\Delta n_{\rm CFC} = n_{\rm CFC0} - n_{\rm CFC}(t)$, $\gamma = k_D^{\rm CFC}/\alpha_r$, and α_r is the recombination coefficient of electrons and positive ions in the plasma.

For $n_{em} = 10^{12}$ cm^{-3}, $T_e = T_g = 240$ K (i.e., we consider the plasma-decay phase in which the driving electric field is absent), and $\alpha_r \simeq 2 \times 10^{-6}$ cm^3 s^{-1}, we obtain that more than 20% of the initial CFC-11 content will be dissociated over 100 μs. The cleaning effect of one pulse can be substantially enhanced if the electron component of the decaying plasma is heated by a low electric field, because the dissociative attachment coefficient decreases with increasing T_e ($k_D^{\rm (CFC\text{-}11)} \simeq 8.86 \times 10^{-8}$ cm^3 s^{-1} for $T_e = 0.027$ eV and $k_D^{\rm (CFC\text{-}11)} \simeq 2.87 \times 10^{-8}$ cm^3 s^{-1} for $T_e \simeq 0.25$ eV). It should be noted that these estimates are very rough and are based on the assumption that the plasma decays via recombination and the dissociative attachment of electrons to CFC molecules is the only destruction mechanism. However, even the first experiments with freely localized microwave discharges showed that the plasma lifetime in the decay phase is abnormally long and the decay cannot be described exclusively by recombination (see Section 3.2). In addition to dissociative attachment, a substantial contribution to CFC destruction can also come from the dissociative charge exchange of negative molecular oxygen ions with CFC molecules, the interaction of CFC molecules with electronically excited atoms, etc. (see Section 3.1). In aggregate, all these effects can lead to a situation in which a single microwave pulse producing a plasma cloud with a density of $n_{em} \simeq 10^{13}$ cm^{-3} will be sufficient for the CFC content in the atmosphere treated by discharges to be substantially reduced.

The energy cost of cleaning the atmosphere with gas discharges can be estimated from the evident relationship

$$q \simeq 0.5\sigma_\omega E_0^2 \tau_E, \qquad (14)$$

where σ_ω is the high-frequency conductivity of the gas-discharge plasma and E_0 is the amplitude of the electric field providing gas breakdown and maintaining the plasma for the time required for CFC decomposition.

Assuming that electron-impact dissociation plays a decisive role, we obtain

$$\tau_E = \tau_d \approx 1/k_d n_{em}. \qquad (15)$$

When dissociative attachment is the main channel for CFC destruction, we have

$$\tau_E \simeq \tau_i, \qquad (16)$$

where τ_i is the characteristic time for air ionization. It is easy to see that, under the conditions of a real atmospheric experiment, we have

$$\tau_d \gg \tau_i, \qquad (17)$$

which results in a relatively low energy cost of CFC destruction.

Assuming that electrons are attached to oxygen molecules predominantly via three-body collisions, it is easy to estimate the altitude starting from which recombination prevails over attachment:

$$H \ge H_m \simeq 7.46\ln(10p_0/\sqrt{\alpha_r n_{em}}), \qquad (18)$$

where p_0 is the normal pressure (in torr). It follows from expression (18) that, for $\alpha_r \simeq 2 \times 10^{-7}$ cm^3 s^{-1} and $n_{em} \simeq 10^{13}$ cm^{-3}, this altitude is

$$H_m \simeq 12 \text{ km}.$$

Consequently, the assumption about the recombination decay of a plasma in the atmosphere is valid only for the upper troposphere near its boundary with the stratosphere. As to the altitudes below H_m, additional experimental and theoretical studies are required in order to answer the question of whether the “nonattachment” mechanism can be responsible for the plasma decay.

Figure 1 shows various schemes of the excitation of a freely localized discharge in the atmosphere. A gas discharge can be excited by a high-power CO_2 laser (Fig. 1a). In this case, the volume occupied by a discharge is relatively small. However, the efficiency of the method can be fairly high, because cleaning will occur not only in the “hot” discharge region, but also in the surrounding air via its ionization by UV radiation from the spark (in the so-called “aureole”). The abnormally long lifetime of this aureole was first revealed in [35, 36].

In principle, it is also possible to employ various electrode discharges in dc, pulsed, or RF fields produced by discharge facilities mounted on special platforms connected to a balloon or an aircraft (Fig. 1a). In the latter case, the aircraft engine can be powered with microwave beams to ensure the environmental safety of the flight.

Note, however, that the method based on freely localized discharges excited by high-power microwave beams is the most promising among all of the gas-discharge methods for air cleaning. Both ground-based (Fig. 1b) and space-based (Fig. 1c) microwave sources can be used. In the first case, two (or more) ground antennas create intense crossed microwave beams focused at a given altitude H. The microwave intensity where the beams meet should exceed the threshold intensity I_{th} for the breakdown in air. An irradiation regime is possible in which a fixed spatial volume is treated and the wind carries away the treated air from the discharge region, which is then replenished with fresh air.

In the other version, the beam-intersection region is displaced in space so that new regions of the atmosphere are involved in treatment.

The microwave sources can also be mounted on satellites (Fig. 1c) [37]. One of the advantages of this scheme is that, in this case, both the problem of the gas-discharge cleaning of the atmosphere and the problem of utilizing “gratuitous” solar radiation can be solved simultaneously [38]. Furthermore, this scheme is convenient because the irradiation from the top can be combined with atmosphere probing and the search for regions with an elevated CFC content (or a reduced ozone content).

Evidently, the air breakdown intensity does not depend on whether the atmosphere is irradiated from the top or from the bottom. The threshold electric field can be determined from the following simple expression [14]:

$$E_{th} \simeq 32(n_m/2.67\times10^{19})[2(1+\omega^2/\nu_{\text{eff}}^2)]^{1/2}\ \text{kV/cm}. \quad (19)$$

Here, E_{th} is the threshold amplitude of the microwave electric field above which atmospheric air breakdown occurs; ω is the circular frequency of microwave radiation; n_m is the molecule density (in cm^{-3}); and ν_{eff} is the effective frequency of electron–neutral collisions (in s^{-1}) [14],

$$\nu_{\text{eff}} \simeq 1.7\times10^{-7}n_m. \quad (20)$$

Table 1 presents the calculated threshold electric field strengths and, accordingly, the threshold intensities of microwave radiation at different altitudes. The values of E_{th} and I_{th} correspond to continuous-wave radiation. In the case of pulsed radiation (or fast scanning by a beam), the threshold field can be found from the condition

$$\tau_f \geq \tau_i \ln(n_{em}/n_{e0}), \quad (21)$$

where τ_f is the microwave pulse duration and τ_i is the characteristic ionization time defined by the formula [14]

$$\tau_i \simeq 2.0\times10^{11}/n_m(E_0/E_{th})^{5.3}. \quad (22)$$

The breakdown electric field required for the excitation of discharges by microwave pulses and determined by condition (21) can be several times higher than the breakdown field in the case of continuous-wave radiation.

Assuming that the diameter of the ground-based antenna is d_a and the beam is Gaussian and axisymmetric, we can easily estimate the diameter of the focal spot from the formula

$$d_f \simeq 2\lambda_f H/\pi d_a \quad (23)$$

and the length of the focal region l_f from the formula

$$l_f \simeq \pi d_f 2/\lambda_f. \quad (24)$$

If the emitting antenna is mounted on a satellite flying at the altitude H_S (such that $H_S \gg H$), we can again use expressions (23) and (24) to determine d_f and l_f after substituting H_S for H.

Assuming $\lambda_f = 0.8$ cm, we obtain from expressions (23) and (24) that, for $H = 10$ km, the radius of the focal spot of a Gaussian beam is on the order of 100 cm and the length of the focal region is $l_f \simeq 400$ m (for the diameter of a ground-based antenna $d_a \simeq 50$ m). In this case, from Table 1 and the formula $P_f = I_f\pi d_f^2/4$ (where I_f is the intensity of the microwave beam at the focus), we obtain that the total microwave power required for breakdown in air at an altitude of $H = 10$ km should be higher than 2.4 GW. This power can be easily produced by modern microwave oscillators, such as gyrotrons [39], MI-389 coaxial inverse magnetrons operating in the centimeter wavelength range [40], and relativistic microwave oscillators [41].

Let us estimate the energy cost (the specific energy deposition) of air cleaning by microwave gas discharges. We assume that the electromagnetic energy delivered into the beam intersection region is totally absorbed there. We also assume that the plasma decays via recombination. As was shown above, the gas-discharge method provides the total decomposition of CFC-11 by irradiating air with a single microwave pulse. In this case, the specific energy deposition can be estimated from formula (14) in view of expression (16). Thus, using expression (22), we obtain

$$q \simeq 4.75\times10^{-16}n_e(E_0/E_{th})^{-3.3}\ \text{J/cm}^3. \quad (25)$$

For $H \simeq 10$ km, $E_0/E_{th} = 2$, and $n_e = 10^{12}\ \text{cm}^{-3}$, we have

$$q \simeq 4.8\times10^{-5}\ \text{J/cm}^3.$$

At such a low q value, the gas temperature can increase by no more than 0.1 K during one pulse. The energy

Table 1

H, km	$n_m\times10^{19}$, cm^{-3}	$\lambda_f = 0.2$ cm		$\lambda_f = 0.8$ cm		$\lambda_f = 2$ cm		$\lambda_f = 5$ cm	
		E_{th}, kV/cm	I_{th}, W/cm^2	E_{th}	I_{th}	E_{th}	I_{th}	E_{th}	I_{th}
5	1.52	27.2	10^6	25.87	0.89×10^6	25.78	0.88×10^6	25.77	0.88×10^5
10	0.86	17.34	4×10^5	14.76	2.89×10^5	14.61	2.83×10^5	14.58	2.82×10^5
15	0.4	11.59	1.8×10^5	7.17	6.83×10^4	6.84	6.21×10^4	6.79	6.11×10^4

cost of the decomposition of one CFC molecule is

$$\Delta\varepsilon \simeq q/n_{\mathrm{CFC0}}. \tag{26}$$

In the case at hand, we have $\Delta\varepsilon^{(\mathrm{CFC\text{-}11})} \simeq 230$ keV/molecule ($n_{\mathrm{CFC0}} \simeq 1.3 \times 10^9$ cm^{-3}).

Let us assume that the total mean microwave power irradiating air is $P = 55$ GW. Then, the capacity of the cleaning system (specifically, the mass of CFC-11 decomposed in a unit of time) is determined by the formula

$$dM/dt \simeq m_{(\mathrm{CFC\text{-}11})} n_{\mathrm{CFC0}} P/q \tag{27}$$

(where $m_{(\mathrm{CFC\text{-}11})}$ is the mass of a CFC-11 molecule) and amounts to

$$dM/dt \simeq 10.7 \times 10^3 \text{ t/year}.$$

With such a high capacity, it is possible to completely clean the air above territories of continental scale (e.g., above Europe) during one year.

The above analysis allows us to draw the following important inferences:

(i) the process of the global cleaning of the troposphere of ozone-destroying CFC molecules seems to be realizable;

(ii) even if the problem cannot completely be solved with the modern level of technology, it is undoubtedly possible to carry out a large-scale field experiment.

When discussing the advisability of field experiments, it should be taken into account that, along with purely physical problems that can be solved using model laboratory devices and mathematical modeling, there are also a number of problems related to aerology, ecology, and economy. Any attempt to solve these problems makes it necessary to move from laboratory experiments to experiments under real atmospheric conditions (this also refers to the concept of compensating for the ozone loss by creating an artificial gas-discharge ozone source in the stratosphere). In this context, the most important problems can be formulated as follows:

(i) The construction of a map of the CFC distribution in the atmosphere and the search for stagnation regions and channels of CFC migration from one region to another (e.g., from Antarctica to Australia). Such maps can provide a more realistic estimate of the requirements for the global cleaning of the atmosphere by the gas-discharge method.

(ii) Assessment of the environmental permissibility of the employment of high-power microwave sources, especially in space (taking into consideration the biological action of microwaves).

(iii) The study of the mechanisms for removing the CFC decomposition products from the atmosphere under real conditions.

Among the most important problems, we can also mention the problem of the environmental safety of the products of plasmochemical reactions in a microwave discharge. For example, it should be kept in mind that, when destroying CFCs, a microwave discharge can simultaneously pollute the atmosphere with nitrogen oxides NO_x. Reaching the stratosphere, nitrogen oxides can destroy the ozone layer (as chlorine does, but less efficiently).

A search for the possibility to employ gas discharges in the Earth's atmosphere with the purpose of improving its environmental quality seems to be interesting and worthwhile, first of all, as the first attempt to extend the field of applications of gas-discharge systems (from laboratory and industrial applications to global ecology). We note that, in recent years, significant progress in studying these problems has been achieved—from rough qualitative estimates of the feasibility of the method proposed (similar to those presented in this section) to the mathematical and laboratory modeling of the processes accompanying the discharge excitation in the atmosphere and their influence on the state of atmospheric air. The results of this modeling, which are presented in the next section, are of practical importance and are of significant interest from the standpoint of the fundamental gas-discharge physics and plasmochemistry.

3. MATHEMATICAL AND LABORATORY MODELING OF MICROWAVE DISCHARGES IN THE ATMOSPHERE

3.1. Theoretical Study of the Problem of the Plasmochemical Consequences of Freely Localized Discharges in the Atmosphere

The Earth's atmosphere is an extremely complicated object. The construction of an adequate theory of the Earth's atmosphere has been the subject of long-term activity of mathematicians and physicists. In order to more or less adequately model atmospheric air, it is necessary to simultaneously solve both the three-dimensional gas-dynamic problem and the problem of modeling chemical and photochemical reactions, transport processes, radiative transfer, diffusion, etc. Undoubtedly, progress achieved in physics of the atmosphere is significant; however, a theory capable of adequately describing the real atmosphere is still far from being completed.

The idea of using gas discharges to affect the environmental situation stimulated theoretical studies and initiated a new direction in physics of the atmosphere—the study of the plasmochemical consequences of the excitation and maintenance of freely localized discharges in the atmosphere. Earlier, such problems were rarely posed in the theory, although, in the context of the present-day understanding of the problem, they were of evident interest in the context of creating artificial RF-reflecting plasma layers in the stratosphere [14]. The discussion of this project began in the 1970s and still continues to attract much attention.

The foundation of the plasmochemical model of a freely localized microwave discharge in the atmosphere was laid by Kossyi *et al.* [23]. The model includes blocks describing both the charge and chemical kinetics of the discharge. The authors proposed one of the most detailed kinetic schemes of a nonequilibrium discharge in a nitrogen–oxygen mixture. The scheme includes more than 450 reactions and allows one to describe the major part of the available experimental data on the chemical and ion composition of a cold ($T_g \le 500$ K) gas with unexcited vibrational states both during the discharge and in the postdischarge phase and to predict the ion and chemical composition of atmospheric air affected by freely localized discharges.

In previous schemes, the processes occurring in the electric discharges in air mixtures were modeled based on reactions involving nitrogen and oxygen atoms produced via the electron-impact dissociation of molecules. In some cases (see [42]), reactions similar to the reaction $N_2 + e \longrightarrow 2N + e$ were considered with allowance for the production of electronically excited atoms $N(^2D)$ efficiently oxidized by oxygen molecules and the influence of the oxygen molecules in the $a^1\Delta_g$ state on the formation of the ozone component during the plasma decay phase was taken into account. The contribution from electronically excited nitrogen molecules to the modification of the chemical composition of the atmosphere received little attention in the literature before the publication [23]. At the same time, there was evidence that, in a nonequilibrium pulsed discharge in an airlike $[N_2] : [O_2] = 4 : 1$ mixture under conditions close to breakdown, reactions with the participation of electronically excited molecules can strongly affect physical and chemical processes (see [43]).

The kinetic scheme elaborated in [23] includes the blocks of reactions describing the excitation of electronic degrees of freedom, the electron-impact destruction and ionization of neutrals, associative ionization, the recombination of electrons and positive ions, the attachment and detachment of electrons, the chemical conversions of the neutral components of the mixture, ion conversion, and the recombination of positive and negative ions. In this context, it is worth noting the completeness of the block describing the processes with the participation of electronically excited particles. The block includes 60 reactions involving electronically excited nitrogen molecules ($N_2(A)$, $N_2(B)$, and $N_2(a')$), oxygen molecules ($O_2(a)$, $O_2(b)$, and $O_2(A, c, C)$), nitrogen atoms ($N(^2D)$ and $N(^2P)$), and oxygen atoms ($O(^1D)$, $O(^1S)$, and $O(^3P)$).

The detailed consideration of electronically excited states, as well as taking into account associative ionization processes, turned out to be very important for constructing a realistic model describing physical and chemical phenomena in the atmosphere under the action of high-power microwaves. The calculation of the electron energy distribution function (EEDF) in a given microwave electric field makes it possible to use the kinetic scheme of [23] to analyze the environmental consequences of discharges that are proposed to be excited in the atmosphere for solving applied problems (including the problem of cleaning the troposphere of CFCs). Below, we consider the results of these calculations. Here, we only note that the scheme presented in [23] was further supplemented with an electrodynamic block describing the change in the parameters of the electromagnetic wave interacting with a produced plasma and a block describing the vibrational states of nitrogen and oxygen molecules.

An attempt to pass from simple estimates similar to those presented in Section 2 to more exact calculations based on the kinetic scheme elaborated in [23] was made by Matveev and Silakov [44].

The CFC content in the atmosphere was assumed to be very low, so that the EEDF could be taken to be equal to that in a discharge excited in a nitrogen–oxygen mixture $[N_2] : [O_2] = 4 : 1$. The EEDF was calculated by numerically solving the Boltzmann equation in the two-term approximation with allowance for the elastic scattering of electrons by neutrals and the excitation of rotational, vibrational, and electronic degrees of freedom of these neutrals. The rate constants for inelastic electron collisions with gas particles (including CFCs) were determined by integrating the calculated EEDF with the corresponding scattering cross sections.

The model of plasmochemical processes occurring in a discharge was based on the kinetic scheme of a nonequilibrium discharge in a nitrogen–oxygen mixture [23]. This scheme was formulated so as to clarify the role of the CFC destruction processes involving electronically excited oxygen atoms and molecules, negative molecular ions, and other active plasma particles. Such studies are of primary importance for solving the problem of cleaning the atmosphere of CFC pollutants, because they can reveal new destruction mechanisms of chlorine- and fluorine-containing molecules, supplementing the dissociative attachment mechanism for the destruction of CFC molecules by electrons [see reactions (4) and (5)].

In calculations, the parameters of the problem were taken as follows: the total neutral density was $n_m = 8.61 \times 10^{18}$ cm^{-3}, the air temperature was $T_g = 233$ K (these n_m and T_g values correspond to an altitude of $H = 10$ km), the wavelength of the microwave radiation exciting a discharge was $\lambda_f = 0.8$ cm, the density of CFC-11 molecules was $n_{\text{CFC0}} = 1.3 \times 10^9$ cm^{-3}, and the initial electron density was $n_{e0} = 1$ cm^{-3}. The variable parameters were the rms value of the electric field strength $\langle E \rangle$ and the microwave pulse duration τ_f. In the first series of calculations, the $\langle E \rangle$ value was varied and it was assumed (according to [14], p. 124) that microwaves do not penetrate into the plasma after the electron density reaches the value $n_e \simeq 0.1\,n_c$, where n_c is the cutoff density for the given microwave wavelength. In the next series of calculations, the $\langle E \rangle$ value was fixed and equal to the known breakdown strength of the electric field and the pulse duration τ_f was varied so that the maximum electron density was always below $0.1\,n_c$.

Calculations showed that, at low values of the specific energy deposition ($\varepsilon \le 10^{-5}$ J/(cm^3 atm)), which are of primary interest for global atmosphere cleaning, the dominant process of CFC destruction at relatively low altitudes ($H \le 10$ km) may be the dissociative charge exchange of negative molecular oxygen ions with CFC molecules [reaction (7)]. Based on the results of these calculations, the authors of [44] proposed the optimal operating conditions for irradiating a chosen region of the atmosphere with a finite number of ultrashort microwave pulses with a total energy deposition of ~10^{-5} J/(cm^3 atm). Figure 3 shows the calculated curves demonstrating the time behavior of different components of a plasma produced by a microwave discharge in air with a CFC-11 admixture (during the active and afterglow phases of the discharge).

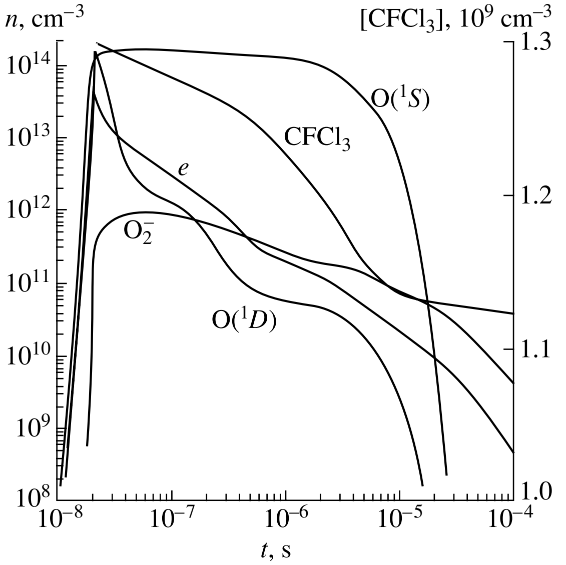

Fig. 3. Computed time evolution of the components of a microwave-discharge plasma and CFC-containing air (during the microwave pulse and in the decaying plasma) for $\lambda_f = 0.8$ cm, $\langle E\rangle/n = 2 \times 10^{-15}$ V cm^2, $\tau_f = 19.5$ ns, $H = 10$ km, and $n_{\mathrm{CFC0}} = 1.3 \times 10^9$ cm^{-3}.

At relatively high values of the specific energy deposition ($\varepsilon \ge 10^{-3}$ J/(cm^3 atm)), dissociative charge exchange is of minor importance. In this case, the contribution from the interaction between CFC molecules and electronically excited oxygen atoms becomes comparable with that from dissociative electron attachment.

Therefore, even the first studies based on the branched kinetic scheme [23] revealed that the gas-discharge method holds much promise for cleaning the troposphere of chlorine- and fluorine-containing molecules harmful to the ozone layer.

In the paper by Kolesnichenko *et al.* [45], published before [44], the efficiency of the destruction of a small CFC admixture with microwave discharges excited at relatively low altitudes ($H \le 10$ km) was considered. The kinetic scheme used in [45] was not as comprehensive as that presented in [44]. In particular, it did not include the processes of dissociative charge exchange, which, according to [44], can substantially affect the efficiency of the gas-discharge method of atmosphere cleaning.

In [45], collisions between CFC molecules and nitrogen molecules excited to high vibrational levels were assumed to be the main mechanism for CFC destruction. However, the authors of [45] did not take into account the important fact that the efficiency of utilizing the vibrational energy in such collisions is very low (see [46]), which substantially decreases the role of the vibrational excitation of nitrogen in the gas-discharge destruction of the ozone present in air.

The scheme used in [44] also cannot be considered perfect. In particular, the role played by UV radiation and the vibrational excitation of CFC molecules themselves in the gas-discharge destruction of CFCs is still unclear. However, although papers [44, 45] are far from being comprehensive, they are undoubtedly of interest for the problem of atmosphere cleaning by means of gas discharges. First of all, it should be noted that, in those papers, a kinetic scheme of a thermally nonequilibrium discharge in a nitrogen–oxygen mixture was used for the first time to analyze the problem of the decomposition of CFCs destroying the atmospheric ozone. A limited set of reactions leading to the decomposition of CFC molecules was incorporated in the model. Nevertheless, the authors of [44, 45] formulated and constructed a basis for a mathematical model that can be easily extended when new data on the rate constants for various processes leading to CFC destruction will be obtained.

Even with such imperfect models, the optimal operating conditions for irradiating air in a given volume (such as a finite number of microwave pulses, each contributing a very low energy, and the use of profiled microwave pulses) can be outlined.

It should also be noted that the initial assumption on the “normal” (theoretically predicted) character of the plasma decay after the discharge, which was adopted in [45], seems to be too hard. At high values of the specific energy deposition, this assumption does not agree with the experimental results that will be discussed in the next section.

When analyzing theoretical studies conducted in recent years and devoted to the problem of destroying the CFC pollutants in the atmosphere by microwave discharges, the paper by Aleksandrov *et al.* [47] deserves special attention. The authors of [47] numerically simulated the kinetics of charged and excited particles and chemical compounds in the afterglow phase of a repetitive microwave discharge in humid air with a CF$_4$ (CFC-14) admixture.

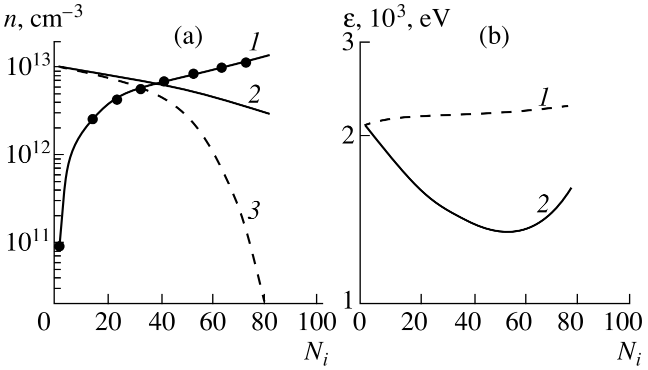

Fig. 4. (a) The computed densities of (*1*) H atoms and CFC molecules (*2*) without and (*3*) with allowance for the catalytic cycle and (b) the computed energy cost of the decomposition of CFC molecules (*1*) without and (*2*) with allowance for the catalytic cycle as functions of the number of pulses N_i for $p = 10$ torr, $n_{\mathrm{CFC0}} = 10^{13}$ cm^{-3}, $n_{e0} = 10^{11}$ cm^{-3}, $\tau = 0.5 \times 10^{-3}$ s, and $E/N = 1.5 \times 10^{-15}$ V cm^2.

The main channel of CCl_4 destruction is assumed to be the process of dissociative attachment,

$$CCl_4 + e \longrightarrow CCl_3 + Cl^-, \tag{28}$$

in the afterglow phase of a microwave discharge. The model incorporates a mechanism substantially enhancing the effect of cleaning air from a CFC-14 admixture, namely, a catalytic cycle closed by the process of the associative destruction of Cl^- ions in collisions with H atoms:

$$\begin{array}{c} CCl_4 + e \longrightarrow Cl^- + CCl_3, \\ Cl^- + H \longrightarrow e + HCl \\ \hline CCl_4 + H \longrightarrow CCl_3 + HCl \end{array}. \tag{29}$$

Atoms, radicals, and excited and charged particles are produced primarily in the active phase of a repetitive microwave discharge with the effective reduced electric field on the order of (1.5–2.0) × 10^{-15} V cm^2.

The parameters of the problem were the reduced electric field, the pressure p, the gas temperature T_g, the initial volumetric fraction of H_2O vapor in the mixture, the initial density of CFC molecules n_{CFC0}, the electron density produced in one pulse n_{em}, and the time between pulses τ.

The rate constants for the interaction between electrons and gas particles in the active discharge phase were determined with the help of a nonequilibrium EEDF, which, in turn, was calculated by numerically solving the Boltzmann equation.

Figure 4 shows the characteristic curves calculated with and without allowance for the catalytic cycle.

Calculations show that there is a range of variables in which the catalytic cycle appreciably intensifies the destruction of CFC molecules in the microwave discharge afterglow. This effect becomes even more pronounced as the initial CFC density and the parameter E_{eff}/n_m increase. The effect becomes weaker with increasing gas pressure. The catalytic effect can halve the energy cost of CFC destruction.

A catalytic cycle of type (29) can take place when H atoms are replaced with CFC molecule radicals. In this case, the catalytic effect can take place in a dried gas mixture. Unfortunately, elementary processes with the participation of radicals are poorly studied, which does not allow one to analyze the catalytic efficiency, as was done in [47] for atomic hydrogen.

Modern theoretical methods allow us to analyze the ecological aspects of atmospheric applications of gas discharges. Among the latter, we should mention, first of all, the most frequently discussed projects of the generation of artificial RF-reflecting layers in the stratosphere for the purpose of long-range radio and TV communication and the creation of stratospheric ozone sources compensating for the continuous ozone loss.

The problem of the environmental safety of stratospheric microwave discharges was first touched on by Askar'yan *et al.* [48–51] in connection with the project of creating artificial plasma mirrors. An analysis showed that the most significant perturbation of the natural state of the stratosphere by microwave discharges may be related to "poisoning" it with nitrogen oxides efficiently produced in the mirror regions. Oxide molecules destroy ozone in the catalytic reactions

$$NO + O_3 \longrightarrow NO_2 + O_2, \;\; NO_2 + O \longrightarrow NO + O_2, \tag{30}$$

$$NO_2 + O_3 \longrightarrow NO_3 + O_2, \;\; NO_3 + O \longrightarrow NO_2 + O_2. \tag{31}$$

It is believed that 75% of the stratospheric ozone loss is determined by the natural content of nitrogen oxide.

To answer the question of the consequences of an increasing amount of such oxides and an excess of their density over the natural level, the authors of [51] carried out calculations over long periods after the end of the discharge, when the plasma has already relaxed. For this reason, the equations describing the kinetics of the ionized component are excluded from the set of equations [23]. At the same time, photochemical processes occurring under the action of solar radiation (the production and destruction of ozone and dioxide molecules, the photodissociation of oxygen, etc.) are taken into account. At a given value of the initial excess NO content $\Delta n_{\mathrm{NO}}^{(0)}$, a set of 22 equations describing the characteristic chemical and photochemical reactions was solved to determine the kinetics of the composition of a perturbed stratospheric layer (first of all, the kinetics of the ozone component). The characteristic time dependences obtained for different $\Delta n_{\mathrm{NO}}^{(0)}$ values are shown in Fig. 5. It can be seen in the figure that, even when $\Delta n_{\mathrm{NO}}^{(0)}$ is on the order of the natural level, the O_3

density appreciably (by tens of percent) decreases in five to six days. For $\Delta n_{NO}^{(0)} = 10^{11}$ cm^{-3}, ozone is destroyed almost completely.

For the limiting cases of the production of small and great quantities of nitrogen oxide, the authors of [52] proposed to use simple evaluating formulas that agree with the computation results. Thus, when the oxide content changes only slightly, one can use the formula

$$\Delta n_{O_3} \approx -\eta \Delta n_{NO} \simeq -10^3 \Delta n_{NO}. \qquad (32)$$

When the nitrogen oxide content increases substantially, we have

$$\Delta n_{O_3} \approx A/(n_{NO})^{\alpha}, \qquad (33)$$

where A is a constant, $\alpha \simeq 1/2$, and η is the catalytic factor equal to the number of ozone molecules destroyed by one nitrogen oxide molecule.

From preliminary calculations and model experiments [29, 51–55], it follows that the energy cost of the production of one oxide molecule in a microwave discharge in the stratosphere is

$$w_{NO} \simeq 100 \text{ eV/molecule}.$$

For a given energy cost, it is easy to determine the production rate of nitrogen oxides in a microwave discharge:

$$N_{NO} \approx P/w_{NO} \text{ molecule/h}, \qquad (34)$$

where P is the average power deposited in the discharge. For $P = 1$ MW and $w = 100$ eV, we obtain $N_{NO} \approx 4 \times 10^{26}$ molecule/h $\simeq$ 20 kg/h.

The density of oxide molecules produced in the discharge is determined by the obvious expression

$$n_{NO} \simeq P/(w_{NO} d_f U_0 \Delta h), \qquad (35)$$

where Δh is the altitude to which the reaction products are spread, U_0 is the wind velocity at the altitude at which the artificial mirror is created, and d_f is the diameter of the focal spot.

Estimation by formula (35) gives a value from 10^{14} to 3×10^{15} oxide molecules per centimeter squared of the mirror area; after spreading to a height of 10 km (the characteristic thickness of the ozone layer), the density of oxide molecules will be from 10^8 to 3×10^9 cm^{-3}. In this case, the produced oxide density is higher than the natural density by a factor of 3. According to formula (33), this can result in a decrease in the ozone density by a factor of about 1.7 in the region of a plume carried by the wind away from the discharge. At the same time, according to the present notion, a depletion of the ozone layer by only tens of percent can be considered a disastrous effect for all living things under the "hole."

Based on simple estimates and computation results, the authors of [48–50] expressed reservations for the environmental safety of the projects of generating artificial RF-reflecting plasma layers in the stratosphere. These reservations was questioned later in [42, 56]. The main argument of the authors of [42, 56] was the results of solving a set of equations describing chemical kinetics in air after the discharge.

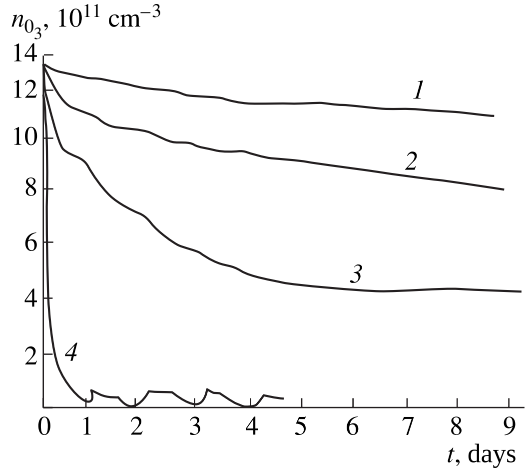

Fig. 5. Time evolution of the ozone density in the stratosphere for different values of the initial NO excess density: $\Delta n_{NO}^{(0)}$ = (*1*) 3×10^9, (*2*) 5×10^9, (*3*) 10^{10}, and (*4*) 10^{11} cm^{-3}.

As a continuation of the discussion on the environmental consequences of stratospheric discharges, Kossyi *et al.* [54] analyzed various projects of creating artificial plasma layers by means of microwave beams. The analysis was based on a kinetic scheme of a nonequilibrium discharge in a nitrogen–oxygen mixture [23]. The scheme included the charge and chemical kinetics of a plasma and, what is very important, the kinetics of electronically excited states of nitrogen molecules. The following projects of creating stratospheric plasma mirrors were tested for environmental safety:

(i) A hypothetical experiment proposed in [42], in which a single microwave pulse produces an artificial plasma object at an altitude of $H = 35$ km; the parameter $\xi \equiv E_{\text{eff}}/n_m$ is about 10^{-15} V cm^2, and the microwave pulse duration is $\tau_f = 10$ μs.

(ii) The maintenance of an artificial plasma region by a method proposed by Borisov *et al.* [14]. A plasma mirror is formed at an altitude of $H = 60$ km, the amplitude of the electric field is $E = 25$ V/cm, the wavelength is $\lambda_f = 1$ m, the pulse duration is $\tau_f = 10$ ns, and the repetition rate is $F = 100$ Hz.

(iii) A field experiment planned in Arecibo. According to [56], the experimental conditions are as follows. An artificial ionized cloud is produced at an altitude of $H = 40$ km by a single microwave pulse with a wavelength of $\lambda_f = 10$ cm, a power of 8×10^8 W ($\xi \simeq 2.2 \times 10^{-15}$ V cm^2), and a duration of $\tau_f = 10$ ns. A ground antenna forms a microwave beam with a focal-spot radius on the order of 10 m.

Figure 6 shows the results of calculations performed under the conditions of the first experiment. According

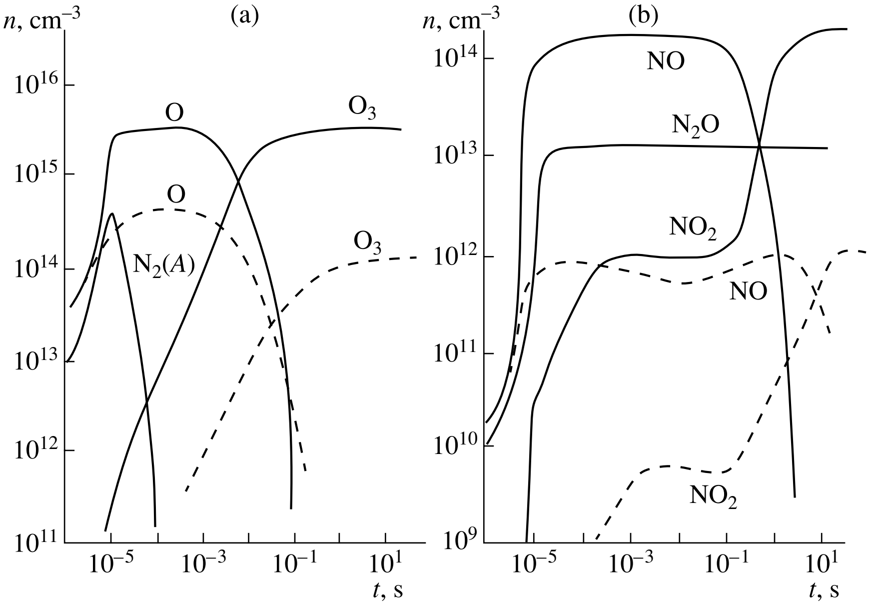

Fig. 6. Computed time evolution of the densities of chemically active particles and the products of chemical reactions in a pulsed microwave discharge in the hypothetical experiment of [41]. The solid lines correspond to calculation by the full scheme, and the dashed lines correspond to calculation by the scheme used in [42]. The $N_2(A)$ symbol designates the $N_2(A^3\Sigma_u)$ molecule.

to the figure, metastable electronically excited molecules (including those in the $N_2(A^3\Sigma_u^+)$ state), atomic oxygen, and NO and N_2O nitrogen oxides are produced during the microwave pulse. The O, NO, and N_2O contents become saturated by the end of the microwave pulse. One millisecond later, the atomic oxygen density begins to rapidly fall, first of all, because of the production of ozone, whose content becomes saturated over a time on the order of 10^{-2} s. The subsequent reoxidation of nitrogen oxide into nitrogen dioxide begins with an even longer time delay (10^{-1} s). In the quasi-steady state, reached after the end of the discharge, the prevalent oxide components are NO_2 and N_2O.

Figure 6 also shows the results of calculations by the model of [23]. It turns out that, when solving a nearly complete set of equations [23], the values of the excess density of nitrogen oxides are almost two orders of magnitude higher than those predicted by the model of [42]. In the opinion of the authors of [54], such a large difference stems from the fact that the model of [42] does not incorporate the kinetics of the electronically excited states of N_2 molecules and ignores the increase in the electron density in the course of a microwave discharge. The presence of $N_2(A^3\Sigma_u^+)$ molecules and other electronically excited molecules manifests itself in the formation of oxides in the reactions

$$N_2(A) + O \longrightarrow NO + N(^2D) \qquad (36)$$

and

$$N_2(A) + O_2 \longrightarrow N_2O + O, \qquad (37)$$

as well as in a substantial increase in the rate of the dissociation reaction of oxygen molecules,

$$N_2(Y) + O_2 \longrightarrow N_2(X) + O + O, \qquad (38)$$

where Y stands for an electronically excited state. In addition, starting from a certain density of $N_2(A)$ and $N_2(a')$ particles, the associative ionization of nitrogen molecules also becomes important.

Since the kinetics of electronically excited nitrogen molecules was not considered in [56], the calculations carried out in that paper give a substantially smaller content of NO in the postdischarge phase.

The energy cost of the production of one NO molecule calculated by the complete model under the conditions of the hypothetical experiment under consideration amounts to nearly 100 eV/molecule.

An analysis based on computation results similar to those presented in Fig. 6 predicts the high rate of NO production in all of the above three versions of creating artificial RF-reflecting ionized regions or proposed field experiments. The analysis confirms the apprehension of a possible “poisoning” of the ozonosphere by nitrogen oxides produced by long-duration microwave discharges.

An available kinetic scheme of a nonequilibrium discharge in a nitrogen–oxygen mixture [23] with necessary supplements can be used to analyze both the environmental safety of various regimes of microwave discharges in the atmosphere and a number of antropogenic factors perturbing the atmosphere. As one of the realizations of the potentialities of the plasmochemical scheme of [23], we consider an analysis performed by Matveev and Silakov [57].

In [57], a mathematical model was developed of an artificial ionized region (AIR) produced in the atmosphere by two crossed intense coherent TE microwave beams. The model is based on the solution of a time-dependent set of Maxwell's equations, the Boltzmann kinetic equation for electrons, and a comprehensive and branched kinetic scheme of plasmochemical processes in humid air. The kinetic scheme includes a set of reactions involving the following gas species: $N_2(X^1\Sigma_g^+)$, $N_2(A^3\Sigma_u)$, $N_2(B^3\Pi_g$, $W^3\Delta_u$, $B'^3\Sigma_u)$, $N_2(a'^1\Sigma_u^-$, $a^1\Pi_g$, $w^1\Delta_u)$, $N_2(C^3\Pi_u$, $E^3\Sigma_g^+$, $a''^1\Sigma_g^+)$, $O_2(X^3\Sigma_g^-)$, $O_2(a^1\Delta_g)$, $O_2(b^1\Sigma_g^+)$, $O_2(c^1\Sigma_u^-$, $C^3\Delta_u$, $A^3\Sigma_u^+)$, $N(^4S)$, $N(^2D)$, $O(^3P)$, $O(^1D)$, $O(^1S)$, O_3, NO, NO_2, N_2O, H_2O, H, H_2, OH, HO_2, and H_2O_2. Besides chemical processes, the photodissociation of O_2, O_3, NO_2, and N_2O molecules under the action of solar radiation was taken into account. Using this model, the authors could correctly and self-consistently calculate the electrodynamic problem of an AIR produced in the stratosphere by crossed microwave beams.

Calculations performed for the stratosphere showed that it is possible to sustain an AIR at high altitudes (~55 km) over a long time under operating conditions providing the minimum energy consumption, high RF-reflecting properties of the plasma object, and insignificant degradation of the ozone layer. In fact, under optimal conditions for the excitation of an AIR ($H = 55$ km and $\lambda_f = 60$ cm), the minimum ozone density in the postdischarge phase is ≈87% of the background ozone density and is reached about 3.5 h after the end of the discharge. As NO molecules diffuse from the treated region, the O_3 density is gradually restored to its background level. Taking into account that an altitude of 55 km corresponds to the upper boundary of the ozone layer (most ozone is concentrated at altitudes of $15 < H < 45$ km), we can conclude that the long-term maintenance of an AIR in this regime is not a serious hazard to the ozone layer as a whole. In addition, the modeling of kinetic and photochemical processes in the postdischarge phase showed that an excess amount of active hydrogen radicals HO_x produced in the discharge only slightly affects the ozone layer because of the high rate of reactions resulting in radical fixation.

Thus, numerous calculations based on a branched plasmochemical scheme of a nonequilibrium gas discharge (see [23, 57]) confirm the reservations expressed in [48–51] concerning the harmful effect of creating artificial mirrors in the lower stratosphere (where most ozone is concentrated) for the purpose of long-range radio and TV communication. However, the same kinetic scheme (see [57]) made it possible to find conditions minimizing the harmful effect of long-duration plasma objects on the ozone layer.

3.2. Laboratory Modeling of Freely Localized Atmospheric Gas Discharges and the Experimental Study of the Gas-Discharge Methods of CFC Utilization

The idea of using gas discharges to clean the atmosphere of ozone-destroying CFCs stimulated the performance of a series of laboratory experiments modeling full-scale atmospheric experiments. Laboratory studies include experiments with microwave discharges, laser sparks, and slipping surface discharges. In this section, we present a brief description of the experimental layouts, a discussion of the results obtained, and the main inferences.

Requirements for the laboratory modeling of cleaning the Earth's atmosphere with microwaves can be formulated as follows:

(i) A discharge should be excited under conditions close to those in the atmosphere; i.e., the gas-discharge column should not be in contact with the chamber walls, electrodes, or any elements of the measurement facility.

(ii) The working gas should be air with a CFC admixture. The working pressure range should correspond to altitudes of $H \le 10$–15 km (i.e., $100 \le p \le 760$ torr). It is also desirable that the concentration of CFC molecules correspond to the natural one ($\sim 10^{-9}$).

(iii) Ultrashort ($\tau_f \le 100$ ns) and super-powerful ($E \approx (2$–$4)E_{th}$) microwave pulses are of most interest.

In model experiments on the neutralization of local CFC exhausts and the utilization of the accumulated CFCs, the CFC concentration in a gas mixture under study can be substantially higher than that in the real atmosphere. In these experiments, in addition to the irradiation of air, as the main gas, the irradiation of some other gases is also of interest.

Figure 7 shows a typical experimental layout of the experiments conducted at the Institute of General Physics of the Russian Academy of Sciences [58].

Two types of discharges excited in the focal region of a microwave beam were studied: self-excited and self-sustained low-pressure discharges and discharges initiated (and then self-sustained) at high gas pressures.

The experiments were conducted with microwaves at wavelengths of $\lambda_f = 0.8$ and 2.5 cm. The parameters of the microwave oscillators are listed in Table 2.

The microwave radiation was focused on the axis of a metal chamber of diameter $\Theta_{ch} \simeq 350$ mm. The focal spot diameter was $d_f \approx \lambda_f \ll \Theta_{ch}$, and the microwave

Table 2

Device	Oscillator type	λ_f, cm	τ_f, μs	P_f, kW	I_f, kW/cm^2	f, Hz
SVECHA	Gyrotron	0.8	≤100	≤400	≤30	≤5
MOSKVA-2	Magnetron	2.5	≤100	≤500	≤10	≤100

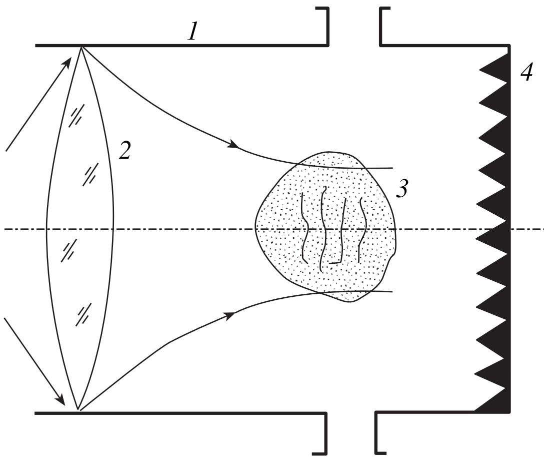

Fig. 7. Typical layout of the experiments with freely localized discharges excited by microwave beams, carried out at the Institute of General Physics of the Russian Academy of Sciences: (*1*) metal vacuum chamber, (*2*) lens forming a convergent microwave beam, (*3*) microwave discharge, and (*4*) microwave absorber.

intensity at the focus was $I_f \simeq 4P/\pi d_f^2$. In some cases, a gas-filled glass or quartz retort of diameter $\Theta \simeq 140$ mm $\gg d_f$ was placed near the beam focus. When operating at high pressures, a discharge initiator (metal needles or a metal–dielectric target) was introduced into the retort.

The chamber (or the retort) was evacuated to high vacuum and then filled with an air–CFC mixture (or, in some experiments, with a nitrogen–CFC or argon–CFC mixture). The working pressure was in the range $10 \le p \le 500$ torr. High-pressure discharges initiated by microwave beams were studied and described in [58–61]. This type of discharge is usually highly inhomogeneous; i.e., there are regions in which the plasma is contracted into filaments (or channels) with a very high electron density ($n_e \ge 10^{16}$–10^{17} cm^{-3}) and relatively high electron and gas temperatures ($T_e \ge 5$ eV and $T_g \le 3000$ K). The filaments are surrounded by a cold ($T_e \simeq 0.5$–0.7 eV) and rarified ($n_e \le 10^{12}$ cm^{-3}) plasma, which is seen as an aureole. Such a high electron density in filaments is predicted by the theory of freely localized high-pressure microwave discharges (see, e.g., [62–64]).

Figure 8 demonstrates typical photographs of microwave discharges.

In experiments with air–CFC mixtures, the CFC content was measured from the absorption of probing IR radiation before and after the irradiation of the gas with a sequence of microwave pulses producing a discharge at the focus of the microwave beam.

Figure 9 shows a typical dependence of the CFC content on the irradiation time *t*. The experiments were conducted with argon–CFC and air–CFC gas mixtures.

Figure 10 shows the energy cost of the destruction of CFC-11 and CFC-12 molecules as a function of their initial concentration in air.

At short irradiation times, the energy cost is determined by the formula

$$\Delta\varepsilon \simeq Pf\Delta t_c\tau_f/\Delta N_{\mathrm{CFC}}, \qquad (39)$$

where ΔN_{CFC} is the number of CFC molecules destroyed; Δt_c is the irradiation time; P is the microwave power; and τ_f and f are the duration and repetition rate of microwave pulses, respectively.

For the cleaning method under consideration, the composition of the gas medium in the postdischarge phase is of prime interest. The gas composition is measured from the absorption spectra before and after the gas is irradiated with high-power microwaves. For this purpose, a chromatograph connected to a mass-spectrometer and an IR spectrograph were used. Table 3 lists stable products that are formed in the processes of CFC decomposition.

As follows from the analysis presented in the previous section, one of the key physical problems of the microwave method for air cleaning is the problem of mechanisms governing the discharge plasma decay. To answer the question as to whether the plasma decay is governed by attachment or recombination, the time behavior of the electron temperature was examined [25, 28, 65]. The electron density n_e was measured (i) by the absorption of diagnostic microwave radiation at the wavelengths $\lambda_d \simeq 0.8$ and 0.2 cm and (ii) with the help of a Leher line crossing the discharge and powered with diagnostic radiation at the wavelength $\lambda_d = 0.8$ cm (Fig. 11). The results obtained with both methods are in good agreement.

Table 3

Original mixture	Identified products of plasmochemical reactions									Measurement method
Air + CFC-12	CF_4	CO_2	C_2F_6	CF_3Cl	CF_2Cl_2	COF_2	SiF_4	$(CH_3)_2SiF_2$	Cl_2	Chromatograph + mass-analyzer (rel. units)
	0.4	1.0	0.03	1.61	0.05	–	–	0.16	–	
Same	+	–	–	+	+	+	+	–	–	IR spectrograph
″	–	–	–	–	–	–	–	–	+	UV spectroscopy

Note: (+) stands for an identified substance.

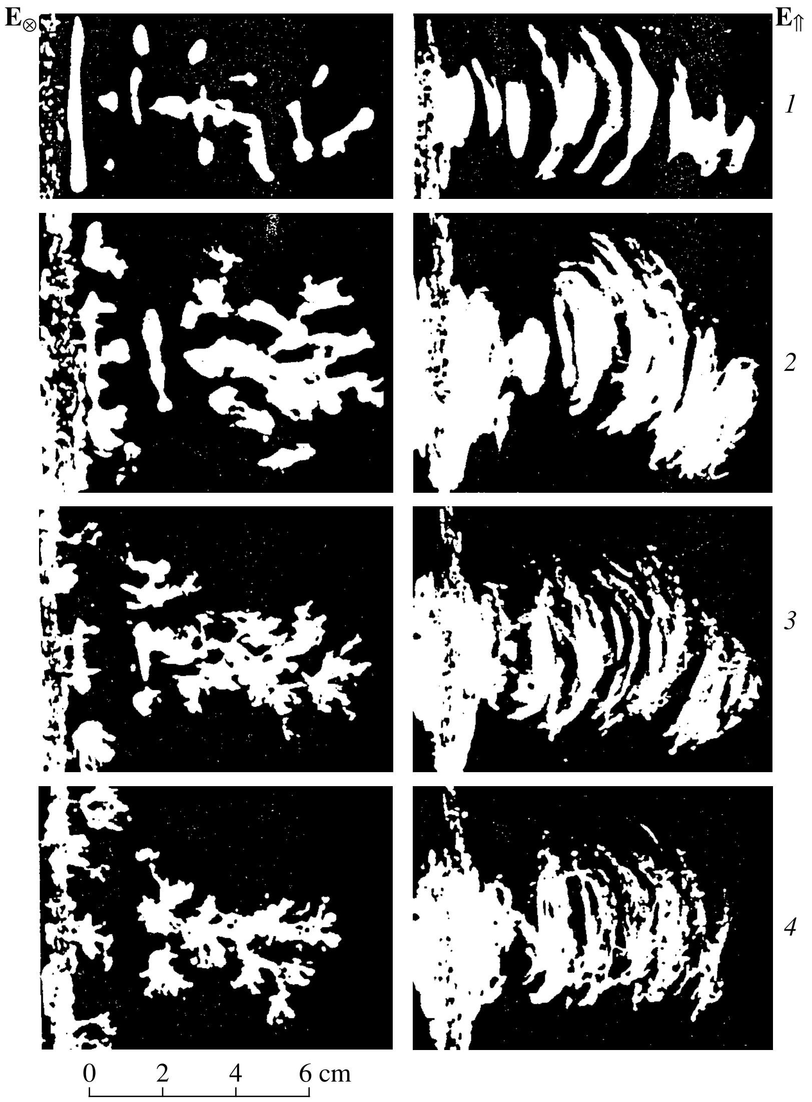

Fig. 8. Typical photographs of a microwave discharge in air observed simultaneously in the parallel (on the left) and perpendicular (on the right) directions with respect to the direction of the microwave electric field for $\lambda_f = 2.5$ cm; $I_f = 35$ kW/cm^2; $\tau_f = 30$ μs; and p = (*1*) 60, (*2*) 90, (*3*) 120, and (*4*) 150 torr.

Figures 12 and 13 show the time evolution of the electron density in the discharge afterglow (for discharges in air and an air–CFC mixture). Figure 14 shows the characteristic decay time of the gas-discharge plasma as a function of the CFC concentration in air.

It is seen in Fig. 12 that the afterglow plasma decays slower than would be expected if the governing decay process were electron attachment to O_2 molecules ($\tau_{att} \le 1$ μs). Moreover, it is seen that the electron density reaches a certain quasi-steady level corresponding to the abnormally long plasma lifetime. Figure 12 shows the calculated curves describing the dynamics of the destruction of CFC-11 and CFC-12 molecules under the assumptions that the CFC concentration in the afterglow is very low, the electron density relaxes by the experimentally determined law, and the CFC destruction is governed by processes (4) and (5). According to the figure, one could expect the almost complete decomposition of CFC-11 and ~50% decomposition of CFC-12 over 10 μs after the end of the discharge. Hence, the rate of cleaning the atmosphere of CFCs in the postdischarge phase is substantially higher than would be expected if the plasma decay occurred via recombination.

It follows from Figs. 13 and 14 that the afterglow plasma decays much slower than would be expected if there were an appreciable amount of CFCs. In fact, even a small number of CFC molecules ($n_{\mathrm{CFC}} \ge 10^{16}$ cm^{-3}) would be sufficient to ensure the rapid decay of the electron component (with a characteristic time of $\tau_e \le 10^{-9}$–10^{-7} s) due to the dissociative attachment of elec-

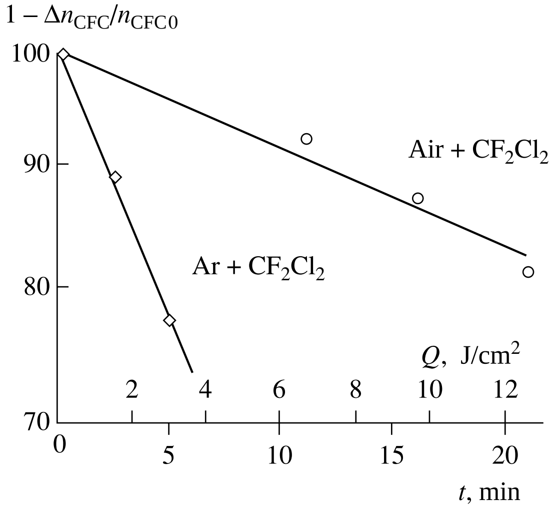

Fig. 9. Time dependence of the CFC-12 content in a gas mixture irradiated by a sequence of microwave pulses for p = 250 torr, $p_{\rm CFC0}$ = 1.7 torr, λ_f = 2.5 cm, I_f = 10 kW/cm^2, τ_f = 30 μs, and f = 2 Hz; Q is the total microwave energy density supplied to a gas target.

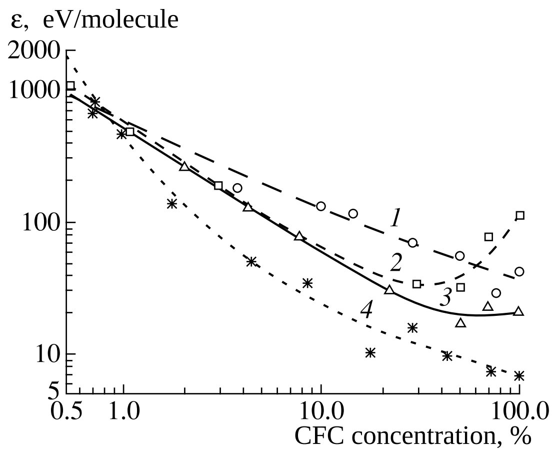

Fig. 10. The energy cost of a CFC molecule as a function of the CFC-11 and CFC-12 concentration in air–CFC mixtures for (*1*) p = 30 torr, τ_f = 30 μs, f = 2 Hz, P_f = 100 kW, and λ_f = 0.8 cm (CFC-12); (*2*) p = 30 torr, τ_f = 30 μs, f = 2 Hz, P_f = 365 kW, and λ_f = 2.5 cm (CFC-12); (*3*) p = 100 torr, τ_f = 200 μs, f = 0.5 Hz, P_f = 100 kW, and λ_f = 0.8 cm (CFC-12); and (*4*) p = 100 torr, τ_f = 55 μs, f = (0.1–1) Hz, P_f = 300 kW, and λ_f = 2.5 cm (CFC-11).

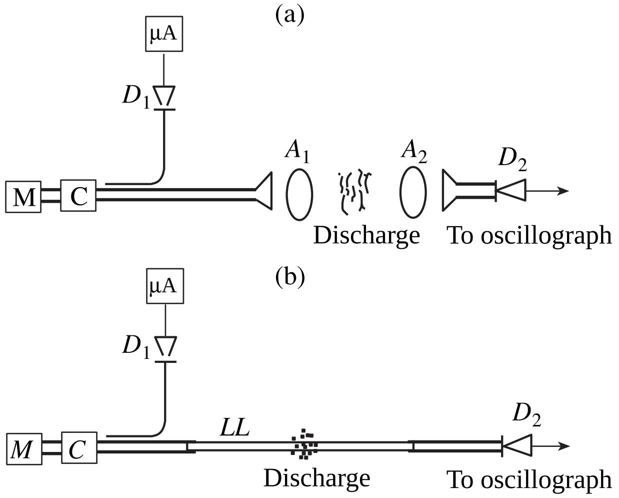

Fig. 11. Schematic of measurements of the electron density in (a) a system with a diagnostic microwave beam and (b) a system with a Leher line: (D_1, D_2) microwave detectors, (*M*) microwave oscillator, (*C*) circulator, (A_1, A_2) horn–lens antennas, (*LL*) Leher line, and (μA) microamperemeter.

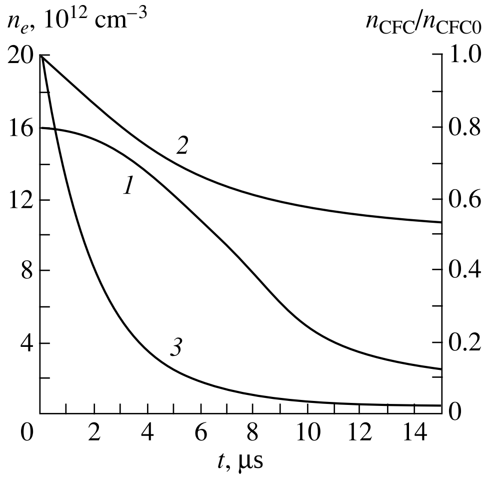

Fig. 12. (*1*) Measured time evolution of the electron density in the decaying plasma of a microwave discharge in air and the calculated (*2*) CFC-12 and (*3*) CFC-11 contents in the postdischarge medium for λ_f = 2.5 cm, I_f = 35 kW/cm^2, τ = 30 μs, and p = 150 torr.

trons to CFC molecules. The abnormally long decay time of the afterglow plasma can be explained by the fact that, in experiments, CFCs are completely decomposed in the contracted regions (channels). According to an analysis of [66], it is also probable that the gas irradiated with UV radiation from the filaments contributes substantially to CFC decomposition. UV radiation can destroy CFC molecules either directly (via photodissociation) or indirectly (via the ionization of various components of the gas mixture).

It follows from measurements that, when the CFC concentration is relatively high (Fig. 10), the energy cost of the decomposition of one CFC molecule amounts to ~10 eV. This means that it is possible to create a plasmochemical reactor with the energy cost of CFC utilization on the order of 2 kW h/kg.

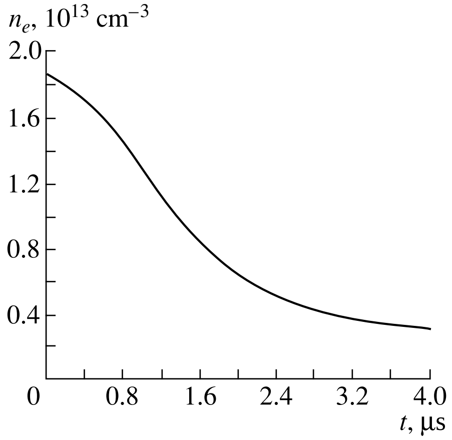

Fig. 13. Time evolution of the electron density in the decaying plasma of a microwave discharge in an air + CFC-12 mixture for $\lambda_f = 2.5$ cm, $I_f = 35$ kW/cm^2, $\tau_f = 30$ μs, $p = 180$ torr, and $p_{CFC} = 3.6$ torr.

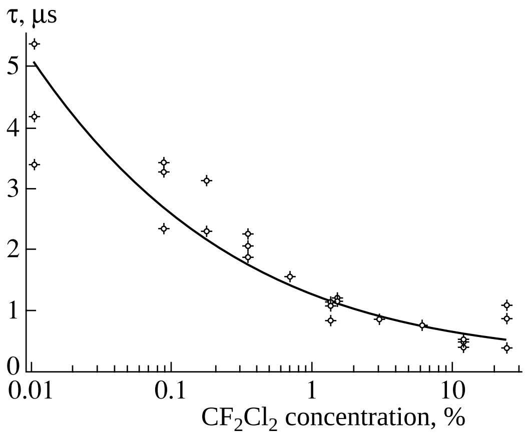

Fig. 14. Characteristic decay time of the microwave-discharge plasma as a function of the initial CFC-12 concentration in air for $\lambda_f = 2.5$ cm, $I_f = 30$ kW/cm^2, $\tau_f = 30$ μs, and $p = 120$ torr.

In view of such a low energy expenditure and the fact that the reactor is “cold” (because the freely localized discharge does not contact the reactor walls), the microwave discharge shows promise for solving the problem of CFC utilization, i.e., the transformation of ozone-destroying CFCs into CFC modifications that are relatively safe for the environment.

One of the key problems of the method under consideration is the negative influence of a CFC-containing gas treated by a discharge on the environmental situation. In this context, the results of measurements presented in Table 3 are of interest. According to the data on the photodissociative decomposition of CFCs (see [2], Fig. 5.1), all the identified products are harmless from the point of view of their possible effect on the ozonosphere.

The results presented in Table 3 are qualitative. Quantitative data on the products of CFC decomposition in freely localized microwave discharges were obtained in [67]. A discharge was excited in mixtures of halocarbons and CFCs (CCl_4, $CFCl_3$, CF_2Cl_2, and CF_3Cl) with argon, nitrogen, or air at high pressures (to about 100 torr). In that paper, for the first time, the quantitative measurements were carried out for almost all of the chlorine- and fluorine-containing products of plasmochemical reactions of CFC decomposition in high-pressure gas discharges. The results obtained allow us to draw the following conclusions:

(i) All of the stable products observed after a sequence of discharges corresponds to a plasmochemical model of [68]. According to this model, the dominant process responsible for the destruction of the original CFC (CFC-12) is nonequilibrium chemical conversion associated with the interaction of vibrationally and electronically excited molecules of a CFC admixture with each other.

(ii) The gas region in which the original CFC molecules are destroyed is substantially larger than the energy deposition region (a region occupied by gas-discharge filaments). Nevertheless, the discharge instability and contraction play a decisive role because the contracted hot dense plasma is a source of radiation exciting CFC molecules in the surrounding gas.

(iii) UV radiation from the contracted gas-discharge plasma not only acts as an initiator and accelerator of the destruction of the original CFC molecules, but also leads to the selective decomposition of the chlorine-containing destruction products, so that only the products that are the most stable against photodissociation remain in the gas mixture. Thus, in discharges in argon with a CFC-12 admixture, CFC-13 (CF_3Cl) and CFC-14 turned out to be the most abundant products of the CFC-12 transformation. According to [2], both these CFCs are highly stable against dissociation under the action of the solar UV radiation. The time behavior of the original CFC-12 and its transformation products are shown in Fig. 15.

The latter circumstance turns out to be important when analyzing the prospects of the microwave method for cleaning the atmosphere of ozone-destroying CFCs. Furthermore, the microwave gas discharge can be regarded as an efficient method of the industrial transformation of ozone-destroying CFCs (CFC-12 and CFC-11) into relatively harmless CFC modifications.

The paper by Brovkin *et al.* [69] also describes experiments on the destruction of CFCs [CFC-10 (CCl_4), CFC-12, CFC-113 ($C_2F_3Cl_3$), and CFC-114 ($C_2F_4Cl_4$)] in a microwave discharge. The experiment was very similar to those described in [58, 59, 61, 65, 66]. A convergent repetitive microwave beam with a wavelength of $\lambda_f \simeq 4$ cm irradiates a quartz retort filled with one of the following mixtures: (i) CFC + air, (ii) CFC + hydrogen, (iii) CFC + argon, and (iv) CFC +

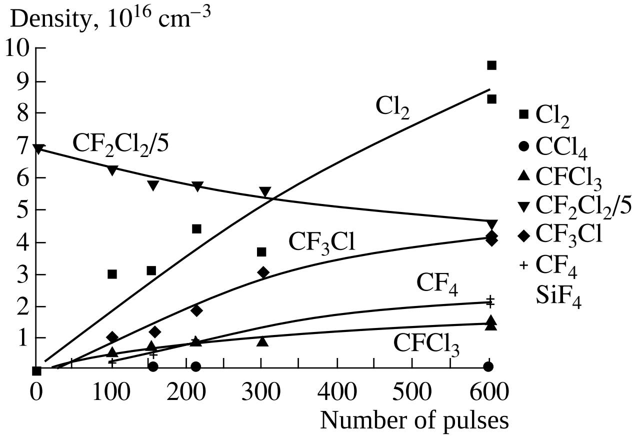

Fig. 15. CFC decay in a discharge excited in an Ar + 10% CFC-12 mixture and the yield of the main products in the initial stage at a total pressure of 105 torr.

water vapor. The energy cost of CFC destruction and its dependence on the partial CFC content are determined. The experimental results are close to those obtained in [65, 66].

Vikharev *et al.* [70] carried out experiments with microwave pulses with the purpose of modeling the gas-discharge cleaning of the atmosphere. A discharge in air was excited by microwave pulses with a duration of $\tau_f \simeq 5$ ns and a peak power of $P = 10$ MW. Microwaves were focused by a cylindrical mirror into a chamber containing a working gas. The specific energy deposited in the discharge varied within the range $3.5 \times (10^{-2}–10^{-1})$ J/(cm^3 atm). The results of the measurements of the discharge afterglow are shown in Fig. 16. At a pressure of $p = 10$ torr, the plasma first decays via recombination; then, the plasma behavior can be best described under the assumption of the three-body attachment of electrons to oxygen.

At $p = 60$ torr, the plasma first decays abnormally rapidly (more rapidly than in the case of the three-body attachment of electrons to O_2 molecules) and, then, abnormally slowly.

Assuming that the afterglow plasma density in the full-scale atmospheric experiment will decrease as is shown in Fig. 16 and neglecting all the possible channels of CFC destruction [except for reactions (4) and (5)], we can easily calculate the rate of CFC destruction after one microwave pulse:

$$N_{\mathrm{CFC}}(t)/N_{\mathrm{CFC0}} \simeq \exp\left(-k_d \int n_e(t)dt\right). \qquad (40)$$

At a pressure of $p = 10$ torr, a discharge excited by a 5-ns microwave pulse can decompose almost 65% of the CFC-11 in the atmosphere (but only 15% at $p = 60$ torr). However, an analysis of the problem of CFC destruction by microwave discharges [28, 44] allows one to assume that the CFC decomposition rate should be substantially higher than the above estimates because destruction channels in addition to the dissociative attachment of electrons to CFC molecules come into play. Thus, according to [44], at $\varepsilon \simeq 10^{-2}$ J/(cm^3 atm), reaction (6) of the interaction of CFC molecules with electronically excited oxygen atoms contributes substantially to CFC destruction.

The problem of cleaning the atmosphere of CFC pollutants by means of gas discharges is closely related to the problem of utilizing ozone-destroying CFC products accumulated in many countries (including Russia). As was mentioned above, the results of [67] show that the microwave discharge can be used to transform harmful CFCs into relatively harmless CFC modifications. Recently, in a number of papers, it was demonstrated that the high efficiency of CFC utilization can be also achieved with discharges other than microwave

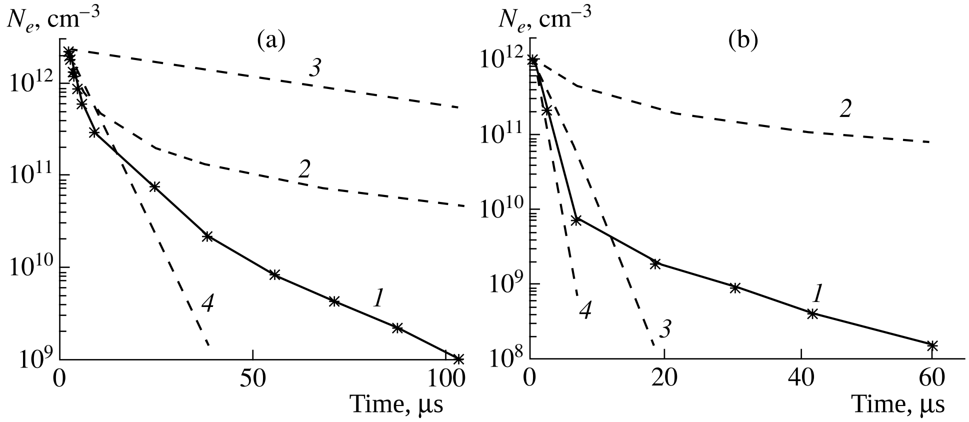

Fig. 16. Decay of the electron density in a microwave discharge in air at a pressure of p = (a) 10 and (b) 60 torr: (*1*) experimental results and the results of calculations under the assumption that the dominant decay mechanism is (*2*) electron–ion recombination, (*3*) three-body attachment, and (*4*) dissociative attachment.

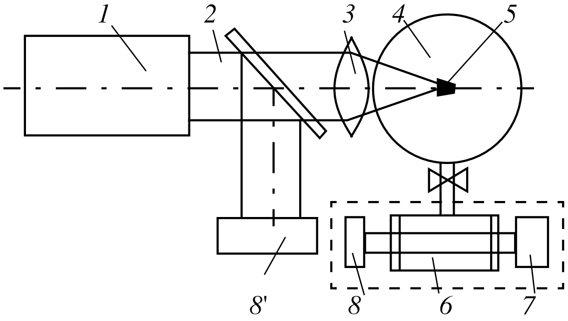

Fig. 17. Schematic of the experiment on CFC decomposition by a laser spark: (*1*) high-power pulsed neodymium-glass laser, (*2*) laser beam, (*3*) lens with a focus length of 8 cm, (*4*) glass retort with a working gas, (*5*) laser spark, (*6*) measuring cell with an IR-transparent window, (*7*) spectrophotometer, and (*8, 8′*) light detectors.

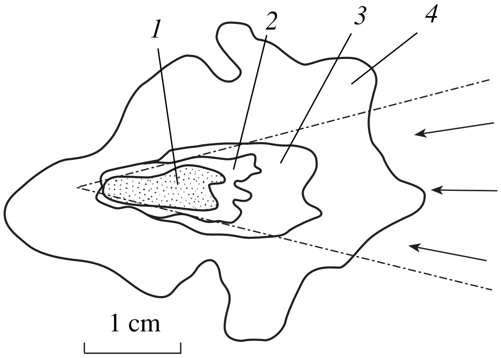

Fig. 18. Integral photograph of a laser spark observed through different neutral filters with T_r = (*1*) 3×10^{-5} (a "core" becomes visible), (*2*) 5×10^{-4}, (*3*) 10^{-3}, and (*4*) 5×10^{-2}. The transmittance T_r is given for λ = 500 nm.

ones. Among those, we mention a spark discharge at the focus of a high-power CO_2 or neodymium-glass laser, whose affect on CFCs was studied by Barkhudarov *et al.* [68] and Askar'yan *et al.* [71]. The efficiency of laser methods depends to a great extent on the actual volume of the treated gas. The problem is whether this volume coincides with a small volume of the energy deposition region (the so-called "core") or substantially exceeds the latter.

In [71], a GOS-1000 neodymium-glass laser was used to excite sparks. The laser generated high-power pulses with a duration of 30–40 ns and energy of $Q_1 \simeq$ 80 J. A schematic of the experiment is shown in Fig. 17. The laser beam is focused into a spherical retort filled with CFC-12 or an air–CFC-12 mixture. Figure 18 demonstrates the integral spark photograph made with light filters with different optical densities. In the photograph, we can see a bright core surrounded by a less intense aureole.

Experiments showed that, with a single laser pulse, the original CFC was destroyed throughout the entire retort volume, which was substantially (more than 30 times) greater than the core volume. The energy cost of CFC destruction (at normal gas pressure) turned out to be ≈6 eV/molecule.

The experimental layout used in [68] was very similar to that shown in Fig. 17. In those experiments, a spark in an air–CFC mixture was excited by a TEA CO_2 laser. The CO_2 laser pulse consisted of a 1-μs spike and a low-intensity "tail" with a duration of 2.5–3.0 μs. The total energy in the pulse was $Q_1 \simeq$ 35–40 J.

Photographs similar to those presented in Fig. 18 also demonstrate the presence of a core and aureole.

The dynamics of CFC destruction was traced in a sequence of laser pulses. The main results are presented in Table 4, where N_1 is the number of laser shots, $\Delta N_{CFC}/N_{CFC0}$ (%) is the relative decrease in the CFC concentration, and ε is the energy cost of CFC destruction.

Experiments show that, in this case, the energy cost of CFC destruction is very low (~10–30 eV/molecule). This means that, as in [66], the gas region treated by a CO_2-laser spark is substantially larger than the energy deposition region (the core).

In the troposphere or in the region of a local CFC exhaust near the Earth surface, a gas discharge can also be excited with the help of electrode systems. It is obvious that this method for plasma generation is the simplest and easiest to implement (as compared to microwaves and lasers). However, as far as the problem of global atmosphere cleaning is concerned, this method encounters problems because both the discharge system and the power supply should be launched to high altitudes. At the same time, the electrode discharge may be used to solve the problem of CFC utilization under laboratory and industrial conditions.

In [68], preliminary results are presented from experiments in which slipping surface discharges were used to decompose ozone-destroying CFCs in air at high (up to atmospheric) pressures. Figure 19 illustrates the design of the discharge system. The plasma source was an annular (toroidal) multielectrode system, in which a low-threshold surface discharge was ignited. A capacitor bank was charged to U = 25 kV, and the stored energy was about 1.5×10^3 J. A vacuum chamber, in

Table 4. Air + CF_2Cl_2, p_0 = 200 torr, p_{CFC} = 30 torr

N_1	$\Delta N_{CFC}/N_{CFC0}$, %	ε, eV/molecule
5	19	19
10	28	27
20	54	32
30	68	33

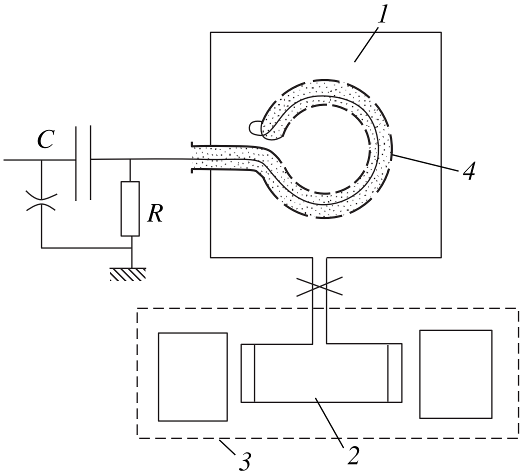

Fig. 19. Schematic of the experiment on CFC decomposition by a slipping surface discharge: (*1*) vacuum chamber, (*2*) retort with a NaCl window, (*3*) Specord-76 IR spectrometer, and (*4*) annular slipping surface discharge.

which the annular plasma source was installed, was filled with argon or air containing a CFC admixture. After a series of pulses, the CFC content and the energy spent on the destruction of one CFC molecule were determined. The experimental results are listed in Table 5, where N_{S1} is the number of pulses.

Experiments showed that, as in the case of microwave and laser discharges, the gas volume cleaned of CFCs in each pulse was substantially (about 15 times) greater than the volume of the plasma generated in a slipping discharge.

The high efficiency of CFC decomposition was also demonstrated in the paper by Akhmedzhanov *et al.* [72], in which a repetitive nanosecond corona discharge was used as a plasma source. The voltage amplitude was 30–40 kV, the pulse duration was $\tau = 50$ ns, the repetition rate was $f = 1$–100 Hz, and the pulse energy was $w \simeq 0.2$ J.

The results of the experimental studies of gas-discharge action on CFC molecules in air can be summarized as follows:

(i) All the types of gas discharges examined for cleaning air of ozone-destroying CFCs demonstrated the high efficiency of CFC destruction.

Table 5. Air + CF_2Cl_2, $p_0 = 200$ torr; $p_{CFC} = 100$ torr

N_{S1}	$\Delta N_{CFC}/N_{CFC0}$, %	ε, eV/molecule
2	9	20
5	24	19
10	36	25
15	59	23

(ii) A very low energy cost of CFC destruction (transformation) was obtained in experiments with high-pressure contracted microwave discharges, laser sparks, and slipping surface discharges. For all the types of discharges, the values of the energy cost of CFC destruction turned out to be close to each other. This allows us to suggest that UV radiation from the energy deposition regions plays an important role in the process of gas cleaning. In microwave discharges, these hot radiating objects are channels (or filaments) forming a complicated discharge structure. In laser sparks, the discharge core is an intense UV source. In slipping surface discharges, energy is deposited locally in a relatively narrow surface gas sheath, which is probably a source of UV radiation destroying CFCs in the surrounding gas. Hence, the generation (in one or another way) of a small-volume discharge characterized by a very high specific energy deposition efficiently treats the gas in a larger volume by intense UV radiation from the hot regions.

(iii) The almost complete (even to atoms) destruction of CFC molecules in hot plasma points (or lines), along with the photodissociation, photoionization, and photoexcitation of CFC molecules in the aureole surrounding the discharge, results in an unexpectedly low energy cost of CFC destruction.

(iv) The expected high conversion efficiency of the plasma energy into UV radiation allows us to suppose that the gas discharges under consideration possess specific selective properties. By the selectivity, we mean the fact that, among all the destruction and transformation products of the ozone-destroying CFCs and other products resulting from the interaction of radicals, only molecules that are insensitive to UV radiation survive.

The problem of the restoration of the stratospheric ozone with the help of gas discharges excited by high-power microwave beams stimulated the performance of laboratory experiments modeling full-scale atmospheric experiments.

A freely localized microwave discharge in air and oxygen was studied by Akhmedzhanov *et al.* [73]. A schematic of the experiment is shown in Fig. 20. Pulsed 3-cm microwave radiation was focused by a spherical mirror. The efficiency of ozone production with relatively long ($\tau_f \simeq 500$ ns) and short ($\tau_f \simeq 6$ ns) microwave pulses was studied. The working pressure range $p = 3$–30 torr corresponded to stratospheric altitudes. The aim of the study was to find the discharge conditions (the pulse duration, the repetition rate, and the value of the reduced electric field) optimal for ozone generation.

Figure 21 shows the results of measurements of the energy cost of ozone production under different conditions in air and oxygen. The minimum energy cost $\varepsilon \simeq 4$ eV/molecule was obtained in discharges excited by short microwave pulses in oxygen at a pressure of $p = 20$ torr and repetition rate of $f = 10$ Hz. In discharges excited by longer microwave pulses, all other factors being equal, the energy cost was substantially higher,

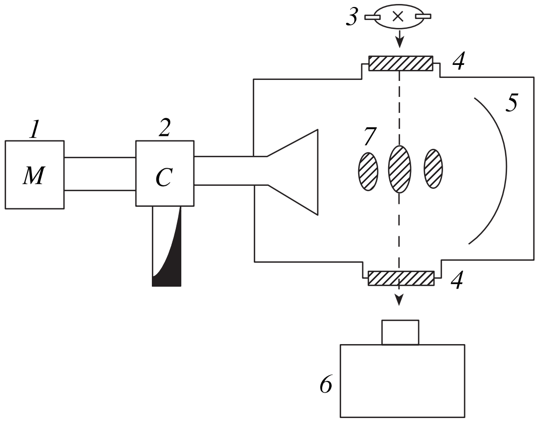

Fig. 20. Schematic of the experiment on CFC decomposition by a microwave discharge: (*1*) magnetron, (*2*) circulator, (*3*) mercury lamp, (*4*) quartz windows, (*5*) spherical mirror, (*6*) optical spectrum analyzer, and (*7*) discharge plasma.

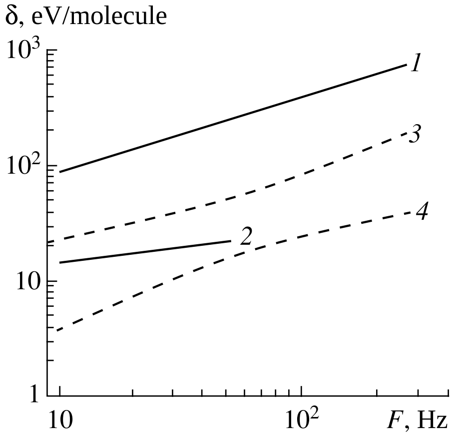

Fig. 21. Energy cost of the production of an ozone molecule in (*1*, *2*) air and (*3*, *4*) oxygen as a function of the repetition frequency of microwave pulses at a gas pressure of p = 20 torr for τ_f = (*1*, *3*) 500 and (*2*, *4*) 6 ns.

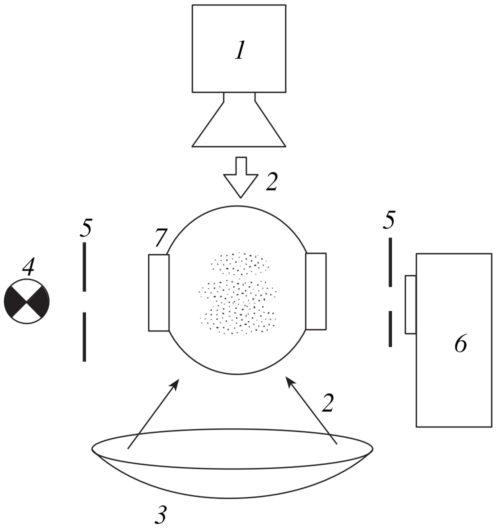

Fig. 22. Schematic of the experimental setup for the excitation of microwave discharges with a relativistic carcinotron: (*1*) microwave oscillator, (*2*) microwave radiation, (*3*) spherical mirror, (*4*) mercury lamp, (*5*) diaphragms, (*6*) multichannel spectrum analyzer, and (*7*) quartz retort cooled with liquid nitrogen.

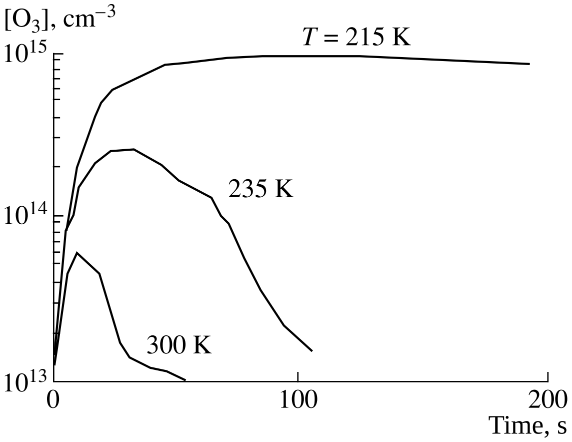

Fig. 23. Time evolution of the ozone density in a gas discharge in air produced by a sequence of microwave pulses for different initial air temperatures at a repetition frequency of f = 3 Hz and gas pressure of p = 30 torr.

attaining $\varepsilon \simeq 23$ eV/molecule. The energy cost increases as the repetition rate of pulses (both short and long) increases.

The ozone production by microwave discharges in dry air was studied by Akhmedzhanov *et al.* [74]. A schematic of the experimental setup is shown in Fig. 22. The microwave oscillator was a relativistic carcinotron with a wavelength of λ_f = 8 mm. The peak power was P = 10–25 MW, the pulse duration was $\tau_f \simeq$ 5 ns, and the repetition rate was f = 1–10 Hz. A microwave Gaussian beam was focused by a metal mirror (Fig. 22) into a spherical quartz retort evacuated and filled with a working gas at pressures in the range p = 10–90 torr (which corresponds to the altitudes $H \simeq$ 15–30 km). The retort wall was cooled with liquid nitrogen. The initial gas temperature equal to the wall temperature could vary in the range $T_g \simeq$ 200–300 K.

Figure 23 illustrates the time dependence of the ozone concentration [74] at a pressure of p = 30 torr and different initial gas temperatures during irradiation by microwaves. It is seen in the figure that, at a relatively high initial temperature, the ozone concentration first increases with time and then falls. At a sufficiently low initial temperature, the ozone concentration arrives at a fairly high steady-state level and then does not vary. Over the entire pressure range under study, as the initial gas temperature decreased to 215 K, the amount of the ozone produced was more than one order of magnitude higher than that produced at higher temperatures. The energy cost of O_3 production in air at $T_g = 220$ K was $\varepsilon \simeq 50$ eV/molecule. No production of NO_2 above a density level of 10^{13} cm^{-3} was detected.

We draw attention to the fact that the values of the energy cost of O_3 production obtained in [73] and [74] differ substantially. Unfortunately, the authors do not comment on the observed difference, which, apparently, is related to the difference in the wavelengths of microwave radiation.

Thus, experiments performed in [73, 74] give the values of the energy cost of ozone production in microwave discharges in air. These values can be used to estimate the efficiency of using microwave discharges as artificial stratospheric ozone sources. At the same time, the results presented in [73, 74] allow us to determine the optimal conditions for the microwave gas-discharge generation of ozone in the stratosphere.

4. CONCLUSION

In summary, we can say that the studies reviewed in this paper constitute a new direction in gas-discharge physics—*the physics of freely localized atmospheric gas discharges.* This direction, which originated from applied problems related to the generation of RF-reflecting stratospheric plasma mirrors, gave rise to a new branch aimed at solving environmental problems associated with the protection and restoration of the Earth's ozone layer.

Although these studies are devoted to applied problems, we note, first of all, the results that are of fundamental physical importance. Among the most important achievements that are of interest for modern gas-discharge physics, we can mention the following:

(i) The most comprehensive kinetic model of a nonequilibrium discharge in a nitrogen–oxygen gas mixture has been developed. The model can be applied to a wide range of fundamental gas-discharge studies carried out in modern physical laboratories.

(ii) The best-developed self-consistent mathematical model of a microwave discharge in a nitrogen–oxygen mixture (including blocks describing the branched kinetics of nonequilibrium plasmochemical processes, as well as electrodynamic, photochemical, and gas-dynamic phenomena) has been constructed.

(iii) Based on the developed mathematical model, an analysis of hypothetical field experiments and data from laboratory experiments have revealed the important role of such processes as the excitation of the metastable electronic levels of oxygen and nitrogen atoms, the excitation of the metastable levels of nitrogen molecules, and the associative ionization of electronically excited gas particles.

(iv) New catalytic (hydrogen) cycles have been revealed in the process of CFC decomposition by a gas discharge.

(v) A foundation has been laid for a new direction in plasma chemistry—*plasma chemistry of gas-discharge media with highly developed instabilities (such as ionizational, thermal–ionizational, and field instabilities).* It has been established that UV radiation from contraction regions plays an important role, promoting a number of plasmochemical processes.

(vi) Original experimental microwave methods have been developed based on the formation of high-power convergent microwave beams exciting gas discharges under conditions such that all of the processes leading to the plasma formation, as well as plasmochemical processes, are volume in nature. Hence, heterogeneous processes, which are very difficult to take into account theoretically, are excluded from consideration, so that it becomes possible to compare the experimental results with theoretical predictions.

The results obtained in solving the applied problem of the protection and restoration of the Earth's ozone layer, as well as the results of theoretical and experimental modeling, allow us to draw the following conclusions:

(i) At present, the gas-discharge method of cleaning the troposphere of ozone-destroying CFCs seems more preferable from the standpoint of overcoming the ozone crisis.

(ii) Preliminary analysis shows that microwave discharges excited in the upper troposphere can selectively clean air of CFC pollutants at a relatively low energy deposition, on the order of ~10^{-5} J/(cm^3 atm). Hence, it is possible to create a kind of barrier preventing the penetration of CFCs into the stratosphere. The results of laboratory modeling of freely localized atmospheric microwave discharges confirm the inference about the high efficiency of the gas-discharge cleaning method.

(iii) Much theoretical and laboratory research is to be performed in order to draw a final conclusion on the advisability of cleaning the atmosphere of ozone-destroying CFC pollutants by means of microwave gas discharges. The challenging problems to be solved are the identification of the most efficient channels of CFC destruction (along with dissociative electron attachment), the study of physical processes responsible for the relaxation of the postdischarge plasma, the assessment of the role of aerosols and water vapor in gas-discharge CFC destruction, etc.

(iv) The studies of microwave discharges, as well as laser sparks and slipping surface discharges, have demonstrated that these discharges can be successfully used for the industrial utilization of the accumulated CFCs.

In conclusion, we note that the results obtained in studying CFC destruction and ozone production by microwave gas discharges can be of considerable interest from the standpoint of field experiments aimed at solving fundamental problems of the physics of the Earth's atmosphere. Freely localized discharges excited in the atmosphere by a high-power pulsed microwave beam (or beams) can appear to be the most convenient method for introducing an excess amount of ozone, nitrogen oxide, and chlorine molecules in a certain region of the atmosphere for the purpose of tracing space and time evolutions of the introduced product, which will make it possible to identify the mechanisms governing photochemical, chemical, and diffusion processes in the Earth's atmosphere.

REFERENCES

1. Atmospheric Ozone, *Proceedings of the XVIII Quadrennial Ozone Symposium, L'Aquila, Italy, 1996,* Ed. by R. D. Bojkov and G. Visconti (Parco Scientifico e Tecnologico d'Abruzzo, 1996), Vols. 1, 2.
2. É. L. Aleksandrov, Yu. A. Izraél', I. L. Karol', and A. Kh. Khrgian, *Ozone Shield of the Earth and Its Alterations* (Gidrometeoizdat, St. Petersburg, 1992).
3. R. S. Stolarski, Sci. Am. **258** (1) (1988).
4. V. L. Syvorotkin, Priroda, No. 9, 35 (1993).
5. J. G. Anderson, D. W. Toohey, and W. H. Brune, Science **251**, 39 (1980).
6. T. H. Stix, J. Appl. Phys. **66**, 5622 (1989).
7. K. T. Tsang, D. D. Ho, A. Y. Wong, and R. J. Siverson, in *Proceedings of the Seventh Piero Caldirola International School of Plasma Physics: Controlled Active Global Experiments, Varenna, 1990*, Ed. by E. Sindoni and A. Y. Wong (Società Italiana di Fisica, Bologna, 1991), p. 143.
8. A. Y. Wong, J. Steinhauer, R. Close, and T. Fukuchi, Comm. Plasma Phys. Control. Fusion **12**, 223 (1989).
9. A. Y. Wong, R. W. Wuerker, J. Sabutis, *et al.*, in *Proceedings of the Seventh Piero Caldirola International School of Plasma Physics: Controlled Active Global Experiments, Varenna, 1990*, Ed. by E. Sindoni and A. Y. Wong (Società Italiana di Fisica, Bologna, 1991), p. 129.
10. A. M. Starik, O. N. Favorskiĭ, O. S. Khabarov, and B. N. Amelin, Vestn. Akad. Nauk **63**, 1082 (1993).
11. A. L. Vikharev, A. M. Gorbachev, O. A. Ivanov, *et al.*, Phys. Lett. A **179**, 122 (1993).
12. R. A. Akhmedzhanov, A. L. Vikharev, A. M. Gorbachev, *et al.*, Phys. Lett. A **207**, 209 (1995).
13. A. V. Gurevich, A. G. Litvak, A. L. Vikharev, *et al.*, Usp. Fiz. Nauk **170** (11), 1181 (2000).
14. N. D. Borisov, A. V. Gurevich, and G. M. Milikh, *Artificially Ionized Region in Atmosphere* (Akad. Nauk SSSR, IZMIRAN, Moscow, 1986).
15. A. L. Vikharev, A. M. Gorbachev, O. A. Ivanov, *et al.*, J. Geophys. Res. **99**, 21097 (1994).
16. N. A. Borisov and A. V. Gurevich, Fiz. Plazmy **17**, 1131 (1991) [Sov. J. Plasma Phys. **17**, 657 (1991)].
17. K. Tsang, K. Papadopoulos, A. Drobot, *et al.*, Radio Sci. **26**, 1345 (1991).
18. I. L. Karol', A. A. Kiselev, and V. A. Frol'kis, Izv. Akad. Nauk, Fiz. Atmos. Okeana **31**, 120 (1995).
19. É. L. Aleksandrov and L. B. Upénék, Khim. Fiz. **16** (2), 48 (1997).
20. A. M. Starik, Prikl. Fiz., No. 1, 11 (1996).
21. G. M. Batanov, I. A. Kossyi, A. A. Matveev, and V. P. Silakov, Fiz. Plazmy **22**, 1046 (1996) [Plasma Phys. Rep. **22**, 950 (1996)].
22. G. M. Batanov, I. A. Kossyi, A. A. Matveyev, and V. P. Silakov, in *Proceedings of the XVIII Quadrennial Ozone Symposium, L'Aquila, Italy, 1996*, Ed. by R. D. Bojkov and G. Visconti (Parco Scientifico e Tecnologico d'Abruzzo, 1996), Vol. 2, p. 833.
23. I. A. Kossyi, A. Yu. Kostinsky, A. A. Matveyev, and V. P. Silakov, Plasma Sources Sci. Technol. **1**, 207 (1992).
24. G. A. Askar'yan, G. M. Batanov, A. É. Barkhudarov, *et al.*, Pis'ma Zh. Éksp. Teor. Fiz. **55**, 500 (1992) [JETP Lett. **55**, 515 (1992)].
25. G. A. Askar'yan, G. M. Batanov, A. É. Barkhudarov, *et al.*, Fiz. Plazmy **18**, 1198 (1992) [Sov. J. Plasma Phys. **18**, 625 (1992)].
26. G. A. Askar'yan, G. M. Batanov, S. I. Gritsinin, *et al.*, Comm. Plasma Phys. Control. Fusion **16**, 43 (1994).
27. G. A. Askar'yan, G. M. Batanov, A. E. Barkhudarov, *et al.*, J. Phys. D **27**, 1311 (1994).
28. G. A. Askar'yan, G. M. Batanov, S. I. Gritsinin, *et al.*, in *Strong Microwaves in Plasmas, 1993* (Inst. of Applied Physics, Nizhni Novgorod, 1994), Vol. 1, p. 227.
29. *Physics and Chemistry of Gas Discharges in Microwave Beams* (Nauka, Moscow, 1994), Tr. Inst. Obshch. Fiz. Ross. Akad. Nauk, Vol. 47.
30. G. F. Reinking, L. G. Christophorou, and S. R. Hunter, J. Appl. Phys. **60**, 493 (1986).
31. *Electron–Molecule Interactions and Their Applications*, Ed. by L. G. Christophorou (Academic, Orlando, 1984), Vols. 1, 2.
32. D. L. Mc Corcle, A. A. Christodoulides, L. G. Christophorou, and J. Szamrei, J. Chem. Phys. **72**, 4049 (1980).
33. A. V. Eletskiĭ and B. M. Smirnov, Usp. Fiz. Nauk **147**, 459 (1985) [Sov. Phys. Usp. **28**, 956 (1985)].
34. F. C. Fehsenfeld, P. J. Crutzen, A. K. Schmeltekopf, *et al.*, J. Geophys. Res. **81**, 4454 (1976).
35. G. A. Askar'yan, M. S. Rabinovich, M. M. Savchenko, and A. D. Smirnova, Pis'ma Zh. Éksp. Teor. Fiz. **1** (6), 18 (1965) [JETP Lett. **1**, 162 (1965)].
36. G. A. Askar'yan, M. S. Rabinovich, M. M. Savchenko, and V. K. Stepanov, Pis'ma Zh. Éksp. Teor. Fiz. **3**, 465 (1966) [JETP Lett. **3**, 303 (1966)].
37. T. Consoli, in *Proceedings of the Seventh Piero Caldirola International School of Plasma Physics: Controlled Active Global Experiments, Varenna, 1990,* Ed. by E. Sindoni and A. Y. Wong (Società Italiana di Fisica, Bologna, 1991), p. 297.
38. V. A. Vanke, V. M. Lopukhin, and V. A. Savin, Usp. Fiz. Nauk **123**, 633 (1977) [Sov. Phys. Usp. **20**, 989 (1977)].
39. N. I. Zaĭtsev and M. I. Petelin, Radiotekh. Élektron. (Moscow) **19**, 1056 (1974).
40. *Magnetron MI-389: Design and Technical Specifications* (Pluton, Moscow, 1990).

41. J. Benford and J. Swegle, *High-Power Microwaves* (Artech House, Boston, 1995).
42. V. F. Larin and S. A. Rumyantsev, Pis'ma Zh. Tekh. Fiz. **15** (6), 87 (1989) [Sov. Tech. Phys. Lett. **15**, 244 (1989)].
43. I. A. Kossyi, A. Yu. Kostinsky, A. A. Matveev, and V. P. Silakov, Pis'ma Zh. Tekh. Fiz. **16** (12), 57 (1990) [Sov. Tech. Phys. Lett. **16**, 465 (1990)].
44. I. A. Kossyi, A. A. Matveev, and V. P. Silakov, Zh. Tekh. Fiz. **64** (9), 168 (1994) [Tech. Phys. **39**, 952 (1994)].
45. Yu. F. Kolesnichenko and D. V. Khmara, Pis'ma Zh. Tekh. Fiz. **19** (10), 36 (1993) [Tech. Phys. Lett. **19**, 308 (1993)].
46. V. D. Rusanov and A. A. Fridman, *Physics of Chemically Active Plasma* (Nauka, Moscow, 1984).
47. N. L. Aleksandrov, S. V. Dobkin, A. M. Konchakov, and D. A. Novitskiĭ, Fiz. Plazmy **20**, 492 (1994) [Plasma Phys. Rep. **20**, 442 (1994)].
48. G. A. Askar'yan, G. M. Batanov, I. A. Kossyi, and A. Yu. Kostinsky, Dokl. Akad. Nauk SSSR **302**, 566 (1988).
49. G. A. Askar'yan, G. M. Batanov, I. A. Kossyi, and A. Yu. Kostinsky, Usp. Fiz. Nauk **156**, 370 (1988) [Sov. Phys. Usp. **312**, 957 (1988)].
50. G. A. Askar'yan, G. M. Batanov, and S. I. Gritsinin, in *Abstracts of the 9th European Sectional Conference on the Atomic and Molecular Physics of Ionized Gases, Lisbon, 1988*, [ECA **12H**, 59 (1988)].
51. G. A. Askar'yan, G. M. Batanov, D. F. Bykov, *et al.*, in *Proceedings of the Seventh Piero Caldirola International School of Plasma Physics: Controlled Active Global Experiments, Varenna, 1990*, Ed. by E. Sindoni and A. Y. Wong (Società Italiana di Fisica, Bologna, 1991), p. 239.
52. G. A. Askar'yan, G. M. Batanov, I. A. Kossyi, and A. Yu. Kostinsky, in *Proceedings of the Tenth Piero Caldirola International School of Plasma Physics: High Power Microwave Generation and Applications, Varenna, 1991*, Ed. by E. Sindoni and C. Warton (Società Italiana di Fisica, Bologna, 1992), p. 207.
53. G. A. Askar'yan, G. M. Batanov, I. A. Kossyi, and A. Yu. Kostinsky, Fiz. Plazmy **17**, 85 (1991) [Sov. J. Plasma Phys. **17**, 48 (1991)].
54. I. A. Kossyi, A. Yu. Kostinsky, A. A. Matveyev, and V. P. Silakov, Comm. Plasma Phys. Control. Fusion **14**, 73 (1991).
55. G. A. Askar'yan, G. M. Batanov, I. A. Kossyi, and A. Yu. Kostinsky, *Problems of Physical Electronics* (Ioffe Physicotechnical Institute and Leningrad Polytechnic Institute, Leningrad, 1990).
56. L. Duncan and G. Milikh, in *Proceedings of the International Workshop on Artificial Ionized Layers in the Atmosphere, Kiev, 1989.*
57. A. A. Matveyev and V. P. Silakov, Phys. Rev. E **54**, 4121 (1996).
58. G. M. Batanov, S. I. Gritsinin, I. A. Kossyi, *et al.*, Tr. Fiz. Inst. Akad. Nauk SSSR **160**, 174 (1985).
59. V. G. Avetisov, S. I. Gritsinin, A. V. Kim, *et al.*, Pis'ma Zh. Éksp. Teor. Fiz. **51**, 303 (1990) [JETP Lett. **51**, 348 (1990)].
60. S. V. Golubev, S. I. Gritsinin, V. E. Zorin, *et al.*, in *High-Frequency Discharge in Wave Fields* (Inst. Prikl. Fiz. Akad. Nauk SSSR, Gorki, 1988), p. 136.
61. V. G. Brovkin and Yu. F. Kolesnichenko, in *Microwave Plasma and Its Applications*, Ed. by Yu. A. Lebedev (Moscow Physical Society, Moscow, 1995), p. 84.
62. I. V. Bezmenov, V. V. Rusanov, and V. P. Silakov, Tr. Inst. Obshch. Fiz. Akad. Nauk **47**, 74 (1994).
63. A. V. Kim and G. M. Fraĭman, Fiz. Plazmy **9**, 613 (1983) [Sov. J. Plasma Phys. **9**, 358 (1983)].
64. A. A. Matveyev and V. P. Silakov, Preprint No. 7 (Institute of General Physics, Russian Academy of Sciences, Moscow, 1998).
65. G. M. Batanov, S. I. Gritsinin, E. G. Korchagina, *et al.*, Comm. Plasma Phys. Control. Fusion **16**, 113 (1994).
66. G. A. Askar'yan, G. M. Batanov, S. I. Gritsinin, *et al.*, in *Microwave Plasma and Its Applications*, Ed. by Yu. A. Lebedev (Moscow Physical Society, Moscow, 1995), p. 24.
67. S. I. Gritsinin, I. A. Kossyi, M. A. Misakyan, and V. P. Silakov, Fiz. Plazmy **23**, 264 (1997) [Plasma Phys. Rep. **23**, 242 (1997)].
68. Z. G. Akhvlediani, É. M. Barkhudarov, G. V. Gelashvili, *et al.*, Fiz. Plazmy **22**, 470 (1996) [Plasma Phys. Rep. **22**, 428 (1996)].
69. V. G. Borovkin, Yu. F. Kolesnichenko, and D. V. Khmara, Prikl. Fiz., No. 4, 5 (1994).
70. A. L. Vikharev, O. A. Ivanov, and A. G. Litvak, in *Microwave Plasma and Its Applications*, Ed. by Yu. A. Lebedev (Moscow Physical Society, Moscow, 1995), p. 391.
71. G. A. Askar'yan, M. G. Korolev, E. G. Korchagina, and K. L. Yakushkin, Pis'ma Zh. Éksp. Teor. Fiz. **60**, 240 (1994) [JETP Lett. **60**, 251 (1994)].
72. R. A. Akhmedzhanov, A. L. Vikharev, A. M. Gorbachev, *et al.*, Teplofiz. Vys. Temp. **35**, 524 (1997).
73. R. A. Akhmedzhanov, A. L. Vikharev, A. M. Gorbachev, *et al.*, Zh. Tekh. Fiz. **67** (3), 9 (1997) [Tech. Phys. **42**, 260 (1997)].
74. R. A. Akhmedzhanov, A. L. Vikharev, A. M. Gorbachev, *et al.*, Phys. Lett. A **207**, 209 (1995).

Translated by N. Larionova

Plasma Physics Reports, Vol. 28, No. 3, 2002, pp. 229–242. Translated from Fizika Plazmy, Vol. 28, No. 3, 2002, pp. 257–271.
Original Russian Text Copyright © 2002 by Ivanov, Klopovskiĭ, Lopaev, Proshina, Rakhimov, Rakhimova, Rulev.

LOW-TEMPERATURE PLASMA

Kinetics of the Reactions Involving CF_2 and CF in a Pure Tetrafluoromethane Plasma: I. Production of CF_2 and CF via Electron-Impact Dissociation

V. V. Ivanov, K. S. Klopovskiĭ, D. V. Lopaev, O. V. Proshina, A. T. Rakhimov, T. V. Rakhimova, and G. B. Rulev †

Skobeltsyn Institute of Nuclear Physics, Moscow State University, Vorob’evy gory, Moscow, 119899 Russia

Received September 26, 2001

Abstract—The kinetics of the production and loss of CF_2 and CF radicals in a glow discharge in pure CF_4 is investigated by the laser-induced fluorescence method. The effective rate constants for electron-impact dissociation of CF_4 molecules along the pathways toward CF_2 and CF radicals are determined within a wide range of the reduced electric field (80–250 Td). It is shown that, along with the direct electron-impact dissociation of CF_4, the radicals are also produced via the dissociation of the C_xF_y polymer fluorocarbon particles that form in the plasma. A detailed analysis of the kinetics of the radical production and loss in a modulated discharge made it possible to evaluate the contribution of the electron-impact dissociation of CF_4 to the production of radicals and, consequently, to determine the dissociation rate constants k_{CF_2} and k_{CF}. A comparison of the obtained k_{CF_2} and k_{CF} values with the results of calculations by the Monte Carlo method and the literature data on the cross sections for electron-impact dissociation of CF_4 molecules enabled the normalization of these cross sections in the threshold region and the construction of the model cross sections for the electron-impact dissociation of CF_4 into neutral products. The calculated cross sections allow a satisfactory description of the experimental results throughout the entire range of E/N under study. A significant scatter (up to 100%) in the experimental data on k_{CF_2} and k_{CF} at low values of E/N is related to the considerable contribution of the C_xF_y polymer molecules (and, probably, $C_xF_y^+$ ions and fluorocarbon grains) to the production of CF_2 and CF radicals both in the plasma volume and on the surface of a fluorocarbon film covering the discharge tube wall. *© 2002 MAIK “Nauka/Interperiodica”.*

1. INTRODUCTION

At present, fluorocarbons are widely used in various fields of application. Thus, fluorocarbon plasma plays a key role in manufacturing semiconductor devices and attracts great attention as a means for depositing thin fluorinated amorphous carbon films, which are regarded as a new brand of insulating layers with low permittivity for future VLSI generation. Further extension of fluorocarbon plasma applications is based, first of all, on a detailed study of the elementary processes with the participation of active particles, such as fluorine atoms, CF_x (x = 1–3) radicals, C_xF_y clusters, multiatom ions, and dust grains. Hence, the study of these processes is of great importance; this is confirmed by the variety of publications on this subject, particularly in recent years. Electron-impact dissociation of the working gas is the main source of active radicals, which, in turn, are the main sources of other active neutral components of the fluorocarbon plasma, such as C_xF_y clusters and dust grains. Moreover, the study of the electron channels for radical production and the determination of the effective rate constants for each dissociation reaction are of great importance for exploring the mechanisms for radical losses (including heterogeneous reactions).

Among the fluorocarbon family, tetrafluoromethane is the most widely used and most extensively studied gas. Hence, great interest in exploring the processes in CF_4 plasma [1–14] is quite natural. At present, there are many models of different types of discharges in CF_4, which use different sets of cross sections for electron scattering by CF_4 molecules [15–25]. A choice in favor of one of them can only be made by comparing the simulation results with a wide set of experimental data. It is this approach that was used in recent studies [19–21]. However, for many elementary processes, such a thorough comparative study is impeded by the lack of reliable data. Consequently, the measured and calculated densities of various active particles in gas-discharge plasmas frequently differ from each other. This difference is not only related to the unreliable rate constants for gas-phase processes or the influence of heterogeneous processes. In [15], an RF discharge in pure CF_4 was modeled using various hypothetical plasma-kinetic

---

† Deceased.

schemes. An analysis of the sensitivity of these schemes to the variations in rate constants showed that, for CF_x radicals, the rate constant for the electron-impact dissociation of molecules of the main gas (CF_4) plays the most important role. Thus, the determination of the channels and cross sections for the impact dissociation of CF_4 molecules by plasma electrons is of key significance in modeling a discharge in CF_4. Hence, it is natural that this problem has recently received much attention.

The electron-impact dissociation of CF_4 molecules was thoroughly investigated mainly with the aim of measuring cross sections for different dissociation reactions. The available data on the cross sections for dissociative ionization, $e + CF_4 \Rightarrow 2e + CF_3^+ + F$ ($2e + CF_2^+$ + products, etc.), and for dissociation into neutral products, $e + CF_4 \Rightarrow e + CF_3 + F$ ($e + CF_2$ + products, etc.), are in fair agreement at electron energies much larger than the threshold energies for these processes. However, there is a considerable discrepancy at electron energies close to the threshold energy. Under the discharge conditions, it is the cross-section behavior near the threshold energies that governs the dissociation yield, so that only the dissociation reactions with the lowest thresholds (first of all, the dissociation of CF_4 into neutral particles—radicals and F atoms) contribute to the production of active radicals. Often (and the CF_4 case is not an exception), there is no exact data on the behavior of cross sections near the threshold energies. Moreover, for CF_4, there is a very wide (more than one order of magnitude) scatter in the data; therefore, it is impossible *a priori* to choose any cross section as a basic one. Since neutral dissociation slightly affects the transport coefficients in CF_4, this choice is also impossible to make using a self-consistent procedure of normalizing the complete set of cross sections for electron scattering in CF_4 by fitting the calculated electron transport coefficients to the experimental data. Thus, only exact and reliable measurements of the yield of the neutral dissociation of CF_4 at low electron energies are the criteria for such a choice. In particular, direct measurements of the rate constants for electron-impact dissociation in CF_4 can be one of those criteria.

In this study, we have measured the rate constants for the dissociation reactions of CF_4 along the pathways toward CF_2 and CF radicals,

$$e + CF_4 \Rightarrow e + CF_2 + \text{products},$$

$$\Rightarrow e + CF + \text{products},$$

under discharge conditions.

These measurements allowed us to thoroughly study the loss of these radicals in the CF_4 plasma, as well as investigate some aspects of the heterogeneous recombination of radicals on the surface of a fluorocarbon film covering the tube wall. A “classical” cylindrical glow discharge was used. This type of discharge was chosen for the following reasons. The low-pressure plasma of a glow discharge in a long cylindrical tube (the electric field is directed along the tube axis) is known to be one of the most suitable objects for the experimental and theoretical studying of the effects of anisotropy and nonlocality of the electron energy distribution function (EEDF), as well as for exploring various plasmochemical processes. The main feature of these discharges is that they are highly nonequilibrium and spatially nonuniform over the radius, whereas they are almost uniform along the discharge axis. This enables comprehensive measurements in the discharge positive column at strictly fixed parameters (primarily, the reduced electric field). Another feature of such discharges is related to the fact that the *pd* parameter (where *p* is the gas pressure and *d* is the tube diameter), which determines the discharge existence domain in such geometry, usually does not exceed 0.1 cm torr for electronegative gases. Thus, the energy of the positive ions incident onto the inner surface of the discharge tube (often covered with a fluorocarbon film) is fairly low—several times lower than the wall sheath potential (under the experimental conditions, the wall sheath potential in plasma is on the order of the gas ionization energy). This greatly decreases the rates of the ion-induced reactions of radical production [1, 13, 26] and allows one to almost completely exclude the influence of ions on heterogeneous processes. The degree of ionization in such discharges is very low, on the order of $\sim 10^{-6}$, which is approximately three orders of magnitude lower than the degree of dissociation. Thus, the processes involving active neutral particles are expected to be of major importance in CF_x kinetics both in the plasma bulk and on the surface.

The paper is organized as follows. In Section 2, the idea of the experiment and the experimental setup are described. Section 3 presents the experimental results and the discussion of the rate constants and partial cross sections for the electron-impact dissociation of CF_4. Conclusions are given in Section 4.

2. EXPERIMENT

The main idea of the experiment is as follows. Whatever the sources of the CF_x ($x = 1$–3) radicals that occur in the steady-state discharge, the electron-impact dissociation of CF_4 is the initial stage that determines the effective production rate of CF_x. If the loss rate of CF_x radicals is of the first kinetic order in the radical density (e.g., this is the case of surface losses), then, under steady-state conditions, we have

$$k_{CF_x}^{\text{eff}} = \frac{\alpha_{CF_x}\nu_{CF_x}}{n_e}, \tag{1}$$

where $k^{\mathrm{eff}}_{\mathrm{CF}_x}$ is the effective rate constant for CF_4 dissociation via a CF_x channel. Here, $k^{\mathrm{eff}}_{\mathrm{CF}_x}$ is regarded as the total sum over all the channels of the electron-impact dissociation of CF_4. It should be noted that, since the radical dissociation energy is lower than the dissociation energy of CF_4, the electron-impact dissociation of the radicals themselves can, in principle, affect the production of radicals with a lower number of atoms, e.g., $e + \mathrm{CF}_{x+1} \longrightarrow e + \mathrm{CF}_x + \mathrm{F}$. In [27], it was shown that, for most discharges (including a glow discharge), this process can be ignored. In Eq. (1), the parameter $\alpha_{\mathrm{CF}_x} = [\mathrm{CF}_x]/[\mathrm{CF}_4]$ is the relative concentration of the CF_x radicals (where $[CF_x]$ and $[CF_4]$ are the steady-state densities of the radicals and CF_4 molecules), ν_{CF_x} is the effective loss frequency of CF_x radicals, and n_e is the electron density. If all the quantities on the right-hand side of Eq. (1) are experimentally determined, then the effective rate constants for the dissociation of CF_4 via different CF_x channels can be found as functions of the reduced electric field. A comparative analysis of these data allows one to evaluate the contribution of direct electron impacts to the dissociation of CF_4 and, thus, determine the rate constants for electron-impact dissociation via each CF_x channel. The latter, in turn, enables one to verify the absolute partial cross sections for corresponding dissociation reactions near the threshold electron energy.

In our experiments, all the quantities on the right-hand side of Eq. (1) were determined in the axial region of the discharge. It is necessary to note that, in this case, the possible influence of the EEDF nonlocality on the experimental results should be minimum, which is important for an adequate analysis of the experimental data.

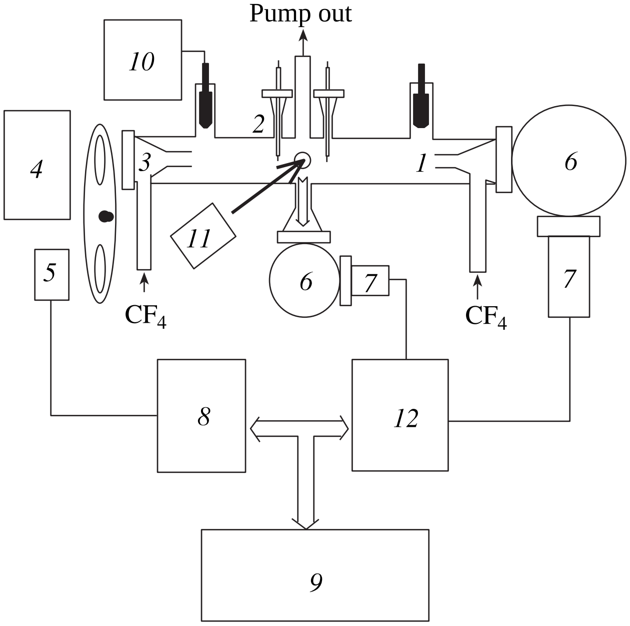

Fig. 1. Schematic of the experimental facility: (*1*) discharge tube, (*2*) movable probes, (*3*) Teflon inserts protecting MgF_2 windows against pollution, (*4*) deuterium lamp, (*5*) chopper, (*6*) VUV and UV monochromators, (*7*) PMT FEU-142, (*8*) lock-in amplifier, (*9*) PC, (*10*) dc and pulsed high-voltage power supply, (*11*) KrF (ArF) excimer laser, and (*12*) gate integrator.

A schematic of the experiment is shown in Fig. 1. A dc glow discharge in pure CF_4 was ignited in a Pyrex tube with an inner diameter of 18 mm and interelectrode distance of 500 mm at pressures of 0.16–2.2 torr and currents of 3–40 mA. The gas flow rate did not exceed 1 m/s. The reduced electric field was determined from the measurements of the electric field with the help of two movable probes (the probe diameter is ~100 μm) and the gas temperature, using the ideal gas equation of state. The probes were at a high constant negative (with respect to the plasma) potential, except for a few seconds during which the electric field was measured. The resulting intense heating of the probe surface under ion bombardment prevented the heavy pollution of the probe surface. The temperature at the discharge axis and the temperature of the tube wall were measured using microthermocouples with diameters of ~0.3–0.4 mm. A thin fluorocarbon film covering the thermocouple surface under the discharge conditions only slightly affected the measurement results. Before the measurements, a high-current-density discharge ran in the flow of pure CF_4 for a fairly long time period (several days) until the plasma parameters became stable. Under these conditions, almost no striation occurred in the discharge. Furthermore, a fluorocarbon film consisting of submicron fluorocarbon particles was deposited onto the inner surface of the discharge tube (see Part II of this paper, which is devoted to plasmochemical processes, including heterogeneous reactions, with the participation of CF_x radicals). Figure 2 shows the reduced electric field at the discharge axis as a function of the rN parameter, where r is the tube radius and N is the gas density at the tube axis. The electron density n_e was derived from the discharge current:

$$n_e = J_d/eV_{dr}\pi r^2,$$

where J_d is the discharge current, e is the electron charge, V_{dr} is the drift velocity corresponding to the measured reduced electric field E/N, and E is the electric field. Note that the difference between the n_e value derived in this way and n_e calculated using the exact nonlocal model of the discharge [14] does not exceed 15%.

The α_{CF_2} and α_{CF} values were determined based on the measured densities of CF_2 and CF, respectively, and the density $[CF_4]$ was obtained from the ideal gas equation of state: $[\mathrm{CF}_4] = P_{\mathrm{CF}_4}/kT_g$. CF_2 and CF radicals

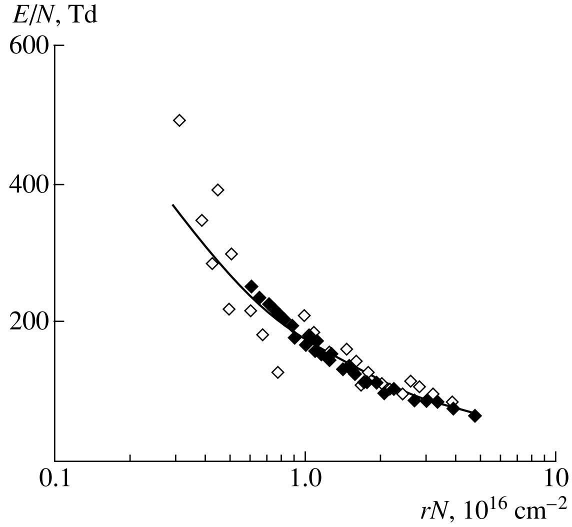

Fig. 2. Reduced electric field E/N at the discharge axis vs. rN parameter (here, r is the tube radius and N is the gas density at the tube axis). Closed symbols show our experimental data, open symbols show the experimental data from [14], and the curve shows the approximation of the experimental data.

were detected using the laser-induced fluorescence (LIF) method. CF_2 radicals were excited by a KrF laser at the $^1A_1(000) \longrightarrow {}^1B_1(060)$ transition ($\lambda = 248.5$ nm). Fluorescence from the CF_2 radicals was recorded at a wavelength of 257 nm from the $^1A_1(020) \longrightarrow {}^1B_1(060)$ transition. The absolute calibration of the LIF signal (corresponding to the absolute CF_2 density) was carried out by measuring the differential absorption in the $^1A_1(000) \longrightarrow {}^1B_1(060)$ and $^1A_1(000) \longrightarrow {}^1B_1(030)$ transitions at 248.5 ± 0.2 and 258.5 ± 0.2 nm, respectively [28], under low discharge currents, when the absorption and scattering of UV radiation by fluorocarbon dust grains produced in the discharge volume can be neglected. The accuracy of this calibration is about ±20%. The CF radicals were excited by an ArF laser ($\lambda = 193.4$ nm) at the $B^2\Delta$, $v = 2 \longrightarrow X^2\Pi$, $v = 0$ band. Fluorescence from CF radicals was recorded at the $B^2\Delta$, $v = 2 \longrightarrow X^2\Pi$, $v = 1$ band at $\lambda = 200$ nm [29]. The absolute calibration of the CF laser-induced fluorescence was carried out with allowance for the known oscillator strength of the $B^2\Delta$, $v = 2 \longrightarrow X^2\Pi$, $v = 0$ transition; the overlap function of the ArF laser radiation with an R-branch of this band (assuming the distribution of CF radicals over the rotational states to be Boltzmann with the gas temperature); and the collecting optics geometrical factor, which was assumed to be equal to that for the CF_2 LIF measurements. Note that this calibration is less precise than the calibration of the CF_2 LIF signal: its accuracy is estimated to be about ±60–70%. The LIF spectra from the CF_2 and CF radicals are shown in Figs. 3a and 3b.

To determine ν_{CF_x} ($x = 1, 2$), we investigated the dynamics of the CF_x density by the LIF method after the discharge was switched on and off. The discharge was modulated at a frequency of 20 Hz; the time during which the discharge was switched off was less than 6 ms. The modulation ensured a better reproduction of the plasma parameters from pulse to pulse and approximately constant temperatures of the gas and, even more important, the tube wall. The latter circumstance allowed us, as a first approximation, to assume that, during the discharge and discharge afterglow, the CF_2 and CF radicals decay in similar ways, because it was found experimentally that the corresponding loss rates depend on the wall temperature. Figure 4 shows, as an example, the dynamics of the CF_2 density decay at pressures of 0.75 and 1.5 torr and different discharge currents after the discharge is switched on and off. It is seen that, at higher pressure, the CF_2 radical decay cannot be described by a single exponential function. The higher the discharge current density, the larger the deviation from the single-exponential decay. The same is true as the pressure increases. These facts indicate that, under the given conditions, the CF_2 losses cannot be attributed solely to the intense escape on the wall with a certain constant loss probability. As was noted in [30], the convexity of the CF_2 density decay curve points to the “effective” increase in the CF_2 loss probability with time, and this increase cannot be explained using the dynamic adsorption–desorption model. Furthermore, the decay curve convexity unambiguously points to the presence of an extra source of these radicals (in the first approximation, the source intensity is proportional to the radical density) in the discharge afterglow. Otherwise, this dependence would be concave, whatever CF_2 loss channels are taken into account. Since the recombination of the CF_4 plasma after the discharge is switched off is rather fast [31, 32], the source of CF_2 and CF radicals in the discharge afterglow is related to the reactions involving neutral particles. Because of the low pressures used in the experiment, the rates of the three-body recombination reactions, such as $F + CF_x + M \longrightarrow CF_{x+1} + M$, are insufficiently high to significantly affect the radical density decay after the discharge is switched. Hence, the production of CF_x in the two-body reactions with the participation of C_xF_y ($x = 1, 2, 3, \ldots$, and …; $y = 1, 2, 3, \ldots$) neutral fluorocarbon particles [1, 9, 30, 33], whose rate constants are high enough, is the most probable. Unfortunately, because of the much lower sensitivity of our recording system to CF radicals, the signal dynamic range was too small to say with a fair degree of confidence that the CF density decay was nonexponential. The kinetics of CF_2 and CF radicals, including the production and loss mechanisms, is considered in detail in Part II of this paper.

Taking into account that, immediately after the discharge is switched off, when the deviation of the CF_x decay curves from exponential is low, the effective loss

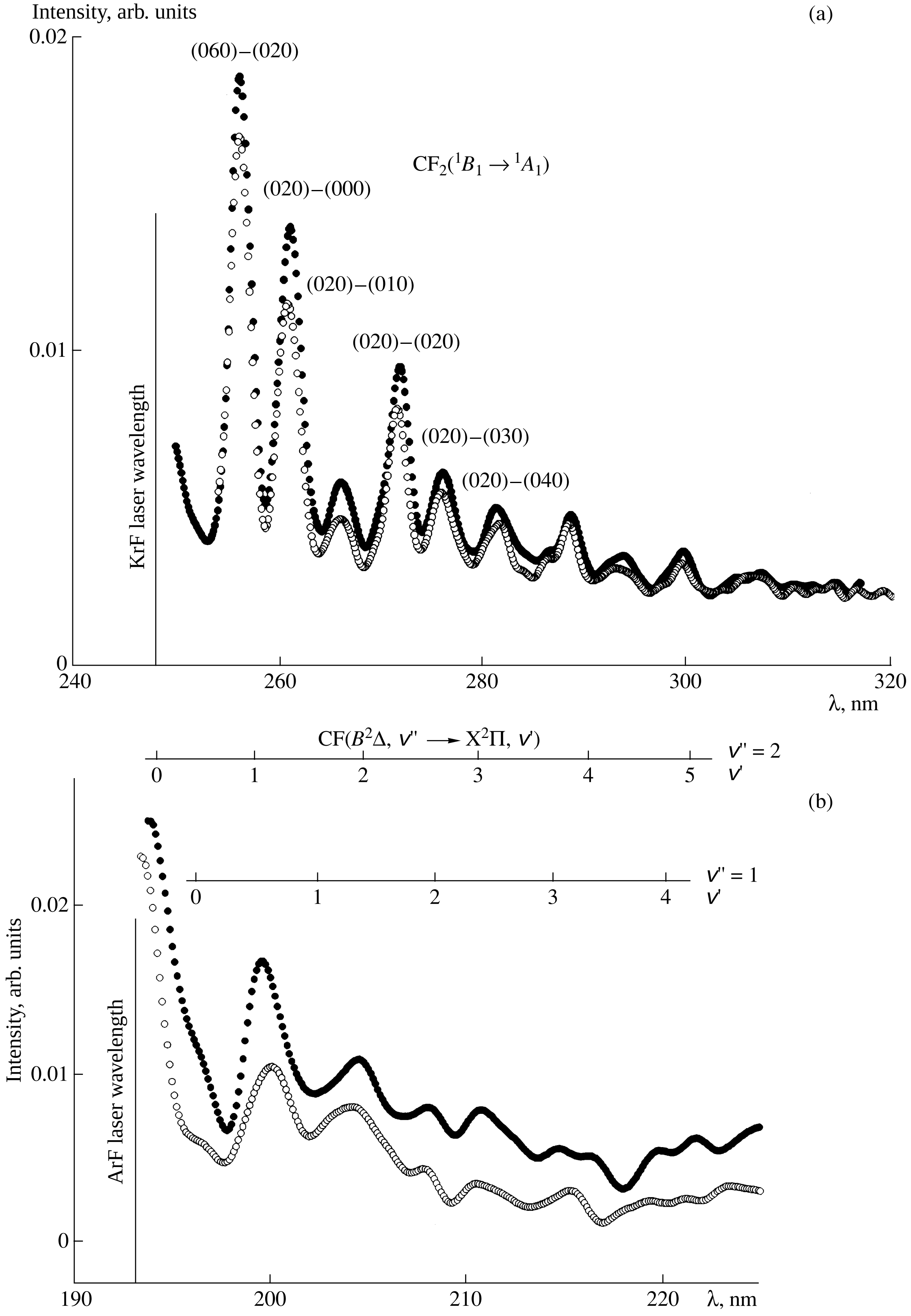

Fig. 3. LIF spectrum from (a) CF$_2$ radicals 0.4 ms after switching off the discharge and (b) CF radicals 0.3 ms after switching off the discharge for the discharge currents $J_d = 15$ (open circles) and 30 (closed circles) mA at $P_{CF_4} = 1$ torr.

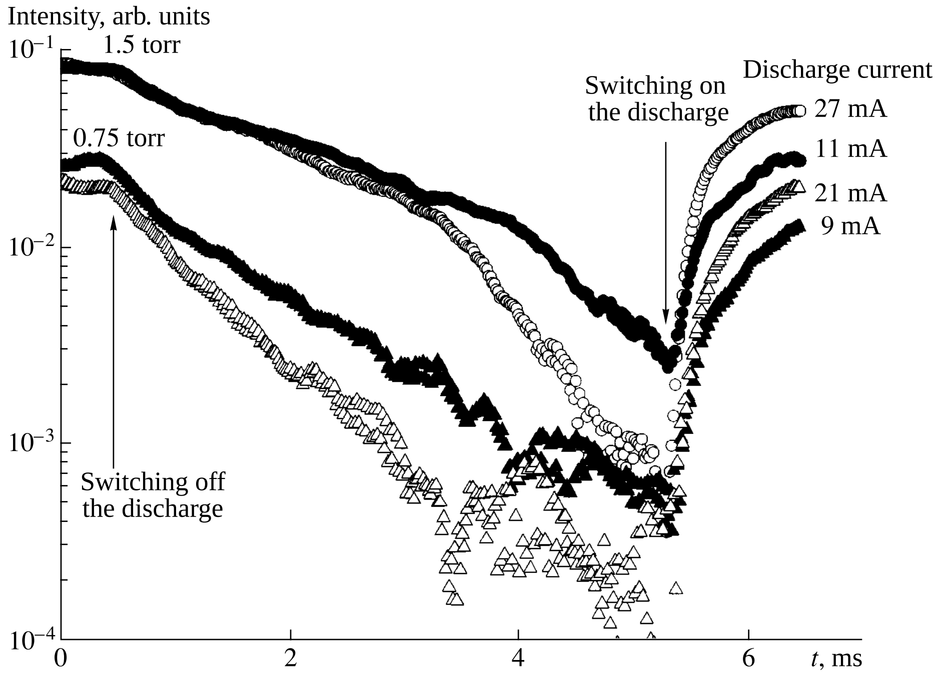

Fig. 4. Kinetics of the CF_2 density growth and decay for pressures of 0.75 and 1.5 torr. The instants at which the discharge is switched on/off are marked with arrows. Numerals by the curves show the corresponding discharge current densities.

frequencies ν_{CF_x} can be fairly accurately estimated using the exponential approximation of the initial stage of the decay. If the main channel of the CF_x production is the dissociation of CF_4 molecules in plasma, then, after switching on the discharge, the CF_x density is restored to its steady-state value during a time close to the inverse radical loss frequency ν_{CF_x}. However, as is seen in Fig. 4, at higher pressures, the effective frequency of the CF_2 density restoration is much higher than the loss frequency. Furthermore, the restoration dynamics cannot be described as a single-exponential curve. Such behavior of the CF_2 density was also observed in a low-pressure RF discharge in CF_2 [11]. All this indicates that, besides the dissociation CF_4 of molecules, an additional radical source appears after the discharge is switched on, the power of this source being, in general, dependent on time. The extra production of the radicals in a fluorocarbon plasma, which was not related to the direct dissociation of the working gas, was observed in various discharges [1, 2, 9, 11, 30, 33–41]. It should be noted that the power of this extra source strongly depends on the pressure and the electron density and, moreover, correlates with the power of the radical source in the discharge afterglow. Thus, it is natural to assume that the CF_x radical source occurring in the discharge is also related to the C_xF_y fluorocarbon particles. In [1], it was shown that the most probable structure of these particles is a polymer structure such as $\alpha[(CF_2)_n]$ ($n = 1, 2\ldots$), where α stands for a certain "core" C_xF_y ($x = 1$–3, $y = 5$–2), in which a fraction of the fluorine atoms may be substituted with hydrogen atoms.

This conclusion was confirmed by the investigations of fluorocarbon polymerization by the method of dissociative electron attachment mass spectroscopy (EAMS) [12, 13], which enabled one to avoid the fragmentation of the heavy multiatom particles in the ionization chamber of an ordinary mass spectrometer. It was shown that the C_xF_y polymer molecules (mainly C_nF_{2n-k}) form in an RF discharge in pure CF_4. Experimentally, the n values up to 10 and the k values from 0 to +4 were observed. It was supposed in many studies (see, e.g., [1, 2, 26, 33, 35–37]) that an extra source of CF_2 and CF radicals could be related to the bombardment of the surface of the fluorocarbon film on the discharge chamber wall by $C_xF_y^+$ ($x, y = 1, 2, \ldots$) positive ions. However, it should be noted that, in those experiments, the incident positive ions possessed a rather high energy ranging from several units to several tens of electronvolts. The latter is a consequence of the fact that, in systems for plasmochemical etching and deposition, a capacitive RF discharge is commonly used; hence, the main surface at which fluorocarbon radicals are lost is the electrode surface [1, 2, 26, 33, 37]. The discharge chamber itself is often used as a grounded electrode. The energy acquired by the fluorocarbon ions in RF sheaths is high enough to stimulate ion–molecular reactions in the sheaths themselves, which can also affect the particle composition in the discharge volume [26, 40]. As for other modern plasma systems (the sources of inductively coupled plasmas and helicon and electron-cyclotron plasmas [36–41]), substantial electric fields caused by plasma transport can arise away from an RF or a microwave antenna (in a separate measurement chamber) at low pressures. Hence, the energy of the positive ions arriving at the chamber wall is substantially higher than the thermal energy. The decomposition of the fluorocarbon film on a substrate or the chamber wall during ion bombardment can be provoked by both ion-stimulated reactions and sputtering processes. This is confirmed by the measurements [35] in which the production of CF_x (x = 1–3) radicals at the fluorocarbon film surface occurred after substituting CF_4 with pure Ar.

We also performed a series of experiments with pure argon instead of tetrafluoromethane with the aim of testing the possible channels for the CF_x production during the ion bombardment of the fluorocarbon film. Even at very high current densities, when the flux of Ar^+ ions incident onto the tube surface was several times the ion flux in CF_4, we recorded no LIF signals from either CF_2 or CF. This fact proves that, under our experimental conditions, the ion energy is rather low, which allows us, as a first approximation, to ignore the production of CF_x radicals due to the destruction (the sputtering and desorption of the chemically adsorbed CF_x radicals) of the fluorocarbon film during ion bombardment. Thus, one can assume that, under our experimental conditions, the processes with the participation of C_xF_y neutral particles are mainly responsible for the extra source of CF_x radicals. It will be shown in Part II that it is only the electron-impact dissociation of C_xF_y neutral particles that allows one to explain the extra production of CF_2 and CF observed after the discharge is switched on. Note that this process can also be responsible for CF_x radical production during the sputtering of the fluorocarbon film by Ar^+ ions. The dissociation of polymer fluorocarbon particles in collisions with plasma electrons results in the production of both neutrals and ions (negative in the case of electron dissociative attachment and positive in the case of dissociative ionization). It should be noted that the thresholds for these processes are much lower for C_xF_y radicals than for CF_4 molecules. This is particularly true for dissociative attachment. For C_xF_y radicals containing more than two carbon atoms, this process is practically nonthreshold (more precisely, its threshold energy is much lower than the electron temperature in the discharge, which amounts to ~3–5 eV [14]). The formation of the charged and neutral products of C_xF_y dissociation after the discharge is switched on substantially affects the loss of CF_x radicals. Indeed, it can be seen in Fig. 4 that, after the discharge is switched on, the loss rate of CF_2 radicals increases (the characteristic time of the radical density growth is determined by the processes of their loss, proceeding at a certain characteristic frequency). Furthermore, at low discharge currents, even a decrease in the CF_2 density was sometimes observed, which probably occurred when the power of the radical extra source substantially decreased because of the rapid dissociation of C_xF_y. Based on the above considerations, the equation for the steady-state CF_x (x = 1, 2) radical density in the discharge can be written as

$$\begin{aligned}\frac{d[\mathrm{CF}_x]}{dt} &\equiv 0 \approx k_{\mathrm{CF}_x} n_e[\mathrm{CF}_4] + S_e^{\mathrm{C}_x\mathrm{F}_y} \\ &+ S_N^{\mathrm{C}_x\mathrm{F}_y} - (\nu_w^{\mathrm{CF}_x} + \nu_p^{\mathrm{CF}_x})[\mathrm{CF}_x]_0,\end{aligned} \tag{2}$$

where k_{CF_x} is the rate constant for direct electron-impact dissociation along the pathways toward CF_x radicals; $[CF_x]_0$ is the steady-state density of CF_x radicals in the discharge; $\nu_w^{\mathrm{CF}_x}$ is the CF_x loss frequency in the afterglow (under our experimental conditions, the radicals are mainly lost on the tube wall); $\nu_p^{\mathrm{CF}_x}$ is the CF_x loss frequency in the plasma volume; and $S_N^{\mathrm{C}_x\mathrm{F}_y}$ and $S_e^{\mathrm{C}_x\mathrm{F}_y}$ are the total rates of CF_x radical production in the discharge with the participation of neutral particles and electrons, respectively:

$$\alpha(\mathrm{CF}_2)_n + \mathrm{F},\ \mathrm{C}_x\mathrm{F}_y \longleftrightarrow \mathrm{CF}_x + \text{products},$$

$$\alpha(\mathrm{CF}_2)_n + e \longleftrightarrow \mathrm{CF}_x + \text{products},$$

$$S_N^{\mathrm{C}_x\mathrm{F}_y} = \sum_N N \sum_{x,\,y>2} k_N^{\mathrm{C}_x\mathrm{F}_y}[\mathrm{C}_x\mathrm{F}_y],$$

$$S_e^{\mathrm{C}_x\mathrm{F}_y} = [n_e] \sum_{x,\,y>2} k_e^{\mathrm{C}_x\mathrm{F}_y}[\mathrm{C}_x\mathrm{F}_y].$$

After the discharge is switched off, only two terms are left on the right-hand side of Eq. (2) and the equation for the CF_x density takes the form

$$\frac{d[\mathrm{CF}_x]}{dt} = S_N^{\mathrm{C}_x\mathrm{F}_y}(t) - \nu_w^{\mathrm{CF}_x}[\mathrm{CF}_x].$$

At the instant t_{off}, when the discharge is switched off, we have $\frac{d[\mathrm{CF}_x]}{dt}(t_{\mathrm{off}}) = S_N^{\mathrm{C}_x\mathrm{F}_y}(t_{\mathrm{off}}) - \nu_w^{\mathrm{CF}_x}[\mathrm{CF}_x]_0$. Hence, having determined the initial derivative $\frac{d[\mathrm{CF}_x]}{dt}(t_{\mathrm{off}})$ from the experimental kinetic decay curves of the CF_x density, we deduce that

$$k_{\mathrm{CF}_x} n_e[\mathrm{CF}_4] + (S_e^{\mathrm{C}_x\mathrm{F}_y} - \nu_p^{\mathrm{CF}_x}[\mathrm{CF}_x]_0) = -\frac{d[\mathrm{CF}_x]}{dt}(t_{\mathrm{off}}). \tag{3}$$

At pressures less than ~0.75 torr, the kinetic curves for both the CF_x density growth and decay can be fairly well approximated by the same exponent with the frequency $\nu_{\mathrm{eff}}^{\mathrm{CF}_x}$; i.e., there was no increase in the CF_2 radical loss rate after the discharge was switched on or, in other words, $\nu_p^{\mathrm{CF}_x} \longrightarrow 0$. Note that, in this case, the characteristic loss frequency $\nu_{\mathrm{eff}}^{\mathrm{CF}_x}$ depends only slightly on the pressure and the discharge current. Both the extra source and the elevated loss rate of CF_2 radicals in the discharge are governed by the processes involving $\mathrm{C}_x\mathrm{F}_y$ fluorocarbon particles. The formation mechanisms for these particles are described in detail in Part II. Here, we only note that the $\mathrm{C}_x\mathrm{F}_y$ density strongly depends on the pressure and the discharge current because the primary processes of $\mathrm{C}_x\mathrm{F}_y$ production are the processes of oligomerization, such as

$$\mathrm{CF}_3 + \mathrm{CF}_3 \longrightarrow \mathrm{C}_2\mathrm{F}_6,$$

$$\mathrm{CF}_2 + \mathrm{CF}_3 \longrightarrow \mathrm{C}_2\mathrm{F}_5,$$

$$\mathrm{CF}_2 + \mathrm{CF}_2 \longrightarrow \mathrm{C}_2\mathrm{F}_4.$$

Therefore, both the $S_e^{\mathrm{C}_x\mathrm{F}_y}$ source power and the radical loss frequency in the discharge must also depend strongly on the discharge parameters. Since it was not the case at pressures of <0.75 torr (the CF_2 loss frequency changed only slightly after the discharge was switched on and off), we can suppose that, at low pressures, the extra production of radicals both in the discharge and the discharge afterglow is small as compared to direct electron-impact dissociation. Then, the rate constant for the electron-impact dissociation of CF_4 molecule via the CF_x channel can be readily determined from Eq. (3):

$$k_{\mathrm{CF}_x} = -\frac{\dfrac{d[\mathrm{CF}_x]}{dt}(t_{\mathrm{off}})}{n_e[\mathrm{CF}_4]}. \tag{4}$$

We can represent $\dfrac{d[\mathrm{CF}_x]}{dt}(t_{\mathrm{off}})$ in the form $\dfrac{d[\mathrm{CF}_x]}{dt}(t_{\mathrm{off}}) = -\nu_{\mathrm{eff}}^{\mathrm{CF}_x}[\mathrm{CF}_x]_0$, where $\nu_{\mathrm{eff}}^{\mathrm{CF}_x}$ is the effective CF_x loss frequency with allowance for the radical extra source $S_N^{\mathrm{C}_x\mathrm{F}_y}$ ($\nu_{\mathrm{eff}}^{\mathrm{CF}_x} = \nu_0^{\mathrm{CF}_x} - \nu_N^{\mathrm{CF}_x}$, where $\nu_N^{\mathrm{CF}_x} = S_N^{\mathrm{C}_x\mathrm{F}_y}(t_{\mathrm{off}})/[\mathrm{CF}_x]_0$), which exactly corresponds to Eq. (1). In this case, as will be shown in Part II, we have $\nu_{\mathrm{eff}}^{\mathrm{CF}_x} \approx \nu_w^{\mathrm{CF}_x}$, where $\nu_w^{\mathrm{CF}_x}$ is the frequency of the heterogeneous loss of radicals on the tube wall.

If it is impossible to ignore the radical extra source, $S_e^{\mathrm{C}_x\mathrm{F}_y} - \nu_p^{\mathrm{CF}_x}[\mathrm{CF}_x]_0$, then, in order to evaluate the k_{CF_x} rate constant from Eq. (4), it is necessary to determine the contribution from every term on the left-hand side of Eq. (3) to $\mathrm{CF}_x - [\mathrm{CF}_x]_0$ (the steady-state density of CF_2). Based on the experimental data, we can only estimate the minimum power of the CF_x extra source. This is easy to do if we use a two-exponential approximation

$$[\mathrm{CF}_x](t) = [\mathrm{CF}_x]_0\left(1 - [\mathrm{CF}_x]_0^S e^{-\nu_p^{\mathrm{C}_x\mathrm{F}_y} t} - [\mathrm{CF}_x]_0^{el} e^{-\nu_{\mathrm{eff}}^{\mathrm{CF}_x} t}\right) \tag{5}$$

to fit the kinetic curves for the CF_x density growth. In formula (5), $[\mathrm{CF}_x]_0 = [\mathrm{CF}_x]_0^S + [\mathrm{CF}_x]_0^{el}$, where $[\mathrm{CF}_x]_0^S$ is the steady-state CF_x radical density governed by the dissociation of $\mathrm{C}_x\mathrm{F}_y$ molecules and $[\mathrm{CF}_x]_0^{el}$ is the steady-state CF_x radical density governed by the direct electron-impact dissociation of CF_4. The fitting parameters are $[\mathrm{CF}_x]_0^S$, $[\mathrm{CF}_x]_0^{el}$, and $\nu_p^{\mathrm{C}_x\mathrm{F}_y}$. This representation is equivalent to Eq. (3) written in the form

$$\nu_{\mathrm{eff}}^{\mathrm{CF}_x}[\mathrm{CF}_x]_0^{el} + \nu_p^{\mathrm{C}_x\mathrm{F}_y}[\mathrm{CF}_x]_0^S = \nu_{\mathrm{eff}}^{\mathrm{CF}_x}[\mathrm{CF}_x]_0,$$

hence, we obtain an estimate for the maximum rate constant for the electron-impact dissociation of CF_4:

$$k_{\mathrm{CF}_x} = \frac{\nu_{\mathrm{eff}}^{\mathrm{CF}_x}[\mathrm{CF}_x]_0^{el}}{n_e[\mathrm{CF}_4]}. \tag{6}$$

Using formula (6), we evaluated the k_{CF_2} rate constant at low reduced electric fields, i.e., at high pressures, when the polymerization of fluorocarbons in the plasma becomes of crucial importance. Obviously, in this case, the accuracy of determining k_{CF_x} depends on the contribution from the electron-impact dissociation of CF_4 to the CF_x production. Since this contribution decreases significantly with increasing pressure or current, the error in determining k_{CF_2} increases substantially (up to ~100%). Because of the low signal-to-noise ratio in the case of CF radicals under discharge conditions, approximation (5) can hardly be applied, which made it practically impossible to determine the k_{CF} electron-impact dissociation rate constant at $E/N <$ 130 Td (1 Td = 10^{-17} V cm^2).

3. RATE CONSTANTS AND PARTIAL CROSS SECTIONS FOR THE ELECTRON-IMPACT DISSOCIATION OF CF_4 WITH THE PRODUCTION OF CF_2 AND CF

The rate constants for the dissociation of CF_4 along the pathways toward CF_2 and CF as functions of the reduced electric field are shown in Fig. 5. The data obtained with formula (4) (they can be called the effective rate constants for E/N production) are marked with open symbols. The data corrected according to formula (6) (they can be treated as the rate constants for the electron-impact dissociation of CF_4) are marked with closed symbols. Under discharge conditions, only the dissociation reactions with the lowest thresholds can really contribute to the CF_x production with the rates actually determined by the initial slopes of the corresponding partial cross sections. The reactions of CF_4 dissociation into neutral products have the lowest thresholds; hence, we may suppose that the processes

$$\left.\begin{aligned} CF_4 + e &\longrightarrow CF_2 + F_2 + e \\ &\longrightarrow CF_2 + 2F + e \end{aligned}\right\} \text{(a threshold of ~15 eV)}, \quad (7a), (7b)$$

$$\left.\begin{aligned} CF_4 + e &\longrightarrow CF + F_2 + F + e \\ &\longrightarrow CF + 3F + e \end{aligned}\right\} \text{(a threshold ~20 eV)}, \quad (8a), (8b)$$

are the main channels for CF_2 and CF production. To verify this, we calculated k_{CF_2} and k_{CF} using the available data on the cross sections for the neutral dissociation of CF_4 [42–48]. The dissociation rate constants are determined by the expressions

$$k_{CF} = \left(\frac{2}{m_e}\right)^{1/2} \int_0^\infty \varepsilon \sigma_{diss}^{CF}(\varepsilon) f(\varepsilon) d\varepsilon, \qquad (9)$$

$$k_{CF_2} = \left(\frac{2}{m_e}\right)^{1/2} \int_0^\infty \varepsilon \sigma_{diss}^{CF_2}(\varepsilon) f(\varepsilon) d\varepsilon, \qquad (10)$$

where $\sigma_{diss}^{CF_2}(\varepsilon)$ and $\sigma_{diss}^{CF}(\varepsilon)$ are the partial cross sections for the CF_4 dissociation into CF_2 and CF radicals, respectively; $f(\varepsilon)$ is the EEDF derived based on the solution to the Boltzmann equation and the normalization condition $\int_0^\infty \sqrt{\varepsilon} f(\varepsilon) d\varepsilon = 1$; and e and m_e are the electron charge and mass. It is seen from formulas (9) and (10) that the rate constant for the dissociation via the CF_x channel is governed by both the dependence of the cross section on the electron energy and the EEDF itself. The determination of the EEDF requires a complete self-consistent set of cross sections for electron scattering by the CF_4 molecule. Several such sets are available [17–25]. The most comprehensive cross-section set is presented in [19] (see also [20, 21]). It was developed by assembling and analyzing the latest experimental and theoretical data on the cross sections for the interaction of electrons with CF_4 molecules. This set is self-consistent in the sense that the sum of all cross sections agrees with the independent measurements of the total scattering cross section. In [20], that cross-section set was used to calculate the drift velocity and the diffusion, ionization, and attachment coefficients in CF_4 by solving the Boltzmann equation in the two-term approximation. The calculation results are in good agreement with all the available experimental data. Thus, the cross-section set from [19] is indeed self-consistent and enables one to accurately describe the experimental data on the transport and kinetic coefficients. As was noted in [20], a minor discrepancy with the experimental data is related to the impossibility of taking into account the scattering anisotropy. Such accounting requires detailed data on the differential cross sections for both elastic and inelastic scattering. However, the data are still lacking; for this reason, in this study, the cross-section set from [19, 20] was used.

The EEDF $f(\varepsilon)$ was calculated by the Monte Carlo method. We used the Monte Carlo method because, at high E/N values, the EEDF anisotropy becomes significant and the use of the two-term approximation is no longer justified [14]. As was mentioned above, to accurately take into account the angular dependence of the electron scattering at CF_4 molecule requires the full set of differential cross sections. In [49], based on a thorough analysis of the available data, model differential cross sections for the elastic scattering and vibrational

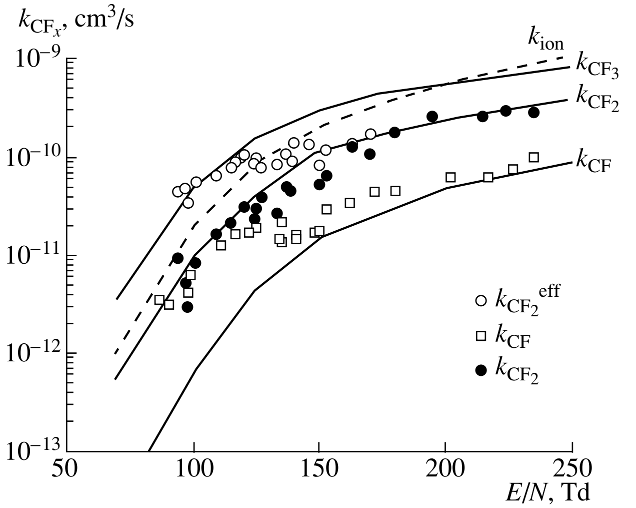

Fig. 5. Rate constants for the dissociation of CF_4 along the pathways toward CF_3, CF_2, and CF as functions of the reduced electric field E/N. Open symbols show the effective rate constants for CF_4 dissociation obtained from formula (4); closed symbols show the rate constants for the electron-impact dissociation of CF_4 obtained from formulas (5) and (6); solid lines show the rate constants for the electron-impact dissociation of CF_4 along the pathways toward CF_3, CF_2, and CF calculated with the help of model cross sections; and the dashed line shows the rate constant for the electron-impact ionization of CF_4.

excitation were developed. A comparison of the transport coefficients calculated by the Monte Carlo method with the experimental data showed that the allowance for the anisotropy of the electron scattering by CF_4 molecules is important because it enables the exact reproduction of the experimental data in a wide range of the reduced field ($E/N = 1–200$ Td). Taking into account both this and the fact that the database on the differential cross sections has not yet been completed, only a rough account of the electron scattering anisotropy was made. The anisotropy of elastic electron scattering was taken into account by using the transport cross section rather than the cross section for elastic scattering. For all of the inelastic processes, one-half of the electron bulk was assumed to be scattered isotropically, whereas the other half was assumed to conserve the motion direction. The one-half factor was chosen in order to provide the best matching between the calculated and measured drift velocities. It should be noted that varying the assumed anisotropy between the two limiting cases of total isotropy and the scattering of all the electrons in the forward direction (i.e., at a zero scattering angle) substantially (by ~30%) changes the drift velocity, which indirectly indicates a considerable anisotropy of the EEDF at high E/N values. To verify our calculations of the EEDF, we compared the calculated drift velocity and the ionization and attachment coefficients with the experimental data from [19]. As in [20, 22], our calculations are in fairly good agreement with the experimental data on the transport and kinetic coefficients in a wide range of the reduced electric field.

The cross section for the dissociation of CF_4 molecule presented in [19, 20] is an "effective" total cross section over all of the possible dissociation channels. As was noted in [20], at present, this is related to the absence of reliable experimental data on the near-threshold partial cross sections for neutral dissociation. It seems that the only experimental attempt to measure the cross sections for neutral dissociation via different channels was made in [44, 45]. However, in the threshold region, the total cross section obtained in those studies is more than one order of magnitude lower than the rest of the literature data; this discrepancy was noticed in many papers (see [15, 19–21, 46–48]). Moreover, computations of discharge kinetics with the use of these partial cross sections result in significantly lower CF_x radical densities in the discharge as compared to the measured ones. To settle the problem, let us briefly consider the literature data on the electron-impact dissociation of CF_4 molecules [42–48].

In [42], the total cross section for the electron-impact dissociation of CF_4 was measured using an original method for monitoring the decay (decomposition) of CF_4 molecules under the action of an electron beam in a specially designed chamber, whose wall and electrodes absorbed both the ion and neutral radical products of CF_4 dissociation without their noticeable return to the gas phase. It was carefully checked and proved that, with a high degree of accuracy, the rate of the pressure change in the reactor was proportional to the rate of the CF_4 density change. Special efforts were undertaken to prevent the contribution from the dissociation of CF_4 molecules at the hot filament of an electron gun. All of the issues concerning both the apparatus and the method for cross-section measurements were studied in detail; moreover, a special test was carried out to verify the validity of the method. Hence, the results obtained are completely reliable. This is very important because the concerned method enables direct measurements of the absolute cross section for molecular dissociation without recourse to the calibration procedure, which is often rather complicated and, therefore, inexact. We have systematically analyzed the obtained results on the dissociation cross section of CF_4 based on the known data on the photon absorption spectra and electron energy loss spectra, as well as the results of theoretical studies. This analysis led us to an important conclusion about the decisive contribution of dissociative ionization to the electron-impact dissociation of CF_4 (more than 70% at electron energies of ~40 eV, the CF_4 ionization energy being ~16.5 eV). However, in the near-threshold region (the dissociation threshold for CF_4 is ~12.5 eV), only the dissociation of CF_4 into neutral products occurs. Beginning with an energy of ~14.5 eV, a new channel for the dissociation of CF_4 appears, which changes the slope of the dependence of the total dissociation cross section on the electron energy. This fact agrees with the experimental evidence on both the photon absorption and the electron energy loss spectra.

In [43], the cross sections for the dissociative electron-impact ionization of CF_4 molecules, including the dissociation channels yielding ion pairs, were measured with the help of time-of-flight mass spectrometry and a multichannel coincidence scheme. Since the total dissociation cross section is the sum of the cross sections for the reactions with the production of the ion and neutral fragments, the cross section for neutral dissociation can be derived by subtracting the cross section for dissociative ionization [43] from the total dissociation cross section [42]. A resultant cross section is shown in Fig. 6 as $\sigma_{\text{tot}}^{1}(\varepsilon)$. Later, in [50, 51], the improvement of the recording technique resulted in an increase in the ionization cross sections measured in [43] by ~20–30%. As was noted in [19], at electron energies higher than 40 eV, the corrected total ionization cross section of CF_4 [51] becomes almost the same as the total dissociation cross section obtained in [42]. Hence, the above-described indirect determination of the cross section for dissociation via neutral channels is incorrect at $\varepsilon > 40$ eV. However, in the energy range up to 30 eV, the total dissociation cross section from [42] significantly exceeds the ionization cross section from [51], so this indirect determination is quite reasonable. The cross section $\sigma_{d,n}$ determined by this method in

[51] is also shown in Fig. 6. It should be noted that this $\sigma_{d,\,n}$ value disagrees with the directly measured partial cross sections for the dissociation of CF_4 into neutral fragments [44, 45].

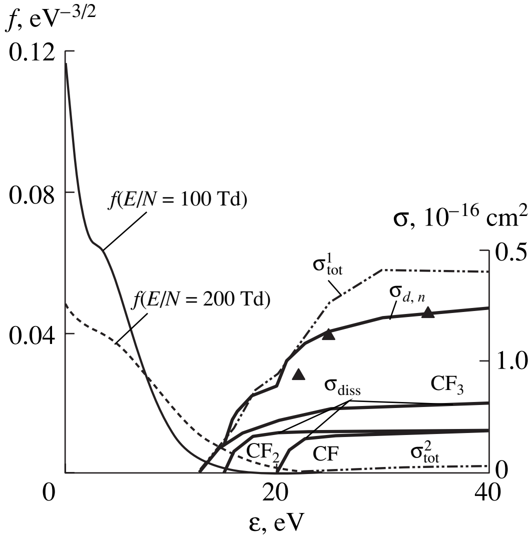

Fig. 6. Electron energy distribution function in pure CF_4 for two values of the reduced electric field E/N = 100 and 200 Td, shown in parentheses near the corresponding curves. Here, $\sigma^1_{tot}(\varepsilon)$ is the total cross section for the dissociation of CF_4 into neutral products [43]; triangles show the data from [46]; $\sigma^2_{tot}(\varepsilon)$ is the total cross section for the dissociation of CF_4 [44]; $\sigma^{CF_3}_{diss}(\varepsilon)$, $\sigma^{CF_2}_{diss}(\varepsilon)$, and $\sigma^{CF}_{diss}(\varepsilon)$ are the model cross sections for the electron-impact dissociation of CF_4 along the pathways toward CF_3, CF_2, and CF, respectively; and $\sigma_{d,\,n}$ is the total cross section for the electron-impact neutral dissociation of CF_4 along the pathways toward CF_3, CF_2, and CF [51].

In [44], the partial cross sections for dissociation of CF_4 along the pathways toward CF_x (x = 1–3) radicals were determined using the threshold ionization mass spectrometry (TIMS) method. The method is based on the fact that the ionization energy of a radical to be detected by a mass spectrometer is less than the dissociation energy of a CF_4 molecule. Thus, by setting the energy of the ionizing electron beam in the mass spectrometer higher than ionization energies of the CF_3, CF_2, and CF radicals but lower than the thresholds for the dissociation of CF_4 via the given CF_x channel, the corresponding partial cross sections for electron-impact dissociation can be determined, provided that the dissociation of CF_4 molecules is ensured by another electron beam. In this way, the absolute cross sections for the electron-impact neutral dissociation of CF_4 with the production of the CF_3, CF_2, and CF radicals were determined. In accordance with [43], at electron energies of ≥35 eV, the total cross section for the neutral dissociation of CF_4 was corrected for the cross section for the dissociative ionization resulting in the F^+ ion formation. The cross section obtained by this method is presented in Fig. 6 as $\sigma^2_{tot}(\varepsilon)$. It is seen that the cross sections $\sigma^1_{tot}(\varepsilon)$ and $\sigma^2_{tot}(\varepsilon)$ differ by almost one order of magnitude in a wide range of electron energies. This discrepancy is rather difficult to explain; it can be the result of many factors. It should be noted that, in [44], the cross sections at near-threshold electron energies were determined as a small signal against the background of the large main signal from the dissociation of CF_4 molecules at the hot-filament cathode of the electron gun used to dissociate CF_4. The use of the hot cathode also leads, especially at low potentials, to a substantial production of negative ions on the filament surface due to the low-threshold processes of dissociative attachment, e.g., $CF_3 + e \Rightarrow CF_2 + F^-$. These processes are of importance, e.g., in depositing diamondlike films using a hot-filament facility. With this idea in mind and based on the description of the experimental facility [44], one can expect that, at a low bias voltage applied to the filament, the fraction of the ion current in the beam current is fairly high. This circumstance could result in underestimated values of the dissociation cross section of CF_4 in the near-threshold region. It is difficult to say whether it is true or not. Perhaps the true reason is completely different. However, the authors pointed out that, in the near-threshold region, there was a large discrepancy between the measured cross sections for the neutral dissociation of CH_4 [52, 53] and CF_4 molecules. The relative behavior of the partial cross sections for the dissociation of CF_4 described in [44, 45] can be regarded as quite correct, assuming that, in the relatively narrow near-threshold range 12–20 eV, the experimental conditions were almost unchanged; i.e., the fraction of the ion current in the beam was approximately constant. Thus, the shape of the total cross section for the electron-impact dissociation of CF_4 in the near-threshold region (i.e., in the electron energy range that is most important for discharge applications) [43] seems to be the most realistic and the relative behavior of the partial cross sections agrees fairly well with the data from [44, 45].

This assumption was recently confirmed in [46–48]. In [46], by the method of intersecting electron and molecular beams, the electron energy loss spectra were obtained for five scattering angles and three values of the electron incident energy. Simultaneously with measuring the loss spectra, all of the positive ion species that are produced in scattering were recorded using time-of-flight mass spectrometry. Based on these experimental data, the angular dependences of the scattering cross sections (both total and in the individual channels) were determined. The elastic and total inelastic cross sections, the total and partial ionization cross sections, and the total cross section for neutral dissociation were measured. Substitution of the approximating analytical functions (obtained by fitting the experimental data) into the angular dependences of these cross sections enabled one to calculate the integral cross sections for three incident electron energies: 22.5, 25, and 34 eV. The total cross sections for the neutral dissociation of CF_4 obtained in [46] in the above way are also shown in Fig. 6. They are less than $\sigma^1_{tot}(\varepsilon)$ from [43] by only ~20–30% and exceed the data from [44] by almost one order of magnitude.

In [48], another indirect estimate of the total cross section for the dissociation via neutral channels was obtained. The total ionization cross section of CF_4 molecules was determined both experimentally and theoretically. A theoretical approach used to determine the ionization cross section of CF_4 allowed one to deduce the ionization cross sections for most of the fluorocarbons. It turned out that the theoretical cross section ranks above the measured one, particularly, in the near-threshold region. An analysis performed in [48] showed that the applied theoretical approach implicitly incorporates a constituent related to the dissociation into neutral products. For this reason, in [48], it was only possible to indirectly estimate the total cross section for neutral dissociation as the difference between the measured and theoretical ionization cross sections of CF_4. Although this estimate is qualitative, we note that the obtained cross section for the neutral dissociation of CF_4 agrees fairly well with the results of [43, 47, 48].

Based on the above results, the model cross sections $\sigma^{CF_2}_{diss}(\varepsilon)$ and $\sigma^{CF}_{diss}(\varepsilon)$ for the dissociation of CF_4 with the production of CF_2 and CF radicals in the electron energy range from the threshold energy to 40 eV were constructed. The $\sigma_{d,n}$ value from [43, 47, 48, 51] was used as a total cross section for the dissociation via all of the neutral channels. We emphasize that the near-threshold behavior of the cross section is of crucial importance for discharge applications, because it governs the values of the dissociation rate constant in the range of the reduced electric fields under study. To illustrate this, Fig. 6 presents the EEDF for two E/N values: 100 and 200 Td. The relative behavior of the partial cross sections for the neutral dissociation of CF_4 via different CF_x (x = 1–3) channels in the near-threshold region is taken from [44]. The absolute cross sections were normalized so that, in the energy range 12.5–16 eV, the total cross section for the dissociation via all the channels corresponds to the data from [43, 48, 51]; i.e., it is equal to $\sigma_{d,n}$. For electron energies higher than 30 eV, the ratio of the cross sections for different channels is $CF_3 : CF_2 : CF \approx 2 : 1 : 1$, which agrees with the data from [44].

The resulting model partial cross sections $\sigma^{CF_2}_{diss}(\varepsilon)$ and $\sigma^{CF}_{diss}(\varepsilon)$ and the total cross section $\sigma_{d,n}$ are shown in Fig. 6 by solid lines. Using these cross sections, the dissociation rate constants k_{CF_2} and k_{CF} were calculated using Eqs. (5) and (6). It is seen from Fig. 5 that the calculated dissociation rate constant k_{CF_2} is in good agreement with the experimental data throughout the entire range $E/N \approx$ 80–250 Td under study. As for the dissociation of CF_4 into CF radical, it is seen from Fig. 5 that the dependence of the calculated k_{CF} rate constant on the reduced electric field is in good agreement with the behavior of the measured rate constant, particularly, at $E/N > 130$ Td. However, the calculated absolute k_{CF} values are lower than the experimental ones by ~30–40%. The most likely reason for this discrepancy seems to be the insufficiently accurate absolute calibration of the CF LIF signal. Indeed, to determine the absolute value of the CF density, a rather complicated and indirect calibration procedure was applied. The procedure used the overlap function of the ArF laser radiation with the R-branch of the $B^2\Delta$, $v = 2 \longrightarrow X^2\Pi$, $v = 0$ band of the CF molecule and the geometrical factor determined from the calibration of the LIF signal from CF_2 radicals (see the description of the experiment). At $E/N < 130$ Td, the k_{CF_x} and $k^{eff}_{CF_x}$ values differ significantly. It is seen in Fig. 5 that this difference increases as the electric field decreases. As was noted above, such a large discrepancy between k_{CF_x} and $k^{eff}_{CF_x}$ at low E/N stems from the presence of another source of radicals in the plasma, which is supplementary to direct electron-impact dissociation. Note that low E/N values correspond to high pressure and high current density, i.e., a large energy deposition in a plasma volume and a large degree of dissociation. The lower E/N (and, consequently, the electron temperature), the larger the role of the channel with the lowest threshold. Under these conditions, the reaction

$$CF_4 + e \longrightarrow CF_3 + F + e \text{ threshold of} \sim 12.5 \text{ eV} \quad (11)$$

is in fact the main channel for the dissociation of CF_4. As was shown above, the extra source of CF_2 and CF radicals is related to reactions with the participation of C_xF_y polymer particles and, in many cases, $C_xF_y^+$ (x, y = 1, 2…) ions [1, 2, 9, 11, 30, 33–36]. Thus, we may suppose that the processes with the participation of CF_3 radicals are of crucial importance for the production of C_xF_y particles in the plasma. An indirect confirmation of this suggestion can be seen in Fig. 5. At low E/N, the effective rate constant for the dissociation of CF_4 with the production of CF_2 radicals is actually the same as the rate constant for process (11). These issues are considered in Part II in more detail, which is devoted to the analysis of the volume and heterogeneous processes of both the production and loss of CF_2 and CF radicals.

Here, we should make an important remark. Expressions (4)–(6) are only valid if, after switching on the discharge, the extra source of CF_x radicals also provides additional channels for their rapid loss with a rate much higher than the loss rate of CF_x radicals in the afterglow. If the mechanisms for the radical loss in the discharge and the discharge afterglow are the same (which, e.g., is the case in heterogeneous losses), then the use of Eqs. (4) and (5) for calculating k_{CF_x} only results in some effective rate constant for the dissociation of CF_4, namely, $k_{CF_x}^{eff}$. If this is the case, then the maximum possible values of $k_{CF_x}^{eff}$ must, in fact, correspond to the rate constant for the most rapid dissociation channel (11), namely, k_{CF_3}. Calculating k_{CF_3} with the help of the known partial cross sections taken from [44, 45] (which was also performed in [25]) results in $k_{CF_x}^{eff}$ values that, at $E/N > 150$ Td, are higher than k_{CF_3} by only a factor of about 1.5. However, at low E/N, $k_{CF_x}^{eff}$ substantially exceeds even the total rate constant over all the known dissociation channels. This indicates the impossibility of properly describing the dissociation of CF_4 in the discharge based on the near-threshold behavior of the cross sections reported in [44, 45].

4. CONCLUSION

In this study, the effective rate constants $k_{CF_2}^{eff}$ and k_{CF}^{eff} for the dissociation of CF_4 along the pathways toward CF_2 and CF radicals were measured within a wide range of the reduced electric field (80–250 Td). These measurements were carried out in a modulated dc glow discharge in pure CF_4. The LIF method was used to monitor the time evolution of the CF_2 and CF radical densities. A comparative analysis of the experimental data and the results of calculations of the k_{CF_2} and k_{CF} rate constants for the electron-impact dissociation of CF_4 was carried out. Calculations were performed using the Monte Carlo method for calculating the EEDF and model cross sections for the dissociation of CF_4. The model cross sections for the dissociation of CF_4 along the pathways toward CF_2 and CF radicals were constructed based on the analysis of the available literature data on the cross sections for the electron-impact dissociation of CF_4. It is shown that the model cross sections constructed in accordance with the data from [43, 44, 46–48, 51] allow one to adequately describe the experimental data at $E/N > 130$ Td. At lower E/N, which correspond to higher pressures and higher current densities, the observed discrepancy between the calculated rate constants k_{CF_2} and k_{CF} and the measured effective rate constants $k_{CF_2}^{eff}$ and k_{CF}^{eff} stems from the presence of an extra source of radicals, which is related to the electron-impact dissociation and reactions involving C_xF_y polymer fluorocarbon particles. A thorough analysis of the kinetic growth and decay curves for the radical densities in the modulated discharge allowed us to indirectly determine the contribution of direct electron impacts to the production of CF_2 and CF under the conditions of fluorocarbon polymerization and, thus, to determine the rate constants for the electron-impact dissociation of CF_4 at low E/N. The measured and calculated k_{CF_2} and k_{CF} values are in fair agreement within a wide range of the reduced electric field, which justifies the correctness of the model partial cross sections for the electron-impact dissociation of CF_4.

ACKNOWLEDGMENTS

We are grateful to M.A. Basova for her help in preparing the paper. We deeply regret the tragic death of our colleague Georgiĭ Rulev, a young and talented scientist and an honorable man, during a mountain trip. This study was supported by the Russian Foundation for Basic Research, project nos. 00-02-16509 and 00-15-96554.

REFERENCES

1. J.-P. Booth, Plasma Sources Sci. Technol. **8**, 249 (1999).
2. J.-P. Booth, G. Hancock, N. D. Perry, and M. J. Toogood, J. Appl. Phys. **66**, 5251 (1989).
3. S. G. Hansen, G. Luckman, G. C. Nieman, and S. D. Colson, J. Appl. Phys. **68**, 2013 (1990).
4. A. D. Tserepi, J. Derouard, J.-P. Booth, and N. Sadeghi, J. Appl. Phys. **81**, 2124 (1997).
5. A. D. Tserepi, W. Schwarzenbach, J. Derouard, and N. Sadeghi, J. Vac. Sci. Technol. A **15**, 3120 (1997).
6. S. Hayashi, H. Nakagawa, M. Yamanaka, and M. Kubota, Jpn. J. Appl. Phys. **36**, 4845 (1997).
7. T. Arai, M. Goto, K. Horikoshi, *et al.*, Jpn. J. Appl. Phys. **38**, 4377 (1999).
8. K. Sasaki, Y. Kawai, C. Suzuki, and K. Kadota, J. Appl. Phys. **82**, 5938 (1997).
9. C. Suzuki, K. Sasaki, and K. Kadota, J. Vac. Sci. Technol. A **16**, 2222 (1998).
10. S. Ito, K. Nakamura, and H. Sugai, Jpn. J. Appl. Phys. **33**, L1261 (1994).
11. M. Haverlag, W. W. Stoffels, E. Stoffels, *et al.*, J. Vac. Sci. Technol. A **14**, 384 (1996).
12. W. W. Stoffels, E. Stoffels, and K. Tachibana, Rev. Sci. Instrum. **69**, 116 (1998).
13. W. W. Stoffels, E. Stoffels, and K. Tachibana, J. Vac. Sci. Technol. A **16**, 87 (1998).
14. V. A. Feoktistov, V. V. Ivanov, A. M. Popov, *et al.*, J. Phys. D **30**, 423 (1997).
15. N. V. Mantzaris, A. Boudouvis, and E. Gogolides, J. Appl. Phys. **77**, 6169 (1995).
16. K. Masek, L. Laska, R. D'Agostino, and F. Cramarossa, Beitr. Plasmaphys. **27**, 15 (1987).

17. D. I. Slovetskiĭ and A. A. Deryugin, in *Plasma Chemistry*, Ed. by B. M. Smirnov (Énergoatomizdat, Moscow, 1987), Vol. 13, p. 240.
18. M. Hayashi, *Handbook of Plasma Material Science* (Ohm, Tokyo, 1992).
19. L. G. Christophorou, J. K. Olthoff, and M. V. V. S. Ra, J. Phys. Chem. Ref. Data **25**, 1341 (1996).
20. M.-C. Bordage, P. Segur, L. G. Christoforou, and J. K. Olthoff, J. Appl. Phys. **86**, 3558 (1999).
21. W. M. Huo and Y.-K. Kim, IEEE Trans. Plasma Sci. **27**, 1225 (1999).
22. A. V. Vasenkov, J. Appl. Phys. **85**, 1222 (1999).
23. W. L. Morgan, Plasma Chem. Plasma Process. **12**, 447 (1992).
24. B. Stefanov and P. Pirgov, Plasma Chem. Plasma Process. **13**, 665 (1993).
25. M. Kurihara, Z. L. Petrovic, and T. Makabe, J. Phys. D **33**, 2146 (2000).
26. R. J. M. M. Snijkers, M. J. M. van Sambeek, M. B. Hoppenbrouwers, and G. M. W. Kroesen, J. Appl. Phys. **79**, 8982 (1996).
27. V. V. Ivanov, K. S. Klopovskiĭ, D. V. Lopaev, *et al.*, Fiz. Plazmy **25**, 716 (1999) [Plasma Phys. Rep. **25**, 657 (1999)].
28. S. Sharpe, B. Hartnett, H. S. Sethi, and D. S. Sethi, J. Photochem. **38**, 1 (1987).
29. S. G. Hansen, G. Luckman, and S. D. Colson, Appl. Phys. Lett. **53**, 1588 (1988).
30. G. Cunge and J. P. Booth, J. Appl. Phys. **85**, 3952 (1999).
31. K. Sasaki and K. Kadota, Jpn. J. Appl. Phys. **38**, 4383 (1999).
32. A. Kono, M. Haverlag, G. M. W. Kroesen, and F. J. de Hoog, J. Appl. Phys. **70**, 2939 (1991).
33. J. P. Booth, G. Cunge, P. Chabert, and N. Sadeghi, J. Appl. Phys. **85**, 3097 (1999).
34. C. Suzuki, K. Sasaki, and K. Kadota, J. Appl. Phys. **82**, 5321 (1997).
35. K. Miyata, M. Hori, and T. Goto, J. Vac. Sci. Technol. A **14**, 2083 (1996).
36. K. Sasaki, H. Furukawa, C. Suzuki, and K. Kadota, Jpn. J. Appl. Phys. **38**, L954 (1999).
37. M. Haverlag, E. Stoffels, W. W. Stoffels, *et al.*, J. Vac. Sci. Technol. A **12**, 3102 (1994).
38. C. Suzuki, K. Sasaki, and K. Kadota, Jpn. J. Appl. Phys. **36**, L824 (1997).
39. C. Suzuki, K. Sasaki, and K. Kadota, Jpn. J. Appl. Phys. **37**, 5763 (1998).
40. I. Ishikawa, S. Sasaki, K. Nagaseki, *et al.*, Jpn. J. Appl. Phys. **36**, 4648 (1997).
41. J. A. O’Neill and J. Singh, J. Appl. Phys. **77**, 497 (1995).
42. H. Winters and M. Inokuti, Phys. Rev. A **25**, 1420 (1982).
43. M. R. Bruce, Ce Ma, and R. A. Bonham, Chem. Phys. Lett. **190**, 285 (1992).
44. T. Nakano and H. Sugai, Jpn. J. Appl. Phys. **31**, 2919 (1992).
45. H. Sugai, H. Toyoda, T. Nakano, and M. Goto, Contrib. Plasma Phys. **35**, 415 (1995).
46. L. Mi and R. A. Bonham, J. Chem. Phys. **108**, 1910 (1998).
47. S. Motlagh and J. H. Moore, J. Chem. Phys. **109**, 432 (1998).
48. H. Nishimura, W. M. Huo, M. A. Ali, and Y.-K. Kim, J. Chem. Phys. **110**, 3811 (1999).
49. A. V. Vasenkov, in *Proceedings of the XXIV International Conference on Phenomena in Ionized Gases, ICPIG, 1999*, Vol. IV, p. 159.
50. M. R. Bruce and R. A. Bonham, Int. J. Mass Spectrom. Ion Processes **123**, 97 (1993).
51. R. A. Bonham, Jpn. J. Appl. Phys. **33**, 4157 (1994).
52. K. Stephan, H. Deutsch, and T. D. Mark, J. Chem. Phys. **83**, 5712 (1985).
53. T. Nakano, H. Toyoda, and H. Sugai, Jpn. J. Appl. Phys. **30**, 2908 (1991).

Translated by N. Ustinovskiĭ

Plasma Physics Reports, Vol. 28, No. 3, 2002, pp. 243–257. Translated from Fizika Plazmy, Vol. 28, No. 3, 2002, pp. 272–288.
Original Russian Text Copyright © 2002 by Ivanov, Klopovskiĭ, Lopaev, Proshina, Rakhimov, Rakhimova, Rulev.

LOW-TEMPERATURE PLASMA

Kinetics of the Reactions Involving CF_2 and CF in a Pure Tetrafluoromethane Plasma: II. Production and Loss of CF_2 and CF in the Processes of Fluorocarbon Polymerization

V. V. Ivanov, K. S. Klopovskiĭ, D. V. Lopaev, O. V. Proshina, A. T. Rakhimov, T. V. Rakhimova, and G. B. Rulev[†]

Skobeltsyn Institute of Nuclear Physics, Moscow State University, Vorob'evy gory, Moscow, 119899 Russia

Received September 26, 2001

Abstract—Mechanisms for the production and loss of CF_2 and CF radicals in a glow discharge in pure CF_4 are investigated by the time-resolved laser-induced fluorescence method. The fluorocarbon polymerization processes are shown to contribute significantly to the production of radicals both in the plasma volume and on the surface of the discharge tube. The effective frequencies of both the volume and surface processes of radical production and loss are determined. An analysis of these frequencies allowed us to study the polymerization mechanism in a CF_4 plasma at a high relative concentration of F atoms and low ion energy. It is shown that, at elevated pressures, when the density of C_xF_y polymer particles in the plasma volume becomes comparable with the density of simple fluorocarbon radicals, the electron-impact dissociation of these particles is the main channel for the production of CF_2 and CF radicals. Another source of CF_2 and CF radicals is related to the reactions of C_nF_{2m+1} unsaturated fluorocarbon particles both in the plasma volume and on the surface of a fluorocarbon film arising on the discharge tube wall. The C_xF_y fluorocarbon polymer particles form both in the discharge volume and on the fluorocarbon film surface also in the course of the film destruction. At lowered pressures, the main channel for the production of CF_2 and CF is the direct electron-impact dissociation of CF_4 molecules, whereas the loss of these radicals at the tube wall is the main loss channel. The probabilities of the heterogeneous losses of CF_2 and CF radicals on the heavily fluorinated surface of the fluorocarbon film at low ion energies are determined. Under these conditions, the surface recombination of the F_{ch} chemisorbed fluorine atoms and CF_x^{ph} physisorbed radicals with the production of an activated complex is shown to be the most probable mechanism for the heterogeneous losses of CF_2 and CF. The approximate activation energies for the production of $F_{ch} \cdot CF_2^{ph}$ and $F_{ch} \cdot CF^{ph}$ surface complexes are found to be 750 ± 70 K and 1030 ± 100 K, respectively.

1. INTRODUCTION

This part of the paper is devoted to studying the volume and heterogeneous reactions of the production and loss of CF_2 and CF radicals in a tetrafluoromethane plasma. In fact, our aim is a detailed consideration of some aspects of fluorocarbon polymerization in a plasma, because it is the radicals that serve as a starting structural material for fluorocarbon polymers. At present, the problem of low-temperature fluorocarbon polymerization in a plasma covers a very wide area of scientific exploration, which includes many fields related to various technical applications [1]. In recent years, owing to the effort of many scientific teams, great progress in understanding the basic features of fluorocarbon polymerization in a plasma has been achieved, although detailed mechanisms for such polymerization have been little studied. First of all, this concerns the mechanism for heterogeneous reactions at a microscopic level. This is evidenced by the fact that there is still no fluorocarbon plasma models allowing an unambiguous prediction of the structure of a growing fluorocarbon film based on the general discharge parameters. This stems from the many-parameter character of fluorocarbon polymerization, which incorporates various catalytic reaction cycles and ion-stimulated reactions. Even the great body of experimental data obtained under various conditions do not permit one to take into account the numerous "free parameters" of this process. Summarizing briefly the main results and conclusions of the latest studies on fluorocarbon polymerization in a plasma [1–26], we can say that this process is characterized by the following common features.

(i) Polymerization processes occur in almost any plasma containing fluorocarbons and lead to the formation of a fluorocarbon coating on the surfaces of the dis-

---

[†] Deceased.

charge chamber and the electrodes. The initial stage of polymerization is characterized by the so-called oligomerization processes—the gas-phase processes involving the simplest fluorocarbon radicals, mainly CF_x (x = 1–3) molecules: $CF_3 + CF_3 \longrightarrow C_2F_6$; $CF_2 + CF_3 \longrightarrow C_2F_5$; $CF_2 + CF_2 \longrightarrow C_2F_4$, etc. This results in the formation of large C_xF_y neutral clusters and $C_xF_y^+$ and $C_xF_y^-$ ion clusters ($x > 1$, $y > 1$). It was shown experimentally [2, 3, 13, 14, 25] that these clusters belong mainly to C_nF_{2n-k} polymer structures, whose main series can be represented by the n values up to 10 and k values from 0 to +4; some fluorine atoms in these structures can be substituted with hydrogen atoms. These polymer particles and ions, which are supposed to be the constituents of the dust grains formed in the plasma volume, substantially affect the growth of fluorocarbon films on surfaces.

(ii) The surface recombination of chemisorbed F^{ch-s} fluorine atoms, physisorbed CF_x^{ph-s} radicals, and $C_xF_y^{ph-s}$ molecules is assumed to be the main process of fluorocarbon radical heterogeneous loss at low pressures. It should be noted that, for such a "reaction" surface as a fluorocarbon film surface under plasma conditions, the division of active states into "chemisorbed" and "physisorbed" is rather relative. These terms are a historic heritage; here, we use them just to mark the type of reaction ability of active surface sites:

$$F^{ch-s} + CF_x^{ph-s} \begin{array}{l} \xrightarrow{\delta} CF_{x+1}^{s}, \\ \xrightarrow{1-\delta} CF_{x+1}, \end{array}$$

$$F^{ch-s} + C_xF_y^{ph-s} \longrightarrow (C_xF_{y+1}^{s})^* \longrightarrow \text{products}.$$

It is suggested that these surface reactions are analogues of the gas-phase recombination reactions

$$F + CF_x + M \longrightarrow CF_{x+1} + M,$$

$$F + C_xF_y + M \longrightarrow (C_xF_{y+1})^* + M$$

$$\longrightarrow \text{products} + M,$$

in which the surface, in fact, plays the role of a third body. Taking into account that the density of the reaction states in the newly formed CF_{x+1}^{s} and $(C_xF_{y+1}^{s})^*$ surface complexes is much higher as compared to the gas phase, the surface recombination reactions are assumed to proceed more efficiently.

(iii) The reactions of surface recombination with the subsequent product desorption also act as the processes of "cleaning" the active centers—first of all, chemically active fluorine atoms and C_xF_{2y+1} unsaturated fluorocarbon radicals, which can again adsorb particles from the gas-phase. To some extent, this resembles the case with carbon coating formation in a hydrogen–methane plasma (e.g., when depositing diamondlike films [27–29]); the process is catalytic in character with the active particles themselves as a catalyzer. Thus, in [2–4], it was supposed that fluorine atoms and the CF_x (x = 1–3) simplest radicals can play the role of such a catalyzer when depositing fluorocarbon coatings.

(iv) The subsequent coagulation of C_xF_y polymer molecules and clusters lead to the formation of rather large (up to a micron in size) dust grains. Plasma recombination on the grain surface substantially affects the plasma parameters and, consequently, all the plasmochemical processes. It is the charging of the grain surface that enables them to stay quite long in the plasma volume due to the rather high electric field in the electrode sheaths and near the reactor wall. However, an increase in the mass and size of the dust grains because of both the coagulation processes and heterogeneous growth reactions leads to the deposition of the heaviest grains onto the reactor wall, which, under certain conditions (particularly, at elevated pressures), can contribute significantly to the growth rate and structure of the fluorocarbon film.

(v) In addition to the above pure "radical" mechanisms for fluorocarbon polymerization, which are important mainly during the discharge afterglow, the CF_x^+ and $C_xF_y^+$ ions incident onto a surface of the fluorocarbon film in the active phase of the discharge significantly (at elevated ion energies and densities, even decisively) affect the polymerization process. Depending on the ion energy, not only the ion-stimulated reactions, but also the ion neutralization and fragmentation processes can substantially modify the mechanism for the growth of the fluorocarbon coating and significantly accelerate the formation of CF_x radicals on the surface. Under certain conditions, e.g., in a dense helicon plasma or under intense ion bombardment in a low-pressure RF discharge, these processes can decisively affect the growth and structure of the fluorocarbon film [2–4, 15, 17–19].

The above-said outlines a qualitative picture of low-temperature polymerization in a fluorocarbon plasma. However, attempts to quantitatively describe this process based on the above model representation often face insurmountable obstacles. This indicates an incompleteness of the above picture of fluorocarbon polymerization in a plasma (some other processes, which need further investigation, also seem to be important) and a sophisticated interrelation between different reaction channels that have not yet been properly incorporated into the models. A striking example is the formation of CF_2 and CF radicals in the interaction of a fluorocarbon plasma with a surface when the intensity of this "surface" source of radicals is comparable with the intensity of electron-impact dissociation of the main gas [2–4, 10–12, 16–26]. Up to the present time, the exact mechanism for this process remains unknown, although its importance is obvious.

2. EXPERIMENT

The formation and loss of CF_2 and CF radicals in a glow discharge in pure tetrafluoromethane were investigated by the time-resolved laser-induced fluorescence (LIF) method. The experiments were carried with a long cylindrical tube (with a diameter of 18 mm and an interelectrode distance of 500 mm) whose wall was precoated with a fluorocarbon film produced by long-term discharge training in pure CF_4. The experiment is described in detail in Part I of this paper. We will present some aspects of the experiment that are important for radical reaction kinetics. The discharge was modulated at a frequency of 20 Hz; the time intervals during which the discharge was switched off were 2–6 ms. This modulation ensured a rather good reproduction of the plasma parameters by the instant when the next modulation cycle began, the temperature of the tube wall being almost constant. The latter circumstance is of crucial importance, because the probability of the heterogeneous loss of CF_2 and CF radicals strongly depends on the surface temperature [11].

In Part I, it was shown that the growth and decay of the CF_2 radical density in the modulated discharge usually cannot be described by a single exponential function, which indicates the complicated dynamics of the CF_2 reaction channels after the discharge is switched on or off. The higher the discharge current density and/or the gas pressure, the larger the deviation of the $[CF_2](t)$ decay from the single-exponential one. Thus, the CF_2 radical losses cannot be attributed solely to the intense losses on the wall occurring with a certain constant loss probability. As was noted in [3], the convexity of the CF_2 density decay curve means the “effective” increase in the CF_2 loss probability with time, which cannot be described by the adsorption–desorption dynamic model. Furthermore, the decay curve convexity unambiguously points to the presence of an extra source of CF_2 radicals (whose intensity, in the first approximation, is proportional to the radical density itself) in the discharge afterglow. Otherwise, this dependence would be concave whatever CF_2 loss channels are taken into account. Since the recombination of the CF_4 plasma after the discharge is switched off is rather rapid [30, 31], the source of CF_2 and CF radicals in the discharge afterglow should be related to the reactions involving neutral particles. Unfortunately, because of the much lower sensitivity of the recording system to CF radicals, the signal dynamic range was too small to say with a fair degree of confidence that the CF density decay was nonexponential. However, taking into account that the CF_x density decay deviates from the single-exponential decay only in the late afterglow, the effective loss frequency $\nu_{\mathrm{eff}}^{\mathrm{C,\,F}_x}$ (and, consequently, the effective loss time $\tau_{\mathrm{eff}}^{\mathrm{C,\,F}_x}$) in the discharge can be estimated using the exponential approximation of the radical decay curves in the early afterglow. If the dissociation of CF_4 molecules is the main channel for the production of CF_2 and CF radicals, then the characteristic time during which the steady-state density of CF_2 radicals is restored after the discharge is switched on should be equal to the radical loss time, i.e., close to $\tau_{\mathrm{eff}}^{\mathrm{C,\,F}_x}$, because the dissociation degree of CF_4 is low (<1%). However, at elevated pressures, the restoration of the CF_2 density after switching on the discharge occurs with another “effective” frequency, which is much higher than the loss frequency. It should be noted that similar dynamics of the CF_2 density was already observed when modulating an RF discharge in CF_4 [12]. All this points to the emergence of (i) a time-dependent radical source in addition to the dissociation of CF_4 molecules after switching on the discharge and (ii) a channel of rapid radical loss because the characteristic restoration time of the steady-state particle density in the plasma is governed by the characteristic time of the particle density decay. Moreover, at low discharge currents, these processes can even lead to a rapid decrease, rather than an increase in the CF_2 density immediately after switching on the discharge. Such a behavior of the CF_2 density was observed only under certain specific conditions at times when the power of the extra source of radicals decreased. Thus, during the discharge, the CF_2 loss frequency can be much higher than in the discharge afterglow. This effect strongly depends on the discharge conditions, mainly, on the energy deposition in a plasma (it sharply increases with current and pressure). Note that the characteristic time of the “rapid” loss of radicals is much shorter than the time of radical diffusion toward the tube wall, which indicates that the volume processes are responsible for this effect. As for the CF radicals, their characteristic loss time, both in the discharge and discharge afterglow, is also much shorter than the diffusion time of CF molecules onto the tube wall over the entire range of experimental conditions. The observed kinetics of the CF density growth does not unambiguously indicate a considerable increase in the CF radical loss rate after the discharge is switched on. Therefore, in a CF_4 plasma, there is an efficient mechanism for the volume loss of CF_2 and CF radicals. This mechanism is closely related to the processes of radical production, which are different from the process of the direct electron-impact dissociation of CF_4. In other words, the process of polymerization in a tetrafluoromethane plasma (seemingly, also in plasmas of other fluorocarbons) is accompanied by catalytic reaction cycles with the participation of the simplest CF_x radicals. The term “catalytic cycle” is used here only in a relative sense, because the rates of CF_x radical production and loss resulting from the conversion of fluorocarbons in the plasma considerably exceed the dissociation rates of CF_4 along the pathways toward CF_x. In Part I, when analyzing the experimental results, we introduced the effective frequency $\nu_p^{\mathrm{CF}_x}$ of the rapid volume loss of CF$_x$ radicals. The quantitative estimate for this frequency was obtained by fitting the experimental results. The data on $\nu_{\mathrm{eff}}^{\mathrm{CF}_x}$ and $\nu_p^{\mathrm{CF}_x}$ as functions of the discharge parameters were used when analyzing both the processes with the participation of CF$_2$ and CF radicals and their role in polymerization reactions in a pure tetrafluoromethane plasma.

3. LOSS PROCESSES FOR CF$_2$ AND CF RADICALS

The characteristic loss times $\tau_{\mathrm{eff}}^{\mathrm{CF}_2}$ and $\tau_{\mathrm{eff}}^{\mathrm{CF}}$ of CF$_2$ and CF radicals in the afterglow as functions of the CF$_4$ pressure are shown in Figs. 1a and 1b, respectively, for different gas temperatures at the discharge axis. The data presented in Fig. 1 were obtained from the dependences of the characteristic loss times $\tau_{\mathrm{eff}}^{\mathrm{CF}_x}$ and $\tau_{\mathrm{eff}}^{\mathrm{CF}}$ and the gas temperature on the discharge current at different pressures. Since the radical density decay in the early afterglow is always exponential, we analyzed the CF$_2$ and CF loss processes in the afterglow by examining the corresponding loss frequencies. It is seen from Fig. 1 that the radical losses are limited by diffusion; hence, at low pressures, the diffusion-limited loss of CF$_x$ radicals on the tube surface is the main loss channel. As was mentioned above, the radical density decay is close to the exponential one; then, in the first approximation, we have

$$\tau_{\mathrm{CF}_x} = \frac{1}{\nu_w^{\mathrm{CF}_x}} + \frac{1}{\nu_{\mathrm{diff}}^{\mathrm{CF}_x}}, \qquad (1)$$

where $\nu_w^{\mathrm{CF}_x} = \gamma_{\mathrm{CF}_x}\frac{v_{Tw}^{\mathrm{CF}_x}}{2R}$ is the CF$_x$ loss frequency on the tube wall (actually, on the fluorocarbon film surface), R is the tube radius, γ_{CF_x} is the probability of the CF$_x$ radical heterogeneous loss, $v_{Tw}^{\mathrm{CF}_x}$ is the thermal velocity of CF$_x$ radicals near the wall, $\nu_{\mathrm{diff}}^{\mathrm{CF}_x} = D_{\mathrm{CF}_x}(2.4/R)^2$ is the diffusion frequency of CF$_x$ in pure CF$_4$, $D_{\mathrm{CF}_x} \approx D_0^{\mathrm{CF}_x}/P(T_g/300)^{3/2}$ is the corresponding diffusion coefficient, $D_0^{\mathrm{CF}} = 91$ cm^2 torr^{-1} s^{-1}, $D_0^{\mathrm{CF}_2} = 61$ cm^2 torr^{-1} s^{-1} [32], P is the pressure, and T_g is the gas temperature. When calculating D_{CF_x} as a function of the gas temperature, we used T_g values at the discharge axis, which led to an overestimation of the diffusion frequency. However, as will be shown below, this does not affect the obtained results and conclusions. The probabilities of CF$_x$ loss processes on the fluorocarbon film surface were the only fitting parameters. The times τ_{CF_2} and τ_{CF} calculated by formula (1) are shown in Fig. 1 by solid lines. It is seen from Fig. 1a that, at lowered pressures, the heterogeneous loss of CF$_2$ radicals is indeed the main loss channel. The CF$_2$ loss probability increases from 0.07 to 0.15 as the tube wall temperature increases (see below). However, as the pressure increases, the increase in the CF$_2$ loss frequency is not as rapid as predicted by formula (1). This is possibly caused by two factors: (i) as the pressure increases, an additional source of radicals appears in the afterglow and/or (ii) the heterogeneous loss probability γ_{CF_2} depends on time (as it was supposed in [3, 4]). In our experiment, the second factor is of minor importance because the CF$_2$ heterogeneous loss rate at high pressure is determined almost entirely by diffusion. In contrast to CF$_2$ radicals, the loss of CF cannot be approximated by for-

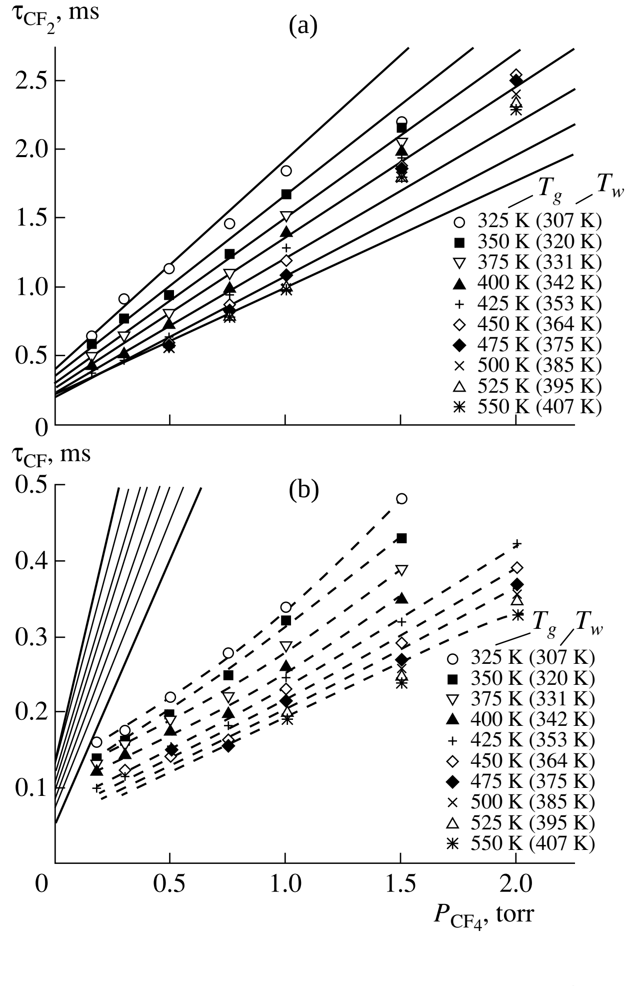

Fig. 1. Characteristic loss times (a) of the CF$_2$ radical $\tau_{\mathrm{eff}}^{\mathrm{CF}_2}$ and (b) CF radical $\tau_{\mathrm{eff}}^{\mathrm{CF}}$ vs. CF$_4$ pressure for different gas temperatures T_g on the discharge axis and, correspondingly, different wall temperatures T_w (both indicated in the figure). The solid lines show the approximation of the experimental data by formula (1), and the dashed lines show the results of fitting the experimental data.

mula (1) even at low pressures. The measured characteristic times of CF loss turn out to be much shorter than the calculated ones (see Fig. 1b), which indicates a significant contribution of the volume processes to the loss of CF radicals. Note that a similar situation was also observed in a helicon plasma at pressures as low as several mtorr [20].

The loss processes for CF_x are closely related to the polymerization processes both in the volume and on the surface. This relation is an intricate many-parameter function of the densities, fluxes, and energies of different plasma components, including the radicals themselves. For this reason, it is rather difficult to unambiguously split the volume and surface processes. For example, the probability of CF_x radical loss on the fluorocarbon film surface depends not only on the surface properties (temperature, composition, etc.) [11, 17], but also on the plasma parameters (gas composition, fluxes of radicals and ions onto the surface, etc.) [2–5, 24, 25]. Thus, the variations in the plasma parameters result in time variations in both the volume and surface radical loss rates. Nevertheless, to better understand the nature of the processes with the participation of the simplest CF_x radicals, we suggest that the probability of the heterogeneous loss of radicals depends only on the film properties (on the wall temperature in an explicit form). Thus, γ_{CF_x} is assumed to be independent of the plasma parameters. In some sense, this is the case because, under the given conditions, the energies of the ions incident onto the tube wall are too low (~0.1–0.4 eV) to significantly stimulate surface processes. In contrast, the fluxes of active neutral particles are rather high; hence, in the first approximation, the sorption equilibrium is established for any of these active components.

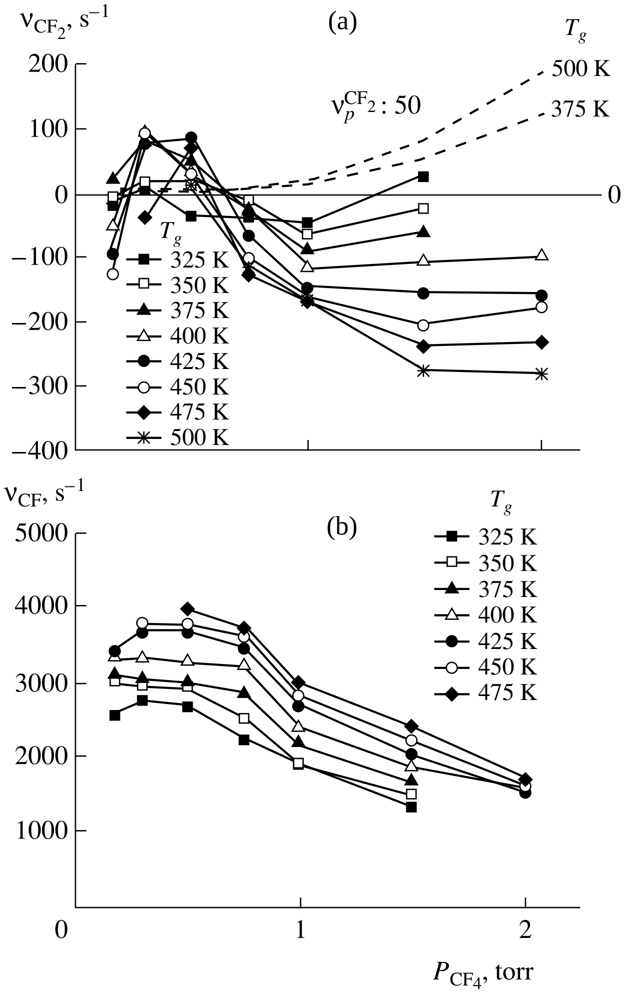

Fig. 2. Volume loss frequencies of (a) CF_2 radicals and (b) CF radicals in the afterglow vs. pressure for different gas temperatures T_g. The dashed lines show the effective frequency $\nu_p^{CF_2}$ of the "rapid" volume loss of CF_2 radicals during the discharge.

3.1. *Losses of CF_x Radicals in the Discharge Volume*

The assumption that γ_{CF_x} is constant allows us to "split" the heterogeneous and volume losses of CF_2 and CF molecules using the $\nu_w^{CF_x}$ frequency obtained from formula (1) as an estimate for the heterogeneous loss frequency. Then, the volume loss frequency of CF_2 (CF) radicals can be estimated as the difference between the measured frequency $\nu_{eff}^{CF_2}$ (ν_{eff}^{CF}) and the frequency ν_{CF_2} (ν_{CF}) = $1/\tau_{CF_2}$ ($1/\tau_{CF}$) calculated by formula (1). These frequencies are shown in Fig. 2 as functions of the pressure for different gas and wall temperatures. The effective frequency $\nu_p^{CF_2}$ of the rapid volume loss of CF_2 radicals in the discharge is shown in Fig. 2a. Since the characteristic times of the CF density growth and decay are close to each other over the entire range of experimental conditions, we can suggest that the CF radical losses in the discharge and discharge afterglow are governed by the same mechanism. However, as is seen in Fig. 2b, this process is obviously volume in nature. In contrast to CF, the CF_2 volume loss frequency in the afterglow turns out to be negative, which indicates the presence of a source of CF_2 radicals when the discharge is switched off. This process of CF_2 production was experimentally observed in various discharges in both CF_4 and other fluorocarbons [2–5, 10–12, 17–25]. The processes of radical production will be discussed in detail below. Note that this "negative" loss frequency (i.e., the production frequency) of CF_2 is much lower than the effective frequency of CF_2 volume loss after the discharge is switched on (see Fig. 2a). Thus, the question naturally arises as to what volume processes are responsible for such high values of the ν_{eff}^{CF} and $\nu_p^{CF_2}$ loss frequencies. Taking into account that the volume loss frequencies of CF_2 and CF radicals are rather high and sharply increase with pressure and discharge current, the processes can only be reactions involving active particles whose density in the plasma is rather high and whose production and loss frequencies sharply and nonlinearly increase with the degree of CF_4 dissociation. Moreover, these particles must be chemically active with respect to CF_2 radicals because they can substantially influence the radical density in the discharge but hardly affect it in the discharge afterglow.

It is known [2–5, 9, 21] that, in the CF_4 plasma at pressures <1 torr, among the active neutral particles, the densities of F atoms and CF_3 radicals are very high because they are the main products of CF_4 dissociation. However, they do not satisfy the above conditions. For example, the CF_2 radical loss frequency in the recombination processes of CF_2 radicals with CF_3 radicals ($CF_2 + CF_3 \longrightarrow C_2F_5$) and F atoms ($CF_2 + F + CF_4 \longrightarrow CF_3 + CF_4$) correspond to $\nu_p^{CF_2}$ only in the case of an extremely high (>30%) degree of CF_4 dissociation, which is more than one order of magnitude higher than the measured one. Furthermore, these processes also affect the CF_2 loss rate in the discharge afterglow due to the rather large lifetimes of F atoms [9, 21, 33] and CF_3 radicals [5, 6]. The direct electron-impact dissociation of CF_2 radicals ($e + CF_2 \longrightarrow e + CF + F$) also cannot enable the observed high loss rate of these radicals after the discharge is switched on. To enable this, the cross section for the electron-impact dissociation of CF_2 must be increased by more than two orders of magnitude. Moreover, at a constant discharge current density, the frequency of this process is almost independent of the pressure.

It is the C_xF_y ($x = 1, 2, 3, \ldots, y = 1, 2, 3, \ldots$) polymer fluorocarbon particles formed in the fluorocarbon plasma at pressures higher than 10^{-2} torr that satisfy the above requirements. Let us consider this issue in more detail. In [2–4], it was shown that the most probable structure of these particles is a polymer structure such as $\alpha[(CF_2)_n]$ ($n = 1, 2\ldots$), where α is a certain "core" C_xF_y ($x = 1$–3, $y = 5$–2) in which a fraction of fluorine atoms may be substituted with hydrogen atoms. This conclusion was confirmed by the investigations of fluorocarbon polymerization in a plasma using the new method of electron attachment mass spectroscopy (EAMS) [13, 14, 25], which enables one to prevent the fragmentation of heavy multiatom particles in the ionization chamber of an ordinary mass spectrometer. It was shown that the C_xF_y polymer particles (mainly C_nF_{2n-k} species) actually form in an RF discharge in pure CF_4. Experimentally, the n values up to 10 and the k values from 0 to +4 were observed, but the densities of C_nF_{2n+2} saturated polymers were the highest. This is typical of a plasma "enriched" with fluorine atoms, when the carbon–carbon bonds are actually saturated with fluorine and the efficiency of polymerization processes is low. However, the EAMS measurements do not exactly represent polymerization kinetics under the discharge conditions, especially at elevated pressures, because the lifetimes of unstable unsaturated fluorocarbon polymers are short and their characteristic path lengths are much shorter than the typical distance to the mass-spectrometer chamber. Thus, we may suppose that the density of the "chemically active" unsaturated C_xF_y polymer particles in the discharge volume is higher than that obtained from mass spectrometry measurements. Most probably, for unsaturated C_nF_{2m+1} fluorocarbon particles, the rate constants for reactions with CF_2 are much higher than for particles with saturated carbon–carbon bonds C_nF_{2m+2}, as is the case of the simplest reaction with CF_3 and CF_2 radicals [21, 34]:

$$CF_2 + CF_3 \longrightarrow C_2F_5,\ k_{CF_3} \approx 8 \times 10^{-13}\ \mathrm{cm^3/s},$$

$$CF_2 + CF_2 \longrightarrow C_2F_4,\ k_{CF_2} \approx 4 \times 10^{-14}\ \mathrm{cm^3/s}.$$

This qualitatively explains the lower polymerization rate in a "fluorine rich" CF_4 plasma as compared to "fluorine poor" C_2F_6 or C_4F_8 plasmas. In the latter case, it is unsaturated polymers whose density is observed to significantly increase [13, 14, 25]. Taking into account the above-said, the kinetics of the volume processes of CF_2 radical production and loss can be qualitatively described as follows. As the current and, particularly, the pressure increase, the polymerization rate significantly increases, thus increasing the density of polymer particles in the plasma. The ion–molecular reactions and the processes with the participation of high-energy electrons result in the production of a variety of polymer "fragments", namely, positive and negative multiatom ions and neutral radical fragments. These reactions (e.g., the dissociative ionization, dissociative attachment, and neutral dissociation of C_xF_y) proceed mainly via the low-threshold channel, generally, along the pathways toward fluorocarbon radicals with unsaturated carbon–carbon bonds. The reactions of CF_2 with these polymer radical fragments ensure the elevated loss frequency of CF_2 in the plasma volume and are an important constituent of the polymerization process in a fluorocarbon plasma. After the discharge is switched off, the recombination of charged particles proceeds rather rapidly, in several hundreds of microseconds [30, 31]. The loss of C_nF_{2m+1} unsaturated polymer particles in reactions with different radicals, mainly, fluorine atoms and CF_x ($x = 1$–3) radicals, also proceeds quite rapidly. Most of them are converted into C_nF_{2m+2} saturated fluorocarbon particles; consequently, in the discharge afterglow, only saturated fluoropolymers actually "survive" and the CF_2 loss rate significantly decreases. This qualitatively explains the presence of two different loss frequencies of CF_2 radicals, $\nu_p^{CF_2}$ in the discharge and $\nu_{\mathrm{eff}}^{CF_2}$ in the discharge afterglow [12].

The lifetime of saturated fluoropolymers in the discharge afterglow is governed mainly by surface losses; removal with the gas flow; and, in the case of large C_xF_y clusters, coagulation processes. Since the probabilities of surface losses of saturated fluoropolymers are, as a rule, quite low (~10^{-4}–10^{-2}), their characteristic lifetimes turn out to be relatively large, longer than a 3- to 6-ms pause between switching off and switching on the discharge. Therefore, after the discharge is switched on, the produced electrons and ions interact not only with molecules of the main gas, CF_4, but also with C_xF_y polymer particles. Since the mean electron energy is rather high (it is determined by electron scattering by the CF_4 molecules of the main gas), the interaction of electrons with C_nF_{2m+2} opens many dissociation pathways (dissociative ionization, dissociative attachment, and neutral dissociation) toward various radical fragments. In this case, conceptually, the radicals of various structures, including the simplest radicals and F atoms, can form. However, the basic channels for the electron-impact dissociation of C_nF_{2m+2} are apparently the channels corresponding to the internal structure of its polymer chains. Thus, it is quite probable that the pathway toward CF_2 radicals is dominant. The above considerations can be illustrated by the following scheme incorporating the volume reactions with the participation of CF_2:

(A) After switching on the discharge:

$$e + CF_4 \longrightarrow e + CF_2 + 2F, \tag{2}$$

$$e + C_nF_{2m+2} \longrightarrow e + C_lF_{2k+1} + \text{products}, \tag{3}$$

$$\longrightarrow e + C_iF_{2j+2} + \text{products}, \tag{4}$$

$$\longrightarrow e + CF_2 + \text{products}, \tag{5}$$

$$C_lF_{2k+1} + C_iF_{2j+2} \longrightarrow C_{l+i}F_{2(k+j+1)+1}, \tag{6}$$

$$C_lF_{2k+1} + C_iF_{2j+2} \longrightarrow \text{products } (CF_2 - ?), \tag{7}$$

$$C_{l+i}F_{2(k+j)+1} + F + M \longrightarrow C_{l+i}F_{2(k+j)+2} + M, \tag{8}$$

$$C_{l+i}F_{2(k+j)+1} + F \longrightarrow \text{products } (CF_2 - ?), \tag{9}$$

$$C_{l+i}F_{2(k+j)+1} + CF_3(CF) \longrightarrow C_{l+i+1}F_{2(k+j+1)+2}(C_{(l+i+1)}F_{2(k+j)+2}), \tag{10}$$

$$C_{l+i}F_{2(k+j)+1} + CF_3(CF) \longrightarrow \text{products } (CF_2 - ?), \tag{11}$$

$$C_{l+i}F_{2(k+j)+1} + CF_2 \longrightarrow C_{l+i+1}F_{2(k+j+1)+1}, \tag{12}$$

$$C_{l+i}F_{2(k+j)+2} + CF_2 \longrightarrow \text{products}, \tag{13}$$

$$C_{l+i}F_{2(k+j)+2} + F(CF_3, CF) \longrightarrow \text{products } (CF_2 - ?), \tag{14}$$

where M is a third body.

(B) After switching off the discharge:

$$C_{l+i}F_{2(k+j)+2} + CF_2 \longrightarrow \text{products}, \tag{13'}$$

$$C_{l+i}F_{2(k+j)+2} + F(CF_3, CF) \longrightarrow \text{products } (CF_2 - ?). \tag{14'}$$

This scheme will agree with the experiment if the loss rates of unsaturated fluoropolymers in reactions (6)–(12) are high enough to significantly decrease their density even in the early afterglow. It is impossible to unambiguously say which of these processes plays a key role. Probably, the reactions of fluoropolymers with fluorine atoms and CF_3 radicals, whose density at low pressures ranks above the densities of all the other radicals, contribute the most. Thorough kinetic studies of F atoms and, especially, CF_3 radicals would be able to reveal the picture of elementary mechanisms for polymerization in a fluorocarbon plasma. We are going to carry out such experiment. The question is what is the density of C_xF_y polymer particles. It can be estimated based on the obtained $\nu_p^{CF_2}$ values assuming $\nu_p^{CF_2} = \sum_{n,m} k_{nm}[C_nF_{2m+1}] \approx k_{CF_2}[C_xF_y]$. Assuming that, at n, $m > 2$, the rate constants for the processes similar to reaction (12) become on the order of the gas-kinetic rate constant $k_{CF_2} \approx 10^{-10}$ cm^3/s, we obtain $[C_xF_y] \approx 10^{14}$ cm^{-3} at a pressure of 1.5–2 torr and current density of ~10–15 mA/cm^2. Thus, at high pressures, the density of fluorocarbon polymer particles in the plasma turns out to be on the order of the density of F atoms and CF_3 (CF_2) radicals. Such high densities of C_xF_y result in their coagulation and coalescence in the discharge volume and the formation of rather large clusters, which are then deposited onto the reactor wall. Consequently, under these conditions, the structure of fluorocarbon coating on the tube surface is rather complicated, nonuniform, and strongly disordered. It is indirectly confirmed by the results of scanning electron microscopy and Raman spectroscopy (see below).

As for CF radicals, it is seen from Fig. 2b that the CF volume loss frequencies in the discharge and early afterglow are close to each other, are on the order of $\nu_p^{CF_2}$, and increase with pressure. At high pressures, they greatly exceed the characteristic frequency of CF heterogeneous loss. Then, following the above qualitative scheme of polymerization processes in a CF_4 plasma, one can suggest reactions (10), (11), and (14) with the participation of fluoropolymer particles to be the main channels for the volume loss of CF radicals, the reaction rates for saturated and unsaturated fluorocarbons being of the same order of magnitude.

It is difficult to unambiguously answer the question of what is the role of reactions between C_xF_y particles and ions (both positive and negative) in the production and loss of CF_x radicals in the plasma volume. It should be noted that, in a fluorocarbon plasma, only $C_xF_y^+$ positive ions with low x and y were observed experimentally [2, 14, 15], whereas, in the recorded negative clusters, x and y are rather high [14, 25, 35]. It seems plausible that the ions can participate in polymerization processes not only on the plasma surface but also in the plasma volume. However, this problem requires further investigation.

3.2. Losses of CF_x Radicals on the Fluorocarbon Film Surface

It is seen in Fig. 1 that, at constant gas and wall temperatures, the characteristic times $\tau_{eff}^{CF_2}$ and τ_{eff}^{CF} tend to a certain constant value as the pressure decreases, which allows one to consider heterogeneous losses as the main radical loss channel. The linear extrapolation of the characteristic loss times at $P_{CF_4} \longrightarrow 0$ was used to estimate, as the first approximation, the probabilities of radical losses γ_{CF_2} and γ_{CF} on the fluorocarbon film surface as functions of the wall temperature. These dependences are shown in Fig. 3. The obtained values of γ_{CF_2} and γ_{CF} agree with the literature data [5, 8, 20, 36]. Based on the above-said, we can make some inferences about the possible mechanism for the loss of CF_2 and CF radicals on the fluorocarbon surface, at least, at a high density of atomic fluorine in the plasma.

First of all, it should be noted that, in an fluorocarbon plasma enriched with atomic fluorine (such as low-pressure CF_4 plasma), most of the active states on the surface (active in the sense of reaction ability, so they can be treated as chemisorption sites) will be occupied by fluorine atoms because of their high reaction ability and the highest flux incident onto the surface [2–5]. To some extent, this is similar to the formation of C : H coating in a methane-containing plasma, in which almost all the active surface sites are occupied by hydrogen atoms [27, 28]. The term active surface site is used in reference to a certain surface area possessing clearly defined chemical properties (something like a "virtual" chemical bond that is not rigidly localized). In some sense, this can be imagined as an essential nonuniformity of both the surface potential and the structural order, which can be various in nature. The active surface sites can be related to surface dislocations, the modification of structural groups due to embedding other elements, the charging of surface traps, and chemical adsorption in its traditional meaning. Generally, such a site can be represented as a defect that accumulates the uncompensated surface charge and induces a strong multipole interaction. The desorption energy from these surface sites can be fairly high (higher than 1 eV). In the energy hierarchy of surface sites, these states occupy an intermediate position between the physadsorption centers created due to the van der Waals interaction and chemisorption sites related to purely chemical forces [37–39].

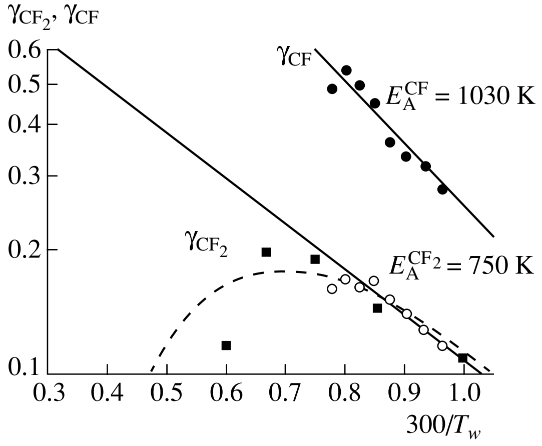

Fig. 3. The probabilities γ_{CF_2} (open circles) and γ_{CF} (closed circles) of CF_2 and CF radical losses, respectively, on the fluorocarbon film surface vs. the inverse wall temperature. Closed squares show the loss probability of CF_2 radicals [11]. The γ_{CF_2} and γ_{CF} values are obtained by a linear extrapolation of the $\tau_{eff}^{CF_2}(P_{CF_4})$ and $\tau_{eff}^{CF}(P_{CF_4})$ curves from Fig. 1 in the limit $P_{CF_4} \longrightarrow 0$. The dashed curve shows the analytical approximation of the measured γ_{CF_2} value by formula (21).

This seems to be the major difference between a real surface and an "atomically pure" surface with a strictly ordered structure, in which the density of these states is very low [38]. They are usually thought of as the localized physadsorption states or, in other words, the so-called "slow" states, whose lifetime ranges from hundreds of microseconds to hundreds of seconds. In contrast to the known "fast" surface states (e.g., the Tamm states), these states, as a rule, are in the forbidden zone and are weakly related to the volume states, which is the main circumstance determining their properties. Thus, they can be regarded as a certain type of surface defect that is always present on real, "atomically dirty" surfaces [38, 39]. In contrast to the well-known phenomenon of physadsorption on the atomically pure and strictly ordered surfaces under the conditions of ultrahigh vacuum, it is adsorption on these surface states that is often interpreted as physadsorption under the real conditions of a plasmochemical experiment or technological process. Primarily, this concerns the physadsorption of radicals [39]. A striking example of this state is the surface hydrogen bonds or the so-called "coordination" bonds. Thus, an addition of hydrogen to a fluorine–carbon mixture leads to the passivation of a fluorinated surface. The loss probabilities of CF_x radicals and F atoms decrease by more than one order of magnitude when H_2 is added to CF_4 [8, 11, 18, 24, 40, 41]. It is suggested that the formation of strong H–F bonds is responsible for this effect. To briefly summarize, we can say that, under the real conditions of a chemically active plasma, the surface is always covered with a certain absorbing layer of chemically active particles. It is the kinetics of this layer that largely governs the features of the plasma–surface interaction. Moreover, the kinetics of the absorbing layer can be substantially modified because of the sophisticated dynamics of the production and loss of the active surface sites themselves, e.g., when bombarding the surface with energetic particles (ions and/or photons) or due to the process of strong "competition" for these sites among various active particles.

The loss of CF_x radicals on the fluorinated surface of a fluorocarbon film can be represented in the simplest way as a certain effective process:

$$Z\mathrm{F} + \mathrm{CF}_x^{ph} \underset{\nu_{de}}{\overset{k_{ad}}{\rightleftarrows}} Z\mathrm{F}\cdot\mathrm{CF}_x^{ph}, \qquad (15)$$

$$Z\mathrm{F}\cdot\mathrm{CF}_x^{ph} \begin{cases} \xrightarrow{\delta\nu_r} (Z\mathrm{F}\cdot\mathrm{CF}_x^{ph})_a \\ \xrightarrow{(1-\delta)\nu_r} Z + \mathrm{CF}_{x+1}^{ph}, \end{cases} \qquad (16)$$

where Z are the chemisorption states, ZF are the chemically adsorbed fluorine atoms, CF_x^{ph} are the physadsorbed CF_x radicals, $Z\mathrm{F}\cdot\mathrm{CF}_x^{ph}$ is the transient "activated" surface complex, $(Z\mathrm{F}\cdot\mathrm{CF}_x^{ph})_a$ is the stable surface complex after the structural relaxation of the transient complex, k_{ad} is the adsorption rate constant, ν_{de} is the desorption frequency, and ν_r is the relaxation frequency of the $Z\mathrm{F}\cdot\mathrm{CF}_x^{ph}$ transient complex (approximately equal to the CF_x surface loss frequency). If the surface diffusion of CF_x radicals does not hamper the formation of the $Z\mathrm{F}\cdot\mathrm{CF}_x^{ph}$ surface complex, then each CF_x radical on the surface reaches a chemisorbed fluorine atom over the period of the radical lifetime, which is determined by the physadsorption potential [42]. This is true for moderate surface temperatures (in general, less than 500–600 K), when the distance between chemisorption sites is shorter than the characteristic path length of the surface diffusion of CF_x radicals. For temperatures slightly higher than room temperature, this is almost always true. In this case, the density of CF_x^{ph} physadsorbed radicals turns out to be a single-valued function of the radical density in the volume. Then,

$$\frac{\partial[\mathrm{CF}_x]}{\partial t} = -\nu_r[Z\mathrm{F}\cdot\mathrm{CF}_x]\frac{2\xi}{R} = -\nu_r\frac{k_{ad}[Z\mathrm{F}]}{\nu_{de}+\nu_r}\frac{2\xi}{R}[\mathrm{CF}_x],$$

where the factor $2/R$ is an S/V ratio for cylindrical geometry (S and V are the tube surface and volume, respectively) and ξ is the factor of surface roughness. For the sake of simplicity, we assume that $\xi = 1$. CF_x losses can also be represented in the conventional form by introducing the radical surface loss probability γ_{CF_x}:

$$\frac{\partial[\mathrm{CF}_x]}{\partial t} = -\gamma_{\mathrm{CF}_x} v_T \frac{2}{R}[\mathrm{CF}_x],$$

where v_T is the mean thermal velocity of CF_x near the surface. From here, we obtain

$$\gamma_{\mathrm{CF}_x} = \frac{4k_{ad}[Z\mathrm{F}]}{v_T}\frac{\nu_r}{\nu_{de}+\nu_r}. \qquad (17)$$

Assuming that reaction channel (16) ranks above CF_x desorption (15) (i.e., $\nu_r \gg \nu_{de}$), it is possible to estimate the density of active surface centers ZF using the measured value of γ_{CF_x} and the rate constant for the gas-phase collisions as k_{ad}. The estimate is $[Z\mathrm{F}] \approx [Z] \approx (3\text{–}5) \times 10^{12}\ \mathrm{cm}^{-2}$. This value is very low and corresponds to the relative density of active centers less than 10^{-3}. In terms of the order of magnitude, this estimate corresponds to the density of defects on a crystal surface. Of course, under plasma conditions, the reaction surface of an amorphous fluorocarbon film greatly differs from the crystal surface. Figure 4 presents a scanning electron microscope image of a fluorocarbon film on the discharge tube wall. A disordered structure consisting of many fluorocarbon grains of different sizes (mainly of submicron size) can easily be seen. Nothing can be said with assurance about the formation mechanisms for these grains. Is their formation a consequence of the surface reactions and stresses originating while the film grows? Or do they form in the plasma volume in the processes of C_xF_y coagulation and only after this are deposited onto the surface? The latter assumption seems to be more probable. Figure 5 presents the Raman spectrum of a fluorocarbon film, which definitely indicates that the particle structure is not poly-

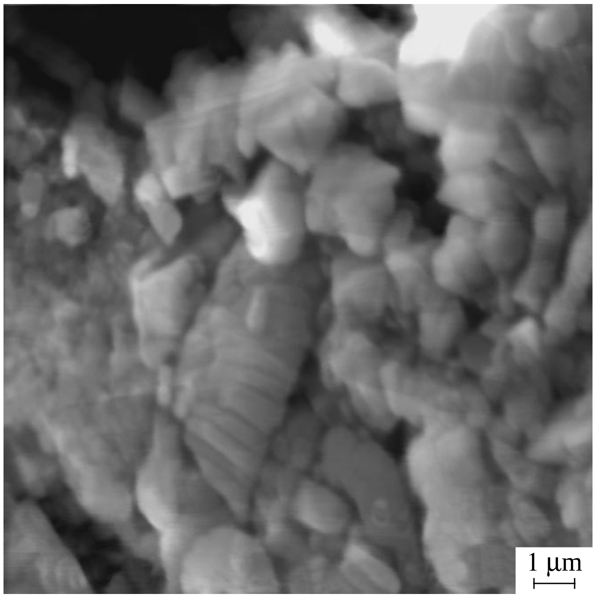

Fig. 4. A scanning electron microscope image of a fluorocarbon film on the discharge tube wall at a magnification of 6250.

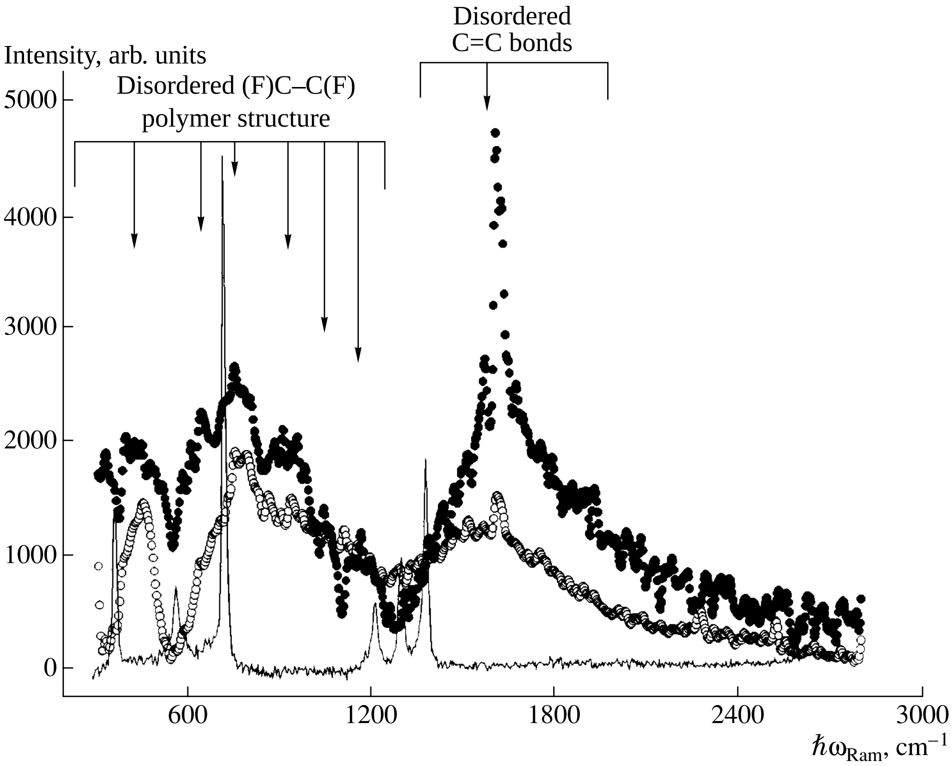

Fig. 5. Raman spectra of a fluorocarbon film on the discharge tube wall. Closed and open circles show the Raman spectra taken from the discharge and tube wall sides of the film, respectively. The arrows indicate the specific features of the spectra. The solid line shows the Raman spectrum of Teflon.

mer. For comparison, the spectrum of Teflon, which is a polymer, is also shown in Fig. 5. A comparison of these spectra shows that, although a disordered polymeric structure is present in the film spectrum, the fluorocarbon particle spectrum also has other structural features. A basic structural feature is a peak at ~1640 cm^{-1}, which indicates the presence of many double C=C bonds embedded in the polymer structure. It is quite probable that there is a certain amount of *sp*^{2} carbon–carbon bonds (the graphite peak at ~1595 cm^{-1}). However, it can be argued that the *sp*^{3} carbon phase, which is responsible for the formation of diamond and glassy graphite (the peaks at 1333 and 1349 cm^{-1}, respectively), is almost absent. In some sense, we can say that fluorocarbon particles have something like a "rigid frame" (double and graphite bonds) surrounded by a polymer envelope capable of constantly creating free surface bonds. These bonds appear to be responsible for particles sticking and growing together in the plasma volume and on the plasma surface. Is this indeed the case? It is not possible to unambiguously answer this question now because of some evidence in favor of other possible mechanisms for the formation of fluorocarbon coatings and dust grains. This problem requires further investigation. It is quite possible that the above scenario is justified only for pure radical polymerization in plasma, when the influence of the ion-stimulated reactions can be neglected. Here, some important remarks should be made. Thus, it may be suggested that $\nu_r \ll \nu_{de}$. Then, we have

$$\gamma_{CF_x} = \frac{4k_{ad}[ZF]}{v_T}P_r, \qquad (18)$$

where $P_r = \nu_r/\nu_{de}$ is the probability of the reaction of CF$_x$ with chemisorbed fluorine atoms. Based on Fig. 4, we can assume that the true surface roughness factor is $\xi \approx 3$–10; consequently, the density of surface centers will be on the order of $[ZF] \approx 10^{14}$–10^{16} cm^{-2}. Then, at a temperature close to 300 K, we have $P_r \approx 10^{-1}$–10^{-3}. Surprisingly, this P_r value coincides with the recombination probabilities of most atoms and radicals on dielectric surfaces. Hence, the exponential growth of γ_{CF_x} with the surface temperature (see Fig. 3) can be interpreted as the Arrhenius dependence of P_r. In [11], under conditions similar to the conditions our experiments, it was experimentally observed that, as the temperature increased, the initial increase in the CF$_2$ loss probability was replaced by a sharp fall. It should be noted that, in [11], the discharge parameters and, consequently, the fluxes of active particles onto the surface did not change when changing the surface temperature. This result indirectly implies that the polymerization rate also sharply decreases when the temperature exceeds a certain level. Such behavior is typical of free-radical polymerization [1]. Thus, it is quite natural to suggest that the mechanism for the recombination of CF_x on the fluorinated surface of a fluorocarbon film is similar to the gas-phase recombination reactions of CF_x with F atoms and C_xF_y composite radicals (unsaturated fluoropolymers). The activated complex mechanism is known to be the most probable for such gas-phase processes. Let us assume that this is also valid in the case of surface recombination. An analysis of [16, 20] indirectly confirms this assumption. Then, in the first approximation, the CF_x loss probability must be proportional to the production probability of the activated complex [43]:

$$P_r(E) \sim \frac{N^{\#}(E)}{N(E)}$$
$$\approx \left(\frac{I^{\#}}{I}\right)^{2-K}\left(\frac{\hbar^2}{2IE}\right)^{K/2}\frac{s\hbar\omega_s}{E}\left(\frac{E-E_a}{E}\right)^{S-1}\prod_i^{S-1}\frac{\omega_i}{\omega_i^{\#}}, \quad (19)$$

where the ordinary Kassel model of the activated complex was used, in which the complex parameters related to the reaction coordinate are fixed in the complex transient state. In formula (19), $N^{\#}(\varepsilon)$ is the number of states of the activated complex; ε is the total energy in the channel with the activation energy E_a (below the activation energy, $N^{\#}(\varepsilon)$ is assumed to be identically zero); $N(\varepsilon)$ is the number of states of the radical–surface complex with the energy ε; S is the number of vibrational modes of the radical–surface complex; $\omega_i^{\#}$ and ω_i are the vibrational frequencies for the ith mode of the activated and radical–surface complexes, respectively; and the index K is either 0 or 2 for the “soft” and “rigid” activated complex configurations, respectively. The rigid configuration corresponds to the case of an activated complex with no internal rotation of the reaction bond; correspondingly, I is the moment of inertia of the radical in the radical–surface complex. In contrast, in a soft configuration, internal rotation is possible and $I^{\#}$ is the reduced moment of inertia for the radical relative rotation in the activated complex. In this case, the energy of zero vibrations was neglected. Averaging formula (19) over the Boltzmann distribution, we finally obtain

$$P_r \sim \frac{S\hbar\omega_S}{kT_w}\exp\left(-\frac{E_a}{2kT_w}\right)$$
$$\times 2^{S-N/2}\Gamma(S)\left(\frac{kT_w}{E_a}\right)^{1/2-N/2}D_{N-2S}\left(\sqrt{2\frac{E_a}{kT_w}}\right), \quad (20)$$

where T_w is the surface temperature; $\Gamma(S)$ is the gamma function; $D_p(z)$ is the function of parabolic cylinder; and $N = 0$ or 1 for the rigid and soft configurations, respectively. Taking into account that the activation energy E_a is much higher than 300 K (see Fig. 3) and, usually, the ratio E_a/kT_w is larger than $|N - 2S|$, we can use an asymptotic expression for the $D_p(z)$ function. This allows us to represent formula (20) in a simpler form:

$$P_r \sim \frac{S\hbar\omega_S}{kT_w}\left(\frac{kT_w}{E_a}\right)^{S-N+1/2}\exp\left(-\frac{E_a}{kT_w}-\frac{s^2kT_w}{E_a}\right). \quad (21)$$

Using expressions (18) and (21) and varying S and E_a, we tried to approximate our data and the data from [11] on γ_{CF_2} (in the latter case, the approximate γ_{CF_2} values were calculated based on the CF_2 radical decay curves obtained by the LIF method at various wall temperatures). We were mainly interested in the relative behavior of the dependence of the loss probability on the surface temperature, because the fitting of γ_{CF_2} in the absolute scale would be too speculative. Of course, even in this case, our approximation is rather rough and does not allow us to exactly determine either s or E_a. Nevertheless, formula (21) correctly reflects the common features of CF_2 loss on a fluorocarbon surface (Fig. 3). Hence, a bit more can be said about the structure of the radical–surface complex, although more qualitatively than quantitatively. The most suitable fitting parameters are $s \approx 2$, $E_a^{CF} \approx 1500 \pm 200$ K, and $E_a^{CF_2} \approx 1200 \pm 200$ K or $s \approx 3$, $E_a^{CF} \approx 1000 \pm 200$ K, and $E_a^{CF_2} \approx 700 \pm 100$ K. These values indicate that, under the conditions of free radical polymerization, the losses of CF_2 and CF on a fluorocarbon film surface result in the formation of soft bonds with the surface, so that the formation of sp^2 and, especially, sp^3 carbon phases is unlikely because of the high activation barrier. If we suggest that the processes of free radical polymerization are also important for the formation of dust grains in a plasma, then it is quite probable that the kinetics of this formation is governed by the activated complex mechanism. However, this assumption requires further verification. It is quite possible that it is valid only in the specific case when the ion influence on the surface processes is relatively low.

4. PRODUCTION OF CF_2 AND CF RADICALS IN THE PLASMA POLYMERIZATION PROCESSES

An extra production of CF_2 and CF radicals can occur both in the plasma volume and on the fluorocarbon film surface. The processes resulting in the production and loss of CF_2 and CF radicals in the positive column of a glow discharge in CF_4 were discussed above and in Part I based on the experimental results. In addition to the key process of CF_x production in the direct electron-impact dissociation of CF_4 molecules, the most probable processes of radical production are the reactions involving C_xF_y fluorocarbon polymer particles. Let us consider these processes in more detail.

The CF_x radical production unrelated to the direct electron-impact dissociation of the main-gas molecules was observed under various discharge conditions [2–5, 10–12, 17–25]. This extra source of radicals is believed to be related to fluorocarbon polymerization in plasma, primarily to the processes on the surface of a fluorocarbon coating that forms on the chamber wall and electrodes when running the discharge. The relationship between the volume and surface sources depends strongly on the plasma parameters, namely, the pressure, mixture composition, plasma density, and ion energy. Thus, under conditions typical of low-pressure (tens of mtorr) discharges, the ion density and energy are such that the ion-stimulated processes prevail [3–5, 10–12, 17–21], whereas the surface of the fluorocarbon film interacting with the plasma serves as an extra source of radicals. Under the conditions of a high-pressure glow discharge (as in our experiments), the contribution from the volume source becomes significant. Indeed, the assumption that the radicals form on the surface of the fluorocarbon film in the course of ion-stimulated reactions and film destruction (see [2, 8–10, 16, 17, 24, 25]) is not justified under our experimental conditions, because the measured time of the radical density growth at the axis is smaller than the time of radical diffusion from the wall toward the tube axis. Moreover, in contrast to [17], with Ar in place of CF_4, there was no LIF signal from CF_2 radicals even when the Ar^+ ion flux exceeded the ion flux by a factor of 2–3. This evidences that the sputtering of the fluorocarbon coating under the action of ion bombardment can also be neglected.

4.1. Production of CF_2 and CF Radicals in the Plasma Volume

The initial stage of fluorocarbon polymerization in a plasma are the reactions of olygomerization:

$$CF_x + CF_y \longrightarrow C_2F_{x+y} \quad (x; y = 1\text{–}3).$$

The main contribution comes from the reactions involving CF_3, whose density exceeds the densities of the other radicals by one order of magnitude (or even higher). This is a consequence of the moderate rate of CF_3 heterogeneous loss and the lowest thresholds for the channels of CF_3 production in dissociation, dissociative ionization, and dissociative attachment. The later stages include similar reactions with the participation of CF_x radicals and C_xF_y multiatom molecules. As was shown experimentally in [2–5, 13, 14, 23–25], these reactions result in the formation of rather heavy polymer structures in the plasma volume. In our experiments, at pressures higher than ~1.5 torr, the frequency of CF_2 and CF volume losses after the discharge is switched off is comparable with the heterogeneous loss frequency (see Fig. 2). The role of fluorine atoms reduces to supporting (through the recombination and etching processes) a certain kinetic balance among these particles [2–4, 9, 33, 40]. Apparently, the change in the plasma composition can result in new mechanisms for the radical production. It was shown above and in Part I that, in a steady-state discharge, reactions with the participation of electrons [see Eqs. (3)–(5)] and neutrals [see Eqs. (7), (9), (11), and (14)] are the most probable volume processes of CF_x radical production in a fluorine-rich CF_4 plasma. Of course, reactions with the participation of ions (both positive and negative) are also possible; however, the ion contribution is insignificant because of their low density and energy. Therefore, what is the real density of C_xF_y particles in the discharge? The above estimate of $[C_xF_y]$ was made based on the assumption that the loss frequency of radicals in the plasma volume is fairly high (see Section 2). For example, at a pressure of ~2 torr and current density of ~15 mA/cm^2, we have $[C_xF_y] \approx 10^{14}$ cm^{-3}. Another estimate can be made using the results of a kinetic analysis performed in Part I. For example, the power of an additional volume source of CF_2 radicals can be estimated based on the initial slope of the radical density growth curve after switching on the discharge, assuming that the first term on the right-hand side of Eq. (2) in Part I is known:

$$\frac{d[CF_2]}{dt} \approx k_{CF_2} n_e [CF_4] + S_e^{C_xF_y} + S_N^{C_xF_y}, \qquad (22)$$

$$S_N^{C_xF_y} = \sum_N N \sum_{x,\,y>2} k_N^{C_xF_y}[C_xF_y], \qquad (23a)$$

$$S_e^{C_xF_y} = [n_e] \sum_{x,\,y>2} k_e^{C_xF_y}[C_xF_y]. \qquad (23b)$$

However, taking into account the conclusions made in Sections 2 and 3 and the fact that the density and composition of C_xF_y particles may change after switching on the discharge, the following estimate seems to be more correct:

$$S_e^{C_xF_y} + S_N^{C_xF_y} \approx \nu_p^{CF_2}[CF_2]_0, \qquad (24)$$

where $[CF_2]_0$ is the steady-state density of CF_2 radicals in the discharge. From the considerations of Section 2, it follows that $S_e^{C_xF_y} \gg S_N^{C_xF_y}$. Then, assuming $S_e^{C_xF_y} \approx n_e k_{C_xF_y}[C_xF_y]$ (where $k_{C_xF_y}$ is the effective rate constant for electron-impact dissociation of C_xF_y and $[C_xF_y]$ is the density of C_xF_y particles in the discharge), the $[C_xF_y]$ value can be obtained from Eqs. (22) and (24). This value corresponds to the above estimate of $[C_xF_y]$ obtained based on the frequency of CF_2 rapid volume loss if we set $k_{C_xF_y} \approx 10^{-8}$–$10^{-7}$ cm^3/s. Such a high $k_{C_xF_y}$ value indicates, first, the large cross section for the electron-impact dissociation of C_xF_y and, second, a very low threshold for this process. This is in agreement with experimental evidence on the cross sections for the electron-impact dissociation of heavy fluorocarbons.

In the afterglow, the situation is completely different. Already in the earliest afterglow (<10 μs), the electron temperature falls so rapidly that the processes of neutral dissociation and dissociative ionization of C_xF_y molecules almost come to a stop. However, the rate of the dissociative attachment of electrons to these particles can be fairly high because this process is almost thresholdless [13, 14, 25]. Later, the dissociative attachment of electrons results in the formation of a cold ion–ion plasma, in which the density of the negative ions exceeds the electron density by 2–3 orders of magnitude. In this case, instead of the positive ions, rather heavy $C_xF_y^-$ negative ions are observed. The question is whether the ion–molecular reactions are able to produce CF_x radicals. For example, the ion–ion recombination resulting in the production of highly excited $C_xF_y^{**}$ complexes is followed by their dissociation. However, at a very low degree of ionization (~10^{-6} in our experiment), this channel for radical production can be neglected. Hence, the reactions between the neutral active particles arising in the active phase of the discharge are the most probable volume source of CF_2 and CF. It is difficult to definitely say what are these reactions. We can suppose that these are the processes of the etching of C_nF_{2m} polymer structures in the discharge volume, mainly, by fluorine atoms. However, based on the above consideration, these processes are more probably related to reactions involving unsaturated fluorocarbons, which is evidenced by the fact that the rate of CF_2 production in the afterglow decreases with time and sharply (nonlinearly) increases with pressure. It should be noted that similar reactions can also occur on the surface of a fluorocarbon film.

4.2 Production of CF_2 and CF Radicals on a Surface

The surface production of CF_2 and CF radicals in a fluorocarbon plasma was repeatedly observed [2–4, 7, 10, 15, 16, 18, 24, 26, 36]. The intensity of this process depends on many parameters, first of all, the gas composition. In carbon-rich gases, such as C_3F_8 and C_4F_8, this intensity is considerably higher [7, 10, 14, 17, 21, 26]. Ion-stimulated processes, whose rates depend strongly on the ion density and energy, are very important [2, 12, 15]. However, in [2], it was noted that, as the ion energy decreases, the ion flux onto the surface fails to provide the observed yield of CF_2 and CF. Hence, a natural question arises of the role of active neutral particles in the surface recombination of radicals.

First of all, recombination reactions (15) and (16) of adsorbed CF_x radicals and adsorbed F atoms (analogous to gas-phase reactions) occur on the fluorinated surface of a fluorocarbon coating [2, 3, 5, 9, 21, 41]. For example, the surface production of CF_2 and the surface loss of CF were experimentally observed in [21]. However, further investigations showed that, at elevated pressures, the yield of CF_2 radicals significantly exceeds the flux of CF molecules onto the surface. We can suggest that, as in the case of CF, CF_2 radicals are also produced in the recombination of heavy unsaturated fluorocarbons with chemisorbed fluorine atoms. The contribution of the more stable C_nF_{2m} saturated fluorocarbons in this process seems to be relatively small. This scheme of fluorocarbon radical surface production qualitatively explains the observed dynamics of the CF_2 density in the afterglow. Indeed, approximately several hundreds of microseconds after the discharge is switched off, when the plasma has already almost completely recombined, the density of the unsaturated polymer fluorocarbon molecules is still fairly high. This results in an additional decrease in the loss frequency of CF_2 radicals in the afterglow because of the existence of an extra radical source related to the reactions with the participation of unsaturated fluorocarbons (the $S_N^{C_xF_y}$ source). As the density of unsaturated fluorocarbons decreases, the power of this source also decreases, which additionally increases the loss frequency of CF_2 radicals, as was observed in experiments carried out at elevated pressures and current densities (Fig. 4 from Part I).

The recombination of ZF chemisorbed fluorine atoms and physadsorbed C_nF_{2m+1} unsaturated fluorocarbon molecules (at lowered pressures, the direct interaction between ZF and C_nF_{2m+1} from the gas phase is much less probable), resulting in the production of CF_2 radicals, is only one of the possible transformation channels of the $(ZF \cdot C_nF_{2m+1})^a$ activated surface complex. It seems plausible that this process can result in both dense structures chemically bounded with the surface and rather porous, highly reactive structures, which can then participate in the surface reactions. The reactive structures can act as Z active sites of chemisorption for chemically active particles, mainly, fluorine atoms and CF_x radicals. Keeping in mind that the fluxes of F atoms and CF_3 radicals onto the surface are the largest, we can suggest that it is these particles that will occupy most of the sites. The reactions of chemisorbed ZF and ZCF_x radicals with the particles physadsorbed on the surface (probably, via the activated complex mechanism) will also lead to the growth of polymer structures on the surface. The higher the contribution of C_xF_y particles in this process, the more nonuniform and disordered the structure of the fluorocarbon film growing on the surface. In contrast, if the film grows mainly via reactions with the participation of free CF_x radicals, then the fluorocarbon coating will have a more uniform structure determined only by the surface processes. This is characteristic of free radical polymerization, when the ion-stimulated processes can be ignored to a first approximation. However, in most of the plasma facilities of modern VLSI submicron technology, a rather dense low-pressure (~1–100 mtorr) plasma is used. In this case, the ion processes are of crucial importance; moreover, a variety of new volume and surface processes related to the use of mixtures of fluorocarbons with other gases (usually, hydrogen) arise. In any case, a significant decrease in the pressure and ion energy makes it possible to significantly reduce the fluorocarbon polymerization rate and to decrease the risk of pollution with the products of this process.

5. CONCLUSION

In this study, a methodical analysis of the mechanisms for the production and loss of CF_2 and CF radicals in both the plasma of a glow discharge in CF_4 and the discharge afterglow has been carried out using the time-resolved LIF method for monitoring the radical densities. An analysis of the $[CF_2](t)$ and $[CF](t)$ dependences obtained when modulating the discharge at various pressures and currents allowed us to determine the effective production and loss frequencies of radicals both on the surface and in the plasma volume. The polymerization processes involving C_xF_y fluorocarbon polymer particles are shown to significantly contribute to the production of radicals both in the plasma volume and on the surface of the discharge tube. This made it possible to study certain aspects of fluorocarbon polymerization in CF_4 plasma at high relative concentrations of F atoms and low ion energies. An increase in the pressure strongly increases the density of C_xF_y polymer particles in the plasma, so that the electron-impact dissociation of these particles becomes the main channel for the CF_2 and CF radical production. There is another source of CF_2 and CF radicals, which is related to the reactions of the C_nF_{2m+1} unsaturated fluorocarbon particles both in the plasma volume and on the surface of a fluorocarbon film formed on the discharge tube wall. The formation of the C_xF_y fluorocarbon polymer particles occurs both in the plasma volume and on the fluorocarbon film surface (as well as in the course of the possible film destruction). However, at lower pressures and discharge currents, the density of polymer particles substantially decreases and the direct electron-impact dissociation of CF_4 molecules becomes the main channel for CF_2 and CF radical production, whereas their losses occur mainly on the discharge tube wall. An analysis of the kinetic decay curves of CF_2 and CF radicals allowed us to determine the probabilities of heterogeneous losses of these radicals on the heavily fluorinated surface of a fluorocarbon film. It is shown that, under these conditions, the surface recombination of chemisorbed F_{ch} fluorine atoms and physisorbed CF_x^{ph} radicals, resulting in the formation of a $(F_{ch} \cdot CF_x^{ph})^a$ activated complex, is the most probable mechanism for the heterogeneous losses of CF_2 and CF. A comparison of the measured probabilities of heterogeneous losses of CF_2 and CF radicals with the model estimates allowed us to approximately determine the activation energies of $(F_{ch} \cdot CF_2^{ph})^a$ and $(F_{ch} \cdot CF^{ph})^a$ surface complexes as 750 ± 70 K and 1030 ± 100 K, respectively.

It should be noted that the above conclusions are only valid when the ion-stimulated processes can be ignored to a first approximation. At a high degree of ionization and/or high energy of the ions incident onto the surface of a fluorocarbon coating (in experiments with a fluorocarbon plasma, such a coating is almost always present on the discharge tube wall), the processes with ion participation can play a decisive role in both the production and loss of fluorocarbon radicals. Hence, a detailed study of fluorocarbon polymerization under such conditions must self-consistently include an analysis of plasma kinetics and processes involving active neutral particles.

ACKNOWLEDGMENTS

We are grateful to M.A. Basova for her help in preparing the paper and to V.G. Pirogov for assistance in performing Raman spectroscopy measurements of a fluorocarbon film. We deeply regret the tragic death of G.B. Rulev, our young colleague, who greatly contributed to this study. This study was supported by the Russian Foundation for Basic Research (project nos. 00-02-16509 and 00-15-96554) and the NATO Science for Peace Program (grant no. 974354).

REFERENCES

1. H. Yasuda, *Plasma Polymerization* (Academic, New York, 1985).
2. J.-P. Booth, Plasma Sources Sci. Technol. **8**, 249 (1999).
3. G. Cunge and J. P. Booth, J. Appl. Phys. **85**, 3952 (1999).
4. J. P. Booth, G. Cunge, P. Chabert, and N. Sadeghi, J. Appl. Phys. **85**, 3097 (1999).
5. A. D. Tserepi, J. Derouard, J.-P. Booth, and N. Sadeghi, J. Appl. Phys. **81**, 2124 (1997).
6. A. D. Tserepi, W. Schwarzenbach, J. Derouard, and N. Sadeghi, J. Vac. Sci. Technol. A **15**, 3120 (1997).
7. S. Hayashi, H. Nakagawa, M. Yamanaka, and M. Kubota, Jpn. J. Appl. Phys. **36**, 4845 (1997).
8. T. Arai, M. Goto, K. Horikoshi, *et al.*, Jpn. J. Appl. Phys. **38**, 4377 (1999).
9. K. Sasaki, Y. Kawai, C. Suzuki, and K. Kadota, J. Appl. Phys. **82**, 5938 (1997).
10. C. Suzuki, K. Sasaki, and K. Kadota, J. Vac. Sci. Technol. A **16**, 2222 (1998).
11. S. Ito, K. Nakamura, and H. Sugai, Jpn. J. Appl. Phys. **33**, L1261 (1994).
12. M. Haverlag, W. W. Stoffels, E. Stoffels, *et al.*, J. Vac. Sci. Technol. A **14**, 384 (1996).

13. W. W. Stoffels, E. Stoffels, and K. Tachibana, Rev. Sci. Instrum. **69**, 116 (1998).
14. W. W. Stoffels, E. Stoffels, and K. Tachibana, J. Vac. Sci. Technol. A **16**, 87 (1998).
15. R. J. M. M. Snijkers, M. J. M. van Sambeek, M. B. Hoppenbrouwers, and G. M. W. Kroesen, J. Appl. Phys. **79**, 8982 (1996).
16. C. Suzuki, K. Sasaki, and K. Kadota, J. Appl. Phys. **82**, 5321 (1997).
17. K. Miyata, M. Hori, and T. Goto, J. Vac. Sci. Technol. A **14**, 2083 (1996).
18. K. Sasaki, H. Furukawa, C. Suzuki, and K. Kadota, Jpn. J. Appl. Phys. **38**, L954 (1999).
19. M. Haverlag, E. Stoffels, W. W. Stoffels, *et al.*, J. Vac. Sci. Technol. A **12**, 3102 (1994).
20. C. Suzuki, K. Sasaki, and K. Kadota, Jpn. J. Appl. Phys., Part 2, **36**, L824 (1997).
21. C. Suzuki, K. Sasaki, and K. Kadota, Jpn. J. Appl. Phys., Part 1 **37**, 5763 (1998).
22. I. Ishikawa, S. Sasaki, K. Nagaseki, *et al.*, Jpn. J. Appl. Phys., Part 1 **36**, 4648 (1997).
23. J. A. O’Neill and J. Singh, J. Appl. Phys. **77**, 497 (1995).
24. K. Sasaki, H. Furukawa, K. Kadota, and C. Suzuki, J. Appl. Phys. **88**, 5585 (2000).
25. K. Teii, M. Hori, T. Goto, and N. Ishii, J. Appl. Phys. **87**, 7185 (2000).
26. K. Takizawa, K. Sasaki, and K. Kadota, J. Appl. Phys. **88**, 6201 (2000).
27. A. von Keudell, Plasma Sources Sci. Technol. **9**, 455 (2000).
28. A. von Keudell and W. Moller, J. Appl. Phys. **75**, 7718 (1994).
29. M. Shiratani, J. Jolly, H. Videlot, and J. Perrin, Jpn. J. Appl. Phys. **36**, 4752 (1997).
30. K. Sasaki and K. Kadota, Jpn. J. Appl. Phys., Part 1 **38**, 4383 (1999).
31. A. Kono, M. Haverlag, G. M. W. Kroesen, and F. J. de Hoog, J. Appl. Phys. **70**, 2939 (1991).
32. T. Arai, M. Goto, D. Takayama, *et al.*, Jpn. J. Appl. Phys. **34**, L1392 (1995).
33. K. Sasaki, Y. Kawai, C. Suzuki, and K. Kadota, J. Appl. Phys. **83**, 7482 (1998).
34. I. C. Plumb and K. R. Ryan, Plasma Chem. Plasma Process. **6**, 205 (1986).
35. E. Stoffels, W. W. Stoffels, and G. M. W. Kroesen, Plasma Sources Sci. Technol. **10**, 311 (2001).
36. J.-P. Booth, G. Hancock, N. D. Perry, and M. J. Toogood, J. Appl. Phys. **66**, 5251 (1989).
37. V. F. Kiselev and O. V. Krylov, *Adsorption Processes on Semiconductor and Dielectric Surfaces* (Nauka, Moscow, 1978).
38. V. F. Kiselev, S. N. Kozlov, and A. V. Zoteev, *Foundations of Physics of Solid Surface* (Mosk. Gos. Univ., Moscow, 1999).
39. V. A. Radtsig, Khim. Fiz. **14**, 125 (1995).
40. K. Usui, K. Sasaki, C. Suzuki, and K. Kadota, Jpn. J. Appl. Phys., Part 1 **38**, 4373 (1999).
41. K. Sasaki, K. Usui, H. Furukawa, *et al.*, Jpn. J. Appl. Phys. **37**, 5047 (1998).
42. Y. C. Kim and M. Boudart, Langmuir **7**, 2999 (1991).
43. V. N. Kondrat’ev and E. E. Nikitin, *Kinetics and Mechanisms of Gas-Phase Reactions* (Nauka, Moscow, 1974).

Translated by N. Ustinovskiĭ